Remodelage dans les explants orthopédiques et au contact des biomatériaux utilisés en chirurgie osseuse

Louis Rony

To cite this version:

Louis Rony. Remodelage dans les explants orthopédiques et au contact des biomatériaux utilisés en chirurgie osseuse. Médecine humaine et pathologie. Université d'Angers, 2021. Français. NNT : 2021ANGE0045 . tel-03623589

HAL Id: tel-03623589
https://theses.hal.science/tel-03623589

Submitted on 29 Mar 2022

THESE DE DOCTORAT

L'UNIVERSITE D'ANGERS

ECOLE DOCTORALE N° 605
Biologie Santé
Spécialité : « Physiologie, physiopathologie humaine »

Par
Louis RONY

Remodelage dans les explants orthopédiques et au contact des biomatériaux utilisés en chirurgie osseuse

Thèse présentée et soutenue à Angers, le 26 novembre 2021
Unité de recherche : GEROM (Groupe d'Etudes Remodelage Osseux et Biomatériaux)
Thèse N° : 227760

Rapporteurs avant soutenance :

Jean BRILHAULT	Professeur des Universités-Praticien Hospitalier, Université de Tours
Elvire SERVIEN	Professeur des Universités-Praticien Hospitalier, Université de Lyon I

Composition du Jury :

Président :	Martine COHEN-SOLAL	Professeur des Universités-Praticien Hospitalier, Université Paris-Diderot
Examinateurs :	Jean BRILHAULT	Professeur des Universités-Praticien Hospitalier, Université de Tours
	Elvire SERVIEN	Professeur des Universités-Praticien Hospitalier, Université de Lyon I
Dir. de thèse :	Daniel CHAPPARD	Professeur des Universités-Praticien Hospitalier, Université d'Angers
Co-dir. de thèse :	Eric AGUADO	Professeur des Universités, ONIRIS, Nantes

REMERCIEMENTS

A Monsieur le Professeur Daniel CHAPPARD,
Je ne saurais jamais assez vous remercier pour votre aide, votre patience et votre temps pour la réalisation de ce travail qui a tant d'importance pour moi. Si parfois, vous aviez l'impression que je n'étais pas assez présent au labo, sachez que j'ai appris énormément à vos côtés et que vos connaissances tant scientifiques que sur les rouages de la publication ont forcé mon respect et mon admiration. Soyez assuré de mon profond respect et de mon amitié.

A Monsieur le Professeur Eric AGUADO,
Cher Eric, je te remercie pour ton accueil au sein de l'Ecole Vétérinaire, j'ai apprécié les moments passés en ta compagnie à opérer toutes ces brebis. Ta passion pour la recherche et ton engagement dans celle-ci m'inspirent un profond respect. Sois assuré de mon profond respect et de toute ma reconnaissance.

A Madame le Professeur Martine COHEN-SOLAL,
Vous me faites l'honneur de présider mon Jury de Thèse d'Université, je tenais par ces quelques lignes à vous dire à quel point j'ai apprécié votre enseignement lors de mon Master 2 parisien. Votre dévouement pour la recherche et l'enseignement forcent mon respect et mon admiration. Soyez assurée de l'expression de ma profonde reconnaissance et de mon profond respect.

A Madame le Professeur Elvire SERVIEN,
Vous me faites l'honneur de juger ce travail, je vous remercie d'avoir accepté de participer à ce jury de thèse. Votre expertise dans le domaine de la chirurgie orthopédique et votre parcours suscitent mon admiration. Soyez assurée de mon profond respect et de toute ma reconnaissance.

A Monsieur le Professeur Jean BRILHAULT,
Je ne saurais par ces quelques lignes vous dire toute ma considération, mon respect et mon admiration pour votre parcours et votre expertise dans plusieurs domaines que j'essaye moi-même de maîtriser. Vous me faites l'honneur , encore une fois, de m'aider à l'accomplissement de mon parcours universitaire. Soyez assuré de mon entière reconnaissance, de mon profond respect et de toute mon amitié.

A l'équipe du GEROM et du SCIAM,
Hélène, Guillaume, Alexandra, Florence P., Romain, Florence M., je ne saurais par ces quelques lignes vous remercier pour les moments passés au laboratoire, ses petits moments suspendus qui sont une bouffée d'oxygène dans la vie d'un chirurgien. Je vous remercie pour votre accueil, votre disponibilité, pour l'aide que vous m'avez apportée dans la réalisation de ce travail. Soyez assurés de toute mon amitié. J'espère continuer à travailler longtemps à vos côtés.

A l'équipe du Service de Chirurgie Osseuse,
Mes amis, mes frères et mes sœurs, je vous remercie de m'avoir permis d'accomplir ce travail qui est un peu le vôtre également. Sans votre soutien indéfectible dans ce marathon, ce travail n'aurait pu aller au bout. C'est aussi pour vous que je l'ai fait et par ces quelques lignes, je tenais à vous dire toute mon amitié et mon dévouement pour ce service.

~

A ma famille de « quand j'étais petit…»,
Mes chers parents et mes chers frères, je vous remercie d'être là, même si nous ne nous voyions pas beaucoup, sachez que vous êtes toujours tout proches dans mon cœur. Je vous remercie pour votre soutien indéfectible. Et même, si je n'ai pas l'occasion de vous le dire tous les jours, je vous aime.

A Papoum et Baba, j'espère que ce travail scientifique vous rendra fiers. Vous m'avez donné le goût des sciences, je ne saurais jamais assez vous en remercier.

A la famille que j'ai fondée,
Julie, mon amour, quelques mots ne seront pas suffisants pour te dire à quel point je suis fier de ce que nous avons réussi à faire tous les deux et de ce que nous accomplirons encore. Ce travail n'aurait pas pu être possible sans ton aide, ton indéfectible soutien quotidien, ta présence... Je t'aime !
A Anatole, tu ne te rends pas compte mon fils, mais tu as commencé l'école alors que Papa n'a pas encore terminé ses études! Tes sorties, tes rires, tes pleurs illuminent mes journées. Je t'aime, mon fils.
A Emmanuelle, ma pucette, ces quelques mots ne sauraient être suffisants pour te dire à quel point je suis comblé par ta présence. Je t'aime, ma fille.

Sommaire

LISTE DES ABREVIATIONS

TABLE DES ILLUSTRATIONS

INTRODUCTION

1. Le Tissu osseux
1.1. Généralités
1.2. Les cellules osseuses
1.3. La matrice osseuse
1.4. Remodelage osseux et unité fonctionnelle de remodelage
2. L'articulation
2.1. Le cartilage articulaire
2.2. L'os sous-chondral
2.3. Les tissus péri-articulaires
3. Les biomatériaux utilisés en orthopédie
3.1. Les matériaux de comblement
3.2. Les prothèses
ARTICLE 1

PARTIE 1 – DEBRIS D'ALUMINE ET TISSUS PERI-PROTHETIQUES

ARTICLE 2
ARTICLE 3
ARTICLE 4

PARTIE 2 – REMODELAGE OSSEUX, OSTEOINTEGRATION ET IMPLANTS EN TITANE

ARTICLE 5
ARTICLE 6

PARTIE 3 – REMODELAGE OSSEUX ET OSTEONECROSE ASEPTIQUE DE LA TETE FEMORALE

ARTICLE 7
ARTICLE 8
EDITORIAL

CONCLUSION

REFERENCES

Liste des Abréviations

ALVAL :	Aseptic Lymphocyte-dominated Vasculitis Associated Lesion
ARMD :	Adverse Reactions to Metal Débris
BMP :	Bone Morphogenetic Proteins
BMU :	Basic Multicellular Unit
BSU :	Bone structure Unit
EDS :	Energy Dispersive Spectroscopy
FGF :	Fibroblast Growth Factor
FGF 23 :	Fibroblast Growth Factor 23
GAP jonctions :	Jonctions serrées
HPT :	Hormone Parathyroïdienne
IGF I :	Insulin-like Growth Factor I
IGF II :	Insulin-like Growth Factor II
IL-1 :	Interleukine 2
IL-6 :	Interleukine 6
MEB :	Microscopie Electronique à Balayage
microCT :	microtomographie aux rayons X
ONA :	OstéoNécrose Aseptique
OPG :	Ostéoprogestérine
PE :	polyéthylène
PMMA :	PolyMéthylMéthacrylate
PTH :	Prothèse Totale de Hanche
RANK :	Récepteur Activateur de NFκ B
RANK-L :	Ligand du Récepteur Activateur de NFκ B
TGF β1 :	Transforming Growth Factor β1
TGF β2 :	Transforming Growth Factor β2
TNF-alpha :	Tumor Necrosis Factor-alpha
THA :	Arthroplastie Totale de Hanche
UHMWPE :	Ultra High Molecular Weight Polyethylene
3D :	Trois dimensions

Table des Illustrations

INTRODUCTION

1. Le Tissu osseux

1.1. Généralités

Le tissu osseux est un tissu conjonctif de soutient résultant de l'association d'éléments inorganiques (les ions calcium et phosphates) et d'une matrice organique protéique principalement constituée de collagène ; l'ensemble conférant au squelette sa rigidité. Sur le plan anatomique, il existe deux types de tissus osseux : l'os cortical et l'os trabéculaire. L'os cortical forme une couche dense de tissu calcifié et compose l'essentiel de la diaphyse des os longs et représente 80 % du squelette. Le reste (20%) est constitué de l'os trabéculaire organisé en travées formant un réseau tridimensionnel où l'on retrouve majoritairement le tissu hématopoïétique (environ 80% de tissu hématopoïétique pour 20% de matrice osseuse)(1).

L'os cortical est le tissu osseux mécaniquement le plus résistant et des rôles de protection et de soutien lui incombent. Ainsi pour un os très robuste comme le fémur, l'os cortical contribue pour 40 à 60 % de sa résistance globale (2, 3). L'ostéon - ou système de Havers - est l'unité structurale du tissu osseux compact, il est orienté selon les lignes de contrainte (reflétant la direction des charges supportées par les éléments osseux en particulier et le corps en général). Le changement d'orientation de ces lignes est en relation avec l'acquisition de la marche, les entraînements physiques intenses, ou encore les fractures et déformations physiques)(4). La taille et le nombre d'ostéons sont en à mettre en relation avec l'adaptation du système squelettique aux charges infligées pendant la locomotion (5).

L'os trabéculaire constitue la majeure partie des os courts et des os plats et forme un réseau tridimensionnel dans la cavité médullaire. Dépourvu d'ostéons, il est constitué de travées osseuses qui forment une trame anisotrope (6). Elles ont une forme se situant entre le plateau parfait (plaques) et le cylindre parfait (pilier), dont l'épaisseur moyenne est comprise entre 100 et 150 µm et qui créent des espaces de 0,5 à 1 mm de large dans la cavité médullaire (7). Ces espaces contiennent la moelle osseuse, faisant de l'os trabéculaire le site de l'hématopoïèse. Les travées s'orientent le long des lignes de contrainte, de fait la structure trabéculaire change beaucoup avec les variations mécaniques (décharge, compression, modifications des contraintes mécaniques locales) (8, 9). Les ostéocytes (contenus dans des logettes situées dans la matrice osseuse) sont nourris par diffusion à partir des capillaires sanguins de la cavité médullaire.

1.2. Les cellules osseuses

Les ostéoclastes sont issus de précurseurs hématopoïétiques. Ce sont de grandes cellules contenant plusieurs noyaux, caractérisées par une zone d'ancrage sur l'os, une bordure ondulée caractéristique, de nombreuses mitochondries et un appareil de Golgi développé. Ils possèdent un équipement enzymatique important qui permet l'acidification et la dissolution de la phase minérale de la matrice osseuse; des ions H^+ sont produits par une anhydrase carbonique intra cytoplasmique et excrétés dans la chambre de résorption par une pompe à protons (10, 11). Parallèlement des enzymes lysosomiales sont sécrétées (phosphatases acides, cathepsine K, métalloprotéases) qui assurent la dissolution de la phase organique de la matrice osseuse, aboutissant à une lacune de résorption (lacune de Howship). L'action de ces cellules est contrôlée par des hormones systémiques, elle est stimulée par l'hormone parathyroïdienne (HPT) et le métabolite actif de la vitamine D, la 1,25 dihydroxy-vitamine D ($1,25(OH)_2$ D), freinée par la calcitonine et par les œstrogènes. Il existe aussi un niveau de régulation locale, par des cytokines qui comprennent, entre autres, l'IL-1, IL-6 et le TNF-alpha [16]. Plus récemment on a découvert le rôle majeur de l'ostéoprotégérine (OPG), qui s'oppose à RANK et RANK-L (récepteur activateur de NFκ B et son Ligand) dans le contrôle de la résorption osseuse, et on a pu notamment souligner l'importance de ce système en pathologie cancéreuse. Les différents agents impliqués dans la régulation de la résorption conditionnent donc la vie des ostéoclastes et la survenue de leur mort ou apoptose (12, 13).

Les ostéoblastes sont des cellules mononuclées, disposées en couches monocellulaires sur les surfaces osseuses. Ils ont pour fonction d'élaborer un os nouveau après l'action des ostéoclastes (il faut 100 à 1000 ostéoblastes pour reconstituer le volume d'os résorbé par un ostéoclaste). Elles ont un précurseur mésenchymateux (la cellule stromale) commun aux fibroblastes, aux chondrocytes et aux adipocytes. Les ostéoblastes synthétisent des protéines qui constituent une matrice non minéralisée (tissu ostéoïde) composée de collagène de type I et de protéines non-collagéniques (14). Ils produisent également des enzymes (phosphatases alcalines) qui permettent le dépôt de cristaux d'hydroxyapatite et assurent ainsi la calcification de la matrice. Un facteur de croissance, le TGF-alpha, libéré de la matrice osseuse lors de la phase de dissolution de l'os par les ostéoclastes, pourrait être un des facteurs de couplage, le médiateur entre la fin de la résorption et l'initiation de la formation (15).

Les ostéocytes, qui sont en fait d' « anciens ostéoblastes », sont contenus dans de petites logettes (les ostéoplastes). Possédant de longs prolongements, les ostéocytes sont reliés les uns aux autres et communiquent avec la surface osseuse par un système de prolongements cellulaires cheminant dans un système de canalicules ménagés entre les fibres de collagène de la matrice osseuse (16). Ces cellules exercent une influence importante sur la vitalité des autres cellules osseuses, en effet le réseau de canalicules joue un rôle de communication et mécano-récepteur très important avec possiblement le déclenchement de l'apoptose de certaines cellules sénescentes qui activerait l'ancrage des ostéoclastes sur les surfaces osseuses et la mise en place du processus de résorption et de remodelage (17). Ces cellules sont aussi impliquées dans l'initiation de la résorption ostéoclastique car elles peuvent sécréter du RANKL soluble.

1.3. La matrice osseuse

La matrice osseuse comporte une fraction minérale (70 %) et une fraction organique (30 %). Cette dernière est constituée à 90 % par du collagène de type I, les 10 % restants étant constitués par des collagènes mineurs et des protéines non collagéniques parmi lesquels les IGF (insulin like growth factor) I et II, le FGF (fibroblast growth factor), le BMP (bone morphogenetic proteins) et surtout les TGF (transforming growth factor) β1 et β2 qui jouent un rôle important dans la régulation locale du remodelage osseux. Après sa synthèse, la matrice protéique osseuse est minéralisée progressivement grâce à l'action de la phosphatase alcaline libérée dans la matrice par les ostéoblastes. Un sel de calcium (en l'occurrence le phosphate de calcium apparenté à l'hydroxyapatite ($[Ca_{10} (PO_4)_6 OH_2]$) se dépose au niveau des zones situées entre les fibrilles de collagène (18).

1.4. Remodelage osseux et unité fonctionnelle de remodelage

Afin de maintenir l'intégrité du tissu osseux et d'assurer une balance phosphocalcique équilibrée, le squelette adulte est soumis à un remodelage continu. Ce remodelage consistant en l'alternance d'une phase de résorption ou dégradation osseuse et d'une phase de formation osseuse, est soumis à une régulation qui fait intervenir des facteurs systémiques hormonaux et des facteurs locaux. Le remodelage procède par des phases successives qui font intervenir des unités cellulaires fonctionnelles de remodelage, les BMU pour « basic multicellular unit », composées d'un ensemble multicellulaire associant des ostéoclastes, des ostéoblastes et des ostéocytes (19). Le travail de ces unités fonctionnelles de remodelage dure plusieurs semaines et est initié par la formation d'une lacune de résorption grâce à l'action des ostéoclastes. Celle-ci sera rapidement comblée par un os nouveau formé par les ostéoblastes qui élaborent une nouvelle unité de structure osseuse (BSU – Bone structure unit) mieux adaptées aux nouvelles contraintes mécaniques ou métaboliques. La surface des BSU est recouverte de cellules constituées principalement de cellules quiescentes inactives - dites cellules bordantes - qui sont en fait des ostéoblastes en stade terminal de différenciation, et de macrophages tissulaires (20). Les ostéocytes jouent un rôle fondamental dans l'initiation du remodelage osseux : du fait de leur localisation dans la matrice et de leurs nombreuses extensions cytoplasmiques qui leur permettent d'entrer en contact avec les autres types cellulaires, les ostéocytes sont directement impliqués dans l'engagement de la première étape du remodelage osseux dite phase d'activation. Ils sont en effet capables de détecter différents signaux qui vont initier le remodelage osseux, signaux qui seront liés soit à des micro-fractures ou lésion osseuse soit à une action hormonale systémique (15). Ces signaux aboutissent à la mort des ostéocytes par apoptose, processus qui induit, comme cela a été démontré, la production par l'ostéocyte apoptotique du RANKL, cytokine indispensable au recrutement et à la différenciation des précurseurs ostéoclastiques en ostéoclastes matures capables de dégrader la matrice minéralisée. Il est à noter que la sclérostine, produite également par l'ostéocyte, joue un rôle important dans la stimulation de la production de RANKL par l'ostéocyte. La phase de résorption suivant la phase d'activation dure approximativement 12 jours et se termine par la mort par apoptose des ostéoclastes. Après disparition des ostéoclastes, des cellules mononucléées probablement de nature macrophagique apparaissent sur la lacune : c'est la phase d'inversion. Ces cellules sont rapidement remplacées par des précurseurs ostéoblastiques provenant de cellules souches pluripotentes mésenchymateuses également présentes dans la moelle osseuse. Ces précurseurs sont attirés dans la lacune de résorption, prolifèrent rapidement et se différencient en ostéoblastes matures qui assurent la phase de formation osseuse au cours de laquelle une nouvelle matrice protéique est produite qui sera secondairement minéralisée. La phase de formation osseuse est plus longue et dure approximativement trois mois. L'ostéocyte joue donc un rôle majeur dans le contrôle du remodelage osseux via la production de RANKL et de sclérostine. On estime que chaque année, 10 % du squelette adulte est renouvelé. Les activités cellulaires du remodelage osseux sont étroitement couplées dans l'espace et le temps et des interactions entre ostéoblastes et ostéoclastes sont indispensables au bon déroulement de ce processus. Dans des conditions physiologiques, ce processus est régulé de façon à assurer un équilibre parfait entre résorption et formation osseuse, équilibre qui à l'âge adulte est indispensable au maintien de l'architecture et de la masse osseuse (6).

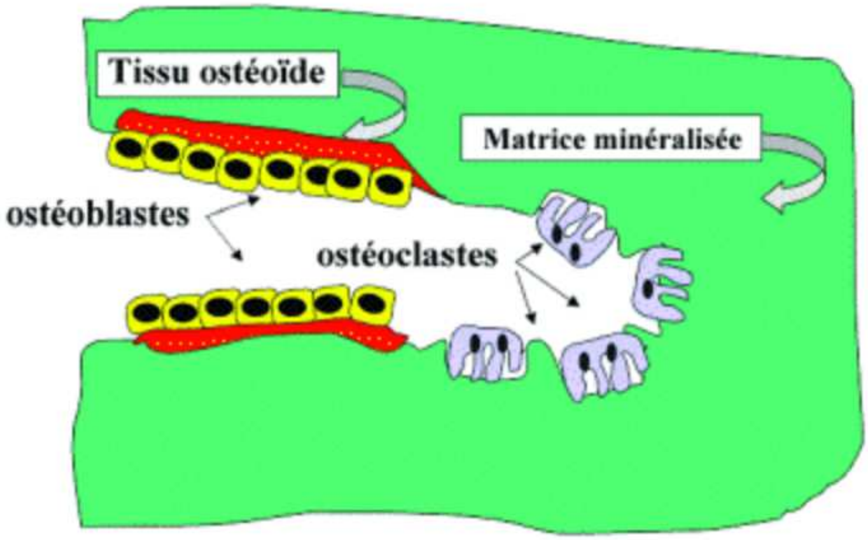

Figure 1 : Organisation d'une Unité Fonctionnelle de Remodelage.

Le remodelage osseux est un phénomène qui est–étudié de longue date (21-24). Il permet l'entretien et l'adaptation du squelette. Il est assuré par les cellules du tissu osseux : les ostéoclastes – cellules résorbantes et les ostéoblastes – cellules formatrices. Le couplage ostéoclastes-ostéoblastes par le biais de différentes hormones est essentiel à l'homéostasie du squelette (25-27). De plus, ce remodelage obéit aux contraintes mécaniques exercées sur le squelette avec de la résorption osseuse dans les zones où les contraintes mécaniques sont faibles et de la construction osseuse dans les zones où les contraintes mécaniques sont fortes (28, 29). Ce phénomène est connu en chirurgie orthopédique puisqu'il peut être observé dans l'ostéointégration des prothèses totales de hanches sans ciment (30-34).

Les techniques modernes d'investigation histomorphométrique ont permis d'améliorer encore la compréhension de ce phénomène (35-37).

2. L’articulation

D’un point de vue histologique, il existe plusieurs types d’articulations : les synarthroses dépourvues de cartilage articulaire et de membrane synoviale, les amphiarthroses où les surfaces osseuses sont recouvertes de cartilage sans membrane synoviale et les diarthroses où les surfaces osseuses sont recouvertes de cartilage articulaire entouré d’une membrane synoviale.

2.1. Le cartilage articulaire

Le cartilage articulaire ou cartilage hyalin est avasculaire et sans innervation. Macroscopiquement, il a un aspect lisse et brillant. Histologiquement, on décrit le cartilage articulaire en quatre couches qui se différencient par leur composition biochimique en protéoglycanes et la disposition des fibres de collagène de type 2.

La partie la plus superficielle au contact du liquide synovial dans l’articulation est la lamina splenda correspondant à une couche acellulaire dont le rôle est de capter les macro-molécules circulant dans le liquide synovial. Sous cette couche, quatre couches sont classiquement décrites : la couche superficielle composée de fibroblastes aplatis qui a une rôle de résistance aux contraintes mécaniques, une couche intermédiaire (ou moyenne) composée de chondrocytes gros et sphériques, une couche profonde (ou radiale) où les chondrocytes sont organisés en colonnes, la couche calcifiée qui est la plus profonde séparée de la précédente par la couche par la *tidemark* (correspondant à une ligne de démarcation) empêchant la pénétration des vaisseaux sanguins dans le cartilage.

Du fait de l’absence de vascularisation, la nutrition du cartilage se fait par diffusion des nutriments à partir du liquide synovial pour sa partie la plus superficielle. Les phénomènes de circulation des fluides au sein de la cavité articulaire sont essentiels pour assurer une trophicité normale du cartilage. Les mouvements intermittents en lien avec le mouvement macroscopique articulaire permettent la pénétration des molécules de haut poids moléculaire en profondeur dans le cartilage (38).

2.2. L'os sous-chondral

L'os sous-chondral, composé d'os trabéculaire, n'a pas qu'une fonction mécanique d'amortisseur, son rôle dans le métabolisme du cartilage est essentiel. En effet, la perfusion des vaisseaux représente plus de 50 % des besoins en glucose, en oxygène et en eau du cartilage. La vascularisation de l'os sous-chondral est une vascularisation terminale. Son atteinte lors de micro ou macro-traumatismes pourrait expliquer des phénomènes de nécrose cartilagineuse retrouvés dans les ostéonécroses, ostéochondrite disséquante ou l'arthrose (39).

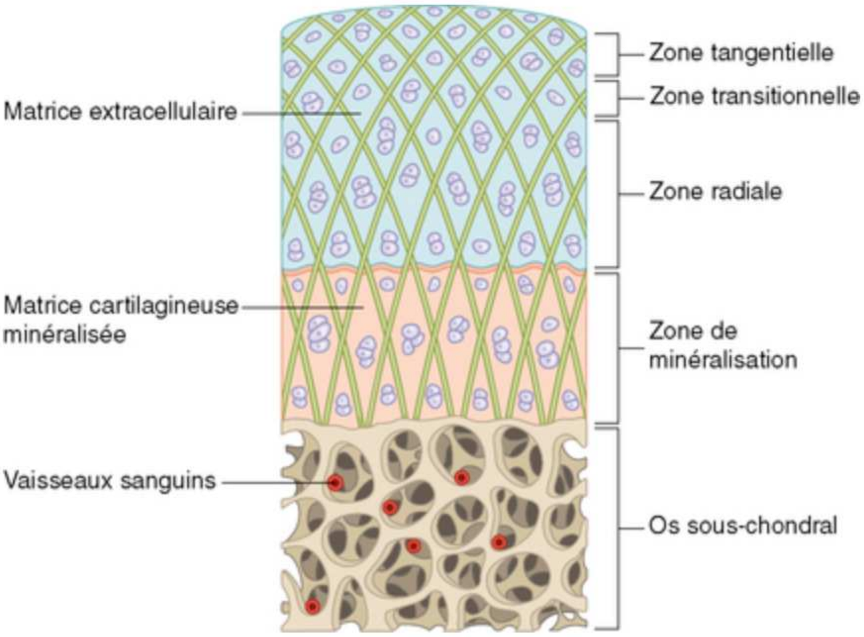

Figure 2 : Organisation du cartilage articulaire

2.3. Les tissus péri-articulaires

Le reste de l'articulation est composé de la membrane synoviale qui a pour rôle de sécréter le liquide synovial qui baigne l'articulation. Il s'agit d'un liquide très visqueux, transparent. Sa composition est schématiquement celle d'un ultrafiltrat du plasma, enrichi de hyaluronate synthétisé par les synoviocytes de type B. Il a pour fonction de réduire la friction en lubrifiant l'articulation, d'absorber les chocs, de fournir de l'oxygène et des nutriments aux chondrocytes du cartilage articulaire en assurant l'élimination des déchets métaboliques (40). Enfin les ligaments, ménisques et capsule articulaire complètent cette structure anatomique fonctionnelle qu'est l'articulation.

Ces éléments d'introduction permettent de mieux comprendre les problématiques qui se posent dans la partie 3 de ce travail où la relation entre le cartilage articulaire et l'os sous-chondral a été étudiée.

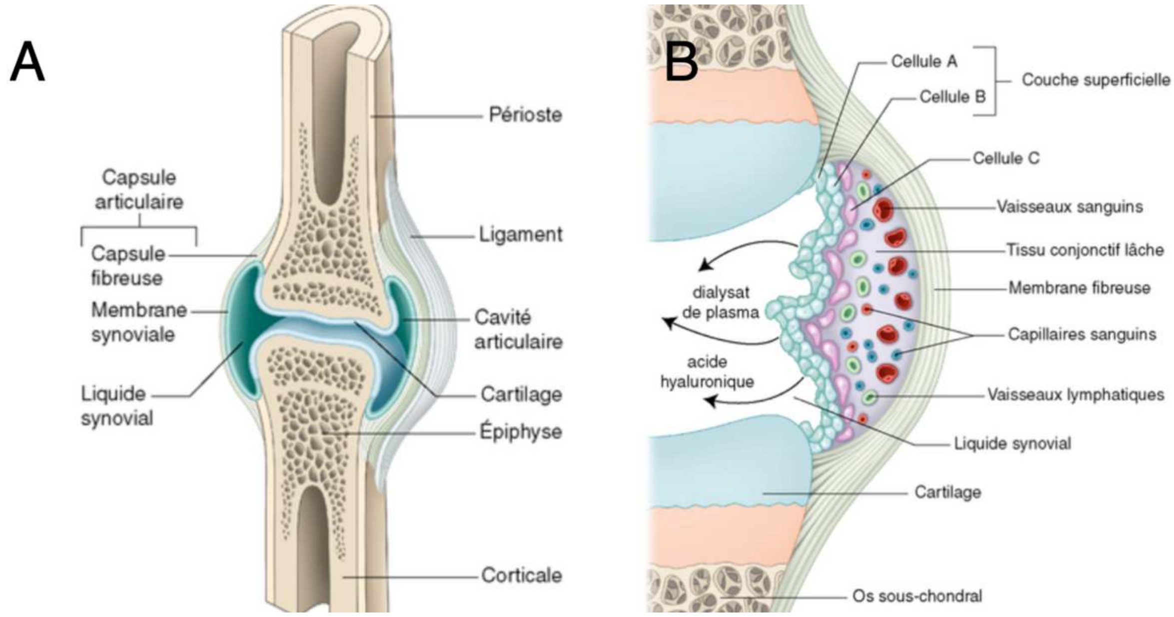

Figure 3 : Organisation d'une articulation de type énarthrose.

3. Les biomatériaux utilisés en orthopédie

Un biomatériau a été défini, selon la Société Européenne des Biomatériaux, comme « matériau conçu pour interagir avec les systèmes biologiques, qu'il participe à la constitution d'un dispositif à visée diagnostique ou à celle d'un substitut de tissu ou d'organe ou encore à celle d'un dispositif de suppléance (ou d'assistance) fonctionnelle ». Il peut ainsi être considéré comme tout matériau utilisé pour remplacer une partie ou une fonction du corps de manière sûre et fiable, acceptable d'un point de vue économique et physiologique.

3.1. Les matériaux de comblement

Les défects cavitaires restent une des problématiques majeures en chirurgie orthopédique. Plusieurs techniques ont été développées pour réaliser le comblement de ces défects cavitaires. Les greffes d'os autologues sont une des techniques à disposition les plus efficaces en termes de restitution du tissu osseux sous-jacent. En effet, il existe tant un effet ostéoconducteur qu'un effet ostéoinducteur. Cependant la morbidité associée et la faible quantité d'os disponible font que leur utilisation doit être faite dans le cadre d'un résultat garanti et d'une absence de lyse de la greffe effectuée (41).

Dans le cadre de la prise en charge de ces défects cavitaires des biomatériaux de synthèse ont été développés, il s'agit de céramiques d'orthophosphates de calcium qui ont pour but de reproduire la phase minérale de l'os. La porosité interconnectée de ces biomatériaux leur apporte des propriétés ostéoconductrices avec une recolonisation par les ostéoblastes au cours du temps avec une ostéointégration progressive (42). Leur utilisation en traumatologie permet d'éviter l'apparition d'un tissu fibreux d'interposition lorsque le défaut osseux de taille critique est atteint dans le cadre d'un défect cavitaire. Il existe deux grands types de céramiques d'orthophosphates de calcium : le phosphate tricalcique ou l'hydroxyapatite (43). Certains laboratoires commerciaux proposent des biomatériaux combinant ces deux biomatériaux, en effet le tricalcium phosphate a une résorption plus rapide que l'hydroxyapatite. Il est important de noter que ces céramiques d'orthophosphates de calcium n'ont que peu de résistance mécanique et sont difficilement implantables en chirurgie orthopédique dans les zones en charge. Afin de pallier ce défaut dans la prise en charge des défects cavitaires où il est nécessaire voire essentiel de pouvoir s'appuyer sur la zone greffée, des biomatériaux métalliques de comblement ont été développés comme le Trabecular Metal™ (Zimmer-Biomet, Warsaw, Indiana, États-Unis). A ce jour, il s'agit du seul biomatériau de comblement métallique ayant l'AMM en Chirurgie Orthopédique (44, 45). D'autres biomatériaux notamment en titane ont été testés en phase préclinique. L'avantage de ces biomatériaux est donc leur résistance mécanique à l'écrasement permettant de supporter la remise en charge tout en associant un degré de porosité interconnectée satisfaisant pour permettre une recolonisation par les ostéoblastes environnants. Cependant, ces biomatériaux autorisent une recolonisation du tissu osseux sur les premiers micromètres du biomatériau à l'interface os-biomatériau. La recolonisation en profondeur du biomatériau n'est probablement pas possible du fait de l'absence de transduction de contraintes mécaniques essentielles à la construction osseuse. Les travaux de la partie 2 de ce travail rapportent l'utilisation en phase pré-clinique de biomatériaux de comblement en titane obtenus par impression 3D.

3.2. Les prothèses

La définition des biomatériaux est très large et englobe les matériaux utilisés pour la confection des prothèses articulaires. Historiquement, plusieurs matériaux ont été utilisés pour la confection des dispositifs médicaux implantables en orthopédie, la première prothèse totale de hanche a été réalisée en ivoire mais les techniques modernes utilisent des alliages métalliques. Les plus utilisés sont le TA6V (Ti6Al4V) composé de titane, il contient également de l'aluminium (jusqu'à presque 7 %) et du vanadium (jusqu'à 4,5 %) ainsi que des traces de carbone, de fer, d'oxygène et d'azote. TA6V ELI correspond à une forme plus pure de l'alliage où la teneur en carbone a été réduite. D'autres alliages de titane comme le TAN (Ti6Al7Nb) utilisent du Niobium à la place du Vanadium, il a été développé en vue de son utilisation dans le secteur médical du fait d'une supposée meilleure biocompatibilité. A ce jour, les industriels utilisent de plus en plus d'alliage de titane au détriment de l'acier inoxydable du fait de meilleures propriétés mécaniques avec un module Young plus proche de celui de l'os (34). De plus, le coût de production des dispositifs en alliage de titane est moindre que celui des produits en acier inoxydable. Outre le corps des prothèses, le titane peut être utilisé comme revêtement pour l'implantation des prothèses sans ciment, en effet, les ostéoblastes possèdent une affinité très forte pour le titane ce qui permet un ancrage très fort entre la prothèse et l'os (46-49).

Les prothèses articulaires sont composées de différentes pièces qui représentent des couples de frottement variables selon la nature des matériaux qui autorisent le mouvement entre les pièces prothétiques. La prothèse totale de hanche peut utiliser plusieurs couples de frottements : des couples durs-durs ou des couples durs-mous. Les couples durs-durs sont représentés par les couples de frottement métal-métal et céramique-céramique. Les propriétés tribologiques permettent à ces couples de frottement une longévité avec une usure linéaire très faible. Pour autant, les couples de frottement métal-métal en acier chrome-cobalt sont le siège d'une corrosion avec une relargage d'ions cobalt, la cobaltémie ne devant pas excéder 2 µg/L. De plus, des complications de type ALVAL (Aseptic Lymphocyte-dominated Vasculitis Associated Lesion) peuvent survenir tout comme des ostéolyses péri-prothétiques sévères ainsi que des pseudotumeurs. Ces complications sont connues sous le nom de ARMD pour Adverse Reactions to Metal Débris (50-54). A ce jour, en France, les couples durs-durs des prothèses totales de hanche sont représentés par l'utilisation de la céramique, là encore, il existe plusieurs types de céramique : la céramique d'alumine pure obtenue par frittage d'oxyde d'alumine, la céramique delta obtenue par le même procédé contient du zirconium (34, 55). Les céramiques présentent d'excellentes propriétés tribologiques tout en ayant l'avantage de ne pas libérer d'ions métalliques. La complication redoutée dans le cadre de l'utilisation de ces biomatériaux est principalement la fracture de la céramique (56).

Même si ces couples de frottement présentent l'avantage d'une usure faible, les couples de frottement dur-mou restent les plus utilisés, ils utilisent l'association d'une bille fémorale en céramique, en acier chrome-cobalt ou en acier inoxydable avec un insert de polyéthylène (PE) (57). L'usure du couple métal-PE a été évaluée à environ 0,1mm par an. Afin de diminuer l'usure du PE, plusieurs méthodes ont été utilisées comme la réticulation du polyéthylène, l'augmentation du poids moléculaire du PE (UHMWPE) ou le dopage des PE à la vitamine E (58-61). Les couples céramique-céramique ont une usure 100 fois moindre que le couple de référence métal-PE (58).

L'utilisation de ces biomatériaux est largement évoquée dans le premier article de ce travail portant sur l'utilisation du métal en chirurgie orthopédique.

ARTICLE 1

Intraosseous metal implants in orthopedics: A review

Les implants métalliques en Chirurgie Osseuse : revue de la littérature

Louis RONY, Romain LANCIGU, Laurent HUBERT

Morphologie 102 : 231-42 (2018)

Cite Score : 2,1 – SIGAPS : NC

Morphologie (2018) **102**, 231—242

ELSEVIER

Disponible en ligne sur
ScienceDirect
www.sciencedirect.com

Elsevier Masson France
EM|consulte
www.em-consulte.com

GENERAL REVIEW

Intraosseous metal implants in orthopedics: A review

Les implants métalliques en Chirurgie Osseuse: revue de la littérature

L. Rony[a,b,*], **R. Lancigu**[b], **L. Hubert**[b]

[a] *Groupe Études Remodelage Osseux et bioMatériaux (GEROM), LabCom NextBone, SFR 42 08, université d'Angers, CHU d'Angers, IRIS-IBS institut de biologie en santé, 49933 Angers cedex, France*
[b] *Département de chirurgie osseuse, CHU d'Angers, 49033 Angers cedex, France*

KEYWORDS
Metal implants;
Biomaterials;
Prosthesis;
Orthopedics

Summary Metal implants are biomaterials widely used in orthopedics. They are both used in osteosynthesis and arthroplasty. Their mechanical properties, biocompatibility and resistance to corrosion make them a widely used option in orthopedics. Alloys are the most commonly used metals in orthopedics. As far as physical traumas are concerned, implants such as screws, plates and/or nails are used for osteosynthesis as they ensure the stability of the fractured area and contribute to bone healing. Prostheses are used in arthroplasty to restore joint function for as long as possible. Contact between bone and the prosthesis induces bone remodeling at the interface between metal and bone even if the metal is recognized as biocompatible. Upon time, the interface between the metal implant and the bony tissue is continuously modified and adapted. Hip prosthesis is a typical example of intraosseous metal implant whose bone/implant interface has been extensively studied. Metal can be altered in vivo by different mechanisms including corrosion and fretting. An altered torque friction leads to wear debris that accumulate in the peri-prosthetic tissues causing metallosis.

Résumé Les implants métalliques sont largement utilisés en orthopédie et appartiennent à la famille des biomatériaux. Ils sont utilisés dans l'ostéosynthèse et l'arthroplastie principalement. Leurs propriétés mécaniques, leur biocompatibilité et leur résistance à la corrosion font qu'ils sont largement employés en orthopédie. Les alliages sont les composants les plus couramment utilisés en orthopédie. Concernant la prise en charge des fractures, des implants tels que des vis, des plaques et/ou des clous sont utilisés pour l'ostéosynthèse, car ils assurent la

---

[*] Corresponding author. GEROM LHEA, université d'Angers, CHU d'Angers, IRIS-IBS institut de biologie en santé, 4 rue Larrey, 49933 Angers cedex, France.
E-mail address: louis.rony@chu-angers.fr (L. Rony).

https://doi.org/10.1016/j.morpho.2018.09.003
1286-0115/

stabilité de la zone fracturée et participent à la guérison de l'os. Les prothèses sont utilisées dans le cadre des arthroplasties pour restaurer la fonction articulaire aussi longtemps que possible. Le contact entre l'os et la prothèse induit un remodelage osseux à l'interface entre le métal et l'os permettant l'ostéointégration du métal reconnu comme biomatériau. L'os étant en perpétuel remodelage, l'interface entre l'implant métallique et le tissu osseux est continuellement modifiée. La prothèse de hanche est un exemple typique d'implant métallique intra-osseux dont l'interface os/implant a été largement étudiée. Un métal peut être altéré in vivo par différents mécanismes notamment la corrosion ou l'usure de contact. Une altération du couple de frottement entre la tête fémorale et le cotyle prothétique provoque la libération des débris qui s'accumulent dans les tissus péri-prothétiques causant ainsi une métallose.

Introduction

The following definition for biomaterials were proposed at the Consensus Conferences in Chester (United Kingdom, 1986, 1991): they represent ''non-viable materials used in a medical device, intended to interact with biological systems, whether they contribute to the constitution of a diagnostic device, a tissue or organ substitute, or even a life support (or assistance) device'' [1]. Biocompatibility means that they are inert in their solid state. This definition is now widely accepted by the scientific and medical communities. In orthopedics, the four biomaterials most commonly used are: metals, polymers, organic materials and ceramics. They must be cyto- and biocompatible and biofunctional. In orthopedics, they also must be hard enough to resist to the mechanical strains that act on cortical bone and they must have a very low friction coefficient like articular cartilage of the joints [2]. Whatever the biomaterial's properties, it will not completely fulfill the characteristics of the human tissues and replacement of a joint with artificial materials can only be a compromise in response to mechanical strains, physicochemical degradation, aging, wear and tear.

In France, more than 2,000,000 people have an orthopedic implant. Industrial engineering constantly adjusts and improves orthopedic devices. The aim is to use the most efficient implants with the best biocompatibility, adapted to each individual and with the longest possible life span [3]. Today, orthopedic implants are mainly produced by metallurgic industry, although there have been attempts in the past to use other types of material such as ivory. One role of the skeleton is to support other organs as bone combines mechanical resistance and elasticity [4]. These properties evolve throughout life as individuals grow and age and depend on a number of genetic and environmental factors (nutrition, hormonal changes, drugs...). Orthopedic devices have different goals depending on their final use: osteosynthesis requires metallic materials that will be possibly removed after bone healing whereas prosthetic devices are used to supply a joint function definitely. Depending on the final function of the device, a metal (or an alloy) can be chosen with an appropriate design (Fig. 1).

Figure 1 Examples of different metal orthopedic devices. A. Total hip prosthesis. B. Cemented femoral stem. C. locking plate for proximal humerus fracture. D. plate for diaphyseal fracture.

The aim of this work was to review the different types of metals used in orthopedic surgery to prepare metal devices for osteosynthesis and prostheses.

Fabrication of devices

Metals exist in the Earth's crust; at the natural state, they exist combined with oxygen or other metals. Different steps are used by the metallurgic industry before the metals can be employed to prepare the orthopedic devices. The process can be resumed in five step:

- mining: extraction of ores in their natural state;
- raw material: a process that transform ores extracted for the Earth's crust into a raw metal material;
- combination of metals, or of a metal with another element to produce an alloy;
- fabrication of the preliminary device: casting, hot isostatic pressing;
- surface treatment: it can be obtained by nitriding, acid etching, polishing or sand blasting.

Figure 2 A. Uncemented femoral stem with a hydroxyapatite coating. B. Uncemented femoral stem with a titanium coating.

On certain devices, it is necessary to have a surface treatment either for cementless femoral stems or for osteosynthesis devices for which a passivation process is essential [5].

The first three steps are common with other industries: car, naval or plane industry... Powdered alloys can be casted at high temperatures. Once the preliminary device has been obtained, additional specific processes are used to prepare the orthopedic devices: polishing remains essential for cemented femoral stems, it also is essential to obtain a low friction torque for implants used for Total Hip Arthroplasty (THA). For uncemented femoral stems, surface treatment increases the roughness thus providing a better anchorage for osteoblasts to recolonize orthopedic devices, e.g. micro or macroporous coatings. They can be obtained by adding metal beads or metal fibers at the surface (Fig. 2). As a high temperature is required to melt these additional materials, this can modify the properties of the original device.

Coarse coatings through sandblasting or corundum grinding are the result of high-speed projection of alumina particles. Such a surface treatment is especially applied to titanium implants.

An alternative is the use of plasma or flame spraying which directly projects the coating onto the desired region. It is a rapid and non-denaturizing process, however, several reports have stressed the inhomogeneity of the deposited layer especially in the case of hydroxyapatite coating [6,7].

Metals used in orthopedics

The most commonly used metals by industry to prepare orthopedic devices are alloys, given that pure metals do not have sufficient mechanical properties to resist the mechanical strains acting on bones. Orthopedic conditions differ in the order of magnitude from those observed in maxillo-facial surgery [8]. Pure metals are never used as such in orthopedics (e.g., platinum, copper or gold) and some metals are highly toxic (e.g., lead).

Stainless steel is commonly used to prepare orthopedic devices. The most common steel has a carbon content of 0.03% and is referred as 316 L (L stands for Low carbon content). It is composed of iron 60—65%, chromium 17—20% and nickel 12—17%. Traces of molybdenum, phosphorus, silicon, manganese sulfur or nitrogen can be found. The low carbon content gives interesting properties with an improve corrosion resistance [6]. Because of its good mechanical resistance properties and relative plasticity, stainless steel remains a first-choice biomaterial for orthopedic devices especially for osteosynthesis [9,10] (Fig. 3).

Cobalt-based alloys are mainly used for arthroplasty devices. There are several cobalt alloys, the most famous being Vitallium® containing cobalt, chromium and molybdenum. The percentage of cobalt in all alloys is greater than 55% and chromium is near 20%. For the ASTM F75 alloy (American Section for Testing Materials), molybdenum represents ~5—7% [6]. Vitallium® remains the most used alloy in orthopedics and is referred as ASTM F75 Co-Cr [11]. Co-Cr alloys are used for their mechanical resistance and good biocompatibility. In addition, some hip prostheses use Co-Cr alloys for their friction torque.

Titanium is never pure but always passivated by a thin Ti oxide layer, the ''commercially pure'' titanium is referred as CP Ti [6,12]. Nevertheless, because of the presence of oxygen, iron, carbon or nitrogen in small amounts, the CP form exists in various ASTM grades and these impurities affect the mechanical resistance. Titanium-based alloys are the most used for orthopedics devices. They are used for osteosynthesis devices and prostheses. Titanium alloys are perfectly compatible and highly resistant to corrosion. The Ti-6Al-4 V alloy (also known as TA6 V) contains aluminum (6%) and vanadium (4%). Its ASTM designation is F136 (grade 5) and it exists in two form: Ti-6Al-4 V or Ti-6AL-4 V ELI (ELI is for Extra Low Interstitial). The ELI form contains less than 0.08% of carbon, 0.0125% of hydrogen, 0.25% of iron, 0.05% of nitrogen and 0.13% of oxygen [6]. Recently, the Ti 6-7™ alloy (ASTM F1295-16, with niobium substituting for vanadium as the beta stabilizing element) was proposed in orthopedic surgery. Titanium alloys are used for osteosynthesis devices like nails or plates because of their high resistance in compression. Furthermore, the Young's module of titanium alloys especially, TAV ELI is close to that of bone. The very good biocompatibility and the great mechanical and corrosion resistances of titanium alloys favor their use for prosthetic stems [13]. Furthermore, generalization of use of titanium devices has reduced the production cost of this type of devices (Fig. 4).

Tantalum has been recently introduced in orthopedic surgery to prepare devices like Trabecular Metal ™ (TM—Zimmer Biomet, USA), a bone filling biomaterial [14]. TM is a scaffold made with more than 98% of tantalum; its pores (550 μm in diameter) create a tetrakaidecahedron shape whose microarchitecture mimics trabecular bone [15]. This confers excellent biocompatibility leading to very good osseointegrative properties (80% of its volume can be

Figure 3 Examples of different stainless steel orthopedic devices.

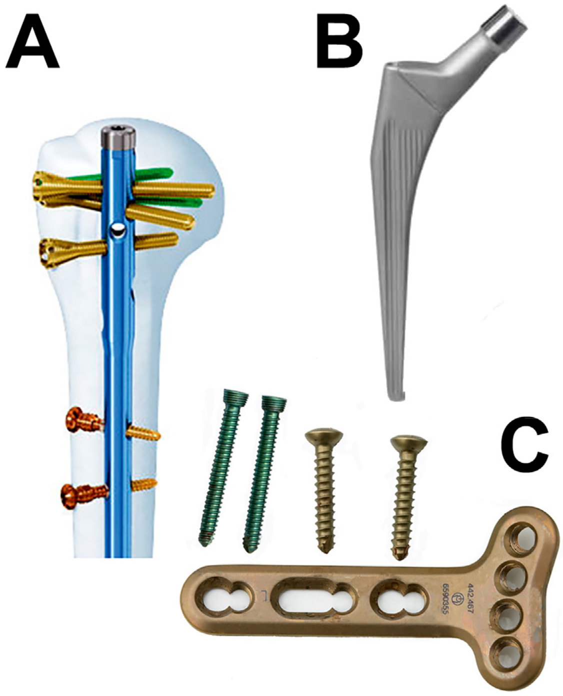

Figure 4 Examples of titanium orthopedic devices. A. Humeral locked nail. B. Femoral stem for hip prosthesis. C. Wrist locked plate with locks screws (left) and regular screws (right).

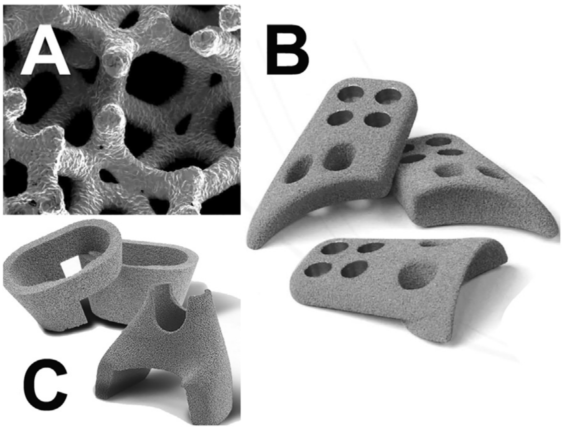

Figure 5 Examples of tantalum orthopedic devices. A. SEM of microarchitecture of tantalum foam. B. Acetabular reconstruction devices for bone defect. C. Knee reconstruction devices for bone defects.

colonized by new bone) [16]. It is mainly used in revisions of total hip or knee arthroplasties as a bone graft in case of cancellous bone defect; however, recently it has been tested for total ankle arthroplasty revision with poor outcomes [17,18] (Fig. 5).

Other types of metals are used as oxides to prepare ceramics such as alumina or zirconia [19]. These ceramics represent another class of biomaterials commonly used in orthopedics implants. Because of their high wear-resistant properties, these inert ceramics are used for their low friction torque. Alumina, a ceramic made with oxide of aluminum Al_2O_3, has been used for more than 40 years for its excellent tribologic properties (friction and wear) for preparing synthetic femoral heads in THA [2]. Zirconia has also been proposed in the same indication mixed with alumina to prepare Ceramic Delta ™ (Ceramtech, France) (Fig. 6).

Implants for osteosynthesis

Osteosynthesis is a surgical procedure, which consists in fixing a fracture with implantable devices made of a biocompatible metal. Its aim is to reduce the bone fragments at the fracture site and stabilize them with implantable devices. There are many devices available for osteosynthesis. For a long time, screws and plates have been the dominant choice in osteosynthesis. Stabilization bring the fractured bone ends together and stabilize the fracture site

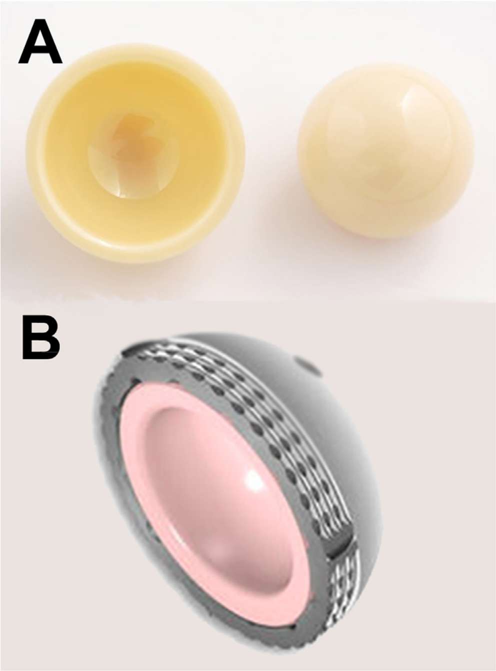

Figure 6 Examples of ceramics used in orthopedics. A. Acetabular and femoral head in alumina. B. Acetabular zirconium inserted in a titanium metal-back.

while healing takes place with a callus. Screws can be used alone or to stabilize a plate. Screws are subject to shearing and tearing stresses and occasionally, fatigue failure of the metal can be observed [20].

Different types of plates have been proposed for various applications:

- neutralization plates, used together with compression screws to avoid fatigue failure of the screws;
- compression plates, they provide static compression along the bone and contribute to the healing process;
- support plates, they protect the fracture from bending loads and shearing stresses;
- tension band wiring plates, they transform the shearing trains into compression strains;
- bridge plates, they align and amplify bone healing by limiting periosteal de-vascularization [21] (Fig. 7).

Stainless steels are most often used to prepare osteosynthesis devices. Advantages are represented by their plasticity and easy technology. Disadvantages are corrosion susceptibility, increased fatigue failure and production cost as it is necessary to heat the alloy at a high temperature for a long time period to obtain alloys with suitable properties [9]. Casted cobalt-chromium alloy is also favored due to its high resistance to corrosion. Its mains disadvantages are low resistance to fatigue, high rigidity and release of chromium in the body fluids. TA6 V is also currently used for its high resistance to fatigue and corrosion. However, the high osseointegrative properties of titanium devices could limit its use for osteosynthesis as it is necessary that devices can be removed easily [22].

Among osteosynthesis procedures, intramedullary nailing (IN) is one of the most recent but remains also one of the best option for diaphyseal fracture [23]. IN is used to stabilize diaphyseal fractures of long bones by inserting a metal nail into the medullary cavity to create a bridge across the fracture fragments. The surgical approach which allows insertion of the materials is generally mini-invasive and represents the best mechanical method for the stabilization of diaphyseal fractures. In order to speed up the insertion of the nail into the medullary cavity and therefore ensure a quicker healing process, the technique of intramedullary reaming was developed by using rasps with increasing calibers to shape the intramedullary canal [24]. This triggers cell signals that stimulate bone healing [25]. The first nailing of a human femur was performed in 1939 by Küntscher, a German surgeon [26,27]. The stable intramedullary nailing of a fracture was performed using a percutaneous approach, which helps wound healing by avoiding loss of the periosteal blood supply. However, this does not avoid the vicious fixation of bone fragments in rotation. It was only in the 1970s that the locking technique was developed and solved the problems caused by rotation [28]. Nowadays, 'locking' nails are the standard: they have holes at each end that can be stabilized with locking bolts to prevent rotation (Fig. 8). The first nails were made from stainless steel, but, today titanium alloy is favored due to its improved mechanical properties [29].

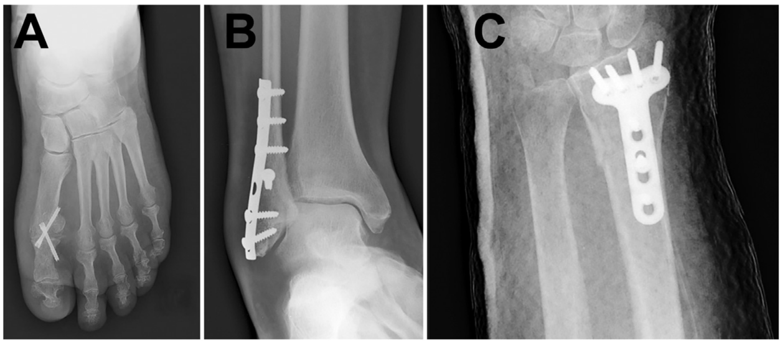

Figure 7 X-ray images of the use of metal implant for osteosynthesis. A. Double screw arthrodesis. B. Osteosynthesis of an ankle fracture. C. Osteosynthesis of a wrist fracture.

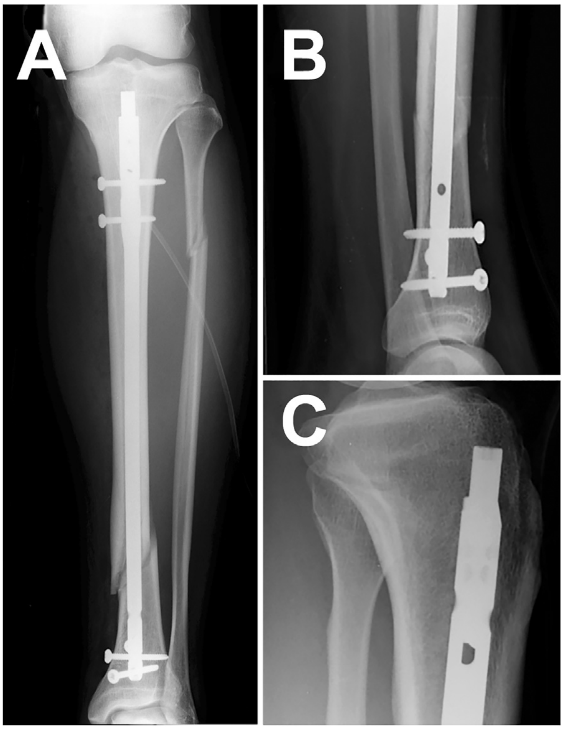

Figure 8 X-ray images of nailing osteosynthesis. A. Tibial fracture with a locked nail. B. Distal locking of the nail a tibial fracture. C. Proximal locking of the nail in a tibial fracture.

Prostheses

Prostheses are designed for the replacement of joints (i.e., arthroplasty). Nowadays, shoulder, elbow, wrist, hip, knee, ankle prostheses... are on the market. These devices have different long-term functional results. For example, hip prosthesis has certainly the best functional results with moreover twenty years of survival [30—32]. The frequency of hip osteoarthritis explains why the development of prostheses especially adapted for this surgery is so successful [33]. Furthermore, the biomechanical function of the joints is a key point for the design of the prosthetic components. Some joints are very complex to model and this may explain why certain prostheses do not have good functional results (e.g., such as elbow or wrist prosthesis) [34]. Another key of a good long-term result for a prosthesis consists in an improved anchorage in bone as a poor anchorage may lead to an aseptic loosening of the prosthesis. Keeping the prosthetic components in the correct position is necessary to ensure that they will last as long as possible. Poor fixation or poor positioning can induce a premature wear with loosening of the prosthesis. Fixation of prostheses with an acrylic cement has been proposed. More recently, alternatives to the use of bone cements have been developed such as surface coatings enabling a direct anchorage in bone [35]. Insuring the most appropriate solution for choosing the friction torque of bearing surfaces is still the matter of debate.

Friction torque is chosen for its biomechanical and tribological properties such as low friction coefficient and low wear production. The misplacement of pieces or the non-anchorage of a prosthesis can induce an abnormal release of wear debris leading to an inflammatory reaction responsible for the prosthesis loosening [36].

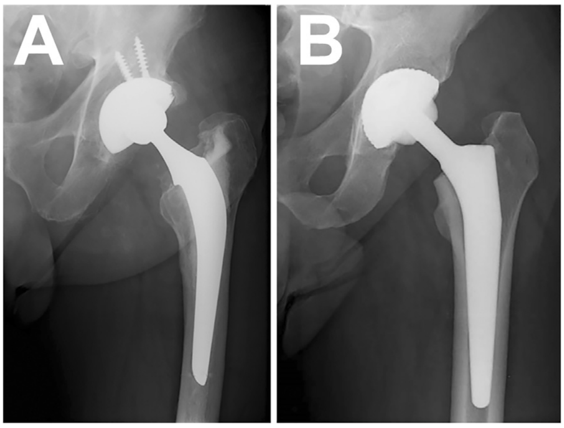

Figure 9 X-ray images of total hip arthroplasties. A. Cemented femoral stem. B. Uncemented femoral stem. Note that the acetabular component is uncemented in each case.

Today, prostheses' pieces are made with metal alloys. Depending on the industry which manufactures the prosthetic pieces, the choice of the alloys will not be the same. Most companies are using Cr-Co alloys for prosthetic pieces but some use Ti-based alloys. The rationale is based on a balance between mechanical properties, resistance at corrosion and production cost. Cr-Co prostheses have a good resistance to corrosion with a low cost of production but the mechanical properties are poorer than Ti-alloys. Moreover, bone anchorage can be a supplementary argument to choose specific metal alloy. Cr-Co alloys can be polished and have less asperities than Ti-Alloys, the goal of this engineering process is favored for prosthesis to be fixed with an acrylic cement (Fig. 9).

Fixation of THA has been thoroughly studied [37]. Cement-free fixation of hip prostheses can be performed in two ways: primary fixation confers stability at the time of implantation (shape, surgical technique, coating); secondary fixation is achieved by improving the implant/bone interface (osseointegration) which guarantees a long-term stability [38,39]. This type of fixation depends on the shape of the implant, the material used and its surface properties. There are many cement-free prostheses available on the market with different shapes: straight stems, anatomic stems, modular stems and tailor-made stems. For the femur, the primary stability can be achieved in two ways [40,41]:

Self-locking stems are straight and are rectangular in section providing diaphyseal locking and sometimes a metaphyseal filling.

Anatomic stems have a metaphyseal part resembling the human anatomy, ensuring an optimal filling and providing a press-fit lockage.

Surface condition must be porous or rough, or alternatively covered with hydroxyapatite (HA) to favor osseointegration. HA coating may occupy parts or the full length of the stem.

Current straight stems are more or less tulip-shaped to help metaphyseal and diaphyseal locking [42].

Anatomic prostheses differ as they are curved in the sagittal plane to fit with the femur shape with an helitorsion axis, so right and left models are provided to achieve metaphyseal locking.

Unlike cemented stems, stems with a polished surface avoid friction and wear and tear of the acrylic cement. Surfaces of cement-free stems are coated to increase their roughness to improve primary bone anchorage and increase the bone/implant interface. Coatings present macro- and microstructures characterized by roughness and porosity. Some coatings prepared with calcium-phosphate deposits are bioactive ceramics.

Bioactive coatings can be calcium-phosphate ceramics such as HA. Since the 1980s, they have been the most often used materials to coat implants. HA is close to the mineral phase of bone. These materials have the advantage of being osteoconductive, i.e. they contribute to bone regrowth and osseous cell colonization. Several studies have shown its biocompatibility, bioactivity, absorbability and its osteoconductive capacity [43,44]. As hydroxyapatite is resorbed, it is replaced by bone. When there is no more hydroxyapatite, bone comes in direct contact with the implant. However, delamination of the HA coatings can lead to loosening of implants stem and final failure *in vivo* [45].

For acetabulum devices, several mechanical solutions can improve the primary stability: impingement, screwing, stabilization with screws or sealing with cement. Impinged cups are used most often. A slightly oversized cup is forcibly slotted into the acetabular cavity — the so-called ''press-fit'' effect. Stability can be improved by adding dewclaws, spikes or screws. The cup can be rigid or elastic (elasticity is obtained through one or many slots which avoid rotation). Coated polyethylene cups can also be impinged and does not require a cement fixation. In screwed cups, primary stabilization is obtained by compression of the implant in bone. However, the holes used for screwing have been found to contribute to migration of wear particles towards the bone acetabulum [46]. Some models possess a screw thread on their external surface which allows a direct insertion in the acetabular cavity [47,48] (Fig. 10).

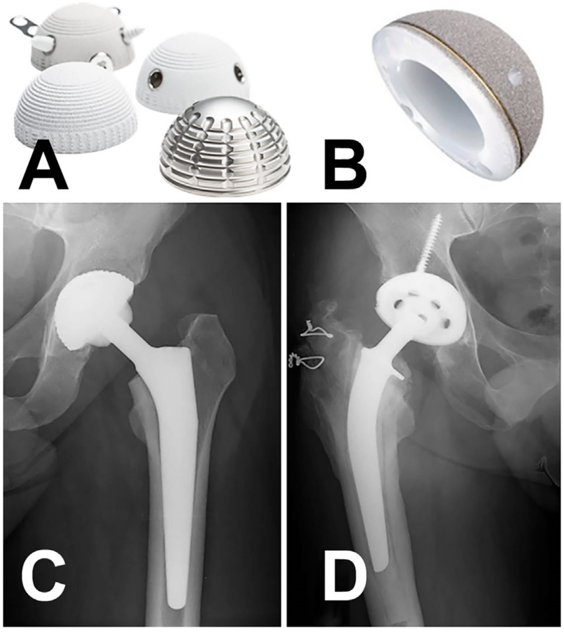

Figure 10 A. Metal-back acetabular component. B. Full polyethylene uncemented acetabular device. C. X-ray of an uncemented acetabular component. D. X-ray of a screwed acetabular component.

Stress shielding

Stress shielding is an adaptive reaction of bone with an implanted device. It can be observed for cementless femoral stems in THA. The difference between the Young modulus of bone and that of a biomaterial used induces modification of mechanical stress resulting in an adaptative remodeling leading to a local reduction in bone density. After THA, a proximal cortical atrophy associated with a distal hypertrophy of periosteal and endosteal envelopes can be observed on X-ray films. Cementless joint replacements rely on an initial ''press-fit'' to obtain a primary mechanical stability. The characteristics of patients, devices, surgical technique, and biomechanical environment determine the extent to which the surrounding bone undergoes remodeling [49]. Whereas there is a decrease in the trabecular bone mass at the proximal femur, it does not generally lead to pain or implant loosening (Fig. 11). The use of a metal prosthetic stem is mandatory, however, it is always a compromise between the mechanical properties and the Young modulus: the stem must be resistant enough but metal alloys being more rigid than bone, they can induce stress shielding. For the acetabular component, the same phenomenon has been observed but differences exist when a full press-fit polyethylene cup is used. These devices have a Young modulus close to bone and stress shielding is rarely observed. Some other prostheses have a metal acetabular cup, and another component (ceramic or polyethylene) is inserted in the metal-back. This induces a loss of iliac trabecular bone at the back of the cup while osteosclerosis is found at the equatorial region of the cup [38]. Stress shielding only concerns press-fit devices used for THA. When a prosthesis is fixed with an acrylic cement, there is no stress shielding because mechanical strains are distributed all over the stem [50]. Even if press-fit devices are commonly used today, the gold standard remains acrylic cement fixation for THA although adding cement as a third component may induce additional problems (see below) [51] (Fig. 12).

Metal corrosion

Corrosion is the destruction of a biomaterial in the body environment [12]. The choice of metals or alloys in orthopedics has been driven by their resistance to corrosion. The need to ensure a minimal corrosion is the major determining factor in the selection of metals or alloys. Noble metals cannot be used to prepare orthopedics devices because of their poor mechanical properties. Furthermore, the cost of these metals limits their use to dentistry or very specific indications for orthopedic (e.g., silver prosthesis in patients with biotherapies for rheumatoid arthritis) [52—54]. Nevertheless, noble metals have the best anti-corrosion properties. The environment to which metal biomaterials are exposed

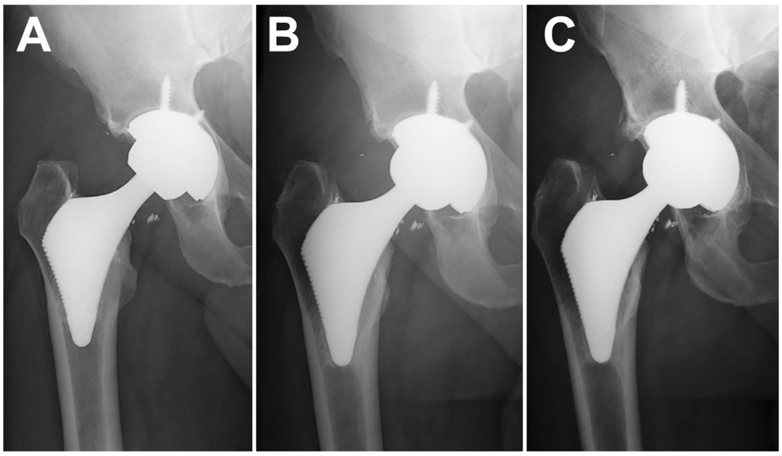

Figure 11 Long-term evolution of an example of femoral stress shielding. A. Immediate postoperative X-ray. B. After three months. C. Twelve months after surgery. Note the progression of osteolysis in the greater trochanter.

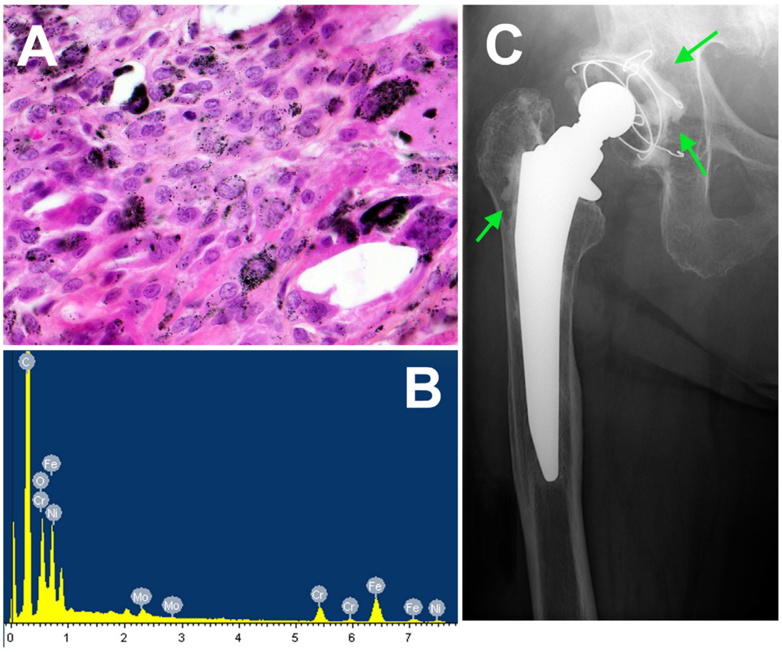

Figure 12 Metallosis (A) histological aspect of metallosis with numerous black wear debris inside the cytoplasm of macrophages. B. Energy X-ray Dispersive Spectrometry of the metal debris with identification of Cr, Ni and Mo. C. X-ray showing the osteolytic foci (green arrows) in the greater trochanter and the coxal bone.

in the human body contains various anions, cations, organic substances and dissolved oxygen. This environment is three time more concentrated than sea water for chloride and four time concentrated for oxygen than air.

Industrial companies use passivated alloys having good mechanical properties and high corrosion resistance. This process consists in oxidizing the superficial layer of the device to prevent reaction between the metal and body fluids [6].

Titanium alloys and stainless steel remains principally used to prepare orthopedic devices. For stainless steel, passivation with chromium oxide is generally used. For Co-Cr-based alloys, chromium oxide remains used for passivation. For titanium alloys, passivation is based on titanium oxide (TiO_x, x indicates that various Ti oxides exist in combination such as TiO_2, Ti_2O_3...). Although passivation is theoretically resistant to corrosion, an *in vivo* corrosion phenomenon is always observed leading to the release of toxic ions at term. It has been reported that Al ions cans be released from TA6 V orthopedic devices and can localize in the immediate bone microenvironment by being complexed with the hydroxyapatite of the bone matrix [55].

Recent papers have shown a release of titanium and deposition in the bone matrix by X-ray fluorescence with a synchrotron [56] and in the nails of the patients [57]. For chromium-cobalt alloys Cr and Co ions can lead to

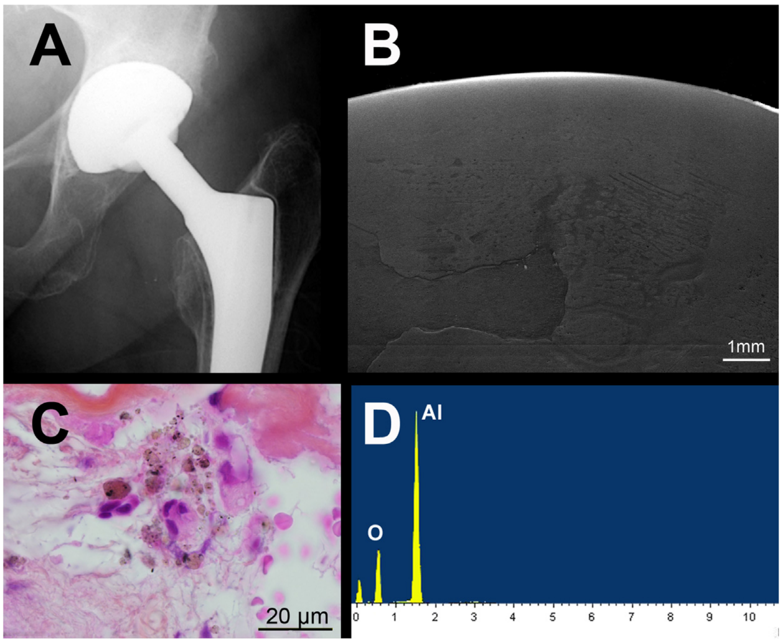

Figure 13 A. Aseptic loosing of an alumina friction torque alumina arthroplasty after five years. B. SEM analysis of the femoral head at low magnification showing a large crater at the surface. C. Histological analysis of the wear debris in the peri-prosthetic tissues. Note the presence of brownish debris in the cytoplasm of macrophages, Hematoxylin-phloxin saffron staining. D. Energy X-ray Dispersive Spectrometry of the ceramic debris with identification of aluminum oxide.

type IV hypersensitivity, a very rare side-effect for metal use in the body [58—60]. Moreover, Cr and Co ions can be nephrotoxic and high concentrations in the blood can lead to irreversible kidney failure. Furthermore, these ions impair the osteoblastic and osteoclastic activities and the mineralization process [61].

There are different specific types of corrosions:

- pitting corrosion is a phenomenon observed for stainless steel implantable devices. In physiological conditions, this localized corrosion can occur as a result of imperfections in the oxide passivation layer. These localized spots will actively corrode and pits will form at the surface of the material;
- fretting corrosion is due to a mechanical process which first remove the passive layer. This kind of corrosion can be observed for osteosynthesis devices when there is a fracture of the material which exposes an internal free surface;
- crevice corrosion is observed for osteosynthesis devices at the area between screws and plate because of the geometry of the interface. Corrosion is due to a difference of potential between the interface between the screw, the plate and body fluids;
- galvanic corrosion is due to the contact between two different metals or alloys [6].

Because of the difference of electric potential, one of the metal will behave as an anode and the other one as a cathode. Thus, there is a displacement of ions dissolved in the body fluid (acting as an electrolyte) and corrosion appears on both metals, thereby mimicking the effect of an electric battery, especially if the environment is acidic [62—64]. The use of different alloy or metals at the same operating area is not recommended in orthopedic surgery.

Metallosis and wear debris

Metallosis is the emission into an organism of metal particles that come from of metal orthopedic devices. It can originate from osteosynthesis devices or prostheses. In the first case, mechanical resistance to fatigue is an essential property of the biomaterial. Stability of a plate or nail is essential for resistance to micro-movements [65]. The material assures the primary stability of the fractured area and avoids the liberation of wear debris. As seen above, fatigue fractures of the device can release metal wear debris in the surrounding tissues (bone, muscle, joint capsule).

For prostheses, metal particles can also be liberated in the surrounding tissues. The most common way is an altered torque friction leading to wear debris. This can occur with metal-on-metal prostheses [66]. The metal-on-metal couple is nowadays less and less popular. With passivated Cr-Co alloys, there is a huge release of metal debris in the tissues and metal ions in the blood [67]. Patients who have received these prostheses need to be followed with Co determination in the blood which must remain $<7\,\mu g/L$ [68]. Some reactions can be very impressive and are known as Adverse Reactions to Metal Debris (ARMD) [69—71], that regroups:

- Aseptic Lymphocytic Vasculitis Associated Lesion (ALVAL) with an incidence of 0.6%;
- liquid or solid mass (pseudo-tumors) developing around a metal-metal prosthesis with an incidence of 0 to 6.5% for heads of diameter $\geq 36\,mm$ and resurfacing;

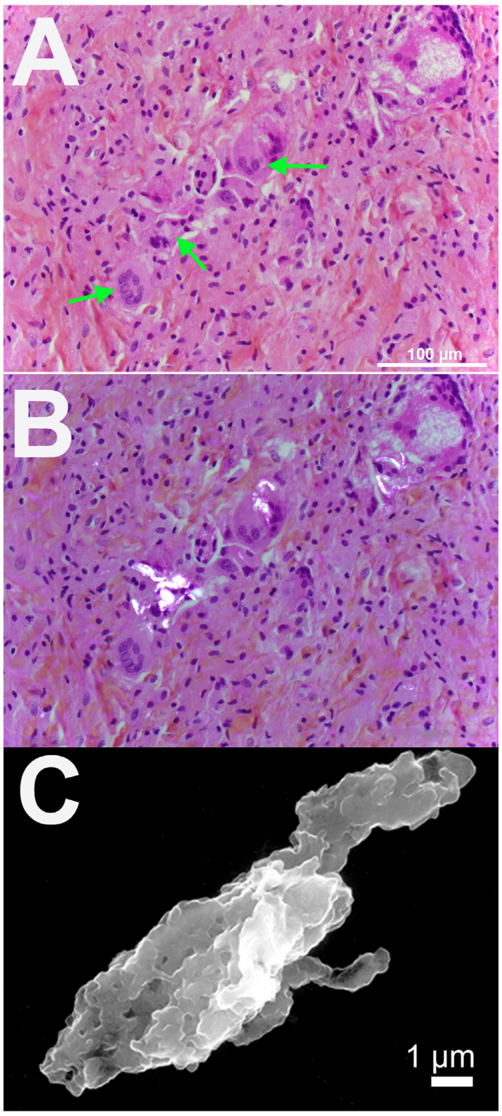

Figure 14 A. Polyethylene wear debris in the periprosthetic tissues retrieved for revision of an aseptic loosening. Hematoxylin-phloxin-saffron staining, bright field imaging. Note the presence of numerous macrophages with an eosinophilic cytoplasm and numerous multinucleated giant cells (green arrows). B. Same field viewed under polarization light: the polyethylene debris are highly birefringent and appear in white. C. SEM analysis of a polyethylene particle isolated from periprosthetic tissues after sodium hydroxide dissolution.

- severe osteolytic peri-prosthetic: hypersensitive type reaction. ARMD reactions are not correlated with a high serum level of Co.

Other hard friction torques are made with alumina ceramics. The alumina-on-alumina couple has been used for several decades because of its high mechanical resistance and excellent biocompatibility [23] (Fig. 13). The tribological properties of the alumina-on-alumina produce a friction torque generating 4000 times less wear particles than the metal-polyethylene couple leading to a low peri-prosthetic osteolysis rate [24,26]. Alumina is one of the hardest material that exists on earth after diamond according to the Mohs' scale. Nevertheless, recent studies have shown that it is possible to find wear debris of alumina in the surrounding tissue of prosthesis [72]. One of the inconvenient of alumina ceramic friction torque is its very high Young modulus that may lead to pain and squeaking after surgery. Moreover, the cost of this ceramic is relatively high. Because of its low wear properties and relatively high cost of production, its use remains restricted to young patients.

The most preferred friction torque consists in a passivated metal alloy head with a polyethylene cup. This friction torque presents some inconvenient such as the release of polyethylene wear debris in the surrounding tissue leading to an inflammatory reaction. Migration of wear debris can also occur in the lymphatic nodes at high distance from the prosthesis [28]. The macrophages try to engulf the polyethylene wear debris but, because of the non-degradability of polyethylene, this induces a chronic inflammatory reaction with giant cells. This chronic inflammatory reaction leads, in turn, to corrosion of the metal head and stem of the prosthesis. In these cases, an association of metallosis and a so-called ''plasticosis'' is observed, aseptic prosthesis loosening being the ultimate complication [73] (Fig. 14).

Conclusion

The use of metals in orthopedic surgery is mandatory. Nevertheless, only certain alloys can be used. The mechanical and also corrosion resistance properties guide the choice of metal alloys. An essential parameter to consider remains the cost of implants indeed. Biocompatibility of the materials used also remains a central issue in the engineering of orthopedic devices for arthroplasty or osteosynthesis. The very serious consequences of these adverse effects are fatigue fracture, corrosion, metallosis and may be avoided by advanced engineering. In addition, the correct use of such materials by surgeons is also a key point to avoid such deleterious consequences. Finally, the increase in demand in orthopedics combined with new technologies such as 3D printing suggest a bright future for the improvement of materials used in arthroplasty and osteosynthesis.

Disclosure of interest

The authors declare that they have no competing interest.

Acknowledgments

SEM and EDS analysis were performed at Service Commun d'Imagerie et d'Analyses Microscopiques (SCIAM), Université d'Angers, thanks to R. Mallet. Many thanks for Prof. D. Chappard for providing the microscopic images.

References

[1] Williams DF. Definitions in biomaterials: proceedings of a consensus conference of the European Society for Biomaterials. Chester, UK: Elsevier; 1987.

[2] Boutin P. Arthroplastie totale de la hanche par prothese en alumine frittee. Étude experimentale et premieres applications cliniques. Rev Chir Orthop Reparatrice Appar Mot 1972;58:229—46.
[3] Moucha CS, Urban RM, Turner TM, Jacobs JJ, Sumner DR, Shanbhag A, et al. Fixation of implants. New York: Taylor and Francis; 2006.
[4] Chappard D, Baslé MF, Legrand E, Audran M. New laboratory tools in the assessment of bone quality. Osteoporos Int 2011;22:2225—40.
[5] Lowry KJ. Contributing to the value equation: how uniform musculoskeletal implant labeling could improve quality and decrease costs for orthopaedic patients. Operative Techn Orthop 2017;27:161—3.
[6] Ratner BD, Hoffman AS, Schoen FJ, Lemons JE. Biomaterials science: an introduction to materials in medicine. Elsevier; 2004.
[7] Yan L, Leng Y, Weng L-T. Characterization of chemical inhomogeneity in plasma-sprayed hydroxyapatite coatings. Biomaterials 2003;24:2585—92.
[8] Guillaume B. Dental implants: a review. Morphologie 2016;100:189—98.
[9] Disegi JA, Eschbach L. Stainless steel in bone surgery. Injury 2000;31:2—6.
[10] Bekmurzayeva A, Duncanson WJ, Azevedo HS, Kanayeva D. Surface modification of stainless steel for biomedical applications: revisiting a century-old material. Mater Sci Engin C 2018;93:1073—89.
[11] Wojnar L, Dąbrowski JR, Oksiuta Z. Porosity structure and mechanical properties of vitalium-type alloy for implants. Mater Charact 2001;46:221—5.
[12] Pohler OE. Unalloyed titanium for implants in bone surgery. Injury 2000;31:D7—13.
[13] Disegi JA. Titanium alloys for fracture fixation implants. Injury 2000;31(4):14—7.
[14] Levine BR, Sporer S, Poggie RA, Della Valle CJ, Jacobs JJ. Experimental and clinical performance of porous tantalum in orthopedic surgery. Biomaterials 2006;27:4671—81.
[15] Zardiackas LD, Parsell DE, Dillon LD, Mitchell DW, Nunnery LA, Poggie R. Structure, metallurgy, and mechanical properties of a porous tantalum foam. J Biomed Mater Res A 2001;58:180—7.
[16] Matsuno H, Yokoyama A, Watari F, Uo M, Kawasaki T. Biocompatibility and osteogenesis of refractory metal implants, titanium, hafnium, niobium, tantalum and rhenium. Biomaterials 2001;22:1253—62.
[17] Aubret S, Merlini L, Fessy M, Besse JL. Poor outcomes of fusion with trabecular metal implants after failed total ankle replacement: early results in 11 patients. Orthop Traumatol Surg Res 2018;104:231—7.
[18] Macheras GA, Lepetsos P, Leonidou AO, Anastasopoulos PP, Galanakos SP, Poultsides LA. Survivorship of a porous tantalum monoblock acetabular component in primary hip arthroplasty with a mean follow-up of 18 years. J Arthroplasty 2017;32:3680—4.
[19] Clarke I, Manaka M, Green D, Williams P, Pezzotti G, Kim YH. Current status of zirconia used in total hip implants. J Bone Joint Surg Am 2003;85:73—84.
[20] Uhthoff HK, Poitras P, Backman DS. Internal plate fixation of fractures: short history and recent developments. J Orthop Sci 2006;11:118—26.
[21] Katthagen JC, Schwarze M, Warnhoff M, Voigt C, Hurschler C, Lill H. Influence of plate material and screw design on stiffness and ultimate load of locked plating in osteoporotic proximal humeral fractures. Injury 2016;47:617—24.
[22] Albrektsson T, Brånemark P-I, Hansson H-A, Lindström J. Osseointegrated titanium implants: requirements for ensuring a long-lasting, direct bone-to-implant anchorage in man. Acta Orthop Scand 1981;52:155—70.
[23] Winquist RA, Sigvard Jr H, Clawson DK. Closed intramedullary nailing of femoral fractures. A report of five hundred and twenty cases. Orthop Trauma Direct 2005;3:29—31.
[24] Hansen ST, Winquist RA. Closed intramedullary nailing of the femur. Küntscher technique with reaming. Clin Orthop Rel Res 1979;138:56—61.
[25] Frost HM. The regional acceleratory phenomenon: a review. Henry Ford Hosp Med J 1983;31:3—9.
[26] Küntscher G. Practice of intramedullary nailing: CC Thomas; 1967.
[27] Küntscher G. The intramedullary nailing of fractures. Clin Orthop Rel Res 1968;60:5—11.
[28] Thoresen B, Alho A, Ekeland A, Strømsøe K, Folleräs G, Haukebø A. Interlocking intramedullary nailing in femoral shaft fractures. A report of forty-eight cases. J Bone Joint Surg Am 1985;67:1313—20.
[29] Hayes J, Richards R. The use of titanium and stainless steel in fracture fixation. Expert Rev Med Dev 2010;7:843—53.
[30] Malchau H, Herberts P, Eisler T, Garellick G, Söderman P. The Swedish total hip replacement register. J Bone Joint Surg Am 2002;84:S2—20.
[31] Romness DW, Lewallen DG. Total hip arthroplasty after fracture of the acetabulum. Long-term results. J Bone Joint Sur Brit 1990;72:761—4.
[32] Lee BP, Berry DJ, Harmsen WS, Sim FH. Total hip arthroplasty for the treatment of an acute fracture of the femoral neck. Long-term results. J Bone Joint Surg Am 1998;80:70—5.
[33] Learmonth ID, Young C, Rorabeck C. The operation of the century: total hip replacement. Lancet 2007;370:1508—19.
[34] Grazioli A, Ek ETH, Rüdiger HA. Biomechanical concept and clinical outcome of dual mobility cups. Int Orthop 2012;36:2411—8.
[35] Malchau H, Herberts P, Ahnfelt L. Prognosis of total hip replacement in Sweden: follow-up of 92,675 operations performed 1978—1990. Acta Orthop Scand 1993;64:497—506.
[36] Nich C, Rampal V, Vandenbussche E, Augereau B. Metal-metal-backed polyethylene cemented hip arthroplasty: mid-term results. Orthop Traumatol Surg Res 2006;92:118—24.
[37] Herberts P, Malchau H. Long-term registration has improved the quality of hip replacement: a review of the Swedish THR Register comparing 160,000 cases. Acta Orthop Scand 2000;71:111—21.
[38] Engh CA, Bobyn J, Glassman AH. Porous-coated hip replacement. The factors governing bone ingrowth, stress shielding, and clinical results. J Bone Joint Surg Br 1987;69:45—55.
[39] Goyenvalle E, Aguado E, Nguyen J-M, Passuti N, Le Guehennec L, Layrolle P, et al. Osteointegration of femoral stem prostheses with a bilayered calcium phosphate coating. Biomaterials 2006;27:1119—28.
[40] Reimeringer M, Nuño N, Desmarais-Trépanier C, Lavigne M, Vendittoli P. The influence of uncemented femoral stem length and design on its primary stability: a finite element analysis. Comput Meth Biomech Biomed Eng 2013;16:1221—31.
[41] Vidalain J-P. Twenty-year results of the cementless Corail stem. Int Orthop 2011;35:189—94.
[42] Sun Y-S, Huang H-H. Biphasic calcium phosphates/tantalum pentoxide hybrid layer and its effects on corrosion resistance and biocompatibility of titanium surface for orthopedic implant applications. J Alloys Compounds 2018;743:99—107.
[43] Søballe K, Overgaard S. The current status of hydroxyapatite coating of prostheses. J Bone Joint Surg Br 1996;78:689—91.
[44] Sumner D, Virdi A. Materials in hip surgery: bioactive coatings for implant fixation. New York; 2013.
[45] Bauer TW. Hydroxyapatite: coating controversies. Orthopedics 1995;18:885—8.
[46] Massin P, Chappard D, Flautre B, Hardouin P. Migration of polyethylene particles around nonloosened cemented femoral

components from a total hip arthroplasty-an autopsy study. J Biomed Mater Res B Appl Biomater 2004;69:205—15.

[47] Clohisy JC, Harris WH. The Harris-Galante porous-coated acetabular component with screw fixation. An average ten-year follow-up study. J Bone Joint Surg Am 1999;81:66—73.

[48] Gaffey JL, Callaghan JJ, Pedersen DR, Goetz DD, Sullivan PM, Johnston RC. Cementless acetabular fixation at fifteen years: a comparison with the same surgeon's results following acetabular fixation with cement. J Bone Joint Surg Am 2004;86:257—61.

[49] Glassman A, Bobyn J, Tanzer M. New femoral designs: do they influence stress shielding? Clin Orthop Relat Res® 2006;453:64—74.

[50] Sumner DR, Galante JO. Determinants of stress shielding. Clin Orthop Relat Res 1991;274:202—12.

[51] Abdulkarim A, Ellanti P, Motterlini N, Fahey T, O'Byrne JM. Cemented versus uncemented fixation in total hip replacement: a systematic review and meta-analysis of randomized controlled trials. Orthop Rev 2013;5:e834—44.

[52] Kose N, Otuzbir A, Pekşen C, Kiremitçi A, Doğan A. A silver ion-doped calcium phosphate-based ceramic nanopowder-coated prosthesis increased infection resistance. Clin Orthop Rel Res 2013;471:2532—9.

[53] Hardes J, Von Eiff C, Streitbuerger A, Balke M, Budny T, Henrichs MP, et al. Reduction of periprosthetic infection with silver-coated megaprostheses in patients with bone sarcoma. J Surg Oncol 2010;101:389—95.

[54] Rodrigues L, Banat IM, Teixeira J, Oliveira R. Strategies for the prevention of microbial biofilm formation on silicone rubber voice prostheses. J Biomed Mater Res B 2007;81:358—70.

[55] Chappard D, Bizot P, Mabilleau G, Hubert L. Aluminum and bone: review of new clinical circumstances associated with Al (3+) deposition in the calcified matrix of bone. Morphologie 2016;100:95—105.

[56] Grenon MS, Robledo J, Ibáñez JC, Sanchez HJ. Titanium diffusion in shinbone of rats with osseointegrated implants. J Microsc 2016;264:182—8.

[57] Berglund F, Carlmark B. Titanium, sinusitis, and the yellow nail syndrome. Biol Trace Elem Res 2011;143:1—7.

[58] Marchetti E, May O, Girard J, Hildebrand H-F, Migaud H, Pasquier G. Biomateriales en cirugía ortopédica. EMC — Téc Quirúrg Ortoped Traumatol; 2010. p. 1—24.

[59] Munro-Ashman D, Miller A. Rejection of metal to metal prosthesis and skin sensitivity to cobalt. Contact Dermat 1976;2:65—7.

[60] Barlow BT, Ortiz PA, Boles JW, Lee Y-y, Padgett DE, Westrich GH. What are normal metal ion levels after total hip arthroplasty? A serologic analysis of four bearing surfaces. J Arthroplasty 2017;32:1535—42.

[61] Mabilleau G, Filmon R, Petrov PK, Baslé MF, Sabokbar A, Chappard D. Cobalt, chromium and nickel affect hydroxyapatite crystal growth in vitro. Acta Biomater 2010;6:1555—60.

[62] Reclaru L, Lerf R, Eschler P-Y, Blatter A, Meyer J-M. Pitting, crevice and galvanic corrosion of REX stainless-steel/CoCr orthopedic implant material. Biomaterials 2002;23:3479—85.

[63] Lucas L, Buchanan R, Lemons J. Investigations on the galvanic corrosion of multialloy total hip prostheses. J Biomed Mater Res A 1981;15:731—47.

[64] Cook SD, Barrack RL, Clemow A. Corrosion and wear at the modular interface of uncemented femoral stems. J Bone Joint Surg Br 1994;76:68—72.

[65] Johnson EE, Marroquin CE, Kossovsky N. Synovial metallosis resulting from intraarticular intramedullary nailing of a distal femoral nonunion. J Orthop Trauma 1993;7:320—420.

[66] Cipriano CA, Issack PS, Beksaç B, Della Valle AG, Sculco TP, Salvati EA. Metallosis after metal-on-polyethylene total hip arthroplasty. Am J Orthop 2008;37:E18—25.

[67] Lardanchet J-F, Taviaux J, Arnalsteen D, Gabrion A, Mertl P. Étude prospective comparative à un an de trois prothèses totales de hanche métal-métal à têtes de gros diamètre : niveau sérique des ions métalliques et résultats cliniques. Rev Chir Orthop Traumatol 2012;98:229—39.

[68] Gleizes V, Poupon J, Lazennec J-Y, Chamberlin B, Saillant G. Intérêt et limite du dosage du cobalt sérique chez les patients porteurs d'une prothèse à couple métal-métal. Rev Chir Orthop Traumatol 1999;85:217—9.

[69] Wiley KF, Ding K, Stoner JA, Teague DC, Yousuf KM. Incidence of pseudotumor and acute lymphocytic vasculitis associated lesion (ALVAL) reactions in metal-on-metal hip articulations: a meta-analysis. J Arthroplasty 2013;28:1238—45.

[70] Hutt JR, Busch C, Hughes RA. Failure of a metal on metal hip prostheses presenting as a destructive soft tissue mass due to ALVAL. Rheumatol Int 2011;31:1401—2.

[71] Gruber FW, Böck A, Trattnig S, Lintner F, Ritschl P. Cystic lesion of the groin due to metallosis: a rare long-term complication of metal-on-metal total hip arthroplasty. J Arthroplasty 2007;22:923—7.

[72] Rony L, de Sainte Hermine P, Steiger V, Mallet R, Hubert L, Chappard D. Characterization of wear debris released from alumina-on-alumina hip prostheses: analysis of retrieved femoral heads and peri-prosthetic tissues. Micron 2018;104:89—94.

[73] Yao Z, Lin T-H, Pajarinen J, Sato T, Goodman S. Host response to orthopedic implants (Metals and plastics). In: Elsevier., editor. Host response to biomaterials. New York: Elsevier; 2015. p. 315—73.

Par ces trois parties, cette thèse a pour but d’améliorer

- de montrer que l’amélioration des techniques de microscopie a permis une analyse plus fine des tissus périprothétiques avec la mise en évidence de particules jusqu’alors non identifiées ou difficilement identifiables.
- d’analyser le remodelage osseux par l’analyse d’une collection de têtes fémorales humaines atteintes d’ostéonécrose aseptique (ONA).
- enfin, nous avons analysé le remodelage du tissu osseux autour d’implants en titane réalisés en impression 3D en nous focalisant sur différentes techniques de mesure de l’ostéointégration.

Partie 1 – Débris d'Alumine et tissus péri-prothétiques

La première partie de ce travail concerne l'analyse des tissus péri-prothétiques dans le cadre d'une reprise de prothèse totale de hanche utilisant un couple de frottement céramique-céramique.

A ce jour en France, il a été réalisé plus de 160 000 arthroplasties totales de hanche. Il existe plusieurs types de prothèses totales de hanche notamment sur l'ancrage osseux utilisant des ciments en PMMA ou *a contrario* des concepts d'ostéointégration sans ciment (34, 62-64). Un autre élément qui peut différer dans les prothèses de hanches est le couple de frottement utilisé, il existe différents concepts, les couples « dur-mou » utilisant un insert acétabulaire en polyéthylène (PE) et une bille fémorale en acier ou en céramique (34, 57). Les couples « dur-dur » sont quant à eux représentés par les couples de frottement métal-métal encore utilisés aux Etats-Unis mais dont l'utilisation en France reste marginale où les couples de frottement alumine-alumine qui sont utilisés (54, 65). Boutin a largement contribué à l'utilisation de ce type de couple de frottement (66, 67).

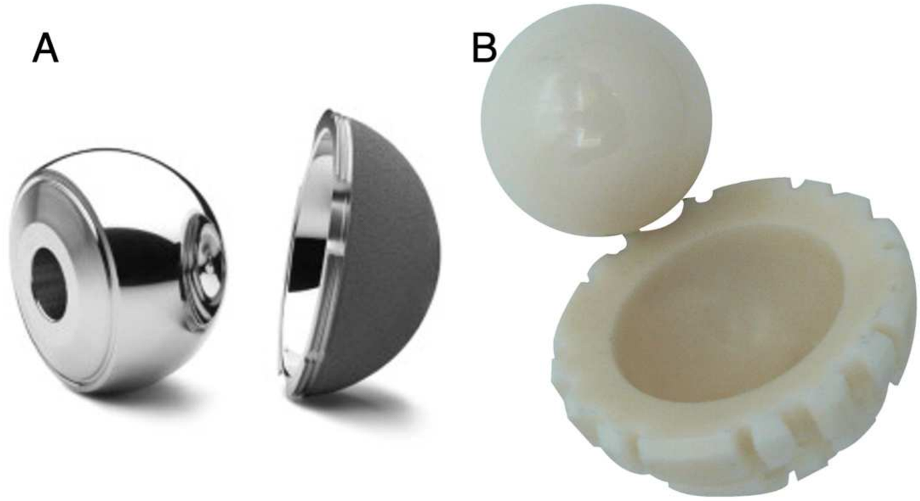

Figure 4 : A- couple de frottement métal-métal. B- couple de frottement céramique-céramique (céramique d'alumine pure).

Le couple de frottement alumine-alumine est utilisé chez les sujets jeunes. En effet, le couple de frottement de référence métal-PE présente une usure linéaire d'environ 0,1mm par an avec un relargage de particules de PE qui est à l'origine d'une réaction inflammatoire entraînant une ostéolyse péri-prothétique (68-72). Cette ostéolyse est responsable à long-terme d'un descellement aseptique conduisant à des reprises prothétiques où une reconstruction osseuse est souvent nécessaire (73-77). Ces chirurgies de reprise sont délicates et les résultats fonctionnels sont moins bons que pour les chirurgies de première intention (78-80). Afin de limiter ce risque de reprise ou tout du moins de le retarder le plus possible, le couple alumine-alumine présente des caractéristiques d'usure bien moindre, en effet son usure linéaire est de 1µm/an soit 1000 fois moins que le couple de référence métal-PE (58, 81, 82). L'utilisation de couple de frottement dur-dur présente également des écueils avec des défauts d'ostéointégration des implants, des phénomènes de squeeking ou d'autres désagréments en lien avec l'implantation de la prothèse qui sont à l'origine de chirurgies de révision prothétique souvent lourdes et péjoratives pour la qualité de vie du patient.

Dans un premier travail, la surface des billes d'alumine de PTH a été analysée, ces têtes en alumine provenaient de patients ayant eu une reprise pour descellement mécanique. L'analyse en microscopie électronique à balayage (MEB) de têtes complètes a permis de retrouver des surfaces endommagées où il existait des cratères avec disparition de la sphéricité de la surface de la bille par rapport à une bille neuve du même diamètre. La présence de ces « érosions » avec mise à jour de la structure interne cristalline de la céramique d'alumine, laisse à penser que des particules d'alumine se déposent dans les tissus péri-prothétiques. Les tissus péri-prothétiques étaient prélevés et adressés simultanément au laboratoire. L'identification de ces particules est très difficile histologiquement, excepté lorsqu'elles sont de grande taille et leur présence est difficilement repérable sur les colorations histologiques de routine (83-87). L'intérêt de ce premier travail était de mettre en évidence d'une part l'érosion des têtes d'alumine laissant suggérer la présence de particules dans les tissus péri-prothétiques. L'analyse histologique des tissus prothétiques mettait en évidence des particules de teinte incolore à beige claire dont seule l'analyse en EDS (Energy Dispersive Spectroscopy) en MEB permettait d'identifier leur composition (aluminium et oxygène) signant leur nature aluminique dans ces échantillons (88, 89)

ARTICLE 2

Characterization of wear debris released from alumina-on-alumina hip prostheses: Analysis of retrieved femoral heads and peri-prosthetic tissues

Louis RONY, Pierre de SAINTE HERMINE, Vincent STEIGER, Romain MALLET, Laurent HUBERT, Daniel CHAPPARD

Micron 104 : 89-94 (2018)

Impact Factor : 1,838 – SIGAPS : C

Micron 104 (2018) 89–94

Contents lists available at ScienceDirect

Micron

journal homepage: www.elsevier.com/locate/micron

Tutorial

Characterization of wear debris released from alumina-on-alumina hip prostheses: Analysis of retrieved femoral heads and peri-prosthetic tissues

Louis Rony[a,b], Pierre de Sainte Hermine[a], Vincent Steiger[a], Romain Mallet[b,c], Laurent Hubert[a,b], Daniel Chappard[b,c,⁎]

[a] *Département de Chirurgie Osseuse, CHU d'Angers, 49933 ANGERS Cedex, France*
[b] *GEROM Groupe Etudes Remodelage Osseux et bioMatériaux – LHEA, IRIS-IBS Institut de Biologie en Santé, CHU d'Angers, Université d'Angers, 49933 ANGERS Cedex, France*
[c] *SCIAM, Service Commun d'Imagerie et Analyses Microscopiques, IRIS-IBS Institut de Biologie en Santé, CHU d'Angers, Université d'Angers, 49933 ANGERS Cedex, France*

ARTICLE INFO

Keywords:
Alumina ceramic
Total hip arthroplasty
Wear debris
Hip joint prosthesis
Scanning electron microscopy
EDS
Polarization microcopy

ABSTRACT

We analyzed by SEM three alumina-on-alumina femoral heads obtained from three patients who underwent revision for an aseptic loosening of the acetabular component. In parallel, the peri-prosthetic tissues were analyzed histologically in search of wear debris coming from the ceramic. Stripe wears, abrasive streaks, craters, and areas with extensive biomaterial removal were evidenced on the three femoral heads by SEM. In the altered area, the structure of the ceramic composed of minute polyhedric grains packed together was evidenced. In the peri-prosthetic tissues, the alumina particles were present in different forms: larges particles appeared transparent and birefringent, small particles engulfed by the macrophages had a light brown tint and were not birefringent. Large particles corresponded to the grains observed by SEM. EDS microanalysis confirmed the presence of aluminum oxide in these particles. Alumina debris are difficult to identify microscopically due to their pleomorphism.

1. Introduction

The placement of a total hip arthroplasty (THA) in patients with end-stage osteoarthritis intends to provide a pain-free and long-lasting functional hip joint in patients with an altered function. Other indications are represented by osteonecrosis of the femoral head and other destructive joint diseases. The total joint implants used to repair the articular surface include a metal component articulating against a polymeric component fabricated from ultra-high molecular weight polyethylene (the classical metal-on-polyethylene couple). This generates high amounts of wear debris in the joint cavity of patients responsible for aseptic loosening as the debris are capable to increase the osteoclastic activity (Massin et al., 2004a,b; Willert, 1977). In addition, these debris can migrate around the prosthesis stem and in the porosity of cortical and trabecular bone (Libouban et al., 2009). They can also accumulate in the lymph nodes at a considerable distance from the prosthesis (Baslé et al., 1996). Several alternatives have been proposed to combine materials with a low friction, good biocompatibility and low wear debris production to ensure a good ten year outcome. Among the different solutions proposed by several surgical groups, total hip prostheses using metal-on-metal (cobalt-chromium CoCr) have been proposed (Garbuz et al., 2010). However, the possibility to develop pseudo-tumors due to metal wear debris has been reported (Pandit et al., 2008). Total hip arthroplasty using alumina ceramic heads and cross-linked polyethylene cups has been proposed (Sugano et al., 1995; Zichner and Willert, 1992). The results in long term studies have reported the possibility for the ceramic head to penetrate in the polyethylene liner and metalback with massive foreign body granulomas (Simon et al., 1998). Zirconia femoral heads were proposed but this ceramic is largely instable and phase changes resulted in a considerable decrease of biomechanical properties with fracture of the material (Hummer et al., 1995). The couple alumina-on-alumina couple have been used for several decades because of the high mechanical resistance and excellent biocompatibility of this ceramic (Hamadouche et al., 2002). The tribological properties of the alumina-on-alumina produce a friction torque generating 4000 times less wear particles than the metal-polyethylene couple and therefore a low peri-prosthetic osteolysis rate is reported (Bizot et al., 2001; Prudhommeaux et al., 2000). Analysis of alumina explants have shown that *in vivo* wear is very low, less than 1 µm/year under normal conditions (Dorlot et al., 1989).

⁎ Corresponding author at: GEROM – LHEA, IRIS-IBS Institut de Biologie en Santé, Université d'Angers CHU d'Angers, 49933 ANGERS Cedex, France.
E-mail address: daniel.chappard@univ-angers.fr (D. Chappard).

http://dx.doi.org/10.1016/j.micron.2017.11.002
Received 26 September 2017; Received in revised form 3 November 2017; Accepted 3 November 2017

The link between the wear of alumina heads and their presence in peri-prosthetic tissues has been seldom studied and only a few studies have concerned the histopathological analysis of peri-prosthetic tissues retrieved at the time of revision of an alumina-on-alumina prosthesis (Lerouge et al., 1996). The aim of our study was to report three patients with a histological analysis of peri-prosthetic tissues taken during revisions of total hip prosthesis with alumina-on-alumina couple and a scanning electron microscope analysis of the removed ceramic beads.

2. Patients and methods

2.1. Patients

2.1.1. Patient #1

This 48 y.o. female patient who presented an aseptic post-traumatic osteonecrosis of the femoral head underwent THA with a prosthesis composed of a hydroxyapatite-coated titanium acetabular component Cerafit HAC™ T-titanium alloy (Ceraver, Roissy CDG, France) an alumina insert, and a short femoral neck (−3.5 mm) receiving an alumina head (28 mm in diameter). The patient presented mechanical hip pain in the postoperative period that were due to a defect in the anteversion of the femoral stem (Fig. 1A). The femoral stem was changed 22 months later; the alumina femoral head was sent for analysis with the peri-prosthetic tissues.

2.1.2. Patient #2

This 61 y.o. female patient underwent THA for an end-stage hip osteoarthritis. The prosthesis was composed of a hydroxyapatite-coated titanium acetabular component Cerafit HAC™ T-titanium alloy (Ceraver), a long neck (+3.5 mm) with an aluminum head (28 mm in diameter). She reported progressive mechanical hip pain which started three years after the THA. X-rays, CTscan and ^{99}Tc-MBP scintigraphy showed an aseptic loosening of the acetabular component (Fig. 1B–C). The revision was done with unipolar change of the acetabular and head components five years after the primary THA.

2.1.3. Patient #3

This 62 y.o. female patient underwent THA for an end-stage hip osteoarthritis. The prosthesis was composed of a hydroxyapatite-coated titanium acetabular component Cerafit HAC™ T-titanium alloy (Ceraver), a short neck (−3.5 mm) with an aluminum head (32 mm in diameter). She reported progressive mechanical hip pain which started five years after the THA. X-rays, CTscan and ^{99}TcMBP scintigraphy showed an aseptic loosening of the acetabular component (Fig. 1D–E). The revision was done with unipolar change of the acetabular and head components eight years after the primary THA.

After examining the transmitted documents and the Rapporteurs' reports, the members of the Ethical Subcommittee of our university hospital approved the use of patient material as the work is retrospective from sampling of bone samples (complementary histological study). Consent was given oral, which is possible in non-interventional study cases. The members of the committee do not raise any objection to the implementation of this study which does not raise ethical questions.

2.2. Histological analysis

The prosthetic materials were carefully harvested at the time of revision, with special precautions being taken to avoid any mechanical damage of the ceramic femoral head during retrieving. The alumina heads were transferred to the laboratory without fixative. Digestion of the remaining organic phase present at the surface of the femoral head was done in a bath of sodium hypochlorite (50% in distilled water) during 24 h. The femoral heads were then extensively rinsed in successive baths of distilled water. They were allowed to dry at room temperature and were glued on brass stubs for scanning electron microscopy (SEM) with a Conductive Carbon Glue (Pelco, Agar Scientifc, Stansted, United Kingdom). They were coated with a 20 nm layer of platinum by sputtering with a high vacuum coater (Leica EM ECA600, Leica, France). Examination was done on an EVO LS10 (Zeiss) field emission microscope equipped with an energy dispersive X-ray microanalysis machine (EDS-INCA- Oxford). Images were captured in the secondary electron mode with an acceleration tension of 3 kV with a 30° tilt and 33 mm working distance. Energy Dispersive X-Ray Spectroscopy (EDS or EDX) is a microanalysis technique that detects X-rays emitted from a sample during bombardment by the electron beam

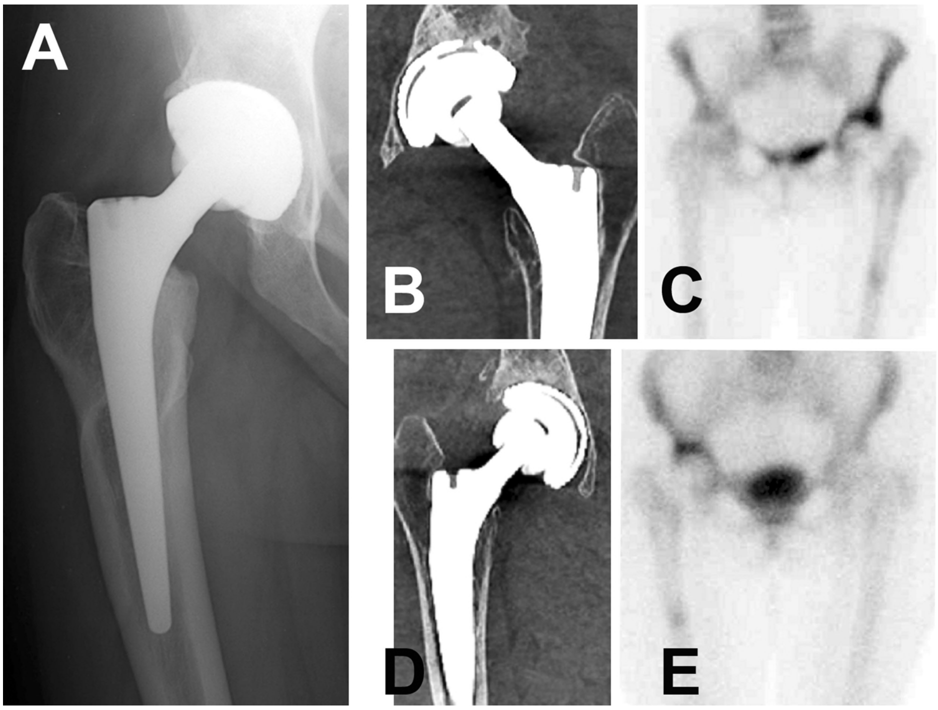

Fig. 1. X-ray analysis of the three patients with aseptic loosening of an alumina-on alumina prosthesis. A) Patient #1 with anteversion of the femoral stem. B-C) Patient #2 CTscan showing an aseptic loosening and ^{99}Tc-MBP scintigraphy showing increased fixation in the iliac bone. D-E) P < ùatient #3 with similar signs on the CTscan and scintigraphy.

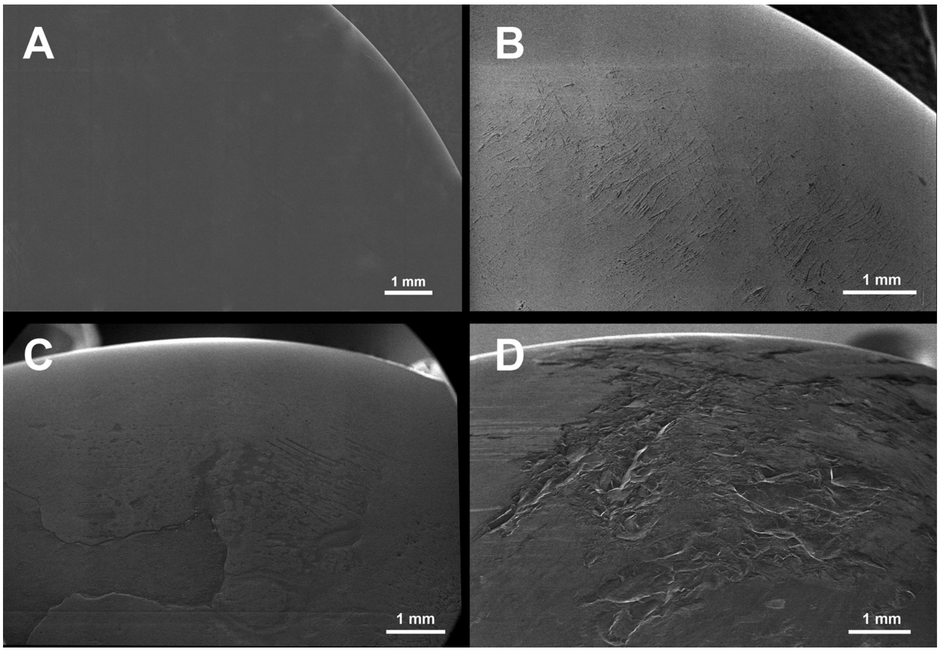

Fig. 2. SEM analysis of the surface of the femoral heads from the alumina prosthesis at low magnification. A) Control surface from a new prosthesis; B) Surface of patient's #1 femoral head showing the occurrence of stripe wears; C) A large planar defect at the surface of patient's #2 femoral head with a marked worn defect of the ceramic material; D) Profound craters observed in patient's #3 femoral head in a wear area.

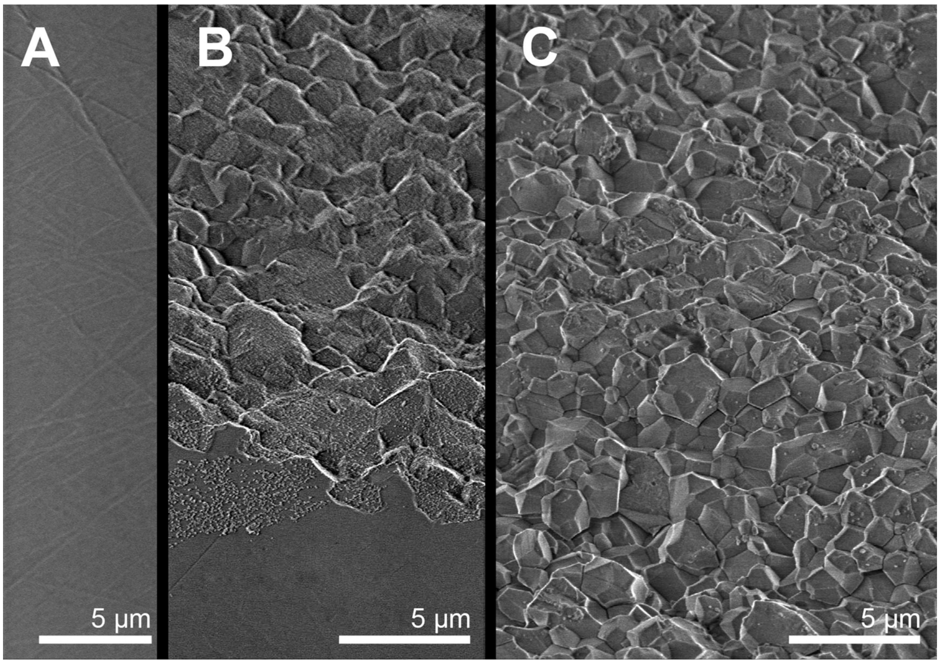

Fig. 3. SEM analysis of the surface of the femoral heads from the alumina prosthesis at high magnification. A) control surface from a new prosthesis with small grooves; B) Surface of patient's #2 femoral head showing the limit between the smooth surface and altered area exposing the ceramic crystals in the depth; C) Surface of patient's #3 femoral head in a deeply altered area showing the exposed grains of the ceramic material.

to characterize the elemental atomic composition present in an analyzed area. The data generated by EDS analysis consist of spectra showing peaks characteristic of the atomic elements of the sample (Goldstein et al., 2012).

In order to compare the surface of the retrieved femoral head with the native aspect of the ceramic, a new prosthesis (32 mm in diameter) from Ceraver was analyzed by SEM.

The peri-prosthetic tissues were harvested during the revision arthroplasty and fixed in formalin. They were embedded in paraffin and sectioned at 5 µm on a rotary microtome. Sections were stained with hematoxylin-phloxin-saffron for routine analysis under bright field and polarized illumination on a BX51 microscope (Olympus, France). The atomic composition of the particles was obtained by analysis of an unstained and dewaxed histological section by SEM and EDS. The sections were carbon-coated by sputtering with a high vacuum coater (Leica EM ECA600). To compare the debris found in peri-prosthetic tissues with true alumina particles, an alumina femoral head was grinded with a rasp. The particles were collected and mounted with NeoEntellan™ (Merck-France) on a histological glass slide. They were analyzed by SEM in the backscattered electron mode at 11 and 20 kV; an EDS analysis was done on the selected particles.

3. Results

3.1. Scanning electron microscopy

The alumina femoral heads from the three patients, made free from any cellular remnants, exhibited various signs of abrasion at their

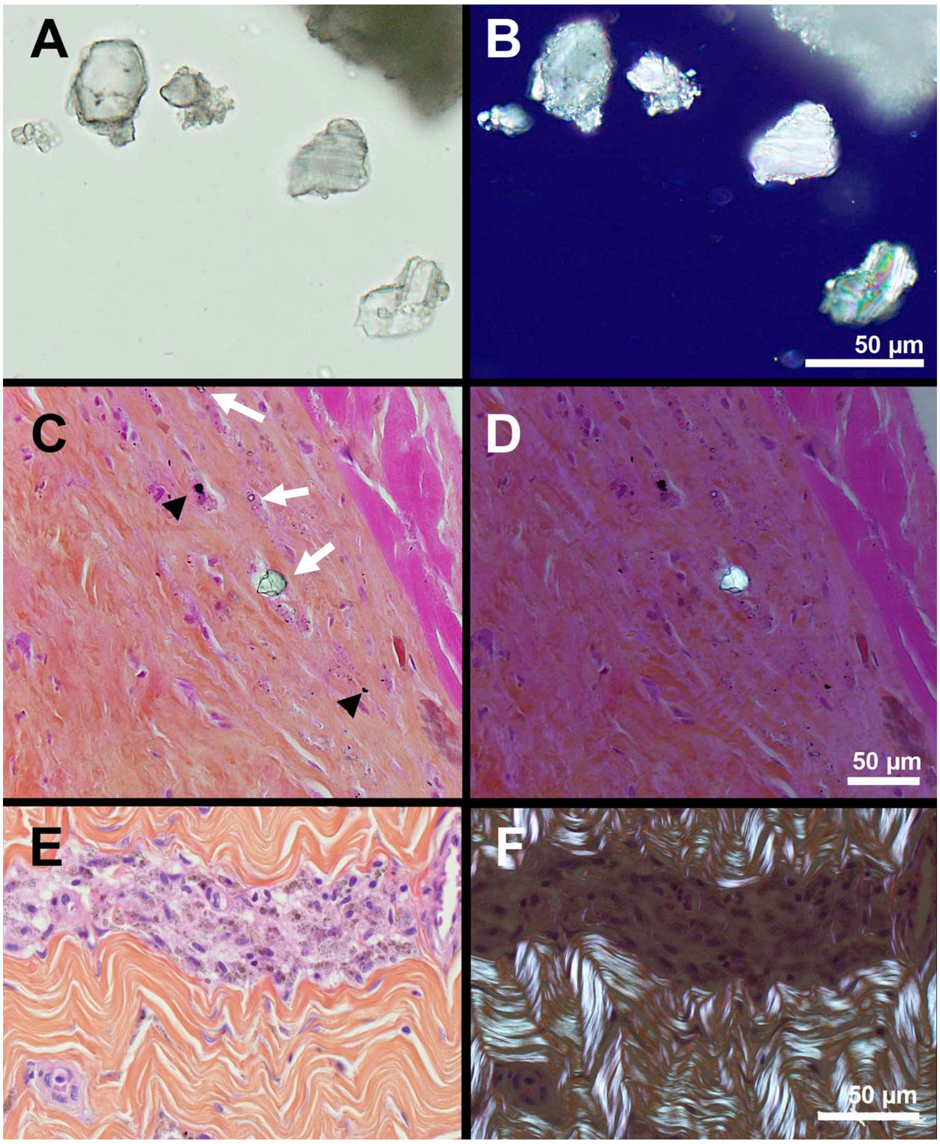

Fig. 4. Microscopic analysis of alumina particles grinded from a control femoral head under bright field microscopy (A) and polarized light with a ¼ waveplate (B). Note the glossy appearance of these large particles which are birefringent. C-D) Peri-prosthetic tissues from patient's #2 analyzed under bright field and polarized light. Large and small alumina particles with the same characteristics than those of Fig. 4A are observed (white arrows). They are associated with metal wear debris (black arrowheads) in macrophages. E) Peri-prosthetic tissues from patient's #3 analyzed under bright field, numerous brownish particles with a variable size are observed in the cytoplasm of macrophages encapsulated in collagenous bundles. F) Same section analyzed under polarized microscopy, the small alumina particles are not birefringent, only the collagen fibers of the fibrosis are birefringent.

surface. Fig. 2 reports the analysis at low magnification of the surface aspects of the ceramic prostheses. The new (unused) femoral head presented a smooth surface with minimal and randomly oriented striations (Fig. 2A). The implanted prostheses had focal areas with profound abrasive streaks, craters, and areas with extensive biomaterial removal (Fig. 2B–D). At higher magnifications, the structure of the ceramic, composed of compacted elementary grains became easily visible in the altered areas (Fig. 3).

3.2. Histological analysis

The alumina particles grinded from the test ceramic head presented a transparent and glossy appearance under bright-field microscopy. Under polarized light (with a ¼ waveplate) these particles were birefringent (Fig. 4A–B). In the peri-prosthetic tissues, the alumina particles were present in two different forms: i) large particles (i.e., 15–20 µm) had the same glossy appearance than the ground particles and were birefringent under polarized light. Smaller particles were also translucent but were not evidenced under polarized light (Fig. 4C–D); ii) small (1–3 µm) particles with a light brownish tint were observed in the cytoplasm of activated macrophages disposed in dense clusters between fibrotic areas (Fig. 4E). These particles were not birefringent under polarized light (Fig. 4F). In the three patients, the presence of black particles corresponding to wear metallic debris was also observed, sometimes associated with the alumina particles.

3.3. EDS analysis

Prosthetic alumina heads: EDS analysis confirmed the atomic composition of the ceramic biomaterial being made of aluminum oxide and gave similar results in the three cases (Fig. 5). The spectra from retrieved femoral heads were similar to those obtained on the new prosthesis. The spectra were similar in the different areas analyzed, at the smooth surfaces on in the altered areas.

Histological sections: EDS analysis performed on each type of particles (small or large) revealed their atomic composition made of aluminum oxide. EDS analysis also confirmed the presence of titanium particles (TA6 V alloy) (Fig. 5F).

4. Discussion

The alumina-on-alumina prostheses were proposed more than four decades ago as an alternative to the polyethylene-metal couple in hip joint surgery. Alumina is reported to be chemically inert and stable. A

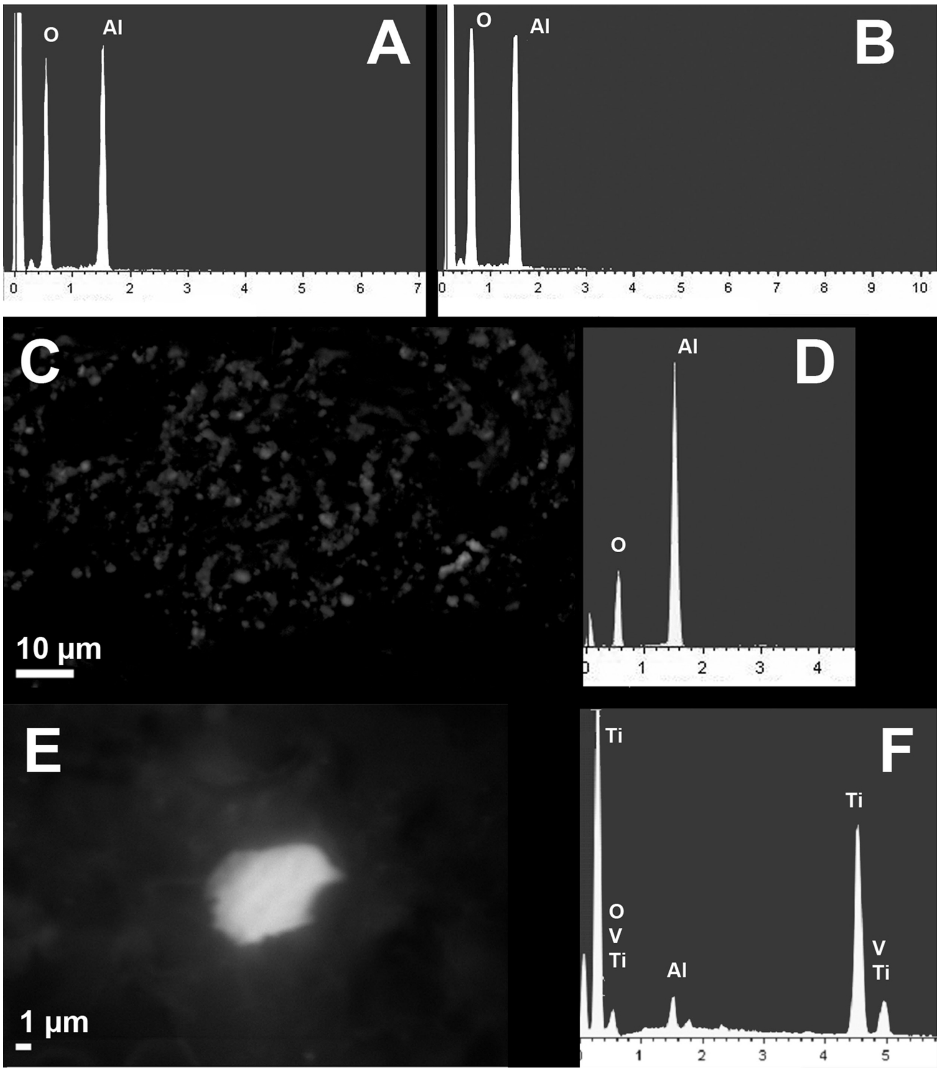

Fig. 5. EDS analysis of the alumina femoral heads and histological section. A) EDS analysis of the new ceramic head and B) EDS analysis of patient's #3 ceramic in an altered area. Both spectra identify aluminum and oxide peaks characteristic of alumina. C) Backscattered image of a dewaxed section showing alumina particles present in the peri-prosthetic tissues of patient #2. D) EDS analysis showing the characteristic peaks for O and Al in these particles. E) Backscattered image of a dewaxed section showing a titanium particle present in the peri-prosthetic tissues of patient #2. F) EDS analysis showing the peaks for Ti, V and Al characteristic of the TA6 V alloy.

number of study have confirmed that the wear debris production is reduced but not suppressed (Prudhommeaux et al., 2000). More recently, it was found that ceramic combining alumina and zirconium oxide had an improved mechanical resistance (Affatato et al., 2001; Massin et al., 2014; Moraes et al., 2004). However, an audible squeak is reported in some patients having an alumina-on-alumina prosthesis and friction of the different components is advocated (Jarrett et al., 2009; Mai et al., 2010). In our series, no patient reported this phenomenon and the revision was indicated after a malposition or an aseptic loosening in two cases. Alumina particles, and also titanium or polyethylene wear debris, can stimulate bone resorption in the vicinity of the prosthesis by inducing the production of inflammatory cytokines (Bylski et al., 2009).

In the present study, we could analyze the surface of three alumina femoral head obtained surgically at the time of prosthetic revision. They exhibited various aspects of erosion of their surface ranging from linear stripe wears to marked craters. In all cases, the elementary alumina grains were observed with sharp facets by SEM. EDS analysis confirmed that alumina was the unique component of these femoral heads. Due to the impossibility to analyze the large acetabular cups in our SEM, only the femoral heads were considered. Other authors have shown wear areas in the acetabular component by macroscopic techniques (Esposito et al., 2012; Park et al., 2006) but a few study have analyzed the surface of alumina femoral heads. Some results were presented by Affato on alumina-zirconium femoral heads analyzed by SEM but the mechanical resistance is markedly different (Affatato et al., 2012). In this study, we were able to analyze both the peri-prosthetic tissues and the femoral heads of these patients. In the literature, the microscopic appearance of these particles is not clearly identified. It is reported that alumina particles are polymorphous and difficult to identify. It is reported that small particles (~1 µm) are amorphous, brown or yellowish and do not bend polarized light (Pizzoferrato et al., 1993). This aspect was observed in our patient #3. Larger particles have a polyhedral aspect that correspond to the ceramic crystals observed by SEM at the surface of the damaged femoral heads. This aspect has also been shown when large samples of peri-prosthetic tissues are analyzed by SEM and EDS (Hatton et al., 2002). In this study, we encountered such large alumina particles that were birefringent under polarized light. They correspond to the detachment of large groups of smaller sized shards. This aspect is confirmed when similar large particles are prepared by grinding a femoral head. Because alumina is not stained by classical dyes such as aluminon or solochrome azurine which only work on undecalcified bone sections, no attempt was done to characterize the particles by these histochemical methods (Chappard et al., 2016). The presence of alumina particles in the peri-prosthetic tissues can come from the intra-articular surface (as shown here), the neck impingement of the acetabular component and from the direct contact of the acetabular cup with the fixation screws (Lerouge et al., 1996). Alumina particles are abrasive and can provoke wear of the titanium stem of the prosthesis. Particles of metal are often observed together with the alumina debris and are phagocytized by activated macrophages. If the stem of the prosthesis is cemented, other types of particles can be encountered such as barium sulfate or zirconium oxide used to make the cement radio-opaque (Lerouge et al., 1996). In this small series of patients, the three stems were uncemented and only titanium particles were observed.

5. Conclusion

Alumina-on-alumina prostheses have been proposed in hip surgery. They can produce wear debris at the acetabulum and femoral head which can migrate in the prosthesis environment. Alumina debris are difficult to identify on microscopic sections due to their pleomorphism. Although the alumina-on-alumina couple is reported to be very stable, wear debris can be identified, polarization microscopy is able to identify large particles but smaller ones are not birefringent.

Conflict of interest

Authors have no conflict of interest.

Acknowledgments

This work was made possible by grants from the French Ministry of Research.

References

Affatato, S., Goldoni, M., Testoni, M., Toni, A., 2001. Mixed oxides prosthetic ceramic ball heads. Part 3: effect of the ZrO 2 fraction on the wear of ceramic on ceramic hip joint prostheses. A long-term in vitro wear study. Biomaterials 22, 717–723.

Affatato, S., Traina, F., De Fine, M., Carmignato, S., Toni, A., 2012. Alumina-on-alumina hip implants. J. Bone Joint Surg. Br. 94, 37–42.

Baslé, M.F., Bertrand, G., Guyetant, S., Chappard, D., Lesourd, M., 1996. Migration of metal and polyethylene particles from articular prostheses may generate lymphadenopathy with histiocytosis. J. Biomed. Mater. Res. 30, 157–163.

Bizot, P., Nizard, R., Hamadouche, M., Hannouche, D., Sedel, L., 2001. Prevention of wear and osteolysis: alumina-on-alumina bearing. Clin. Orthop. Rel. Res. 393, 85–93.

Bylski, D., Wedemeyer, C., Xu, J., Sterner, T., Löer, F., von Knoch, M., 2009. Alumina ceramic particles, in comparison with titanium particles, hardly affect the expression of RANK-, TNF-α-, and OPG-mRNA in the THP-1 human monocytic cell line. J. Biomed. Mater. Res.—Part A 89, 707–716.

Chappard, D., Bizot, P., Mabilleau, G., Hubert, L., 2016. Aluminum and bone: review of new clinical circumstances associated with Al deposition in the calcified matrix of bone. Morphologie 67, 3–8.

Dorlot, J.M., Christel, P., Meunier, A., 1989. Wear analysis of retrieved alumina heads and sockets of hip prostheses. J. Biomed. Mater. Res.—Part A 23, 299–310.

Esposito, C., Walter, W., Roques, A., Tuke, M., Zicat, B., Walsh, W., Walter, W., 2012. Wear in alumina-on-alumina ceramic total hip replacements. J. Bone Joint Surg. Br. 94, 901–907.

Garbuz, D.S., Tanzer, M., Greidanus, N.V., Masri, B.A., Duncan, C.P., 2010. The John Charnley award: metal-on-metal hip resurfacing versus large-diameter head metal-on-metal total hip arthroplasty: a randomized clinical trial. Clin. Orthopaedics Relat. Res. 468, 318–325.

Goldstein, J., Newbury, D.E., Echlin, P., Joy, D.C., Romig Jr., A.D., Lyman, C.E., Fiori, C., Lifshin, E., 2012. Scanning Electron Microscopy and X-ray Microanalysis: a Text for Biologists, Materials Scientists, and Geologists. Springer Science & Business Media.

Hamadouche, M., Boutin, P., Daussange, J., Bolander, M.E., Sedel, L., 2002. Alumina-on-alumina total hip arthroplasty. J. Bone Joint Surg. Am. 84, 69–77.

Hatton, A., Nevelos, J., Nevelos, A., Banks, R., Fisher, J., Ingham, E., 2002. Alumina–alumina artificial hip joints. Part I: a histological analysis and characterisation of wear debris by laser capture microdissection of tissues retrieved at revision. Biomaterials 23, 3429–3440.

Hummer, C.D., Rothman, R.H., Hozack, W.J., 1995. Catastrophic failure of modular Zirconia—Ceramic femoral head components after total hip arthroplasty. J. Arthroplasty 10, 848–850.

Jarrett, C.A., Ranawat, A.S., Bruzzone, M., Blum, Y.C., Rodriguez, J.A., Ranawat, C.S., 2009. The squeaking hip: a phenomenon of ceramic-on-ceramic total hip arthroplasty. J. Bone Joint Surg. Am. 91, 1344–1349.

Lerouge, S., Huk, O., Yahia, L.H., Sedel, L., 1996. Characterization of in vivo wear debris from ceramic—ceramic total hip arthroplasties. J. Biomed. Mater. Res.—Part A 32, 627–633.

Libouban, H., Massin, P., Gaudin, C., Mercier, P., Baslé, M.F., Chappard, D., 2009. Migration of wear debris of polyethylene depends on bone microarchitecture. J. Biomed. Mater. Res. B Appl. Biomater. 90, 730–737.

Mai, K., Verioti, C., Ezzet, K.A., Copp, S.N., Walker, R.H., Colwell, C.W., 2010. Incidence of 'squeaking'after ceramic-on-ceramic total hip arthroplasty. Clin. Orthop. Rel. Res. 468, 413–417.

Massin, P., Chappard, D., Flautre, B., Hardouin, P., 2004a. Migration of polyethylene particles around nonloosened cemented femoral components from a total hip arthroplasty-an autopsy study. J. Biomed. Mater. Res. B Appl. Biomater. 69, 205–215.

Massin, P., Viguier, E., Flautre, B., Hardouin, P., Astoin, E., Duponchel, B., 2004b. Migration of polyethylene debris along well-fixed cemented implants. J. Biomed. Mater. Res. B Appl. Biomater. 68, 140–148.

Massin, P., Lopes, R., Masson, B., Mainard, D., 2014. La céramique composite Biolox® Delta limite-t-elle le risque de rupture? Rev. Chir. Orthop. Traumatol. 100, S162–S166.

Moraes, M.C.C.D.S., Elias, C.N., Duailibi Filho, J., Oliveira, L.G.D., 2004. Mechanical properties of alumina-zirconia composites for ceramic abutments. Mater. Res. 7, 643–649.

Pandit, H., Glyn-Jones, S., McLardy-Smith, P., Gundle, R., Whitwell, D., Gibbons, C., Ostlere, S., Athanasou, N., Gill, H., Murray, D., 2008. Pseudotumours associated with metal-on-metal hip resurfacings. Bone Joint J. 90, 847–851.

Park, Y.-S., Hwang, S.-K., Choy, W.-S., Kim, Y.-S., Moon, Y.-W., Lim, S.-J., 2006. Ceramic failure after total hip arthroplasty with an alumina-on-alumina bearing. J. Bone Joint Surg. Am. 88, 780–787.

Pizzoferrato, A., Stea, S., Sudanese, A., Toni, A., Nigrisoli, M., Gualtieri, G., Squarzoni, S., 1993. Morphometric and microanalytical analyses of alumina wear particles in hip prostheses. Biomaterials 14, 583–587.

Prudhommeaux, F., Hamadouche, M., Nevelos, J., Doyle, C., Meunier, A., Sedel, L., 2000. Wear of alumina-on-alumina total hip arthroplasties at a mean 11-year followup. Clin. Orthop. Rel. Res. 379, 113–122.

Simon, J.A., Dayan, A.J., Ergas, E., Stuchin, S.A., Di Cesare, P.E., 1998. Catastrophic failure of the acetabular component in a ceramic-polyethylene bearing total hip arthroplasty. J. Arthroplasty 13, 108–113.

Sugano, N., Nishii, T., Nakata, K., Masuhara, K., Takaoka, K., 1995. Polyethylene sockets and alumina ceramic heads in cemented total hip arthroplasty. A ten-year study. Bone Joint J. 77, 548–556.

Willert, H.G., 1977. Reactions of the articular capsule to wear products of artificial joint prostheses. J. Biomed. Mater. Res. 11, 157–164.

Zichner, L.P., Willert, H.-G., 1992. Comparison of alumina-polyethylene and metal-polyethylene in clinical trials. Clin. Orthop. Rel. Res. 282, 86–94.

Le deuxième travail a consisté à la mise en évidence des particules d'alumine dans les tissus péri-prothétiques autrement qu'en utilisant la microscopie à balayage associée à l'EDS. L'identification des ions aluminium est possible par différentes techniques histologiques mais elles ne sont pas spécifiques de l'alumine (mais de l'ion aluminium qui est couplé à l'hydroxyapatite de la matrice osseuse). On peut citer par exemple la coloration au solochrome-azurine par exemple (90-93). Or, dans les tissus péri-prothétiques, les particules d'usure sont composées par de l'alumine et il n'y a pas d'hydroxyapatite, à la différence de la matrice osseuse. Récemment, un colorant fluorochrome, le lumogallion, a été utilisé pour caractériser histologiquement les dépôts d'aluminium dans les lobes temporaux des patients atteints de maladie d'Alzheimer (94). Les tissus péri-prothétiques de patients opérés d'une reprise de prothèse totale de hanche avec un couple de frottement alumine-alumine ont été analysés avec une coloration au lumogallion afin de mettre en évidence les particules d'usure d'alumine. L'analyse en microscopie à fluorescence a donc pu mettre en évidence des particules d'alumine dans les tissus péri-prothétiques d'une part mais également dans le cytoplasme des macrophages et dans les cellules endothéliales.

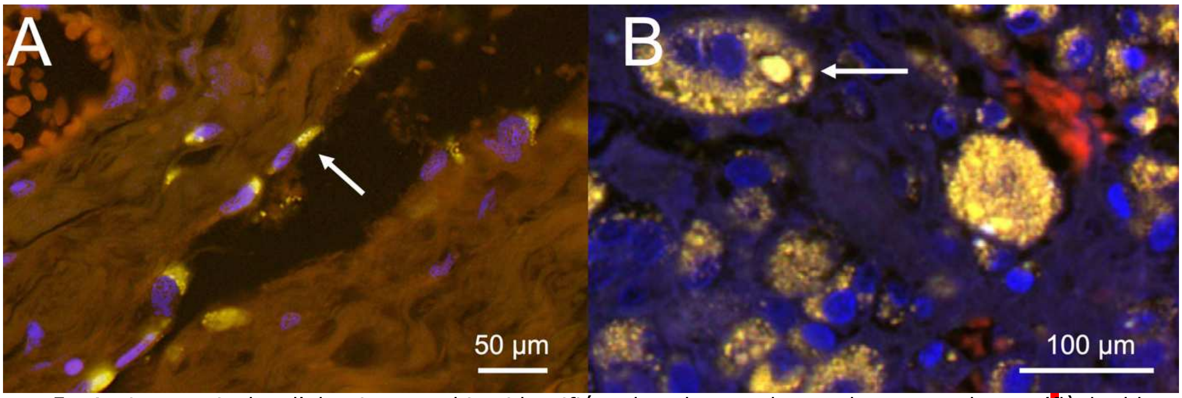

Figure 5 : A - Les particules d'alumine sont bien identifiées dans le cytoplasme des macrophages (flèche blanche). De minuscules particules d'alumine sont présentes dans le cytoplasme des cellules endothéliales (flèche blanche).

De plus, l'analyse des coupes a révélé des plages de fibrose. Ces plages de fibrose pourraient expliquer les épaississements capsulaires retrouvées en routine clinique (95-97). Ce travail a montré qu'il existait de nombreuses particules d'alumine dans les tissus péri-prothétiques et que leur existence avait été jusque-là sous-estimée car non identifiable. Néanmoins, la réaction tissulaire obtenue n'est pas la même que pour les particules de polyéthylène car il s'agit d'une réaction macrophagique n'entraînant semble-t-il pas d'ostéolyse (98).

ARTICLE 3

Histochemical identification of wear debris released by alumina-on-alumina hip prostheses in the periprosthetic tissues

Louis RONY, Florence PASCARETTI-GRIZON, Laurent HUBERT, Daniel CHAPPARD

Orthopaedics & Traumatology : Surgery & Research 107(1): 19-25 (2021)

Impact Factor : 2,256 – SIGAPS : D

Orthopaedics & Traumatology: Surgery & Research 107 (2021) 102636

Contents lists available at ScienceDirect

Orthopaedics & Traumatology: Surgery & Research

journal homepage: www.elsevier.com

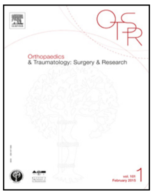

Original article

Histochemical identification of wear debris released by alumina-on-alumina hip prostheses in the periprosthetic tissues

Louis Rony[a,b], Florence Pascaretti-Grizon[a], Laurent Hubert[a,b], Daniel Chappard[b,*]

[a] Groupe Etudes Remodelage Osseux et bioMatériaux, GEROM, EA-4658, SFR-4208, Univ-Angers, IRIS-IBS Institut de Biologie en Santé, CHU-Angers, 49933 Angers, France
[b] Département de chirurgie osseuse, CHU-Angers, 49033 Angers, France

ARTICLE INFO

Article history:
Received 25 September 2019
Accepted 18 March 2020

Keywords:
Alumina
Wear debris
Hip prosthesis
Lumogallion
Histochemistry

ABSTRACT

Background: Tribological studies have shown that the most used couples for hip prostheses consist of metal-on-polyethylene and alumina-on-alumina prostheses. Over time, wear products accumulate in the joint cavity and in the periprosthetic tissues. Although polyethylene and metal are easily identifiable by microscopy in periprosthetic tissues, alumina particles are very difficult to identify.
Hypothesis: The fluorescent azo-dye lumogallion was evaluated as a suitable histochemical stain for alumina particles in periprosthetic tissues.
Material and method: In 28 patients who had a prosthetic revision of an alumina-on-alumina prosthesis, periprosthetic tissues were removed and embedded in paraffin; sections were stained with HPS (for conventional diagnosis) or with lumogallion. Sections were examined for wear particles in light and fluorescence microscopy. Some sections were counter-stained using DAPI for visualization of cell nuclei.
Results: The wear particles of the alumina-alumina prostheses were very difficult to identify on the HPS stained sections; they were clearly evidenced by lumogallion staining with a bright orange fluorescence. The stain revealed large quantities of particles (of the order of several thousand per section). Only two patients had no particles. The staining technique identified numerous particles that were not visible on HPS-stained sections in macrophages, synoviocytes and fibroblasts.
Conclusion: This staining, which has been validated in neuromuscular pathology for the identification of alumina used as a vaccine adjuvant, gave successful results in the present study. Alumina particles are modified when they are phagocytized by macrophages. lumogallion staining easily shows the presence of thousands of wear particles released by alumina-on-alumina prostheses in periprosthetic tissues.
Level of evidence: V expert opinion study.

1. Introduction

The goal of total hip arthroplasty (THA) is to treat painful end-stage arthritis to provide a pain-free and long-lasting functional hip joint. Ceramic-on-ceramic (alumina being the most used) [1] and ceramic-on-cross-linked polyethylene (PE) [2,3] have been proposed. When using metal on PE bearings, the production of wear particles in the joint cavity and periprosthetic tissues of patients is responsible for aseptic loosening in the long-term function [4]. Debris are capable to stimulate osteoclastic activity and it has been shown (for metal-on-PE prostheses) that millions of particles are released and can migrate around the prosthesis stem and in the porosity of cortical and trabecular bone [5]. They can also accumulate in the lymph nodes at a considerable distance from the prosthesis and give a tumor mass mimicking a lymphoma [6]. The nature of the debris is variable and depends, of course, of the biomaterials used to prepare the different parts of the prosthesis. Metal debris are usually 10–50 μm large and appear as black particles in the periprosthetic tissues; their atomic composition can be analyzed by energy dispersive X-ray spectrometry (EDS-SEM) under a scanning electron microscope [7]. Energy Dispersive X-Ray Spectroscopy (EDS) is a microanalysis technique that detects X-rays emitted from a sample during bombardment by the electron beam to characterize the elemental atomic composition present in an analyzed area. PE particles are transparent under light microscopy and become highly birefringent under polarized

---

[*] Corresponding author at: GEROM, IRIS-IBS Institut de Biologie en Santé, Université d'Angers, CHU d'Angers, Angers, France.
E-mail address: daniel.chappard@univ-angers.fr (D. Chappard).

https://doi.org/10.1016/j.otsr.2020.03.027

light; in addition, they can be stained by lipid stains such as oil red O [6,8]. When the femoral stem has been cemented with a methacrylic-based cement, particles of the cement, containing zirconium or barium (always used as a radio-opacifying agent) can be observed as small round dots, 1 µm or less in diameter [9]. Using ceramic-on-ceramic seems to eliminate the risk of particle-induced osteolysis as wear is below the detectable threshold of conventional radiographic exploration. Alumina particles are more difficult to identify: large particles (i.e., 15–20 µm) are birefringent under polarized light, but smaller ones are not and they appear with a light brownish tint when they have been internalized by macrophages [10]. EDS-SEM is the gold standard to identify the presence of Al and O in these particles, but the method is not available in every laboratory and finding the particles on the tissue sections is tedious. Histochemical methods for identification of Al ions by the aluminon, Morin or solochrome azurine do not work properly as these techniques can identify Al when coupled to the mineralized phase of the bone matrix (hydroxyapatite crystals) or they can cross-react with other metals [11–14]. Recently, the use of the fluorescent azo-dye lumogallion (4-chloro-6-(2,4-dihydroxyphenylazo)-1-phenol-2-sulfonic acid, CAS number 4386-25-8) has been proposed to identify Al in the brain of patients with Alzheimer disease and alumina particles in muscle biopsies of patients with macrophagic myofasciitis lesions [15,16].

We hypothesized:

- that alumina wear particles are poorly identified on routinely-stained histological sections;
- that lumogallion histochemical staining could be of interest in the identification of alumina wear debris.

The method was applied to a series of periprosthetic tissues harvested from patients during revision of a total hip arthroplasty with an alumina-on-alumina prosthesis.

2. Material and methods

2.1. Patients

We included 28 patients who have undergone a THA revision for aseptic loosening of an alumina-on-alumina prosthesis. In the present series, the ceramic used for friction torque was pure alumina (CERAVER, Roissy, France). Samples were send to our histopathological bone unit fixed in formalin for routine analysis. All subjects gave their informed consent to participate in the study that was approved by the Ethical committed of Angers University Hospital. In this retrospective study, the blocks from patients harvested from 2010 to 2019 were considered. Clinical data and causes for revision appear on Table 1. For the twelve patients with pain, all investigations (CT analysis for checking the position of implants, bacteriologic analysis with articular puncture) were negative. None of the patients were referred for osteolysis or presented osteolytic foci on plain X-ray images.

Table 1
Clinical data (the minimum and maximum are indicated in brackets).

Age (years)	56.6 ± 14.4 (29–78)
Male	15 (53.6%)
Female	13 (46.4%)
Interval between implantation and revision (years)	3.6 ± 2.8 (0.5–9.5)
Reasons for revision	
Pain	12 (42.9%)
Cup aseptic loosening	5 (17.9%)
Squeaking	3 (10.7%)
Instability	2 (7.1%)
Femoral stem aseptic loosening	2 (7.1%)
Infection	1 (3.6%)
Malposition of the prosthesis	1 (3.6%)
Leg length difference	1 (3.6%)
Fracture of the insert	1 (3.6%)

2.2. Microscopic analysis

Because these samples may contain remnants of bone particles, they were systematically decalcified in an acidic fluid and embedded in paraffin. Sections (5 µm thick) were routinely prepared on a Minot microtome. They were stained by hematoxylin-phloxin-saffron (HPS) for routine diagnosis with bright field microscopy.

In order to characterize the collagen fibrotic reaction, an additional section was stained with picro-Sirius and examined under polarization microscopy [17,18]. This method allows an identification of collagen type I, II and III similar to immunochemistry and has been used in a considerable number of papers on fibrotic diseases [19]. Two additional sections were prepared for alumina identification with lumogallion. After dewaxing, sections were incubated in a pH 4.0 acetate buffer. They were transferred in the staining lumogallion solution prepared extemporaneously ($2.5\ 10^{-3}$ mol/l in a pH 4.0 acetate buffer). Staining was done overnight at room temperature in the dark. Sections were rinsed in three baths of acetate buffer (5 min each) and in 3 baths of distilled water (5 min each) and then mounted with Fluoromount™ (Sigma). If a counterstaining of the cell nuclei is desired, a post-staining with DAPI (0.01 mg/ml in distilled water) during 10 min in the dark is possible before the final rinses.

Sections were analyzed with an Olympus BX51 microscope equipped for bright field, Nomarski (DIC) and fluorescence microscopy with the following cubes: U-MWIB3 excitation filter 460–495 nm, emission filter 510 nm, dichromatic mirror 505 nm to detect lumogallion-stained particles in orange and U-MNU2; excitation filter 360–370 nm, emission filter 420 nm, and dichromatic mirror 400 nm to detect the blue fluorescence of the nuclei.

When a combined image of DAPI and lumogallion was needed, one image was captured with each cube. RGB (red-green-blue) images were acquired on a DP71 color digital CCD camera and stored in the .tif format. The images were transferred to Photoshop™ (release CS5, RGB (red-green-blue) Adobe). The image of the alumina particles was decomposed into its three layers and the blue one was black-painted. On the image of the cell nuclei, only the blue layer was retained, copied and pasted to the blue layer of the alumina particles image.

In 12 cases, the atomic composition of the particles was obtained by analysis of an unstained and dewaxed histological section by scanning electron microscopy on an EVO LS10 (Zeiss) and energy X-ray dispersive spectrometry (SEM-EDS EDS-INCA- Oxford) in the backscattered electron mode at 11 and 20 kV. The data generated by EDS analysis consist of spectra showing peaks characteristic of the atomic elements of the sample [20].

3. Results

3.1. Standard stained sections

In the peri-prosthetic tissues, the alumina particles were present in two different forms:

- large particles (i.e., 15–20 µm) were translucent and highly birefringent under polarized light. However, these particles were defined rarely;
- small (1–3 µm) particles presented a light brownish tint in unstained or HPS sections (Fig. 1A).

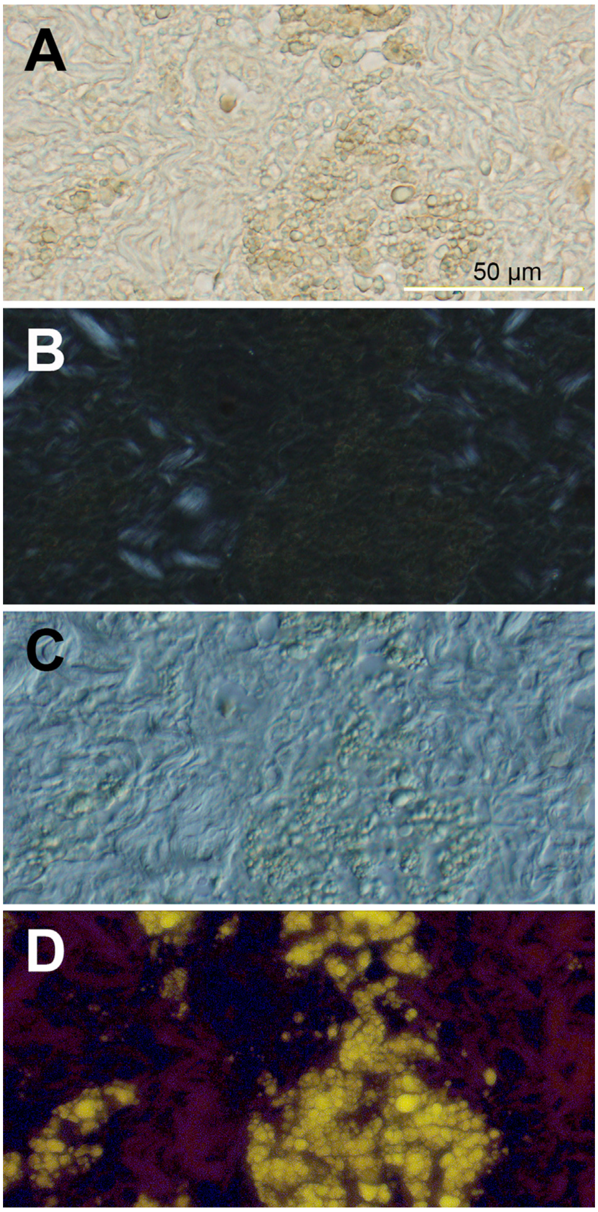

Fig. 1. A. Histological appearance of alumina particles in periprosthetic tissues in an unstained section. Note the brownish tint of the particles. B. Same field in polarization microscopy. The particles are not birefringent. C. DIC (Nomarsky interference microscopy) showing the particles. D. Same field in fluorescence microscopy after lumogallion staining. The alumina particles are clearly identified in yellow, even the smallest ones that were otherwise invisible; the background tissues have a red autofluorescence.

They were observed in the cytoplasm of activated macrophages disposed in dense clusters between fibrotic areas. These particles were not birefringent under polarized light but could be identified by Nomarski (DIC) microscopy (Fig. 1B–C). However, these particles were sometimes difficult to identify and, in 16 patients, no particle could be detected on HPS sections. EDS performed on SEM images identified alumina particles by showing the Al and O peaks characteristic of alumina in 8 cases (Fig. 2). This may be due to the small size of the particles and their almost absence of staining on HPS sections. In the remaining patients, the alumina particles could not be evidenced by backscattered electron imaging. As for the two patients, with instability, few metallic wear debris were encountered on the periprosthetic tissues, for the other patients no metallic debris was found.

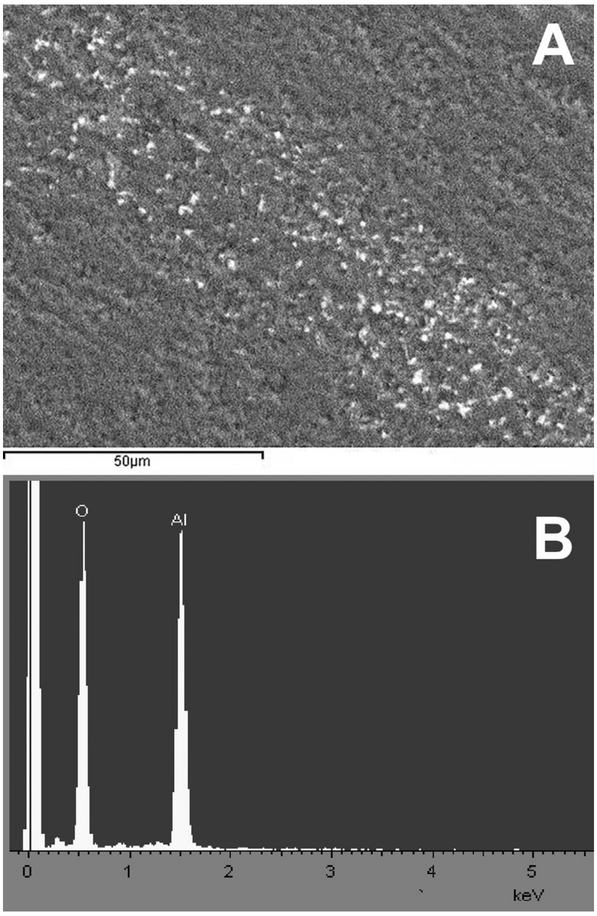

Fig. 2. A. SEM imaging in the backscattered mode of alumina particles on a dewaxed paraffin section. The particles appear as white spots. B. EDS analysis of one particle identifying the Al and O atoms corresponding to alumina.

Sections stained with picro-Sirius evidenced large bundles of collagen fiber around the macrophage clusters (Fig. 3A). Under polarization microscopy, the fibers had a red tint, characteristic of type I collagen (Fig. 3B).

3.2. *Lumogallion-stained sections*

The alumina particles (0.5–5 μm) were clearly identified against a red background; the particles boundaries were well delineated ((Fig. 1D and 4 A–B). The particles were present in the cytoplasm of mononucleated macrophages and thousands of particles were identified in a single section. Macrophages were often were grouped in tight bands, enclosed in the connective tissue of the joint capsule (Fig. 4B). In some sections containing synovial fringes, alumina particles were also identified in the synoviocytes and the chorion of the fringes (Fig. 4C). On the combined DAPI-lumogallion images, nuclei appeared in blue, alumina particles in orange-yellowish and the connective tissues in red (Fig. 5A). The macrophages were most often mononucleated; rare binucleated macrophages were occasionally found (Fig. 5B). Particles were also evidenced in the cytoplasm of some endothelial cells (Fig. 5C). When comparing the HPS and the lumogallion slides, it was evident that 57% of the alumina particles were not shown with the routine HPS stain. Lumogallion staining identified large amount of macrophages with alumina particles in 26 patients. Because the tissues samples were harvested in different size and location, it was not possible to estimate the number of particles. Any attempt

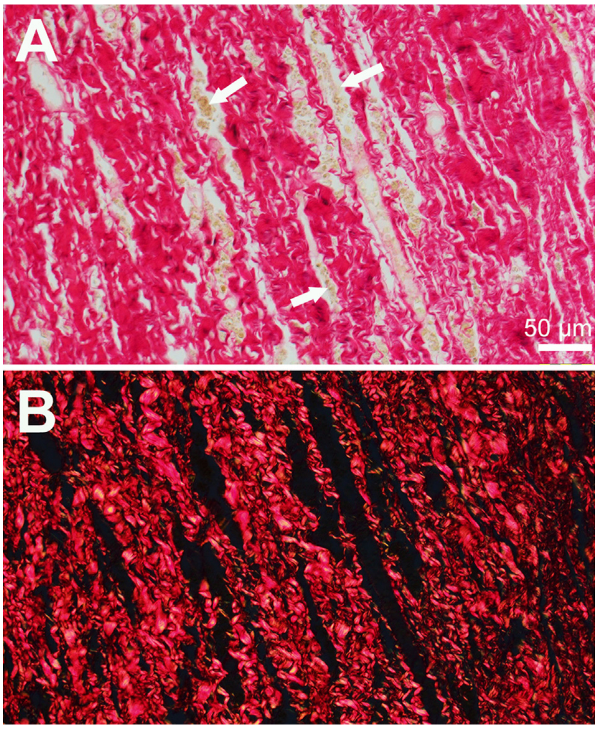

Fig. 3. Histological section stained with picro-Sirius. A. Bright field microscopy showing several packets of light brown-yellowish alumina particles (arrows) present in clusters of macrophages (the cell components are not stained with this method). B. Same field under polarized light. The collagen fibers encapsulating the macrophage clusters have a red birefringence, characteristic of type I collagen. Note that the alumina particles are not birefringent.

to quantify particle density on these tissue sections would also be scientifically and stereologically incorrect.

4. Discussion

The most interesting finding was that thousands of alumina particles could be identified by lumogallion in 26 out of 28 (92%) of these patients when the HPS sections failed to identify them in only 57% (16/28) of cases by a trained histopathologist. The second hypothesis was also verified: the lumogallion histochemical technique identified accurately the alumina particles present in the macrophages and sometimes in the synoviocytes and endothelial cells.

The use of DAPI is not systematically necessary, only when a cell type needs to be identified.

The alumina-on-alumina prostheses were proposed as an alternative to the polyethylene-metal couple in hip joint surgery [21]. Alumina is reported to be a chemically inert and stable bioceramic. A number of histopathologic studies have confirmed that the wear debris production is reduced in alumina-on-alumina prostheses but not suppressed [22]. More recently, industry has proposed ceramics combining alumina and zirconium oxide that should possess an improved mechanical resistance [23–26]. An audible squeak is reported in some patients having an alumina-on-alumina prosthesis but it was not the main cause for revision in this series [27–29]. In the present study, the prosthesis revision was most frequently due to isolated pain, all investigations in search of aseptic loosening, malposition of the implants or septic loosening were normal.

Lumogallion staining has been validated in neuromuscular pathology for the staining of aluminum used as an adjuvant in veterinary and human vaccines [15,16,30,31]. It is also effective for the identification of aluminum and alumina in plants [32,33]. This stain appears superior to other techniques such as Morin, aluminon or solochrome azurine that can only be used in undecalcified bone sections.

A previous SEM study of alumina femoral heads explanted during the revision, we have shown the presence of scratches or craters on their surface with exhibition of the ceramic grains [10]. The grains are modified when phagocytized by macrophages, losing their birefringence [34], and acquiring a brownish hue very difficult to identify in HPS sections where they are visible only in high amounts [9]. Alumina particles are observed in the cytoplasm of

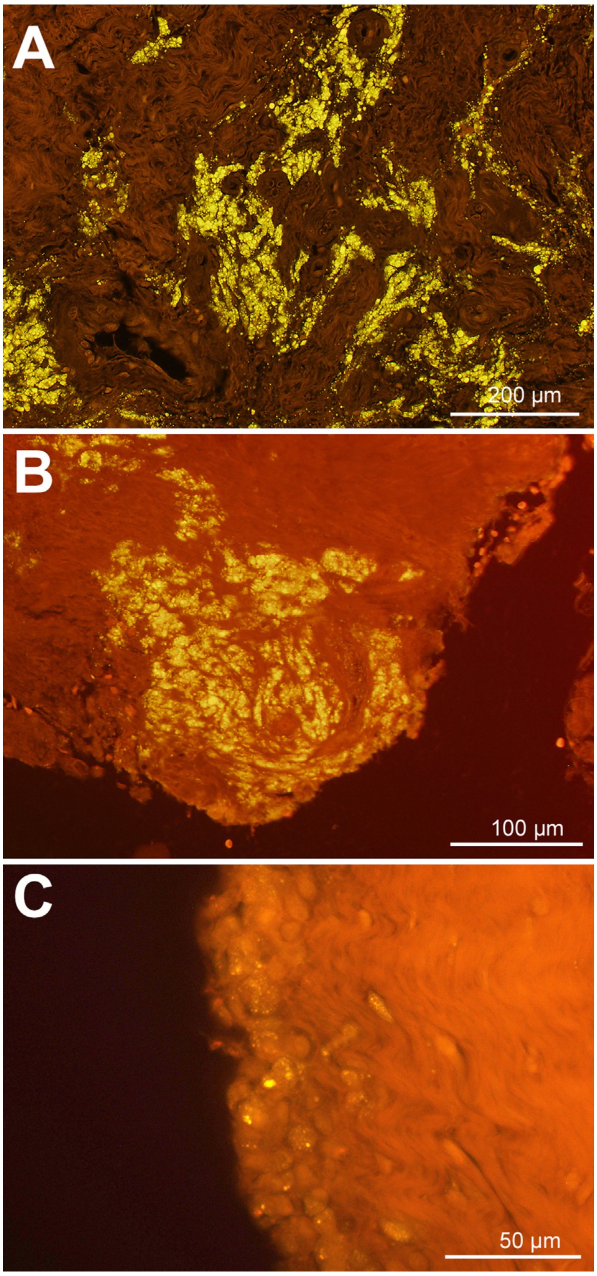

Fig. 4. Histological sections stained with lumogallion without counter staining. A. periprosthetic tissues infiltrated with numerous macrophages with cytoplasm filled with alumina particles (in orange-yellow), the collagen fibers have a red autofluorescence. B. At a higher magnification, a group of macrophages having phagocytized alumina particles is present in the connective tissues, note that the unstained nuclei appear as a hole in the macrophages. C. Synoviocytes having phagocytized alumina particles.

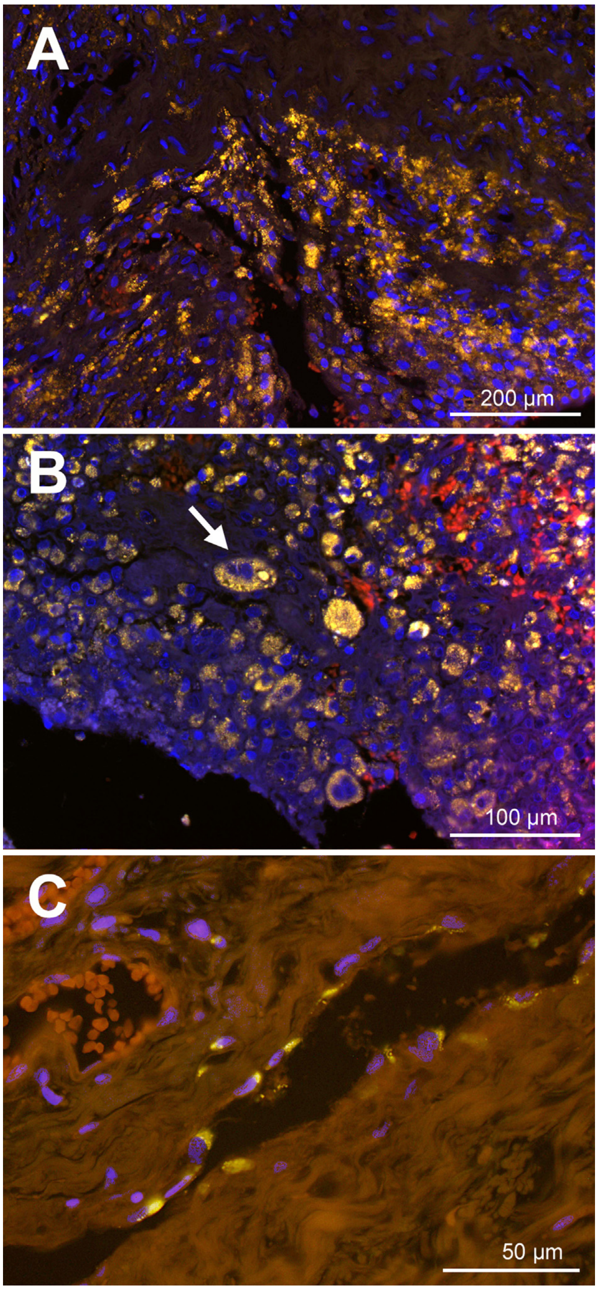

Fig. 5. Histological sections stained with lumogallion with DAPI counterstaining. The lumogallion-stained particles have a yellow fluorescence and the cell nuclei are blue-stained. B. At a higher magnification, the alumina particles are well identified in the cytoplasm of macrophages. Some binucleated cells can be encountered (arrow). C. Presence of minute alumina particles in the cytoplasm of endothelial cells.

macrophages, synoviocytes and endothelial cells. Giant cells are not observed with alumina particles contrary to polyethylene particles released by metal-on-polyethylene prosthesis [7,35]. It is likely that alumina particles present in cells of the reticulo-endothelial system can also migrate throughout the rest of the body. However, in this study, no patient had symptoms of chronic fatigue nor macrophagic myofasciitis reported with aluminum-adjuvanted vaccines [36]. Aluminum adjuvants are either a semi-crystalline form of aluminum hydroxide or amorphous salts of aluminum hydroxyphosphate [37]. They are not inert deposits at the vaccine injection sites and can release biologically reactive aluminum [38]. Alumina particles released by alumina-on-alumina prostheses are supposed to be inert and induce less osteolysis and muscle degeneration [39,40]. However, the histological changes noted here (e.g., loss of birefringence) seem to indicate that modification of the composition may occur.

There are several limitations in the present series: the number of patients represents a limited sample but the high percentage of them in which alumina particles were identified histochemically make us confident with the high value of the method. As mentioned above, a quantitative analysis of the number of released particles would have been of the upmost interest. However, histologically this is not realistic and a true determination after tissue digestion is questionable due to the sensitivity of aluminum to strong acids and bases [41]. A possible solution could be to analyze the periprosthetic tissues by nanocomputed tomography thus providing a direct 3D measurement. This was not feasible with this series but we planned it for future cases.

5. Conclusion

The histochemical staining with lumogallion easily demonstrates the presence of alumina wear particles. The periprosthetic tissues retrieved from this series of 28 patients evidenced the presence of alumina particles in 92% (26/28) of cases whatever the cause for revision.

Disclosure of Interest

The authors declare that they have no competing interest.

Funding

This work was supported by grants from the French Ministère de l'Enseignement supérieur et de la Recherche. This work was made possible by grants from Angers CHU (University hospital) project MOCONA.

Contributions of each author

L. Rony selected the patients and contributed to write the manuscript.

F. Pascaretti-Grizon developed and adapted the lumogallion and lumogallion-DAPI histological technique to periprosthetic soft tissues.

L. Hubert coordinated the study and reviewed the article.

D. Chappard performed the histopathological analyses, designed the study and wrote the manuscript.

Acknowledgments

Mrs. N. Gaborit and S. Lemière are thanked for their technical help with microCT analysis. They also wish to thank all the orthopedic surgeons from our hospital who were involved in the recruitment of the patients: Pr. Pascal Bizot, Dr. Florian Ducellier, Vincent Steiger, Augustin Coupry, Nicolas Ruiz, Clément Marc, Antoine Peyronnet and Romain Lancigu.

References

[1] Hamadouche M, Boutin P, Daussange J, Bolander ME, Sedel L. Alumina-on-alumina total hip arthroplasty. J Bone Joint Surg Am 2002;84:69–77.
[2] Sugano N, Nishii T, Nakata K, Masuhara K, Takaoka K. Polyethylene sockets and alumina ceramic heads in cemented total hip arthroplasty. A ten-year study. Bone Joint J 1995;77:548–56.
[3] Zichner LP, Willert H-G. Comparison of alumina-polyethylene and metal-polyethylene in clinical trials. Clin Orthop Rel Res 1992;282:86–94.
[4] Willert HG. Reactions of the articular capsule to wear products of artificial joint prostheses. J Biomed Mater Res 1977;11:157–64.

[5] Libouban H, Massin P, Gaudin C, Mercier P, Baslé MF, Chappard D. Migration of wear debris of polyethylene depends on bone microarchitecture. J Biomed Mater Res B Appl Biomater 2009;90:730–7.
[6] Baslé MF, Bertrand G, Guyetant S, Chappard D, Lesourd M. Migration of metal and polyethylene particles from articular prostheses may generate lymphadenopathy with histiocytosis. J Biomed Mater Res 1996;30:157–63.
[7] Rony L, Lancigu R, Hubert L. Intraosseous metal implants in orthopedics: a review. Morphologie 2018;102:231–42.
[8] Schmalzried TP, Jasty M, Rosenberg A, Harris WH. Histologic identification of polyethylene wear debris using oil red O stain. J Appl Biomater 1993;4:119–25.
[9] Lerouge S, Huk O, Yahia LH, Sedel L. Characterization of in vivo wear debris from ceramic—ceramic total hip arthroplasties. J Biomed Mater Res - Part A 1996;32:627–33.
[10] Rony L, de Sainte Hermine P, Steiger V, Mallet R, Hubert L, Chappard D. Characterization of wear debris released from alumina-on-alumina hip prostheses: Analysis of retrieved femoral heads and peri-prosthetic tissues. Micron 2018;104:89–94.
[11] Chappard D, Bizot P, Mabilleau G, Hubert L. Aluminum and bone: review of new clinical circumstances associated with Al deposition in the calcified matrix of bone. Morphologie 2016;100:95–105.
[12] Fernandez-Martin J, Menendez P, Acuna G, Canteros A, Gómez C, Cannata J. Staining of bone aluminium: comparison between aluminon and solocbrome azurine and their correlation with bone aluminium content. Nephrol Dial Transplant 1996;11:80–5.
[13] Kaye M, Hodsman AB, Malynowsky L. Staining of bone for aluminum: use of acid solochrome azurine. Kidney Int 1990;37:1142–7.
[14] Mold MJ, Kumar M, Chu W, Exley C. Unequivocal imaging of aluminium in human cells and tissues by an improved method using morin. Histochem Cell Biol 2019:1–11.
[15] Mirza A, King A, Troakes C, Exley C. The identification of aluminum in human brain tissue using lumogallion and fluorescence microscopy. J Alzheimer's Dis 2016;54:1333–8.
[16] Mold M, Shardlow E, Exley C. Insight into the cellular fate and toxicity of aluminium adjuvants used in clinically approved human vaccinations. Sci Rep 2016;6:31578.
[17] Michalak S, Rousselet MC, Bedossa P, Pilette C, Chappard D, Oberti F, et al. Respective roles of porto-septal fibrosis and centrilobular fibrosis in alcoholic liver disease. J Pathol 2003;201:55–62.
[18] Junqueira LCU, Bignolas G, Brentani RR. Picrosirius staining plus polarization microscopy, a specific method for collagen detection in tissue sections. Histochem J 1979;11:447–55.
[19] Junqueira L, Cossermelli W, Brentani R. Differential staining of collagens type I, II and III by Sirius Red and polarization microscopy. Arch Histol Japon 1978;41:267–74.
[20] Goldstein J, Newbury DE, Echlin P, Joy DC, Romig Jr AD, Lyman CE, et al. Scanning electron microscopy and X-ray microanalysis: a text for biologists, materials scientists and geologists. Springer Science & Business Media; 2012.
[21] Boutin P. Total arthroplasty of the hip by fritted alumina prosthesis. Experimental study and 1st clinical applications. Orthop Traumatol Surg Res 2014;100:15–21.
[22] Prudhommeaux F, Hamadouche M, Nevelos J, Doyle C, Meunier A, Sedel L. Wear of alumina-on-alumina total hip arthroplasties at a mean 11-year followup. Clin Orthop Rel Res 2000;379:113–22.
[23] Affatato S, Goldoni M, Testoni M, Toni A. Mixed oxides prosthetic ceramic ball heads. Part 3: effect of the ZrO 2 fraction on the wear of ceramic on ceramic hip joint prostheses. A long-term in vitro wear study. Biomaterials 2001;22:717–23.
[24] Massin P, Lopes R, Masson B, Mainard D. La céramique composite Biolox® Delta limite-t-elle le risque de rupture? Rev Chir Orthop Traumatol 2014;100:S162–6.
[25] Moraes MCCdS, Elias CN, Duailibi Filho J, Oliveira LGd. Mechanical properties of alumina-zirconia composites for ceramic abutments. Mater Res 2004;7:643–9.
[26] Massin P, Lopes R, Masson B, Mainard D, French Hip & Knee Society (SFHG). Does Biolox® Delta ceramic reduce the rate of component fractures in total hip replacement? Orthop Traumatol Surg Res 2014;100:S317–21.
[27] Jarrett CA, Ranawat AS, Bruzzone M, Blum YC, Rodriguez JA, Ranawat CS. The squeaking hip: a phenomenon of ceramic-on-ceramic total hip arthroplasty. J Bone Joint Surg Am 2009;91:1344–9.
[28] Mai K, Verioti C, Ezzet KA, Copp SN, Walker RH, Colwell CW. Incidence of 'squeaking'after ceramic-on-ceramic total hip arthroplasty. Clin Orthop Rel Res 2010;468:413–7.
[29] Chevillotte C, Trousdale RT, An KN, Padgett D, Wright T. Retrieval analysis of squeaking ceramic implants: are there related specific features? Orthop Traumatol Surg Res 2012;98:281–7.
[30] Asín J, Molín J, Pérez M, Pinczowski P, Gimeno M, Navascués N, et al. Granulomas following subcutaneous injection with aluminum adjuvant-containing products in sheep. Vet Pathol 2019;56:418–28.
[31] Mile I, Svensson A, Darabi A, Mold M, Siesjö P, Eriksson H. Al adjuvants can be tracked in viable cells by lumogallion staining. J Immunol Methods 2015;422:87–94.
[32] Arroyave C, Barceló J, Poschenrieder C, Tolrà R. Aluminium-induced changes in root epidermal cell patterning, a distinctive feature of hyperresistance to Al in *Brachiaria decumbens*. J Inorg Biochem 2011;105:1477–83.
[33] Zhou P, Yang F, Ren X, Huang B, An Y. Phytotoxicity of aluminum on root growth and indole-3-acetic acid accumulation and transport in alfalfa roots. Env Exp Bot 2014;104:1–8.
[34] Pizzoferrato A, Stea S, Sudanese A, Toni A, Nigrisoli M, Gualtieri G, et al. Morphometric and microanalytical analyses of alumina wear particles in hip prostheses. Biomaterials 1993;14:583–7.
[35] Massin P, Viguier E, Flautre B, Hardouin P, Astoin E, Duponchel B. Migration of polyethylene debris along well-fixed cemented implants. J Biomed Mater Res B Appl Biomater 2004;68:140–8.
[36] Exley C, Swarbrick L, Gherardi RK, Authier F-J. A role for the body burden of aluminium in vaccine-associated macrophagic myofasciitis and chronic fatigue syndrome. Med Hypotheses 2009;72:135–9.
[37] Shardlow E, Mold M, Exley C. Unraveling the enigma: elucidating the relationship between the physicochemical properties of aluminium-based adjuvants and their immunological mechanisms of action. Allerg Asthma Clin Immunol 2018;14:80.
[38] Exley C. An aluminium adjuvant in a vaccine is an acute exposure to aluminium. J Trace Elem Med Biol 2019;57:57–9.
[39] Hernigou P, Roussignol X, Delambre J, Poignard A, Flouzat-Lachaniette C-H, Ceramic-on-ceramic THA. associated with fewer dislocations and less muscle degeneration by preserving muscle progenitors. Clin Orthop Rel Res 2015;473:3762–9.
[40] Hernigou P, Zilber S, Filippini P, Poignard A. Ceramic-ceramic bearing decreases osteolysis: a 20-year study versus ceramic-polyethylene on the contralateral hip. Clin Orthop Rel Res 2009;467:2274–80.
[41] Chappard D. Effects of aluminum on cells and tissues. Morphologie 2016;100:49–50.

Enfin un dernier travail a visé à identifier en 3D ces particules d'usure dans les tissus périprothétiques. En microCT (microtomographie aux rayons X), des tissus péri-prothétiques de patients avec reprise de prothèse de hanche ont été analysés. Nous avons ainsi comparé des tissus présentant une métallose avec plasticose (prothèses métal-PE), des dépôts d'alumine (prothèses alumine-alumine) et des dépôts liés à la fragmentation du ciment orthopédique (baryum ou zircone) utilisé comme radio-opacifiant ont pu être identifiés grâce à leur capacité d'arrêter les rayons X utilisés en microCT. L'analyse en microCT permet de montrer la quantité considérable de particules dans les tissus péri-prothétiques. Elle permet aussi de voir en 3D et en animation l'importance de cette réaction à corps étrangers. Cependant, actuellement la microCT ne permet pas une identification chimique des particules. De plus, seules les particules absorbant les rayons X sont détectables, de sorte que les particules de polyéthylène (radio-transparentes) ne sont pas visibles par cette méthode.

ARTICLE 4

Wear debris released by hip prosthesis analysed by microcomputed tomography

Daniel CHAPPARD, Louis RONY, Florian. DUCELLIER, Vincent STEIGER, Laurent HUBERT.

Journal of Microscopy 282(1): 13-20 (2021)

Impact Factor : 1,575 – SIGAPS : D

Journal of
Microscopy

Journal of Microscopy, Vol. 282, Issue 1 2021, pp. 13–20 doi: 10.1111/jmi.12971

Received 26 June 2020; accepted 18 October 2020

Wear debris released by hip prosthesis analysed by microcomputed tomography

D. CHAPPARD*, L. RONY*,†, F. DUCELLIER†, V. STEIGER† & L. HUBERT*,†

**Groupe Etudes Remodelage Osseux et bioMatériaux, Univ-Angers, IRIS-IBS Institut de Biologie en Santé, CHU-Angers, Angers, France*

†Département de Chirurgie Osseuse, CHU-Angers, Angers, France

Key words. Alumina particles, bone cement, hip prosthesis, metallosis, microCT, wear debris.

Summary

Total hip arthroplasty uses commercial devices that combine different types of biomaterials. Among them, metals, ceramics and metal oxides can be used either in the prosthesis itself or in the cement used to anchor them in the bone. Over time, all of these materials can wear out and release particles that accumulate in the periprosthetic tissues or can migrate away. We used histology blocks from 15 patients (5 titanium metallosis, 5 alumina prostheses, 5 with altered methacrylic cement) to perform a microCT study and compare it with conventional histology data. An EDS-SEM analysis was done to characterise the atomic nature of the materials involved. A morphometric analysis was also performed in 3D to count the particles and assess their density and size. The metallic particles appeared to be the largest and the ceramic particles the finest. However, microCT could not reveal the wear particles of radiolucent biomaterials such as polyethylene and the very fine zirconia particles from cement fragmentation. MicroCT analysis can reveal the extent of the accumulation of these debris in the periprosthetic tissues.

Introduction

Joint prostheses are intended to restore function and mobility of the joints. The most frequent arthroplasties are those of the hip (THA – total hip arthroplasty) and then of the knee and shoulder. Historically, the first hip prosthesis was proposed by the Judet brothers in 1946.[1] They used a Plexiglas® (poly methylmethacrylate) sphere to replace the femoral head. However, very quickly, the polymer was found to wear out and they proposed to replace this plastic head by a metal one. In England, McKee proposed to change both the femoral head and the acetabulum, both of which being made of metal. However, the causes of loosening were frequent and related to the seizing between the two metal parts, which was responsible for wear.[2] In the 1960s, Charnley, in England, proposed a prosthesis, cemented with methyl methacrylate, with a small-diameter metal head gliding on a polyethylene cup.[3] Other solutions were proposed, in particular the use of ceramic prostheses with an alumina-on-alumina friction torque, proposed in 1970 by Boutin,[4] or the use of a cementless fixation of the femoral stem. At present, several solutions exist, but it should be noted that a THA prosthesis includes materials of different types: the metal is now most often titanium (TA6V) for the femoral stem, polyethylene (PE), ceramic, hydroxyapatite coating, and of course, methacrylic cement may also be used in the case of a cemented prosthesis (Fig. 1).

All these materials are placed in a chemically aggressive and corrosive environment with many anions and cations as well as dissolved oxygen and free radicals. This highly corrosive environment, at body temperature, has a Cl concentration equivalent to one third of that of seawater and an oxygen concentration equal to one quarter of that of air.[5,6] This may be responsible for chemical corrosion mechanisms; in addition stress (or fatigue) corrosion, wear and friction corrosion cause the formation of debris in the microenvironment of the prosthesis. The accumulation of particles released into the joint cavity acts as an abrasive and thus increases wear. The release of metal particles can be extremely severe and can lead to blackish metal deposits in the periprosthetic tissues (metallosis).[7,8] The wear of polyethylene cups produces nondegradable particles that also remain locally and can generate inflammation leading to aseptic loosening of the prosthesis.[9,10] Aluminium-on-alumina prostheses can also degrade and release particles.[11,12] Finally, methacrylic cements can fragment and release polymer fragments containing zirconia particles used as a radio opacifier.[13]

As many wear particles are radiopaque, the aim of this study was to see if microtomography analysis (microCT) could be used to analyse periprosthetic tissues by correlating the results obtained with bright field microscopy. The energy X-ray

Correspondence to: Daniel Chappard, Groupe Etudes Remodelage Osseux et bioMatériaux, Univ-Angers, IRIS-IBS Institut de Biologie en Santé, CHU-Angers, Angers, France. Tel: (33) 244 68 83 43; e-mail: daniel.chappard@univ-angers.fr

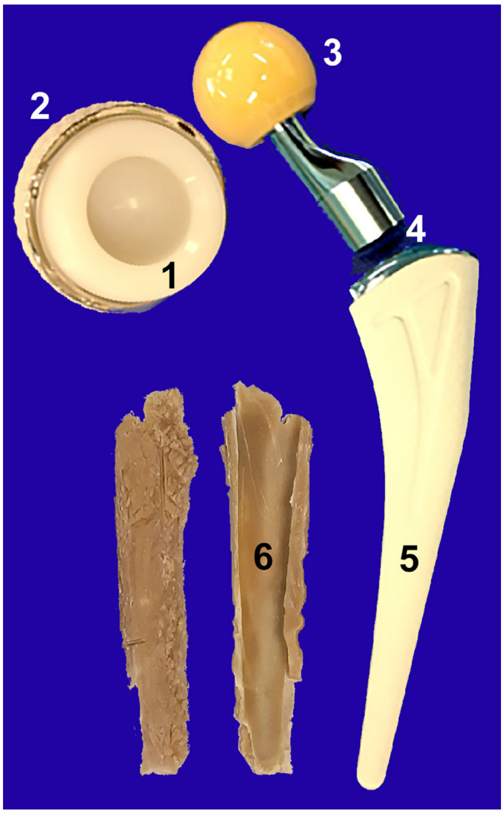

Fig. 1. The different materials encountered in the subparts of a hip prosthesis: (1) polyethylene cup, (2) acetabular socket (metal back), (3) ceramic femoral head, (4) titanium artificial neck, (5) metal femoral stem covered with hydroxyapatite coating, (6) poly (methyl methacrylate) cement used for sealing the femoral stem.

dispersive spectroscopic (EDS) analysis in scanning electron microscopy (SEM) characterised the atomic composition of these wear particles.

Material and methods

Patients and microscopic analysis

We included 15 patients who have undergone a THA revision for aseptic loosening of THA. All subjects gave their informed consent to participate in the study that was approved by the Ethical committed of Angers University Hospital. In this retrospective study, the blocks from patients harvested from 2010 to 2019 were considered. In the present series, three groups of patients were selected: five patients with a known metallosis (TA6V often associated with the presence of PE debris); five patients with metal debris associated with bone cement particles (often associated with metal debris) and five patients with ceramic debris coming from alumina-on-alumina prosthesis (CERAVER, Roissy, France).

The mean time prior to the THA revision was 11.2 ± 6.1 years for the metallosis, 3.3 ± 2.2 years for the alumina prostheses and 9.7 ± 6.3 years for the cemented prostheses.

Samples have been sent to our histopathological bone unit fixed in formalin for routine analysis. The histopathologic analysis has been done routinely on tissues embedded in paraffin and sectioned at 5 μm. Sections were stained by haematoxylin–phloxin–saffron (HPS) for routine diagnosis. In addition, sections from patients with a ceramic prosthesis were stained by the fluorescent azo-dye lumogallion (4-chloro-6-(2,4-dihydroxyphenylazo)-1-phenol-2-sulphonic acid, CAS number 4386-25-8; Merck) as recently described.[14] Sections were analysed with an Olympus BX51 microscope (Olympus France, 94150 Rungis, France) equipped for bright field and fluorescence microscopy with a U-MWIB3 cube, excitation filter 460–495 nm, emission filter 510 nm, dichromatic mirror 505 nm to detect the alumina particles. The atomic composition of the particles was obtained on unstained and dewaxed histological sections by scanning electron microscopy on an EVO LS10 (Carl Zeiss SAS, 78160 Marly le Roi, France) and EDS (SEM-EDS, EDS-INCA, Oxford, UK) in the backscattered electron mode at 11 and 20 kV.[15]

Microcomputed tomography (microCT)

The paraffin blocks were trimmed with a scalpel and a sample (~2 × 7 mm) was obtained for each patient. The paraffin sample was fixed with plasticine on a brass stub and analysed with a Skyscan 1272 X-ray computerized microtomograph (Bruker microCT, Kontich, Belgium) equipped with a microfocus tube. The following parameters were used: 30 kV, 200 μA, no filter, 2K binning, pixel size 3 μm with a 0.10° rotation angle at each step and 2 images averaging during a 180° rotation. Cross-section 2D images of the samples were reconstructed from the projection images using a modified Feldkamp cone-beam algorithm, implemented in the NRecon software (Bruker release 1.7.3.0). For each block, a stack of 2D sections was obtained in indexed grey levels ranging from 0 to 255. The CTAn Software (Bruker) was used for obtaining morphometric analysis of particles after thresholding. The volume of interest (TV, in mm^3), the fraction of the volume occupied by particles (PV/TV, in %) and the number of radio-opaque were determined. The density of particles (PD in particles mm^{-3}) and their diameter (D, in μm) were derived.

3D models were then obtained using a volume-rendering programs VG Studio MAX 2.1 software (Volume Graphics GmbH, Heidelberg, Germany; release 3.2).

Results

On the X-ray projection images obtained during the acquisition of the different types of blocks, the appearance of the wear debris was different depending on the nature of the particles (Fig. 2). Metallic particles were very numerous and very

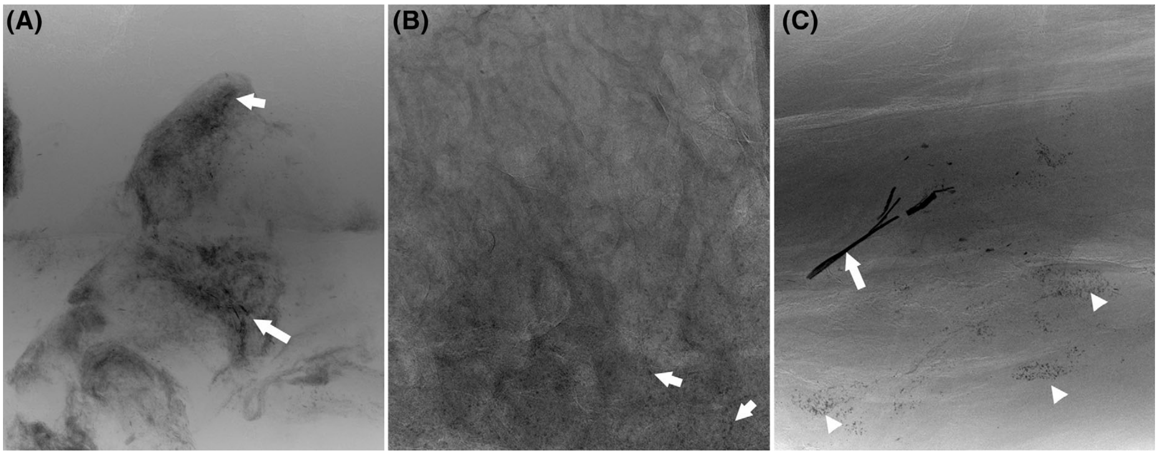

Fig. 2. X-ray projection images obtained by microCT. (A) Titanium wear debris in a case of metallosis. Arrows point to small spindle-like debris. (B) Alumina debris released by an alumina-on-alumina prosthesis. The small round debris (arrows) are less radio-opaque than a metal. (C) Clusters of zirconia particles grouped in different packs corresponding to fragmented cement pieces (arrowheads). Note that large titanium debris are also present (arrow).

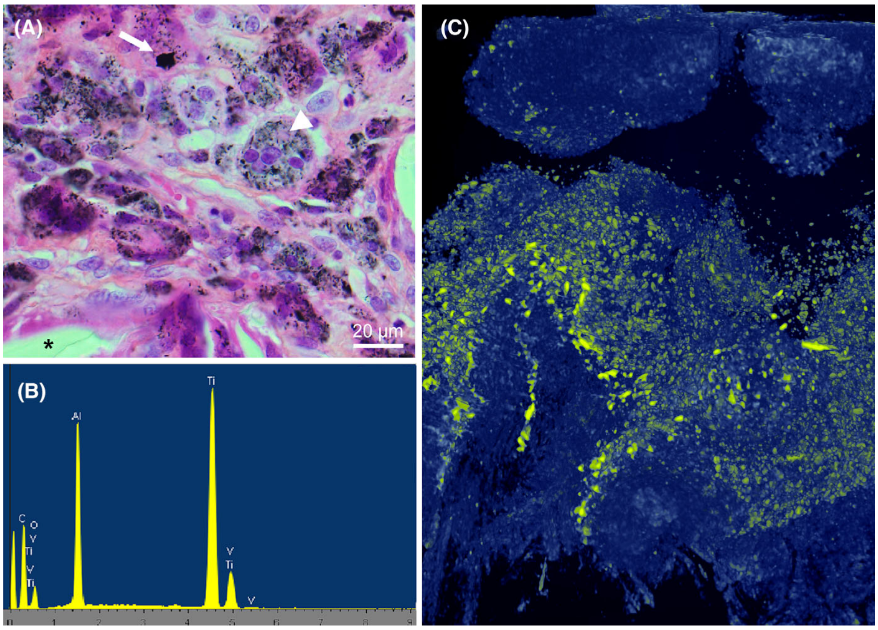

Fig. 3. Metallosis due to titanium wear debris. (A) Histological aspect of a patient's periprosthetic tissues with metallosis showing numerous black wear debris inside the cytoplasm of macrophages and giant cells (arrowhead). A large metal particle $> 5\ \mu$m is also observed between the macrophages (arrow). A polyethylene particle is also encountered (*) (HPS staining). (B) EDS analysis of the metal debris with identification of TA6V containing titanium, aluminium and vanadium. (C) MicroCT aspect showing numerous metal particles (with a yellow pseudo-colour) among the connective tissue of the periprosthetic structures (with a blue pseudo colour).

radio-opaque in patients with metallosis and they were of variable size and shape. Most often, they formed elongated wear debris (Figs. 2A and C). In cases with alumina particles or cement debris, such metallic particles were also encountered in lesser amount. Alumina particles were often grouped in large clusters (Fig. 2B). This radio-opaque biomaterial had a less intense X-ray absorption than a metal. Cement debris appeared as small clusters in the soft tissues (pseudo cystic appearance) with many radio-opaque particles scattered inside (Fig. 2C). Isolated radio-opacifier particles were also encountered freely in the soft tissues.

Metallosis

On histological sections, numerous small black particles were observed in the cytoplasm of macrophages and

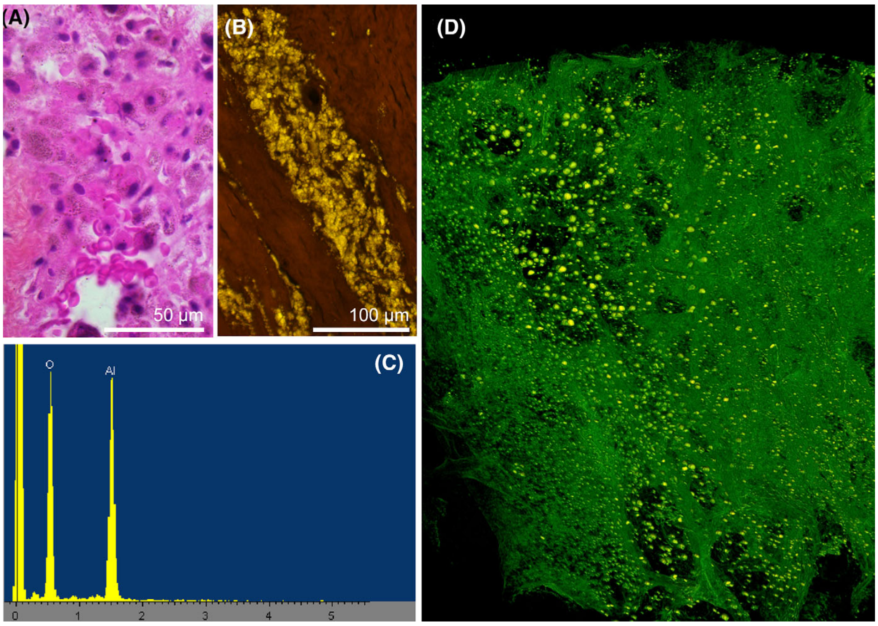

Fig. 4. Debris due to wearing of an alumina-on-alumina prosthesis. (A) Histological aspect of the periprosthetic tissues showing numerous brownish wear debris inside the cytoplasm of macrophages (HPS staining). (B) Section of the same periprosthetic tissue stained with lumogallion and analysed under fluorescent microscopy. Countless particles are revealed by this histochemical method. (C) EDS analysis of the debris with identification of alumina (aluminium oxide). (D) MicroCT aspect showing numerous round ceramic particles (with a yellow pseudo-colour) among the dense connective tissue of the periprosthetic structures (with a green pseudo colour).

appeared black. These particles were sometimes less than a 3–4 micrometre in size. Larger particles were occasionally observed between the collagen fibres of the periprosthetic connective tissue or between cells (Fig. 3A). In these cases with metallosis, polyethylene debris was also observed because the THA were done with a metal-on-polyethylene prosthesis. Since PE causes the formation of multinucleated giant cells, metal particles were also observed in the cytoplasm of the giant cells. In SEM-EDS analysis, the particles were composed of titanium, aluminium and vanadium corresponding to the TA6V alloy (Fig. 3B). In microCT, the large and small metallic particles were clearly identifiable within the periprosthetic tissues (Fig. 3C) (Movie S1).

Alumina

On histological sections, alumina particles were difficult to identify in the cytoplasm of mononucleated macrophages and appeared with a light brownish tint (Fig. 4A). On sections stained with lumogallion and analysed by fluorescence microscopy, the particles were readily identified as brilliant orange-yellow spots (Fig. 4B). SEM-EDS analysis confirmed that the particles were composed of aluminium and oxygen (Fig. 4C). MicroCT analysis evidenced the numerous alumina particles and the fibrosis streaks around the bands of macrophages overloaded with microparticles (Fig. 4D) (Movie S2).

Cement debris with radio-opaque particles

Histologically, the radio-opacifying particles mixed with methacrylic cement were present in two different but constantly associated forms: (i) wide clear pseudo cystic formations surrounded by macrophages and fibrosis contained agglomerates of large particles (~10–20 μm) often polyhedral in shape. This configuration corresponded to complete fragments of cement whose polymer had been dissolved by histological solvents, leaving these large particles in place (Fig. 5A). (ii) In the vicinity and at a distance from these pseudo-cystic formations, mononucleated macrophages contained a large number of round micro- and nanoparticles with a light centre and a dark peripheral border (Fig. 5B). SEM-EDS analysis showed that both were zirconium oxide particles, also containing traces of Hafnium, a known zirconium contaminant (Fig. 5C) (https://minerals.usgs.gov/minerals/pubs/commodity/zirconium/mcs-2012-zirco.pdf). The micro and nanoparticles thus correspond to a fragmentation of the large particles present in the cement fragments and that were phagocytised by macrophages (Movie S3).

Morphometric analysis

The morphometric analysis of the different types of particles appears on Table 1 and Figure 6. The largest particles were observed in cases of metallosis, the smallest in patients with

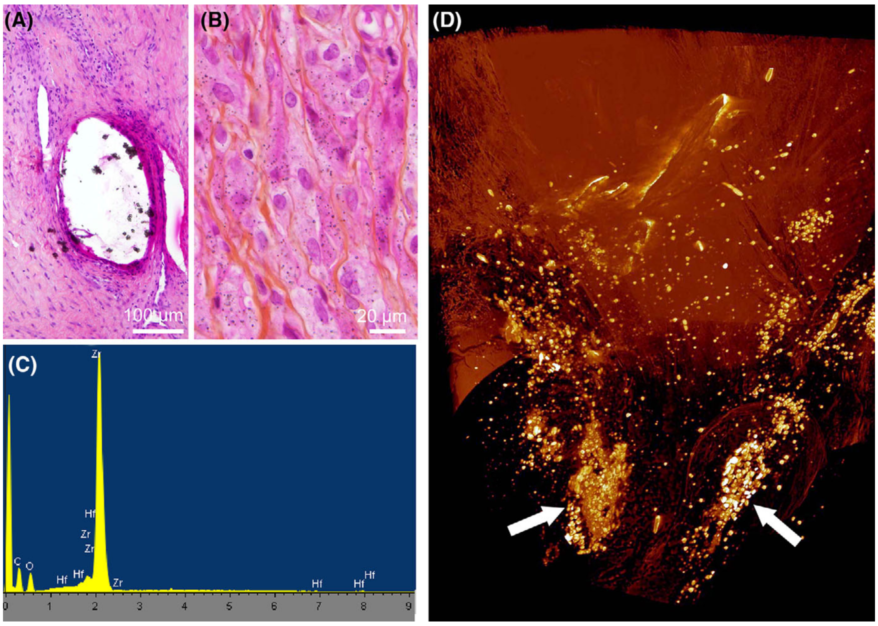

Fig. 5. Debris due to the fragmentation of a methacrylic cement containing zirconium oxide particles as a radio-opacifier (A) Histological aspect showing a large encapsulated pseudo-cyst with large agglomerates of Zr particles. The methacrylic component of the cement was dissolved by histological solvents leaving a void space (HPS staining). (B) Section of the same periprosthetic tissue at a higher magnification. A large number of microparticles with a light centre and a dark peripheral seam were phagocytised by macrophages. (HPS staining). (C) EDS analysis of the debris with identification of zirconium and hafnium. (D) MicroCT aspect showing several cluster particles forming pseudo-cysts (arrows) with margination of the particles (with a white-yellow pseudo-colour). Free particles are disseminated among the connective tissue of the periprosthetic structures (with a red pseudo colour).

Table 1. Morphometric analysis of the different types of particles.

	Volume of interest TV in mm^3	Fraction occupied by particles PV/TV in %	Particle density PD in particles mm^{-3}	Particle diameter D in μm
Metallosis (titanium)	60.847 ± 11.863	0.607 ± 0.340	1847 ± 1751	9.67 ± 9.81
Alumina	46.037 ± 28.814	0.299 ± 0.366	1230 ± 1289	4.31 ± 3.13
Bone cement (zirconium)	71.004 ± 22.621	0.027 ± 0.025	80 ± 83	7.58 ± 7.25

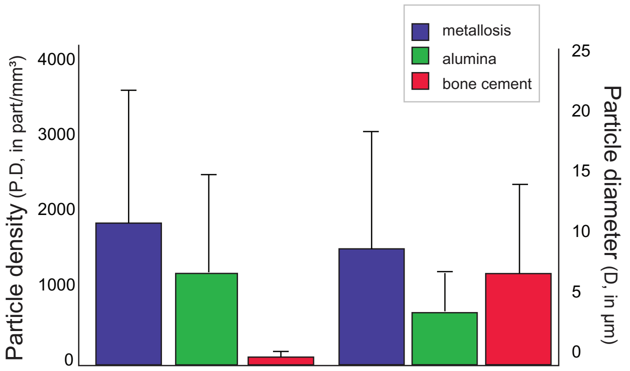

Fig. 6. Graphical analysis of the 3D density of the three types of particles and their mean diameter ± standard deviation.

alumina-on-alumina THA. As expected, the density of particles was the highest in metallosis and the lowest in patients with zirconia particles. In these cases, only the largest particles were detected, small particles, <2 μm, were below the resolution threshold of the technique.

Discussion

MicroCT imaging of whole blocks of tissue embedded in paraffin or polymers is a new imaging modality to create 3D reconstruction of whole tissue block with microscopic level resolution.[16,17] The method has been used on invaded lymph nodes, placental villi, nerves, bones, lung and is promised to new developments.[18–21] The detection of wear particles from implanted biomaterials has been a problem in orthopaedic surgery for decades. These particles are capable of causing a localised inflammation, which can lead to an aseptic loosening of the prosthesis. The chemical nature of the biomaterial debris conditions the cellular reaction as well as the importance of the inflammatory reaction.[22] PE particles locally cause a foreign body reaction with giant cells and eosinophilic macrophages associated with very strong inflammation.[9] Metal as well as alumina or zirconia particles do not cause giant cells formation but accumulate inside the cytoplasm of the macrophages. The alumina particles induce a fibrous encapsulation reaction.[11,14] Finally, all these particles can migrate away from the prosthesis and have systemic toxicity. The radiolucent PE particles cannot be detected by microCT.

Metal particles are most easily detected because of the high atomic number of the metal alloys. In this series of patients, only titanium prostheses were analysed as they represent the most commonly used device in our hospital. Other metal such as Cr-Co gave similar metallosis.[23] Metallosis reactions related to the accumulation of metal particles can be very dense, giving a grey-black tint to the periprosthetic tissue at surgery.[7] In this series, the density of the metal particles appeared very high but with a great variability as shown by the large standard deviations observed for particle density and diameter. The metallic particles were also those that reached the largest size as seen on histological sections where these particles may be in extracellular situation. The density of the metallic particles is such that their number is certainly much higher than suggested by the morphometric analysis. Indeed, in 3D it is difficult to separate particles that are joined together, whereas algorithms have been described for this purpose in 2D.[24,25]

Ceramic-on-ceramic (alumina being the most used)[26] and ceramic-on-cross-linked PE[27,28] have been proposed. The alumina-on-alumina has excellent tribological properties and generates 4000 times less wear particles than the metal-PE couple. A low periprosthetic osteolysis rate is evidenced but fibrosis around the alumina particles is reported.[14,29–31] Histological analysis of prosthetic periprosthetic tissues is difficult in cases of alumina-on-alumina prosthesis because the particles are often not easily visible.[12] For this reason, histochemical identification by lumogallion appears to be very valuable.[14] In microCT, alumina particles are radio-opaque and can be easily identified between fibrosis strips. Here again, it should be noted that there is a wide dispersion of particle density values depending on the patient. In the whole series analysed, these particles appeared to be the smallest, arranged in groups enclosed by fibrosis bands. EDS analysis confirmed that alumina was present in all cases.

Methacrylic cements are used for the fixation of prostheses. During THA, the cement fills the space between the prosthetic stem and the bone shaft. The cement mechanically holds the prosthesis in place by adhering to the metal. On the bone surface, the surface irregularities of the polymerised cement are related to penetration through the trabecular meshwork. The cement acts as an intermediate elasticity zone located between the rigid prosthetic stem and the bone with more elastic characteristics.[32] The cement can deteriorate considerably over time and fragmentation occurs after about ten years, releasing polymer fragments and radio-opaque particles.[33,34] Two types of radio-opacification particles have been used over time in cements: barium sulphate and zirconium oxide, barium sulphate being less radio-opaque than zirconia. Regardless of the radio-opacifier, concentrations of 8.0–15.0% are used in commercial cements. Currently, zirconium dioxide is the most widely used because it is believed to cause less osteolytic damage than barium sulphate.[35] In addition, barium ions are toxic and can be released into the circulation. In our hospital, the cement (PALACOS R pro Heraeus Medical GmbH, 61273 Wehrheim, Germany) used has zirconium dioxide particles in it for many years. Cement fragments containing the particles can accumulate in the periprosthetic tissues and cause a localised encapsulation fibrosis.[13,36] The use of histological solvents for the preparation of the sections solubilises the polymer, which is responsible for a pseudo-cystic appearance on tissue sections in which only agglomerates of radio-opaque particles persist. They present a large size and are easily detectable in microCT where this pseudo-cystic aspect is also observed. However, the 1–2 μm particles contained in the cytoplasm of the macrophages are not visible given the resolution used here in microCT (3 μm pixel^{-1}). The density of these particles appears low because small particles are not detected.

Conclusion

Biomaterials used in prosthetic devices for THA are susceptible to wear and release particles that accumulate locally and can migrate at distance. MicroCT appears to be an interesting method to quantify the different types of radio-opaque particles in 3D. This paper represents the first attempt to image and quantify in 3D the number of particles released in the periprosthetic tissues. Because determination of the number of particles on 2D sections is stereologically incorrect, a number of papers have tried to isolate the particles after alkali or acid digestion of the tissue followed by SEM analysis.[37–39] Nevertheless, these techniques do not allow seeing the particles in their microenvironment in 3D. MicroCT appears able to analyse the metal wear debris but is not capable currently to detect the polyethylene debris released by the acetabular cups. In addition, the technique does not allow a precise discrimination of particles that are agglutinated or close together in 3D. It also does not allow the quantification of radiolucent biomaterial particles such as PE or very small particles below the detection limit. However, it does make it possible to realise the immeasurable amount of these particles released into the human body.

Acknowledgements

Mrs. F. Pascaretti, N. Gaborit and S. Lemière are thanked for their technical help with microCT analysis and histotechnology. SEM and EDS analysis were performed at Service Commun d'Imagerie et d'Analyses Microscopiques (SCIAM), Université d'Angers, thanks to R. Mallet.

Funding

This work was made possible by grants from Angers CHU (University hospital) project MOCONA and the French Ministry of Research.

Conflict of interest

No conflicts of interest, financial or otherwise, are declared by the authors.

References

1. Judet, J., Judet, R., Crepin, G. & Rigault, A. (1947) *Essais de Prothèse Ostéo-Articulaire*. Masson, Issy les Moulineaux, France.
2. McKee, G. & Watson-Farrar, J. (1966) Replacement of arthritic hips by the McKee-Farrar prosthesis. *J. Bone Jnt. Surg. Br.* **48**, 245–259.
3. Charnley, J. (1960) Surgery of the Hip-joint. *Br. Med. J.* **1**, 821.
4. Boutin, P. (2014) Total arthroplasty of the hip by fritted alumina prosthesis. Experimental study and 1st clinical applications. *Orthop. Traumatol. Surg. Res.* **100**, 15–21.
5. Hanawa, T., Kaga, M., Itoh, Y., Echizenya, T., Oguchi, H. & Ota, M. (1992) Cytotoxicities of oxides, phosphates and sulphides of metals. *Biomaterials* **13**, 20–24.
6. Chappard, D., Libouban, H., Bizot, P., Massin, P. & Baslé, M.F. (2008) Devenir des biomatériaux. *Progrès en Dermato-Allergologie*, pp. 75–85. John Libbey Eurotext Esher, Arcueil, France.
7. Korovessis, P., Petsinis, G., Repanti, M. & Repantis, T. (2006) Metallosis after contemporary metal-on-metal total hip arthroplasty. Five to nine-year follow-up. *J. Bone Joint Surg. Am.* **88**, 1183–1191.
8. Rony, L., Lancigu, R. & Hubert, L. (2018b) Intraosseous metal implants in orthopedics: a review. *Morphologie* **102**, 231–242.
9. Massin, P. & Achour, S. (2017) Wear products of total hip arthroplasty: the case of polyethylene. *Morphologie* **101**, 1–8.
10. Schmalzried, T., Jasty, M. & Harris, W.H. (1992) Periprosthetic bone loss in total hip arthroplasty. Polyethylene wear debris and the concept of the effective joint space. *J. Bone Jnt. Surg. Am.* **74**, 849–863.
11. Lerouge, S., Huk, O., Yahia, L.H. & Sedel, L. (1996) Characterization of in vivo wear debris from ceramic – ceramic total hip arthroplasties. *J. Biomed. Mater. Res. – Part A.* **32**, 627–633.
12. Rony, L., de Sainte Hermine, P., Steiger, V., Mallet, R., Hubert, L. & Chappard, D. (2018a) Characterization of wear debris released from alumina-on-alumina hip prostheses: analysis of retrieved femoral heads and peri-prosthetic tissues. *Micron* **104**, 89–94.
13. Rosenberg, A.E., Nielsen, G.P. & Reith, J. (2011) Surgical pathology of joint prostheses. *Seminars in Diagnostic Pathology*, pp. 65–72. WB Saunders, Philadelphia, USA.
14. Rony, L., Pascaretti-Grizon, F., Hubert, L. & Chappard, D. (2020) Histochemical identification of wear debris released by alumina-on-alumina hip prostheses in the periprosthetic tissues. *Orthop. Traumatol. Surg. Res.* in press, https://doi.org/10.1016/j.otsr.2020.1003.1027.
15. Goldstein, J., Newbury, D.E., Echlin, P., Joy, D.C., Romig Jr, A.D., Lyman, C.E., Fiori, C. & Lifshin, E. (2012) *Scanning Electron Microscopy and X-Ray Microanalysis: A Text for Biologists, Materials Scientists, and Geologists*. Springer Sci. & Bus. Media, Plenum Press, New York, USA.
16. Senter-Zapata, M., Patel, K., Bautista, P.A., Griffin, M., Michaelson, J. & Yagi, Y. (2016) The role of micro-CT in 3D histology imaging. *Pathobiology* **83**, 140–147.
17. Perilli, E., Baruffaldi, F., Visentin, M., Bordini, B., Traina, F., Cappello, A. & Viceconti, M. (2007) MicroCT examination of human bone specimens: effects of polymethylmethacrylate embedding on structural parameters. *J. Microsc.* **225**, 192–200.
18. Xu, B., Teplov, A., Ibrahim, K. *et al.* (2020) Detection and assessment of capsular invasion, vascular invasion and lymph node metastasis volume in thyroid carcinoma using microCT scanning of paraffin tissue blocks (3D whole block imaging): a proof of concept. *Mod. Pathol.* 1–9 https://doi.org/10.1038/s41379-41020-40605-41371.
19. Barapatre, N., Aschauer, B., Kampfer, C., Schmitz, C., von Koch, F. & Frank, H.-G. (2020) Air contrast of the intervillous space enables non-disruptive Micro-CT analysis of paraffin-embedded archival placental tissue. *Placenta* **100**, 66–68.
20. Norvik, C., Westöö, C.K., Peruzzi, N. *et al.* (2020) Synchrotron-based phase-contrast micro-CT as a tool for understanding pulmonary vascular pathobiology and the 3-D microanatomy of alveolar capillary dysplasia. *Am J Physiol. – Lung Cell. Mol. Physiol.* **318**, L65–L75.
21. Bikis, C., Thalmann, P., Degrugillier, L., Schulz, G., Müller, B., Kalbermatten, D.F., Madduri, S. & Hieber, S.E. (2018) Three-dimensional and non-destructive characterization of nerves inside conduits using laboratory-based micro computed tomography. *J. Neurosci. Meth.* **294**, 59–66.
22. Bijukumar, D.R., Segu, A., Souza, J.C.M., Li, X., Barba, M., Mercuri, L.G., J. Jacobs, J. & Mathew, M.T. (2018) Systemic and local toxicity of metal debris released from hip prostheses: a review of experimental approaches. *Nanomed. Nanotechnol. Biol. Med.* **14**, 951–963.
23. De Pasquale, D., Stea, S., Squarzoni, S., Bordini, B., Amabile, M., Catalani, S., Apostoli, P. & Toni, A. (2014) Metal-on-metal hip prostheses: correlation between debris in the synovial fluid and levels of cobalt and chromium ions in the bloodstream. *Int. Orthop.* **38**, 469–475.
24. Russ, J.C. & Dehoff, R.T. (2012) *Practical Stereology*. Springer Sci. & Bus. Media, NY.
25. Serra, J. (1983) Connectivity criteria. *Image Analysis and Mathematical Morphology*, pp. 374–423. Academic Press, Inc., Orlando, USA.
26. Hamadouche, M., Boutin, P., Daussange, J., Bolander, M.E. & Sedel, L. (2002) Alumina-on-alumina total hip arthroplasty. *J. Bone Joint Surg. Am.* **84**, 69–77.
27. Sugano, N., Nishii, T., Nakata, K., Masuhara, K. & Takaoka, K. (1995) Polyethylene sockets and alumina ceramic heads in cemented total hip arthroplasty. A ten-year study. *Bone Joint J.* **77**, 548–556.

28. Zichner, L.P. & Willert, H.-G. (1992) Comparison of alumina-polyethylene and metal-polyethylene in clinical trials. *Clin. Orthop. Rel. Res.* **282**, 86–94.
29. Bizot, P., Nizard, R., Hamadouche, M., Hannouche, D. & Sedel, L. (2001) Prevention of wear and osteolysis: alumina-on-alumina bearing. *Clin. Orthop. Rel. Res.* **393**, 85–93.
30. Prudhommeaux, F., Hamadouche, M., Nevelos, J., Doyle, C., Meunier, A. & Sedel, L. (2000) Wear of alumina-on-alumina total hip arthroplasties at a mean 11-year followup. *Clin. Orthop. Rel. Res.* **379**, 113–122.
31. Dorlot, J.M., Christel, P. & Meunier, A. (1989) Wear analysis of retrieved alumina heads and sockets of hip prostheses. *J. Biomed. Mater. Res. – Part A*. **23**, 299–310.
32. Kühn, K.-D. (2012) *Bone Cements: Up-to-Date Comparison of Physical and Chemical Properties of Commercial Materials*. Springer-Verlag, Berlin-Heidelberg.
33. Topoleski, L.D., Ducheyne, P. & Cuckler, J.M. (1990) A fractographic analysis of in vivo poly(methyl methacrylate) bone cement failure mechanisms. *J. Biomed. Mater. Res.* **24**, 135–154.
34. Pazzaglia, U.E. (1990) Fragmentation of methylmethacrylate: a cause of late failure of total hip replacement. A case report. *Arch. Orthop. Trauma Surg.* **109**, 49–52.
35. Sabokbar, A., Fujikawa, Y., Murray, D.W. & Athanasou, N.A. (1997) Radio-opaque agents in bone cement increase bone resorption. *J. Bone Jnt. Surg. Br.* **79**, 129–134.
36. Schunck, A., Kronz, A., Fischer, C. & Buchhorn, G.H. (2016) Release of zirconia nanoparticles at the metal stem–bone cement interface in implant loosening of total hip replacements. *Acta Biomater*. **31**, 412–424.
37. Böhler, M., Mochida, Y., Bauer, T.W., Plenk Jr, H. & Salzer, M. (2000) Wear debris from two different alumina-on-alumina total hip arthroplasties. *J. Bone Jnt. Surg. Br.* **82**, 901–909.
38. Catelas, I., Bobyn, D., Vali, H., Medley, J., Campbell, P., Zukov, D., Pétit, A. & Huk, D. (2000) Changes in metal-metal wear particle characteristics with isolation protocols. *46th Annual Meeting, Orthopaedic Research Society*. Orlando, Florida, USA.
39. Billi, F., Benya, P., Ebramzadeh, E., Campbell, P., Chan, F. & McKellop, H.A. (2009) Metal wear particles: what we know, what we do not know, and why. *Int. J. Spine Surg.* **3**, 133–142.

Supporting Information

Additional supporting information may be found online in the Supporting Information section at the end of the article.

Movie S1: 'Movie_metallosis1.mp4' illustrates the metal particles (with a yellow pseudo-colour) released among the periprosthetic connective tissues (with a blue pseudo colour).
Movie S2: 'movie_alumina_debris.mp4' illustrates the numerous round ceramic particles (with a yellow pseudo-colour) among the dense connective tissue of the periprosthetic structures (with a green pseudo colour).
Movie 3: 'movie_zirconium_debris.mp4' shows several cluster particles forming pseudo-cysts (with white-yellow pseudo-colour). Free particles are disseminated among the connective tissue of the periprosthetic structures (with a red pseudo colour).

Partie 2 – Remodelage osseux, ostéointégration et implants en titane

La deuxième partie de ce travail a consisté à analyser l'ostéointégration d'implants en titane poreux comme matériau de comblement dans le cas de grands défauts osseux. Nous avons étudié deux microarchitectures différentes afin de savoir si celle-ci influençait l'ostéointégration des implants.

Le titane est utilisé depuis très longtemps en chirurgie orthopédique ou dentaire (46, 90, 99). Son ostéointégration est également connue depuis longtemps et les ostéoblastes ont une affinité forte pour ce métal (100). En chirurgie orthopédique, il est utilisé en clinique comme revêtement macroporeux pour l'ostéointégration d'implant sans-ciment (47-49, 101, 102). Depuis quelques années, des implants en tantale sont utilisés en chirurgie orthopédique pour le comblement de défects cavitaires notamment pour les reconstructions de perte osseuse dans les chirurgies de reprise prothétique (44, 103, 104). Les implants poreux en tantale ont une forme tétrakaïdécahédronique et sont obtenus par des processus non divulgués par l'industrie (45, 105). Il est probable, compte tenu de la forme, qu'il soit obtenu en utilisant des mousses en polyuréthane donnant cette architecture. Ce même procédé est utilisé pour la confection des céramiques d'orthophosphates de calcium. Ces implants ont l'avantage par rapport aux céramiques de phosphate tri-calcique d'avoir une résistance mécanique et de permettre l'ostéointégration (44, 45).

Les biomatériaux à porosité interconnectée présentent des capacités d'ostéointégration plus élevée qu'il s'agisse de céramiques ou d'implants métalliques (5, 106-108). Les implants en titane utilisés pour ce travail ont été obtenus par impression 3D avec une porosité interconnectée dans le cadre d'une coopération franco-belge avec un groupe de biomatériaux français (Kasios, l'Union) et un centre technologique wallon (SIRRIS- Liège). Deux types de cylindres ont été produits, l'un reproduisait la structure de l'os trabéculaire alors que l'autre reproduisait une architecture géométrique utilisée pour des cages de fusion intersomatique vertébrale (109, 110). Les implants ainsi obtenus ont été passivés par un mélange d'acide nitrique - acide fluorhydrique pour les nettoyer des billes élémentaires en titane qui n'ont pas été fusionnées lors de la fabrication additive par laser (35, 111, 112).

L'analyse des implants en titane utilisés dans ce travail a montré qu'il existait des différences entre les paramètres mesurés lors de l'expérimentation et ce qui pouvait être préalablement calculé. Les paramètres portaient notamment sur la résistance à l'écoulement et la circularité des pores, ceci est probablement lié à l'utilisation du titane et à l'effet de nettoyage de l'acide fluorhydrique qui entraîne une irrégularité des surfaces et modifient ainsi ces paramètres.

L’implantation de ces implants a été faite dans des condyles médiaux de fémur de brebis à l’Ecole Vétérinaire de Nantes (ONIRIS) avec un chirurgien vétérinaire spécialisé en chirurgie osseuse de l’animal. Ce modèle a permis d’utiliser un animal qui présente le même type d’os trabéculaire que l’homme avec des os larges permettant la réalisation de défauts osseux de grande taille, il permet donc d’être facilement extrapolable à la physiologie humaine (113-115). Afin de ne pas conclure à une différence d’ostéointégration qui aurait pu être liée à la durée d’implantation, l’analyse a été faite à 3 mois et à 9 mois post-implantation. L’allongement de la durée de stabulation permet d’obtenir des résultats robustes et limite les biais d’analyses (115, 116). Cette étude a été scindée en deux articles montrant en utilisant des techniques différentes (nanotomographie, histomorphométrie, écoulement de fluides…).

ARTICLE 5

Osseointegration of two types of titanium cylinders with geometric or trabecular microarchitecture: A nanotomographic and histomorphometric study

Ostéointégration de deux types de cylindres en titane avec microarchitecture géométrique ou trabéculaire : étude nanotomographique et histomorphométrique

Louis RONY, Eric AGUADO, Bruno VERLEE, FLorence PASCARETTI-GRIZON, Daniel CHAPPARD

Morphologie – In Press

Cite Score : 2,1 – SIGAPS : NC

Morphologie xxx (xxxx) xxx—xxx

Disponible en ligne sur
ScienceDirect
www.sciencedirect.com

Elsevier Masson France
EM|consulte
www.em-consulte.com

ORIGINAL ARTICLE

Osseointegration of two types of titanium cylinders with geometric or trabecular microarchitecture: A nanotomographic and histomorphometric study

Ostéointégration de deux types de cylindres en titane avec microarchitecture géométrique ou trabéculaire : étude nanotomographique et histomorphométrique

L. Rony[a], **E. Aguado**[a,b], **B. Verlee**[c], **F. Pascaretti-Grizon**[a], **D. Chappard**[a,d,*]

[a] *GEROM - Groupe Etudes Remodelage Osseux et bioMatériaux, LabCom NextBone, Univ-Angers, IRIS-IBS Institut de Biologie en Santé, 49933 Angers, France*
[b] *ONIRIS, Ecole Vétérinaire de Nantes, 44307 Nantes Cedex 3, France*
[c] *SIRRIS Liège Science Park, Rue du bois St Jean 12, 4102 Seraing, Belgium*
[d] *SCIAM, Service Commun d'Imagerie et Analyses Microscopiques, IRIS-IBS Institut de Biologie en Santé, Univ-Angers, 49933 Angers Cedex, France*

KEYWORDS
Titanium ;
Trabecular scaffold ;
Osseointegration ;
Geometric architecture ;
Histomorphometry

Summary Porous biomaterials promote osseointegration. We have prepared porous titanium cylinders by additive manufacturing from titanium beads. Two types of morphology were tested: cylinders with geometric pores or mimicking trabecular microarchitecture. Cylinders were decontaminated and cleaned by HF/HNO_3 to remove unmelted balls. Surgical implantation in ewes was performed under general anesthesia and the animals were housed for 90 and 270 days. The femoral condyles were collected and analyzed by nanoCT, embedded in pMMA and analyzed by histomorphometry. No significant difference was found in terms of bone volume or bone/titanium interface between the two types of cylinders. There was no evolution over time except for the mineralization rates which decreased, reflecting the effect of the aging of the animals. The influence of the pores (geometrical or ''natural'') did not influence osseointegration. HF/HNO_3 etching treatments are effective on the outermost surfaces but do not seem to reach the central cavities of the samples. Finally, osseointegration seems to occur only in

---

* Corresponding author. GEROM - LHEA, IRIS-IBS Institut de Biologie en Santé, Université d'Angers, 49933 Angers Cedex, France.
Adresse e-mail : daniel.chappard@univ-angers.fr (D. Chappard).

https://doi.org/10.1016/j.morpho.2021.03.001

Pour citer cet article : L. Rony, E. Aguado, B. Verlee et al., Osseointegration of two types of titanium cylinders with geometric or trabecular microarchitecture: A nanotomographic and histomorphometric study, Morphologie, https://doi.org/10.1016/j.morpho.2021.03.001

the few millimeters around the periphery of the implants and does not extend in the center. This is explained by the absence of stress transmission within the very rigid metal cylinders, preventing bone modeling and remodeling.

Résumé Les biomatériaux poreux favorisent l'ostéointégration. Nous avons préparé des cylindres en titane poreux par fabrication additive à partir de billes de titane. Deux types de morphologie ont été testés : cylindres avec des pores géométriques ou mimant la microarchitecture trabéculaire. Les cylindres ont été décontaminés et nettoyés par HF/HNO_3 pour enlever les billes non fondues. Une implantation chirurgicale chez la brebis a été effectuée sous anesthésie générale et les animaux ont été stabulés pendant 90 ou et 270 jours. Les condyles fémoraux ont été prélevés et analysés par nanoCT, puis inclus en pMMA et analysés par histomorphométrie. Nous n'avons pas retrouvé de différence significative en termes de volume osseux ou d'interface os/titane entre les deux types de cylindres. Il n'y avait pas d'évolution au cours du temps sauf pour les vitesses de minéralisation qui ont diminué, ceci reflétant l'effet du vieillissement des animaux. L'influence des pores (géométriques ou « naturels ») n'a pas eu d'influence sur l'ostéointégration. Les traitements par gravure HF/HNO_3 sont efficaces sur les surfaces les plus externes mais ne semblent pas atteindre les cavités centrales des prélèvements. Enfin, l'ostéointégration semble n'intéresser que les quelques millimètres en périphérie des implants et s'étend peu en profondeur des cylindres. Ceci est expliqué par l'absence de transmission de contraintes au sein des cylindres métalliques très rigides, empêchant le modelage et le remodelage osseux.

Introduction

Biomaterials are increasingly being used today for tissue reconstruction and regeneration. For bone, bone grafts occupy an important place in the therapeutic arsenal, particularly to regenerate a sufficient bone volume in case of a cavity defect [1]. Numerous studies have reported the use of autologous bone to fill a bone loss. In orthopedic surgery, there are many sites for harvesting bone: iliac bone, fibula, ribs... However, autograft complicates the surgical protocol and an additional operation on a second harvesting site makes the surgical procedure more cumbersome and leads to secondary morbidity. The inconveniences of autografts have a frequency that has been estimated at 20% [2,3].

Because of these problems, many solutions have been searched such as the use of allogeneic bone from bone banks. However, packaging and preparation methods vary from one bank to another and are associated with biomechanical or structural modifications of the bone matrix of the graft. Companies have proposed variable physicochemical processes for the treatment, cleaning and sterilization of allografts, which are also applied to bone xenografts, most often of bovine origin. In this case, companies can deliver the biomaterial in the form of granules, blocks of trabecular bone, cortical or cortico-trabecular blocks. There is no ideal treatment and, moreover, significant alterations in the bone matrix are induced by the manufacturing processes that affect the cellular compatibility of the grafts [4]. The risk of transmission of unconventional infectious agents (prions) has also been raised with both allo and xenografts. This risk cannot be ruled out in the presence of procedures that allow the organic fraction of the bone matrix to persist, even if it is partially removed. Finally, allografts most often use bone tissue from osteoarthritic femoral heads whose nature, texture, biomechanical properties and microarchitecture of the trabecular bone are abnormal [5,6]. Synthetic biomaterials (β-TCP, hydroxyapatite, etc.) offer significant viral and bacterial safety. However, they present different disadvantages: granular forms are friable when places in weight bearing areas, massive porous forms are very slowly resorbed and do not osseointegrate when they have a non-interconnected porosity [7]. For all these reasons, it would be interesting to develop biomaterials with an interconnected porosity and with a high mechanical resistance that can be placed in large cavity defects in load-bearing bones. The development of metallic foam may appear as an interesting solution, especially if the metal used is biocompatible.

In the present study, porous titanium cylinders were fabricated by additive manufacturing; they were prepared with an interconnected porosity to be placed in large supercritical bone defects. We tested two different microarchitectures: either geometric (computer-modelled) or trabecular, mimicking bone tissue with interconnected trabeculae and pores. The study was conducted by implanting these cylinders in the sheep femoral condyles for two time-periods of 90 and 120 days. The analysis was conducted by nanotomography (nanoCT) and histology after embedding in pMMA (poly methylmethacrylate).

Material and methods

Cylinder preparation

Geometric cylinders

A mathematical model of a cylinder with a geometric microarchitecture was made with square cross-section pores measuring 650 µm on each side. The porosity was interconnected and the 3D model was produced.

Trabecular cylinders

For the manufacture of the trabecular cylinders, we used a natural mature bovine bone whose microarchitecture is close to that of man. The tibial plateau was selected because it provided a large volume of bone. The bone was analyzed by microcomputed tomography (microCT) and the stack of 2D cross-section images was sent to Sirris to prepare the 3D model.

Preparation of titanium cylinders by additive manufacturing from .stl models

The 3D models of both types of cylinders were first imported into a specific software for processing and preparing .stl files for additive manufacturing (Magics® - Materialise Leuven, Belgium). A support for holding the cylinders was also added to separate them from the built plate of the 3D printer and to evacuate the heat generated locally by the laser during fusion of the powder. The global files containing all the parts and their supports were then imported into the MTT Autofab Marcam® slicing software (Release 1.6, Renishaw Benelux, Brenda, Netherland) to virtually slice the parts into thin 30 µm layers. The contours were produced at 100 W and 500 mm/s, and the internal hatching at 190 W and 600 mm/s, with a hatching distance of 120 µm between passes.

The sliced files were sent to the additive printer (SLM 250HL®, SLM Solutions, Lübeck, Germany). Printing took place in a closed chamber under a protective atmosphere (argon), by spreading successive layers of powder and selectively melting it in order to build up the parts layer by layer. The building plate was heated to 100 °C to limit internal stresses in the material. Powdered material used was a Ti6Al4 V ELI titanium alloy powder from TLS Technik (Bitterfeld-Wolfen, Germany) atomized under argon, with a spherical shape and a particle size dispersion of 20-63 µm. After manufacture, the cylinders were cut out of the tray using a band saw without lubricating liquid. As much unmelted powder as possible was manually removed from the cylinders in successive steps using a vacuum cleaner and a vibrating table. This cleaning step was completed by passing through an ultrasonic bath under isopropanol. The cylinders were then placed in a drying oven and the supports were removed. The cylinders thus realized measured 2 cm in length with a diameter of one centimeter.

Biomaterial cleaning

Cylinders obtained by additive manufacturing received a post-treatment to improve surface parameters such as roughness and to remove unmelted metallic powder beads. Removal of these unmelted particles together with surface etching was done by a chemical post-processing using a hydrofluoric/nitric acid (HF/HNO_3) solution. The method used was adapted from those used to clean dental implants [8]. Briefly, the cylinders were treated by strong acids (HNO_3 65% (5 vol.) + HF 58% (1 vol.) and cleaning solutions (sodium perborate, tetracetylene diamine and tensio-active reagents). Extensive washing was done in distilled water using ultrasonic waves during cleaning. Cylinders were dried and sterilized by gamma radiation.

Scanning electron microscopy (SEM)

Surface morphology of the raw and cleaned cylinders was analyzed on an EVO LS10 (Carl Zeiss Ltd., Nanterre, France). Images were captured in the secondary electron mode with an acceleration tension of 20 kV.

Microcomputed tomography (microCT)

MicroCT of the bovine bone and the crude titanium cylinders was performed using a Skyscan 1272 X-ray computerized microtomograph (Bruker microCT, Kontich, Belgium) equipped with an X-ray. For bone, the tube worked at 90 kV, 111 µA, pixel size corresponding to 13.24 µm, with 180° rotation and exposure with an Aluminum 0.5 mm + Copper 0.038 mm filter. For the titanium cylinders, the following characteristics were used: 100 kV/100 µA, pixel size corresponding to 10 µm; the rotation step at 0.2° with 360° rotation and exposure with a 0.11 mm copper filter. For each sample, a stack of 2D-sections (.jpg format) was obtained, reconstructed using NRecon software (Bruker) and the morphometric analysis was done with the CTAn software (Bruker, release 1.13.11.0). Three-dimensional reconstructions were obtained using CTVox software (Bruker, release 2.5).

Morphometry of the cylinders

The 3D models of the cylinders were used to compute morphometric characteristic and computational fluid dynamics. Morphometric analysis of the cylinders was done with the CTAn software (Bruker nanotomography, Kontich, Belgium) and the following parameters were determined:

- porosity (expressed in %) represents the global amount of the cylinder occupied by pores;
- pore diameter (in µm).

Morphological characteristics of the geometric pores was obtained by analysis of images with ImageJ (NIH https://imagej.nih.gov/ij/). The following form factors were derived from measurements of area and perimeters of the pores imaged on 2D microCT scans and theoretical models composed of perfect squares:

- circularity (4π*area/perimeter^2);
- solidity (area/convex hull area) is sensitive to indentations of the pores boundaries. Solidity should be one for a profile without any indentations and, has a value of < 1 if there are irregularities.

Animal and surgical procedure

The animal study was conducted on 18 cull-aged sheep Vendean sheeps (non-GMOs) purchased from local breeders and acclimated at the Veterinary School of Nantes' sheepfold (ONIRIS, France) between 10 days and 21 days before surgery. All animals received a titanium cylinder in the femoral condyles; left knees were filled with a geometric cylinder and right knees were filled with a trabecular cylinder. Nine ewes sacrificed after 90 days constituted the first group (group A) and nine ewes sacrificed after 270 days constituted the second group (group B). The ewes were operated by a trained veterinarian surgeon under general anesthesia performed with a standardized protocol comprising two hypnotic drugs by intravenous perfusion (Isoflurane and Ketamine) and a benzodiazepine (Diazepam). General anesthesia was maintained after endotracheal intubation with halothane provided by an anesthetic apparatus. An injection of amoxicillin trihydrate (500 mg) was administered before incision. A cutaneous incision was made longitudinally, parallel to the femur axis. The medial side of medial femoral condyle was reached through the *sartorius* muscle. A blind tunnel (1 cm in diameter, 2 cm in depth) was made using drills of progressive size with an electric rotary instrument at low speed (400 rpm) under irrigation with physiologic saline to remove the bone debris. Titanium cylinders were impacted in these blind-tunnels. Once tunnel was filled, periosteum, the muscle fascia, the subcutaneous tissues and the skin were sutured with resorbable thread.

In the A and B groups, two subgroups were obtained: filled with geometric titanium cylinder (g subgroup) or filled with trabecular titanium cylinder (t subgroup). So, four subgroups were considered: A-g and A-t subgroups sacrificed at 90 days and B-g and B-t subgroups sacrificed at 270 days.

Towards the end of each of the two study periods, a double calcein labeling was done to determine the mineral apposition rate (MAR) and a ''2 days on, 10 days off and 2 days on'' schedule was used (calcein dose: 30 mg/kg; IM route). Sacrifice of animals was done by a lethal injection of phenobarbital. Both knees were retrieved for analysis and fixed in 10% formalin.

Nanocomputed tomography of the bone blocks

The large blocks of bones containing the titanium implants were transferred while in the fixative in a X-ray computed nanotomograph (Nanotom, Phoenix, GE, USA) using polychromatic X-rays to limit artefacts due to titanium. NanoCT analysis was done at 100 kV and 220 μA and a copper filter. The rotation angle was 0.2° with a pixel size of 12.82 μm. Image reconstruction was done on the projection images with the DATOS software (Phoenix, GE) and a stack of 2D sections was obtained for each specimen.

Morphometric analysis of the cylinders was done with the CTAn software (Bruker nanotomography, Kontich, Belgium) and the following parameters were determined:

3D models were obtained with VG StudioMax 3.2 (Volume Graphics GmbH, Heidelberg, Germany). On the 3D models, re-slicing is possible to expose the different areas of interest and select the most representative 2D sections.

Histological and histomorphometric analysis

Samples were embedded in poly(methylmethacrylate) for histological analysis as previously described [9,10]. Blocks were then sectioned with a diamond saw (Accutom, Struers, France) in 500 μm thick slices. Slices passing through the central position of the cylinders were selected and polished on an automatic polishing machine (Struers) to a 1 μm finish with diamond particles. Some slices were left unstained and analyzed with polarization microscopy on an Olympus BX 51 microscope (Olympus, France). Other slices were surface-stained with borax-toluidine blue during 45 min.

Morphometric analysis was done on a semi-automatic image analyzer. The standardized nomenclature for bone histomorphometry of the ASBMR was used [11]. The following parameters were determined:

- volume of trabecular bone grown inside the cylinder (BV/TV, in %);
- percent of titanium surface covered by bone (BS/TitS, in %).

Ethical consideration

This project was approved by the National Ethical Committee for Animal Experimentation (EAEC) under the reference number: CEEA.2012.257. This study took into account the rule of 3Rs aimed at limiting the number of subjects necessary for experimentation [12].

Statistical analysis

The SYSTAT software (Systat, San José, CA, release #13.00.05) was used to perform statistical analysis. All results were expressed as mean ± standard deviation (SD). For the morphometric analysis, a Student t test was used after Bonferroni correction. For the animal study, due to the small number of bone samples used in this study, a Kruskall-Wallis nonparametric analysis of variance was used to compare differences among groups. The comparison between groups was obtained by *post-hoc* tests. Differences were considered significant for $p < 0.05$.

Results

Surgical procedure

There was no mortality nor septic complications following the placement of the titanium cylinders (Fig. 1).

The titanium cylinders

An image of the bovine bone used to prepare the cylinders appears in Fig. 2A. The trabecular microarchitecture is clearly anisotropic with the presence of large vertical plates (parallel to the gravity exerted on the tibia) joined together by transverse pillars. The image of a titanium cylinder from this block appears in Fig. 2B. A geometrically shaped cylinder appears in Fig. 2C.

The effectiveness of decontamination treatments is shown in Fig. 3. Fig. 3A shows a trabecular cylinder obtained by additive manufacturing and subjected to a vibrating table to remove most of the unmelted titanium powder particles. Some deep cavities in the trabecular network remained filled with non-adherent powder particles. Cylinders with geometric microarchitecture do not have such

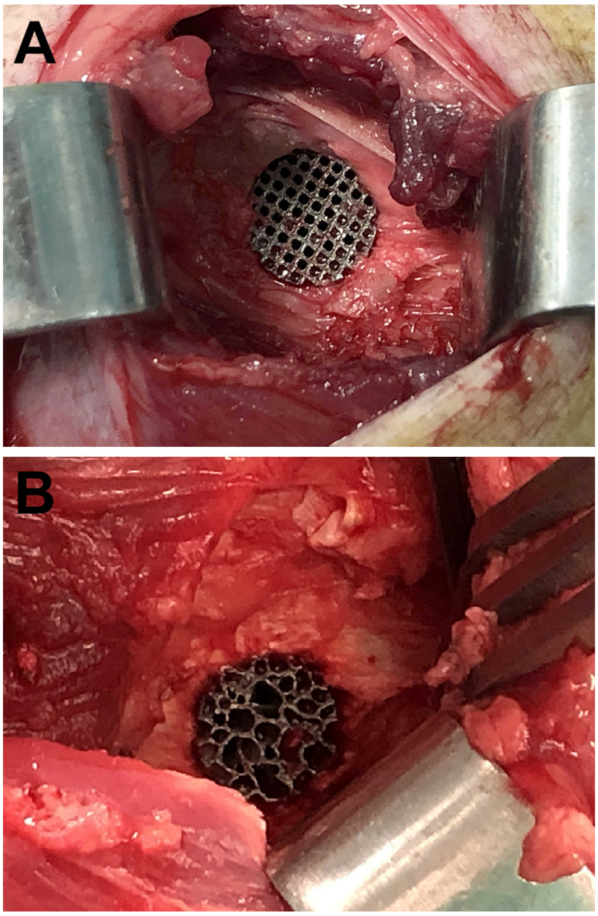

Figure 1 Surgical placement of the two types of implants in the ewe. A) Cylinder with geometric microarchitecture. B) Cylinder with trabecular microarchitecture.

titanium powder sequestrations (Fig. 3B). Finally, treatment with ultrasonic bath and isopropanol allows the removal of particles contained in the deep cavities of the cylinders (Fig. 3C). In all cases, a 3D and 2D aspect is provided in Fig. 3.

SEM analysis visualizes the surface of the biomaterial that will come into contact with the bone cells. After the decontamination treatments, many titanium beads remain adhering to the deep plane where the metal has melted, but most often simply stuck tangentially (Fig. 4 A & C). These beads are removed by an HF/HNO_3 treatment which etches the surface and gives the titanium surfaces a typical appearance with a slight superficial erosion (Fig. 4B & D).

The morphometric characteristics of the two types of cylinders are shown in Fig. 5A. The geometrical and trabecular cylinders did not differ in porosity, however the pore size was significantly larger for the trabecular cylinders. The comparison of the pore morphology on the geometric cylinders compared to their theoretical model, showed differences in the form factors circularity and strength. Both parameters suggested a modification of the shape with an increase in the irregularity of the contours on the Ti models (Fig. 5B).

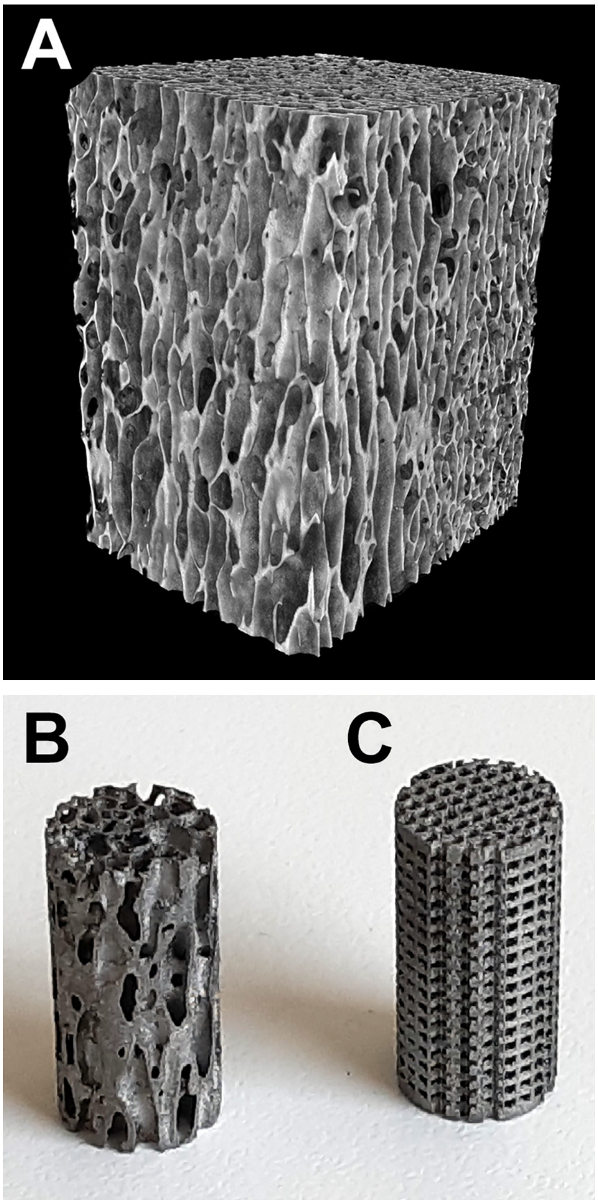

Figure 2 A) a large block of anisotropic trabecular bone from an aged ox (side = 5 cm). Note the plates with a vertical disposition connected by transverse pillars, this creates an interconnected porosity. B) A titanium cylinder prepared by additive manufacturing from this block of ox bone. C) A titanium cylinder prepared with a geometric microarchitecture by additive manufacturing.

Nanocomputed tomography of the bone blocks

NanoCT analysis of very large blocks allows the implants and their geometry to be clearly seen, as well as the surrounding bone tissue. The anchoring of bone on the surface of the cylinders is clearly visible (Fig. 6). The amount of newly formed bone is much greater when studying the insertion areas close to cortical bone of the implanted femur. Anchorage of bone is easier to evidence when considering 2D sections perpendicular to the major axis of the

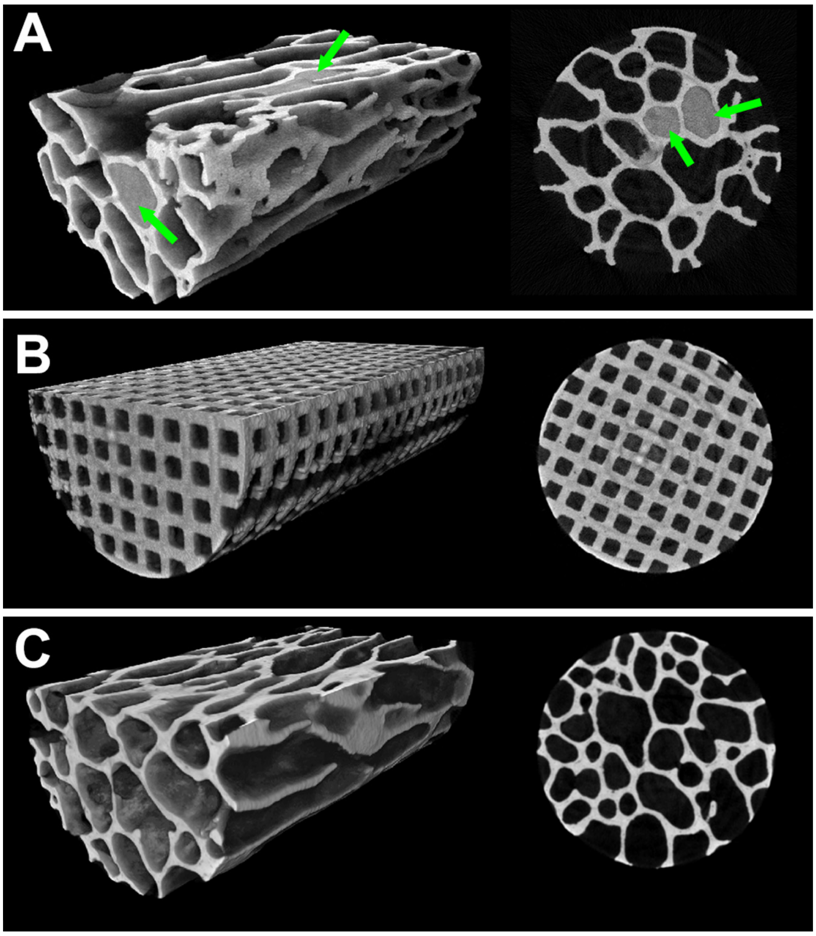

Figure 3 MicroCT analysis of titanium cylinders. A) 3D model of a crude Ti cylinder with trabecular microarchitecture showing the presence of unmelted titanium powder filling some cavities difficult to reach. The 3D model is sectioned to evidence the plain cavities. On the right side, a 2D section enhancing the persistence of Ti powder (green arrows). B) 3D model and 2D section of a titanium cylinder with a geometric microarchitecture. The interconnectedness of the porosity favors elimination of unmelted Ti particles. C) 3D model and 2D section of a Ti cylinder after extensive treatment to eliminate the residual Ti particles.

cylinder than on sections parallel to this axis (Fig. 6B & E). This is related to the amount of titanium interfering during the reconstruction of images. However, despite the use of the polychromatic radiations used by the nanoCT, it was very difficult to visualize and to threshold bone that has penetrated into the interior of the cylinders due to reconstruction artefacts due to the thickness and absorbance of the metal. Therefore, a morphometric analysis could not be conducted.

Histological and histomorphometric analysis

Analysis of the thick sections surface-stained with toluidine blue showed that at 90 and 270 days, all the cylinders are osseointegrated with bone anchored to the surface of the biomaterial (Fig. 7A—D). At 90 days, fine trabeculae consisting of lamellar and woven bone are observed inside the cylinders. These trabeculae may sometimes extend to the center of the specimen, but most often they are confined to the first few millimeters. This aspect is similar regardless of the geometric or trabecular microarchitecture. In fluorescence microscopy, the double labeling is clearly visible in the external trabeculae and in those inside the cylinders. However, a blurred labeling is noted in areas of rapidly growing bone that corresponded to woven bone in polarized microscopy as shown by others [13,14] (Fig. 7E—F). At 270 days, the amount of bone has not increased between the two types of implants. Near the cortical insertion, more bone was observed extending from the periphery of the drilled hole extending from the periphery to the center of the cylinder. Quantitative analysis was possible and revealed that BV/TV did not change over time and there was no significant difference between 90 and 270 days (Fig. 8). Because the bone/titanium interface was studied on thick polished slides (and not tissue sections coming from a microtome, it was not possible to quantify the amount of osteoid tissue [10]. The bone marrow present inside the cylinders was only represented by adipocytes and inflammatory clusters of cells were never identified.

The mineralization rate was high in both groups, but no significant difference was observed when measured in the

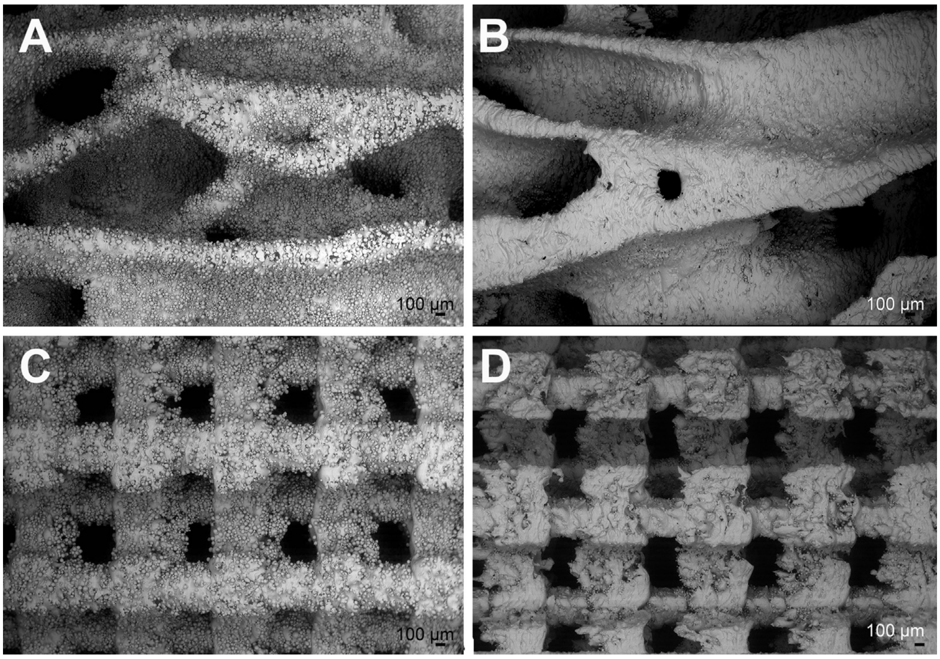

Figure 4 SEM analysis of the Ti cylinders obtained by additive manufacturing. A) Trabecular cylinder with numerous Ti beads, attached to the surface but probably not firmly. B) Appearance after HF/HNO_3 treatment. C) Geometric cylinder with many beads tangentially glued to the surface. D) Appearance of these cylinders after HF/HNO_3 treatment.

bone affixed to the titanium or at distance at 90 and 270 days. Over time, the mineralization rate was significantly reduced, either in contact or at distance from the titanium cylinders; here again, no difference was noted between the two types of microarchitecture.

On histological sections, residual beads were present in the very center of the porous cavities in both types of cylinders. The beads are detached from the rest of the metal and some free microbeads are osseointegrated and covered with bone (Fig. 7G—H).

Discussion

Only the use of large animals such as goats or sheep allows precise studies to be carried out on biomaterials that can be used in orthopedics, in particular for prostheses or biomaterials for filling bone cavities in load-bearing areas. It is therefore possible to use large specimens of biomaterials in bone defects of critical size, close to the lesions observed in humans [15,16]. The sheep presents a trabecular microarchitecture close to that of humans, which permits histomorphometric and histodynamic analyses to evaluate the osseointegration of biomaterials at the tissue level [17,18].

In this study, we evaluated the capacity of titanium cylinders with two microarchitectures to be used as scaffolds for bone reconstruction in a load-bearing site in the ewes. Titanium has been widely used for many years in dental as well as in orthopedic surgery. This metal has an excellent tolerance in the body and promotes osseointegration [19—21]. The biocompatibility of titanium has been recognized since the 1960s and its biomechanical properties are more favorable than those of stainless steel (see reviews in [22,23]). In addition, the use of porous titanium devices has been shown to favor osseointegration [24,25].

Additive manufacturing, also known as 3D printing, is a way of industrial production that enables the creation of lighter and stronger systems. The method uses a data computer-assisted-design (CAD) software handling .stl files that ''slice'' the object into ultra-thin layers. This directs the printer to deposit material, layer upon layer, in precise and complex geometric shapes. By contrast to traditional industrial methods where material is removed through milling, machining, carving or shaping additive manufacturing adds material to create a 3D object [26]. Here, the ''ink'' that was used for printing the two types of cylinders was a powder of titanium microbeads. These were fused layer by layer by a laser. Each successive layer was melted to the preceding layer of material. As metal is cured, the layers fuse together to form a three-dimensional object. The unmelted beads have to be eliminated by the use of a vibrating table. However, in this study, although the cylinders with a geometrical microarchitecture were correctly cleaned, it was not the same with cylinders with a trabecular microarchitecture. Indeed, microarchitecture of cancellous bone is made of trabeculae (plates and pillars) which are richly anastomosed to ensure the mechanical strength of bone [27]. Trabeculae create cavities in which the hematopoietic marrow is located. While trabecular microarchitecture appears extremely resistant, fluid accessibility to certain areas can be difficult due to the tortuosity of the flows within these complex networks. MicroCT has shown that some internal cavities remain completely filled by trapped and unmelted titanium microbeads and this method is becoming indispensable in the technological and industrial evaluation of

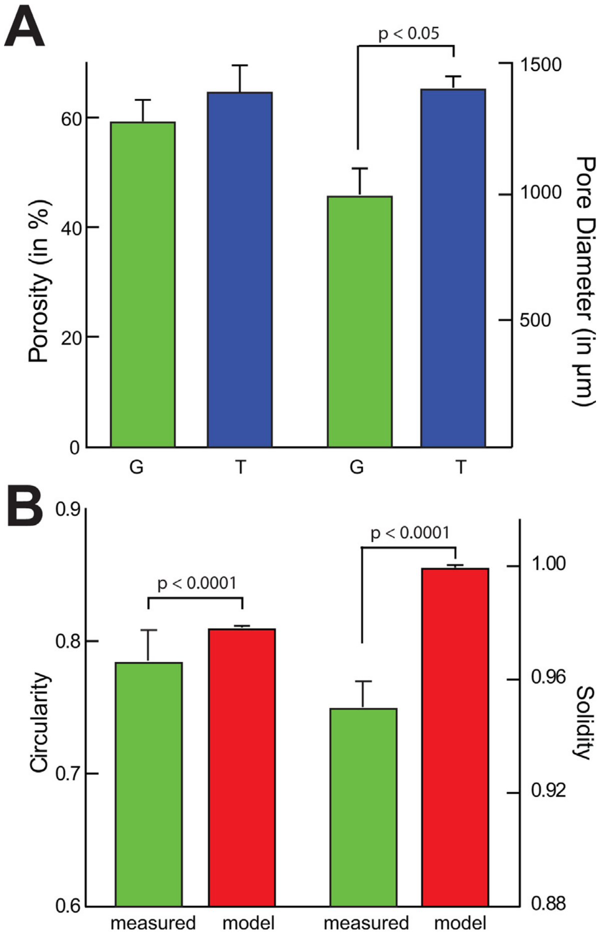

Figure 5 Morphometric analysis of titanium cylinders. A) Porosity and pore diameter in cylinders with geometrical (green) or trabecular (blue) microarchitecture. B) Measurement of form factors (circularity and solidity) of the square cavities of geometric cylinders. In green, measurement made on 2D images of microCT (measured values), in red measurement made on mathematical models (model values).

such materials prepared by additive manufacturing [28]. For this reason, additional treatments were necessary such as ultrasonic baths in isopropanol to remove these deposits of unmelted beads.

Scanning electron microscopy analysis of the cavities and surfaces of the cylinders showed that many beads remained tangentially attached to the deep plane that allowed them to stick on the material without fusing. It has been shown that additional treatments must be conducted in these cases to remove these beads that remain unsteadily attached to the surface. Scanning electron microscopy has therefore shown that the use of a HF/HNO_3 treatment allows the removal of these unstable beads and attacks the titanium surface like that observed on dental implants to promote the osteoblasts anchorage [8,22,29].

Osseointegration of the cylinders was analyzed by nanoCT and histology. However, the nanoCT of large blocks like here (5 × 7 cm) is facing problems of image reconstruction even with a device using polychromatic X-rays. Apposition of bone trabeculae on the external surface of the material was well demonstrated (especially on cross sections) by nanoCT, but it was impossible to identify bone extending in depth into the material between the meshes of the 2 types of cylinders. For this reason, histology without decalcification, after inclusion in pMMA and cutting on a diamond saw, remains the method of choice for observation. It allows the morphological analysis of the tissue and cells as well as the histodynamic analysis of the double labelling. Here, we have shown that the amount of bone tissue remained small inside the cylinders while it was more important on the surface. This can be explained by the absence of mechanical stress transmitted within the implants whose pores create a protected volume disconnected from the strains exerted on the graft. The absence of stress is known to be deleterious for bone remodeling [30]. The phenomenon has been well described in orthopedic surgery and is known for hip arthroplasty as ''stress-shielding'' [23,31]. In cylinders grafted in the ewes, it can be assumed that integration occurs at the periphery where there is sufficient mechanical stress to promote remodeling whereas at the core of the cylinders, the stresses are too low, and the bone cells do not perceive the signal. So, the absence of stress prevents modeling and remodeling. A tantalum metallic foam (Trabecular metal® - Zimmer US) is currently available on the market

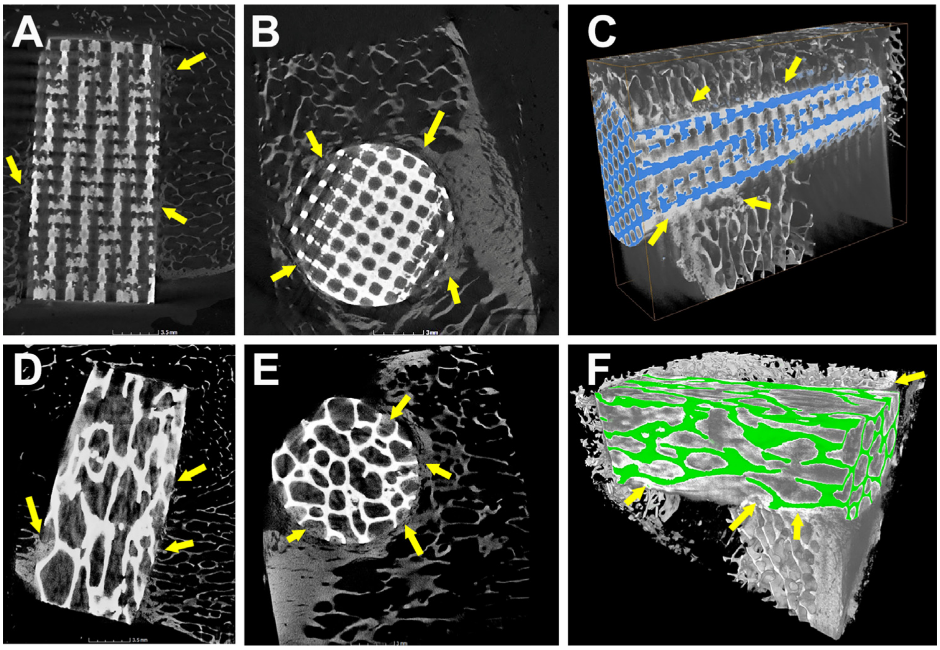

Figure 6 NanoCT aspects of cylinders implanted in the ewes. A-C) cylinder with a geometric microarchitecture. A) 2D section parallel to the major axis of the cylinder showing the presence of peripheral foci of bone apposition (yellow arrows). B) 2D section perpendicular to the major axis of the cylinder, bone appositions are better defined and some areas of bony invasion to the interior of the cylinder can be avocated. C) 3D model, titanium has been pseudo-colored in blue; the bone anchorage areas are highlighted. D-F) Cylinder with a trabecular microarchitecture. D) 2D section parallel to the major axis of the cylinder; some bone apposition foci are highlighted but the reconstruction artefacts are numerous as shown by the presence of grayish streaks in the center of the cylinder. E) 2D section perpendicular to the major axis of the cylinder, bone appositions are much better defined. F) 3D model, titanium has been pseudo-colored green.

for orthopedic surgery to replace large bone defects as this metal is also known to be biocompatible. This foam has an interconnected porosity, and the microporous microarchitecture of the biomaterial (tetrakaidecahedron) is reported to favor osseointegration. Our histological results appear to be very similar to those obtained with Trabecular metal® tantalum in which osseointegration is limited to the most superficial areas of the implanted blocks [32—34]. In addition, it has been reported, in a series of 11 patients with these porous tantalum implants placed in the ankle that poor integration of the biomaterial results with non-union with bone [35]. One of explanation could be the difference in Young's modulus. Young's modulus of tantalum is 186 GPa whereas Young's modulus of Titanium is 110 GPa, which is two less than that of steel and therefore closer to that of bone (20 GPa). The biomechanical resistance of our cylinders could not be evaluated with our Instron 5942 machine limited to 50 kN. However, the cylinders appeared to have a considerable compressive strength, well above 20 kN like all porous spinal fusion cages produced in the same way by industry (the maximum mechanical load of bone is 15 kN). In a recent paper, cylinders of porous titanium (6 mm in diameter) were also prepared by 3D printing with a mathematical model based on Voronoi 3D partition method [36]. In their study, the metal trabeculae were estimated to be 200 μm in thickness with a porosity of 0.75 to 0.90% (sic) without mentioning the pore size. The mechanical resistance of the cylinders was 4KN. Histological analysis revealed that bone from these young sheeps (2 y.o.) had partially colonized the network by osteoconduction, but no tetracycline labeling was done. In the present series, a larger defect was created with the use of larger titanium cylinders.

Moreover, only histological methods allowed to notice that residual beads were present in the very center of the porous cavities, whatever the type of cylinder analyzed. These unstable beads may detach under the effect of fluid movements and remain free in the cavities. As titanium is biocompatible, these free microbeads can be osseointegrated and covered with bone. The accessibility of the HF/HNO_3 etching fluids (whose action is well evidenced on the surface by SEM) may not be similar in the central parts of the specimens. Unfortunately, we were not able to section cylinders to analyze this characteristic.

One of our working hypotheses was that the geometrical shape of the cavities represented a lower factor of osseointegration compared to a ''natural'' structure mimicking that of bone [37—39]. However, we did not observe any histomorphometric or histodynamic differences. This may be because there are discrepancies between the mathematical model and the 3D printed object as shown by the variations in shape factors (solidity and circularity), which indicate that the cavities obtained by printing are not perfectly geometric but have irregularities conducive to osteoblastic anchorage. Implants with a similar geometric microarchitecture serve as fusion cages in neurosurgery with satisfactory results for spinal fusion [40,41]. The only significant morphometric

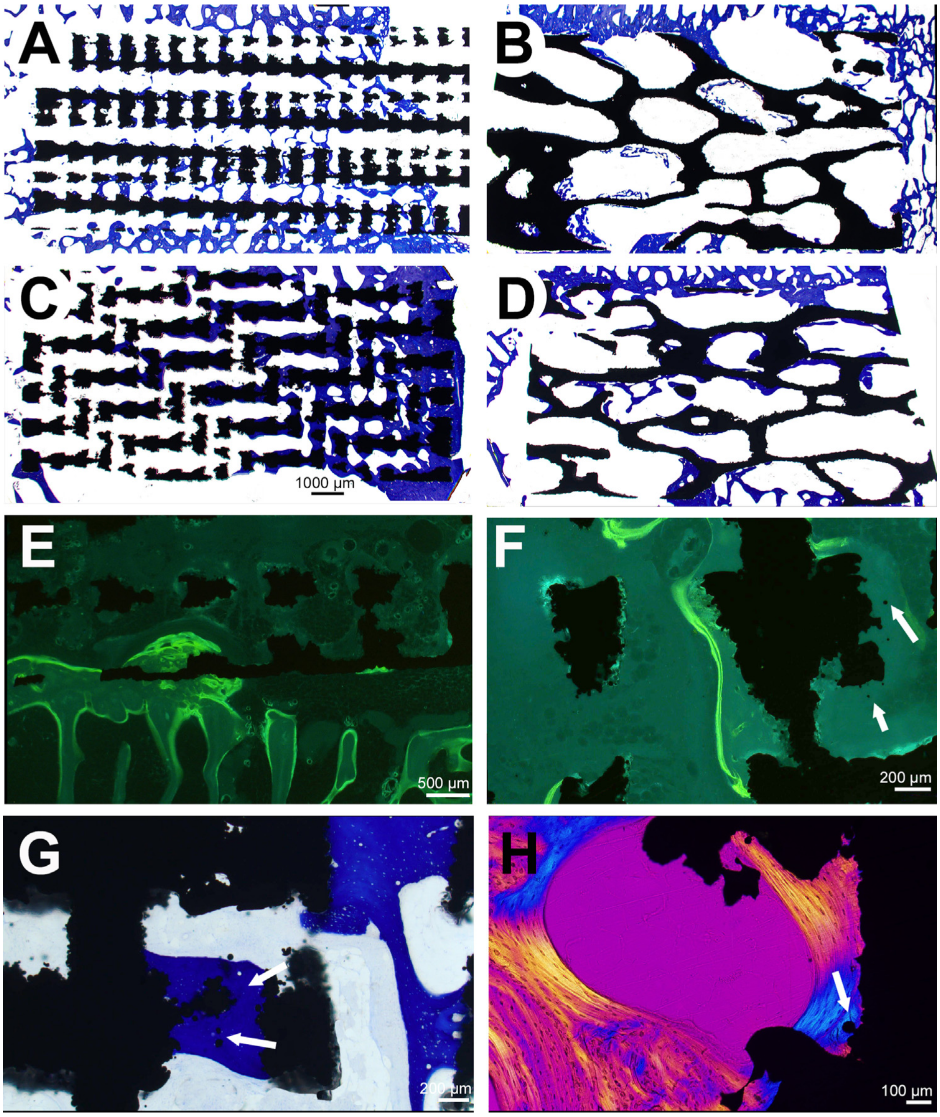

Figure 7 A - D) Histological aspects of the cylinders with geometrical (A-C) and trabecular (B-C) microarchitecture; A and B were taken from animals sacrificed after 90 days, C and D after 270 days. Photomontages of several microscopic images per view showing the whole of the implanted cylinders. Toluidine blue surface-staining. All images are taken at the same magnification: the bar represents 1000 microns. Note the presence (in B) of a significant amount of bone tissue in the area close to the cortical drill hole. (E) Double labeling at 90 days in a geometric microarchitecture cylinder. Note the abundance of labels in the trabeculae anchored at the cylinder periphery and the presence of a blurred labeling in an area of rapidly growing bone (woven bone) in the center of the cylinder. F) Double labels in a geometric microarchitecture cylinder, at 270 days. Note the presence of clearly defined double labels on the trabeculae anchored to the surface of the titanium. G) High magnification showing osseointegration of a titanium cylinder with geometric microarchitecture. Note the presence of free titanium beads that have separated from the rest of the metal (white arrows) and covered by bone, this area was analyzed in the center of a cylinder at 270 days. H) Polarization microscopy on a titanium cylinder with trabecular microarchitecture. Note the presence of lamellar bone at 270 days and unfused beads covered by bone tissue (white arrows).

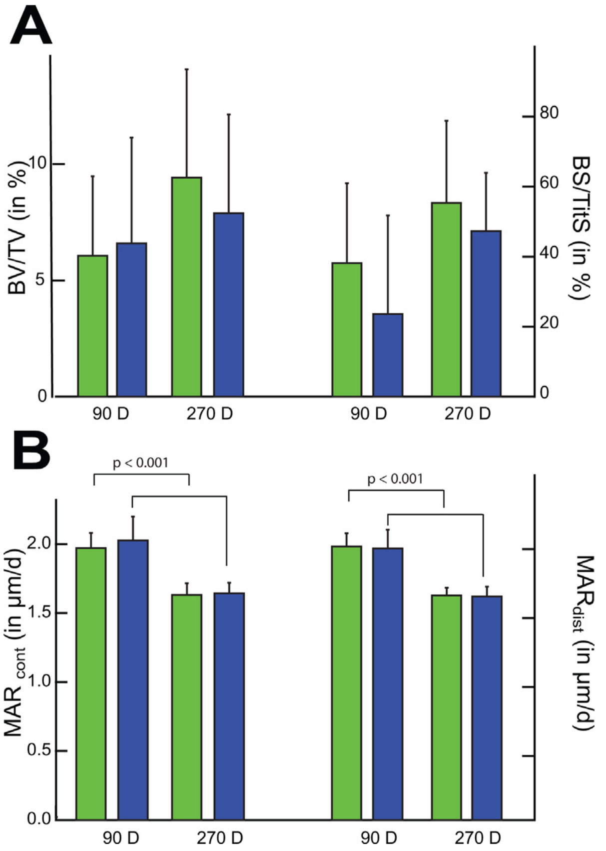

Figure 8 Histomorphometric analysis result showing osseointegration of the cylinders. A) Amount of bone (BV/TV) affixed inside the cylinders with microarchitecture geometric (in green) or trabecular (in blue). There is no significant difference between the different groups. The measurement of the titanium/bone contact interface (BS/TiS) shows no significant difference. B) Measurement of the MARs in contact with or at a distance from the cylinders. There is no significant difference in the values measured at each time in these two locations. There is a significant reduction in the mineralization rate in the two zones between 90 and 270 days.

parameters showing an evolution over time correspond to a reduction in the mineralization rate but this effect seems to be linked to the aging of the animals.

Conclusion

Titanium implants provide long-term osseointegration over time. Although the microarchitecture of implant used does not seem to influence the quality of osseointegration, it may not be necessary to reproduce a microarchitecture close to natural bone whereas a geometrical architecture is easier to design and produce industrially.

Disclosure of interest

The authors declare that they have no competing interest.

Funding

This work was partially supported by the Walloon Region (CWALity project NEXTBONE: Convention n_1610093). This work was made possible by grants from Angers CHU (University hospital) project MOCONA and the French Ministry of Research.

Acknowledgments

Mrs. N. Gaborit, S. Lemière and F. Pascaretti are thanked for their histotechnical help and microCT analysis and Mrs I. Pavageau and I. Leborgne for their surgical help. SEM and EDS analysis were performed at Service Commun d'Imagerie et d'Analyses Microscopiques (SCIAM), Université d'Angers, thanks to R. Mallet. The 2021 cover image of Morphologie is derived from this study.

Références

[1] Sporer SM, Paprosky WG, O'Rourke M. Managing bone loss in acetabular revision. J Bone Joint Surg 2005;87:1620—30.
[2] Arrington ED, Smith WJ, Chambers HG, Bucknell AL, Davino NA. Complications of iliac crest bone graft harvesting. Clin Orthop Rel Res 1996;329:300—9.
[3] Younger EM, Chapman MW. Morbidity at bone graft donor sites. J Orthop Trauma 1989;3:192—5.
[4] Dumas A, Gaudin-Audrain C, Mabilleau G, Massin P, Hubert L, Baslé MF, et al. The influence of processes for the purification of human bone allografts on the matrix surface and cytocompatibility. Biomaterials 2006;27:4204—11.
[5] Hunter DJ, Spector TD. The role of bone metabolism in osteoarthritis. Current Rheumatol Rep 2003;5:15—9.
[6] Li B, Aspden RM. Composition and mechanical properties of cancellous bone from the femoral head of patients with osteoporosis or osteoarthritis. J Bone Miner Res 1997;12:641—51.
[7] Li S, de Wijn JR, Li J, Layrolle P, de Groot K. Macroporous biphasic calcium phosphate scaffold with high permeability/porosity ratio. Tissue Eng 2003;9:535—48.
[8] Geurs NC, Jeffcoat RL, McGlumphy EA, Reddy MS, Jeffcoat MK. Influence of implant geometry and surface characteristics on progressive osseointegration. Int J Oral Maxillofac Impl 2002;17.
[9] Chappard D. Technical aspects: how do we best prepare bone samples for proper histological analysis? Bone Cancer. 2nd Edition Elsevier; 2015. p. 111—20.
[10] Schenk RK, Olah AJ, Herrmann W. Preparation of calcified tissues for light microscopy. In: Dickson GR, editor. Methods of Calcified Tissue Preparation. Amsterdam: Elsevier; 1984. p. 1—56.
[11] Dempster DW, Compston JE, Drezner MK, Glorieux FH, Kanis JA, Malluche H, et al. Standardized nomenclature, symbols, and units for bone histomorphometry: a 2012 update of the report of the ASBMR Histomorphometry Nomenclature Committee. J Bone Mineral Res 2013;28:2—17.
[12] Richmond J. Refinement, reduction, and replacement of animal use for regulatory testing: future improvements and implementation within the regulatory framework. ILAR J 2002;43:S63—8.
[13] Ott SM. Histomorphometric measurements of bone turnover, mineralization, and volume. Clin J Am Soc Nephrol 2008;3. S151-S56.
[14] Ott SM. Bone histomorphometry in renal osteodystrophy. Semin Nephrol 2009;29:122—32.

[15] Harris JS, Bemenderfer TB, Wessel AR, Kacena MA. A review of mouse critical size defect models in weight bearing bones. Bone 2013;55:241—7.

[16] Aguado E, Goyenvalle E. Modèles animaux et biomatériaux. In: Guillaume B, Audran M, Chappard D, editors. Tissu osseux et biomatériaux en chirurgie dentaire. Paris: Quintessence Int; 2014. p. 307—22.

[17] Turner A. The sheep as a model for osteoporosis in humans. Veterinary J 2002;163:232—9.

[18] Rony L, Aguado E, Pascaretti-Grizon F, Hubert L, Chappard D. Hyaluronic acid stimulates osseointegration of b-TCP in Young and Old Ewes. Calcif Tissue Int 2019;105:487—96.

[19] Stiehler M, Lind M, Mygind T, Baatrup A, Dolatshahi-Pirouz A, Li H, et al. Morphology, proliferation, and osteogenic differentiation of mesenchymal stem cells cultured on titanium, tantalum, and chromium surfaces. J Biomed Mater Res - Part A 2008;86:448—58.

[20] Hirota M, Hayakawa T, Shima T, Ametani A, Tohnai I. High porous titanium scaffolds showed higher compatibility than lower porous beta-tricalcium phosphate scaffolds for regulating human osteoblast and osteoclast differentiation. Mater Sci Engin C 2015;49:623—31.

[21] Albrektsson T, Brånemark P-I, Hansson H-A, Lindström J. Osseointegrated titanium implants: requirements for ensuring a long-lasting, direct bone-to-implant anchorage in man. Act Orthopaed Scandinav 1981;52:155—70.

[22] Guillaume B. Dental implants: a review. Morphologie 2016;100:189—98.

[23] Rony L, Lancigu R, Hubert L. Intraosseous metal implants in orthopedics: a review. Morphologie 2018;102:231—42.

[24] Sirak SV, Giesenhagen B, Kozhel IV, Schau I, Shchetinin EV, Sletov AA, et al. Osteogenic potential of porous titanium. An experimental study in sheep. J Natl Med Assoc 2019;111:310—9.

[25] Chen Z, Yan X, Yin S, Liu L, Liu X, Zhao G, et al. Influence of the pore size and porosity of selective laser melted Ti6Al4V ELI porous scaffold on cell proliferation, osteogenesis and bone ingrowth. Mater Sci Eng C 2020;106:110289.

[26] Horn TJ, Harrysson OL. Overview of current additive manufacturing technologies and selected applications. Sci Prog 2012;95:255—82.

[27] Chappard D, Baslé MF, Legrand E, Audran M. Trabecular bone microarchitecture: a review. Morphologie 2008;92:162—70.

[28] Du Plessis A. X-ray tomography for the advancement of laser powder bed fusion additive manufacturing. J Microsc 2020, http://dx.doi.org/10.1111/jmi.12930.

[29] Grizon F, Aguado E, Huré G, Baslé MF, Chappard D. Enhanced bone integration of implants with increased surface roughness: a long term study in the sheep. J Dent 2002;30:195—203.

[30] Simon U, Augat P, Ignatius A, Claes L. Influence of the stiffness of bone defect implants on the mechanical conditions at the interface—a finite element analysis with contact. J Biomech 2003;36:1079—86.

[31] Bugbee WD, Culpepper WJ, Engh CA. Long-term clinical consequences of stress-shielding after total hip arthroplasty without cement. J Bone Joint Surg 1997;79:1007—12.

[32] Breer S, Hahn M, Kendoff D, Krause M, Koehne T, Haasper C, et al. Histological ex vivo analysis of retrieved human tantalum augmentations. Int Orthop 2012;36:2269—74.

[33] Cohen R. A porous tantalum trabecular metal: basic science. Am J Orthop 2002;31:216.

[34] Christie MJ. Clinical applications of trabecular metal. Am J Orthop 2002;31:219—20.

[35] Aubret S, Merlini L, Fessy M, Besse J-L. Poor outcomes of fusion with trabecular metal implants after failed total ankle replacement: early results in 11 patients. Orthop Traumatol Surg Res 2018;104:231—7.

[36] Ragone V, Canciani E, Arosio M, Olimpo M, Piras LA, von Degerfeld MM, et al. In vivo osseointegration of a randomized trabecular titanium structure obtained by an additive manufacturing technique. J Mat Sci Med 2020;31:1—11.

[37] Barba A, Diez-Escudero A, Maazouz Y, Rappe K, Espanol M, Montufar EB, et al. Osteoinduction by foamed and 3D-printed calcium phosphate scaffolds: effect of nanostructure and pore architecture. ACS Appl Mater Interf 2017;9:41722—36.

[38] Graziano A, d'Aquino R, Angelis MGCD, De Francesco F, Giordano A, Laino G, et al. Scaffold's surface geometry significantly affects human stem cell bone tissue engineering. J Cell Physiol 2008;214:166—72.

[39] Marques A, Miranda G, Silva F, Pinto P, Carvalho Ó. Review on current limits and potentialities of technologies for biomedical ceramic scaffolds production. J Biomed Mater Res - Part B 2020;109:377—93.

[40] Gittens RA, Olivares-Navarrete R, Schwartz Z, Boyan BD. Implant osseointegration and the role of microroughness and nanostructures: lessons for spine implants. Acta Biomater 2014;10:3363—71.

[41] Seaman S, Kerezoudis P, Bydon M, Torner JC, Hitchon PW. Titanium vs. polyetheretherketone (PEEK) interbody fusion: meta-analysis and review of the literature. J Clin Neurosci 2017;44:23—9.

ARTICLE 6

Microarchitecture of titanium cylinders obtained by additive manufacturing does not influence osseointegration in the sheep

Louis RONY, Eric AGUADO, Bruno VERLEE, Florence PASCARETTI-GRIZON, Daniel CHAPPARD

Regenerative Biomaterials 8(4): 1-10 (2021)

Impact Factor : 6,353 – SIGAPS : B

Regenerative Biomaterials, 2021, 1–10
doi: 10.1093/rb/rbab021
Research Article

Microarchitecture of titanium cylinders obtained by additive manufacturing does not influence osseointegration in the sheep

Louis Rony[1], Eric Aguado[1,2], Bruno Verlee[3], Florence Pascaretti-Grizon[1] and Daniel Chappard [1,4,*]

[1]GEROM—Groupe Etudes Remodelage Osseux et bioMatériaux, LabCom NextBone, Univ-Angers, IRIS-IBS Institut de Biologie en Santé, 49933 Angers, France [2]ONIRIS, Ecole Vétérinaire de Nantes, 44307, Nantes Cedex 3, France [3]SIRRIS Liège Science Park, Rue du bois St Jean 12, Seraing 4102, Belgium [4]SCIAM, Service Commun d'Imagerie et Analyses Microscopiques, IRIS-IBS Institut de Biologie en Santé, Univ-Angers, Angers Cedex 49933, France

*Correspondence address. Daniel Chappard, GEROM—LHEA, IRIS-IBS Institut de Biologie en Santé, Université d'Angers, CHU d'Angers, 49933 Angers Cedex, France. Tel: +33-2-44-68-83-43; E-mail: daniel.chappard@univ-angers.fr

Received 14 December 2020; revised 19 March 2021; accepted on 25 April 2021

Abstract

Large bone defects are a challenge for orthopedic surgery. Natural (bone grafts) and synthetic biomaterials have been proposed but several problems arise such as biomechanical resistance or viral/bacterial safety. The use of metallic foams could be a solution to improve mechanical resistance and promote osseointegration of large porous metal devices. Titanium cylinders have been prepared by additive manufacturing (3D printing/rapid prototyping) with a geometric or trabecular microarchitecture. They were implanted in the femoral condyles of aged ewes; the animals were left in stabling for 90 and 270 days. A double calcein labeling was done before sacrifice; bones were analyzed by histomorphometry. Neither bone volume, bone/titanium interface nor mineralization rate were influenced by the cylinder's microarchitecture; the morphometric parameters did not significantly increase over time. Bone anchoring occurred on the margins of the cylinders and some trabeculae extended in the core of the cylinders but the amount of bone inside the cylinders remained low. The rigid titanium cylinders preserved bone cells from strains in the core of the cylinders. Additive manufacturing is an interesting tool to prepare 3D metallic scaffolds, but microarchitecture does not seem as crucial as expected and anchoring seems limited to the first millimeters of the graft.

Keywords: titanium; trabecular scaffold; osseointegration; geometric architecture; histomorphometry

Introduction

Cavitary bone loss is common in orthopedic and traumatology surgery: osteolysis due to wear of polyethylene particles of a total hip prosthesis, comminuted metaphyseal fracture, revision prosthesis with intraoperative fracture. The subsequent bone reconstruction becomes a challenge [1]. For reconstruction of trabecular bone loss, it is necessary to fill the areas with osteoconductive biomaterials to prevent the development of fibrosis and loss of bone tissue function [2, 3].

The biomaterials that can be used are mainly calcium orthophosphate ceramics that do not have stress resistant properties and only allow osteoconduction from the surrounding bone. Phosphocalcic ceramics allow bone regeneration in the injured area as shown in a large number of publications [4–6]. This is possible in maxillofacial surgery but cannot be achieved in orthopedic surgery [7]. Indeed, their lack of mechanical resistance to crushing would require immediate post-operative unloading of the operated area. Moreover, the lack of mechanical stress is also detrimental to the regeneration of the bone tissue [8, 9].

To overcome these disadvantages, certain materials have been developed to counteract the problem of mechanical strength and allow the area of bone loss to be filled while providing mechanical resistance [1, 10–12]. Titanium alloys are commonly used in orthopedic surgery and bone adapts particularly well to titanium, so much so that the word ‘osseointegration’ has been widely used in dental implantology [8, 13]. Furthermore, osteoblasts have a natural affinity for titanium and for concave-convex surfaces, and bone regeneration is favored on non-geometric surfaces [14, 15]. Therefore, it can be hypothesized that titanium implants that mimic a natural bone architecture would allow for better osseointegration than if a geometric architecture was designed as conventionally [16, 17].

The objective of this work was to determine whether the architecture of the component influences its osseointegration. The implantation time was also studied to determine if it had a significant influence. We therefore prepared two types of titanium cylinders by 3D printing (synonyms: 3D printing, rapid prototyping): one reproducing a geometrical architecture similar to the fusion cages used in spine surgery and the other one reproducing the microarchitecture of an ox bone. The results were compared using the same methodology at 3 and 9 months after an implantation in sheep.

Material and methods

Biomaterials

In additive manufacturing, printing with metal powders offers the possibility to produce objects of any shape in a single production step from a 3D model. The 3D model of the cylinders with a trabecular microarchitecture was obtained from the tibial plateau an old ox. This model was chosen after a considerable number of testing because it provided a largest amount of bone, with anisotropic and mature trabecular microarchitecture. In addition, bovine bone has the same microarchitecture [18–20] and biomechanical strength [21] as young humans (human cadavers from anatomy laboratory are most often osteoporotic). The dry sample was analyzed by X-ray microtomography and the images were sent to Sirris to be converted into STL files (Standard Triangle Language). The 3D model of the cylinder with a geometrical microarchitecture was imported into a specific software (e.g. Magics®, Materialise Leuven, Belgium) for processing and preparation of the STL file. A support for holding the cylinders was also added to separate them from the built plate of the 3D printer. The STL files combining the cylinders and their supports were then imported into the MTT Autofab Marcam® slicing software (Release 1.6, Renishaw Benelux, Brenda, The Netherlands) to virtually slice the parts into 30-µm thin layers. Contours were produced at 100 W and 500 mm/s, and the internal hatching at 190 W and 600 mm/s, with a hatch distance of 120 µm between passes. The sliced files were sent to the additive printer (SLM 250HL®, SLM Solutions, Lübeck, Germany). Printing took place in a closed chamber under protective atmosphere (argon), spreading successive layers of powder and melting them selectively to build up the parts layer by layer. The build plate was heated to 100°C to limit internal stress in the material. The powder material used was an argon atomized Ti6Al4V ELI titanium alloy powder from TLS Technik (Bitterfeld-Wolfen, Germany) with a spherical shape and a particle size dispersion of 20–63 µm. After fabrication, the cylinders were cut out of the tray using a band saw without lubricating liquid. A maximum of unmelted powder was manually removed from the cylinders in successive steps using a vacuum cleaner and a vibrating table. This cleaning step was completed by a passage in an ultrasonic bath under isopropanol. The cylinders were then placed in a drying oven and the supports were removed. The resulting cylinders were 1 cm in diameter and 2 cm in length (Fig. 1A).

Biomaterial cleaning

Cylinders obtained by additive manufacturing require post-processing to improve surface parameters such as roughness and to remove unmelted metallic powder particles. Removal of these unmelted particles as well as the etching of the surface was achieved by a chemical post-processing using a hydrofluoric/nitric acid (HF/HNO_3) solution. The method was adapted from those used to clean dental implants [22]. Briefly, the cylinders were treated by strong acids (HNO_3 65% (5 vol.) + HF 58% (1 vol.) and cleaning solutions (sodium perborate, tetracetylene diamine and tensio-active reagents). A thorough washing was performed in distilled water using ultrasonic waves during cleaning. The cylinders were dried and sterilized by gamma radiation.

Scanning electron microscopy

Surface morphology of the raw and cleaned cylinders was analyzed on an EVO LS10 (Carl Zeiss Ltd., Nanterre, France). Images were captured in the secondary electron mode with an acceleration tension of 20 kV.

Computational fluid dynamics through the cylinders

The cylinders were transferred to an X-ray computed nanotomograph (Nanotom, Phoenix, GE, USA) using polychromatic X-rays to limit artefacts due to titanium. NanoCT analysis was performed at 100 kV and 220 µA and with a copper filter. Five projection images were averaged every 500 ms and the rotation angle was 0.2° with a pixel size of 12.82 µm. Image reconstruction was done on the projection images with DATOS software (Phoenix, GE) and a stack of 2D sections was obtained for each specimen.

Morphometric analysis of the cylinders was performed with CTAn software (Bruker microtomography, Kontich, Belgium) and the following parameters were determined:

i. Porosity (expressed in %) represents the overall amount of the cylinder occupied by pores,
ii. Pore diameter (in µm),
iii. Thickness of the titanium trabeculae (in µm) and
iv. Density of titanium trabeculae (in/mm).

The 3D models were obtained with VG StudioMax 3.2 (Volume Graphics GmbH, Heidelberg, Germany). Once the 3D models were obtained, the ‘Transport Phenomena Simulation’ add-on module of VG Studiomax was used to compute computational fluid dynamic (CFD) simulations on the two types of cylinders [23]. The boundary conditions were defined as follows: first, the cylinder was cut to obtain a square-section parallelepiped, aligned with the major axis of the cylinder. A superior plan was defined; then, a opposite parallel plane (separated by 6700 µm) was selected. The following parameters were used for the simulation: an outlet pressure of 1 Pa; then, the wall boundaries were defined as sealed faces, the physical properties for the dynamic viscosity of the fluid was set at $\eta = 0.00155$ Pa.s (similar to that of extracellular fluids) [24]. The computation was performed with a simulation cell size of 3-voxel and 1000 iterations. The following parameters were obtained:

i. Absolute permeability (k): it is a measure of the capacity of a cylinder to let fluids pass. The unit of measurement is the milliDarcy [25, 26].
ii. Hydraulic tortuosity (T): it is a parameter describing the average elongation of fluid streamlines in a porous medium relative to a free flow (with a value = 1). Hydraulic tortuosity is a dimensionless quantity, but is always > 1 [27, 28].

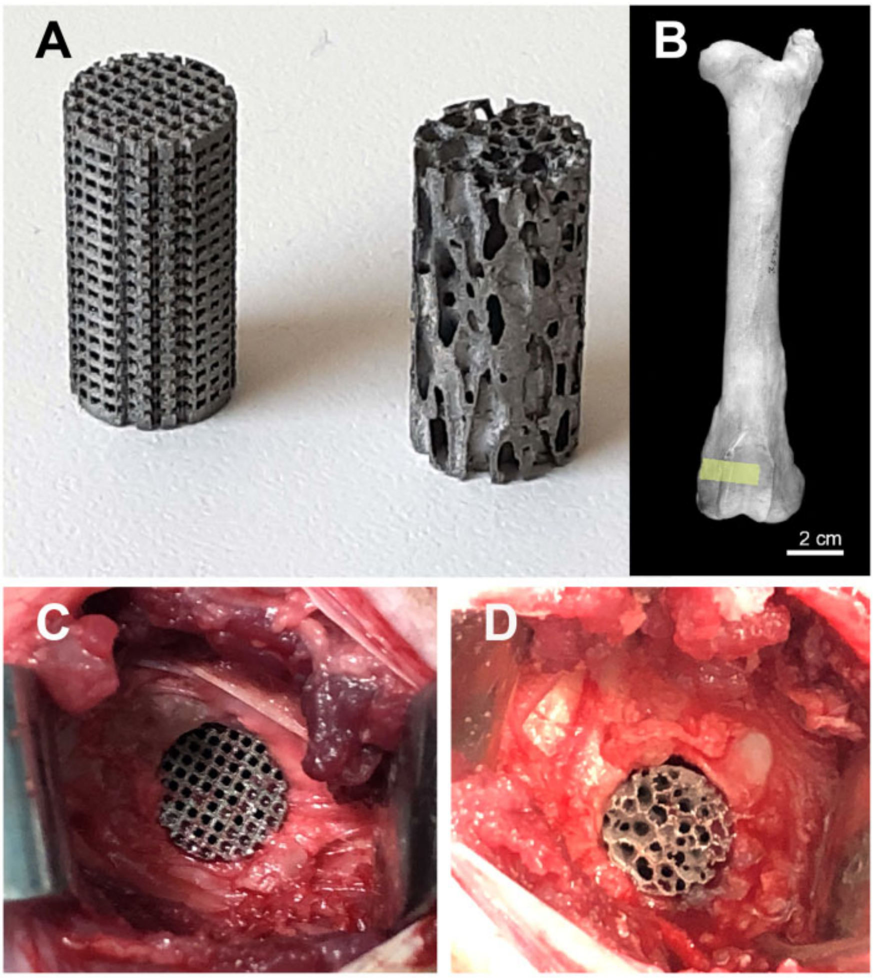

Figure 1. (**A**) Titanium cylinders prepared by additive manufacturing: left: geometric microarchitecture; right: trabecular microarchitecture. (**B**) The surgical site where the implants were placed in the femoral condyle appears in yellow. (**C**) Surgical placement of the two types of implants in the ewe. Right: geometric microarchitecture; left: trabecular microarchitecture

iii. Total flow rate: it indicates the total volume of fluid per second transported through the cylinder volume [29]. The unit of measurement is mm^3/s.

In addition, the graphical analysis illustrates the calculated velocity distribution in a color-coded manner according to a LUT (look up table). The streamlines, superimposed in white, illustrate the flow direction between the titanium cylinder meshes.

Morphometric and CFD analysis were done in triplicate for both cylinder types.

Animal and surgical procedure

The animal study was conducted from January 2019 to October 2019 with two parallel open arms for 270 days. Nine ewes sacrificed after 90 days constituted the first group (Group A) and nine ewes sacrificed after 270 days constituted the second group (Group B). The subjects of the study were cull Vendean ewes (non-GMOs (non-genetically modified organisms), ~6 years old) from local breeders. The ewes were acclimated at the Veterinary School of Nantes' sheepfold (ONIRIS, France) between 10 and 21 days before surgery. They were operated by a trained veterinarian surgeon in an operating room dedicated to animal experimentation at ONIRIS.

The ewes were operated under general anesthesia performed with a standardized protocol including two hypnotic drugs by intravenous infusion (Isoflurane and Ketamine) and a benzodiazepine (Diazepam). General anesthesia was maintained after endotracheal intubation with halothane supplied by an anesthetic machine. An injection of amoxicillin trihydrate (500 mg) was administered before the incision. The field allowed access to the posterior and the medial side of both knees. A skin incision was made longitudinally, parallel to the axis of the femur. The subcutaneous tissues were carefully coagulated to avoid postoperative hematoma. The medial side of medial femoral condyle was reached through the *sartorius* muscle. The periosteum was carefully dissected and a blind tunnel (1 cm in diameter, 2 cm in depth) was made using progressively sized drills with a low speed (400 rpm) electric rotary instrument under physiologic saline irrigation to remove bone debris (Fig. 1B). Titanium cylinder was impacted in these blind tunnels; left knees were filled with a geometric cylinder and right knees with a trabecular cylinder. Once the tunnel was filled, the periosteum was carefully closed to prevent the graft from spreading into the adjacent soft tissues. The muscle fascia was also sutured with absorbable thread as was the subcutaneous tissue and skin. The dressing was made sterile and stapled before avoiding any contamination in sheepfold.

In Groups A and B, two subgroups were obtained: filling with a geometric titanium cylinder (Subgroup g) or filling with a trabecular titanium cylinder (Subgroup t; Fig. 1C and D). Thus, four subgroups were considered: A-g and A-t subgroups sacrificed at 90 days and Subgroups B-g and B-t sacrificed at 270 days.

Towards the end of each of the two study periods, a double calcein labeling was performed to determine the mineral apposition rate (MAR) and a ‘2 days on, 10 days off and 2 days on’ regimen was used (calcein dose: 30 mg/kg; IM route). Animals were sacrificed by lethal injection of phenobarbital. Both knees were removed for analysis and fixed in 10% formalin. In all groups, an additional bone sample from the tibial metaphysis was harvested for measurement of MAR at distance from the surgical site.

Histological and histomorphometric analysis

The samples were embedded in poly(methylmethacrylate) for histological analysis as previously described [30]. The blocks were then sectioned with a diamond saw (Accutom, Struers, France) into 500-µm thick slices. The slices passing through the central position of the cylinders were selected. The slices were polished on an automatic polishing machine (Struers) to a 1 µm finish with diamond particles. Then, the slices received one of the following treatments. (i) Slices for fluorescence microscopy were left unstained and analyzed on an Olympus BX 51 microscope (Olympus, France) with a U-MWIB3 cube (excitation filter 460–495 nm, emission filter 510 nm, dichromatic mirror 505 nm). (ii) Surface staining was performed after acid etching of the surface with 0.1% formic acid in distilled water for 4 min followed by staining with borax-toluidine blue during 45 min.

Morphometric analysis was done on a semi-automatic image analyzer. The standardized nomenclature for bone histomorphometry of the ASBMR (American Society for Bone and Mineral Research) was used [31]. The following parameters were determined:

i. Volume of titanium in the cylinder volume (TitV/TV, in %),
ii. Volume of trabecular bone grown inside the cylinder (BV/TV, in %),
iii. Percent of titanium surface covered by bone (BS/TitS, in %),
iv. Mineralization rate in bone in direct contact with titanium (MAR_{cont}, in µm/D) and
v. Mineralization rate in bone at distance (>2000µm) from the cylinder (MAR_{dist}, in µm/D).

Ethical consideration

This project was approved by the National Ethics Committee for Animal Experimentation (CEEA) under the reference number: CEEA.2012.257. This study took into account the 3Rs rule (Replace, Reduce, Refine) aimed at limiting the number of subjects needed for the experimentation [32].

Statistical analysis

The SYSTAT software (Systat, San José, CA, release no. 13.00.05) was used to perform statistical analysis. All results were expressed as mean ± SD. Due to the small number of bone samples used in this study, a Kruskall–Wallis non-parametric analysis of variance was used to compare differences among groups. The comparison between groups was obtained by *post hoc* tests. Differences were considered significant for $P < 0.05$.

Results

Biomaterial scanning electron microscopy

All cylinders were prepared in the same way; 3D printing provided raw cylinders with imperfections related to the printing technique. In order to avoid the elementary microbeads which that were not fused by the laser used during the 3D printing, from coming off the final component, a HF acid treatment was performed. This treatment resulted in wavy and concave surfaces (Fig. 2).

Morphometric analysis and CFD through the cylinders

The morphometric characteristics of the two types of cylinders are shown on Table 1 with the CFD parameters. The porosity did not differ between the two types of cylinders; but the parameters describing their microarchitecture were significantly different. Figure 3 illustrates the principle and results of the CFD simulation applied to two types of cylinders. Figure 2A and B illustrate the conditions of the simulation applied to the parallelepiped volumes cut into the cylinders: the sidewalls of the volume of interest were cut with a clipping box and defined as no-slip faces. The axis-flow was in the vertical direction starting from the pink inlet plane to the opposite plane in yellow that constituted the outlet face. The calculated fluid velocity is color-coded according to the LUT that was the same for all analyses. The streamlines are also shown. The other pictures correspond to 2 D images of the two types of microarchitecture (geometric or trabecular). It is easy to see that the fluid permeation through the geometric cylinders is rather uniform. On the contrary, the fluid velocity inside the trabecular cylinders is very heterogeneous with areas associated with strong fluid movements and areas with very low flow. The geometric cylinders had significantly higher absolute permeability and flow rate than the corresponding trabecular cylinders. On the contrary, the tortuosity (measuring the length of the flow path) was significantly higher in the trabecular cylinders because the streamlines trajectories were more complex and elongated.

Histological analysis

At both 90 and 270 days, all cylinders were osseointegrated with bone anchored to the surface of the material. At 90 days, the presence of trabeculae made of lamellar bone was observed apposed to the titanium. Some trabeculae were also observed within the both types of metal scaffolds, and in polarized light, some areas were composed of woven bone at 90 days but all trabeculae were composed of lamellar bone at 270 days. Under fluorescence microscopy, double labeling was evident on trabeculae located on the outside of the cylinders and anchored to their surface while fuzzy labeling was noted in areas of woven bone. The microarchitecture of the cylinder did not appear to influence osseointegration at 90 days as at 270 days (Figs 4 and 5). Near the cortices, more bone was present extending from the edges of the hole.

Histomorphometry

Results of histomorphometric parameters are summarized on Table 2.

Cylinders with geometric architecture contained significantly more titanium than those with trabecular architecture. The TitV/TV of the cylinders was similar between the two time series of analysis.

BV/TV did not differ between the two types of cylinders microarchitecture at 90 and 270 days. There was a slight increase in bone volume between 90 and 270 days but it did not reach significance.

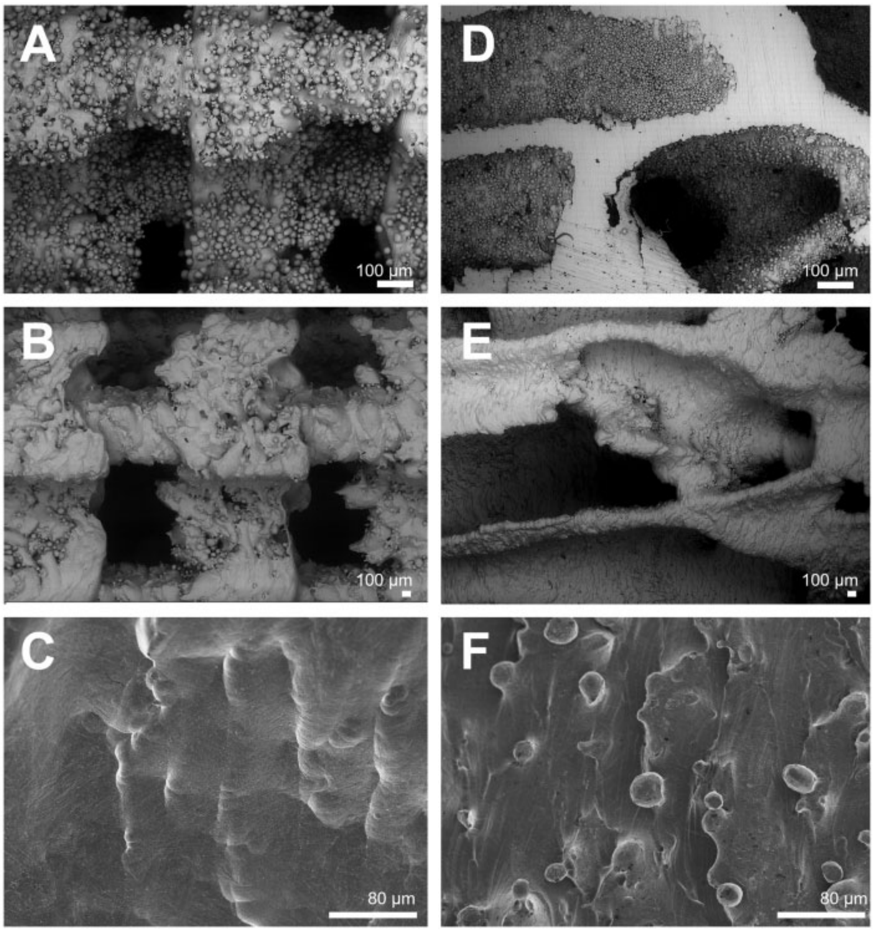

Figure 2. Scanning electron microscopy analysis of the two types of titanium cylinders with a geometric or trabecular microarchitecture. (**A**) Raw cylinder with geometric architecture showing the presence of numerous elementary microbeads. (**B**) Same sample after treatment with HF/HNO_3, note the disappearance of microbeads and many asperities on the titanium surfaces. (**C**) Same sample at higher magnification: note the smooth surface etched by the chemical treatment. (**D**) Raw cylinder with a trabecular bone architecture showing the presence of numerous elementary microbeads. (**E**) Same cylinder showing the effect of treatment with HF/HNO_3, microbeads have been removed and many asperities on titanium surfaces. (**F**) Same sample at higher magnification: note the smooth surface etched by the chemical treatment

Table 1. Morphometric parameters and CFDs through the two types of cylinders

	Unit	Geometric	Trabecular	*P*
Porosity	%	66.7 ± 1.9	68.0 ± 1.28	NS
Pore diameter	µm	981 ± 77	1399 ± 33	0.05
Trabecular thickness	µm	488 ± 10	656 ± 24	0.05
Trabecular density	/mm	0.68 ± 0.03	0.48 ± 0.003	0.05
Absolute permeability	mD ($\times 10^6$)	4.81 ± 0.8	1.05 ± 0.36	0.05
Tortuosity		1.15 ± 0.09	2.1 ± 0.17	0.05
Flow rate	mm^3/s	0.38 ± 0.02	0.09 ± 0.03	0.05

Similarly, the bone/titanium interface (BS/TitS) did not differ between the two types of cylinders microarchitecture and the increase was not significant between 90 and 270 days regardless of microarchitecture (Fig. 6).

The mineralization rate measured at the cylinder contact also did not differ between the two types of implants and was not altered at a 270 day after surgery. Similar results were observed for MAR_{dist} and surprisingly MAR_{cont} and MAR_{dist} did not differ at any time point.

Discussion

Most of the studies concerning the osseointegration of biomaterials have been conducted on small laboratory animals [33, 34]. They are difficult to extrapolate to humans because the critical size defects are different [35, 36]. Filling a cavitary bone defect—which is similar to a critical size defect—in human orthopedic surgery remains a major problem [2, 37]. Studies in large animals such as ewes (which have large bones and a trabecular microarchitecture very similar to humans), are needed to qualitatively and quantitatively evaluate the bone response and the osseointegration process at the tissue level [4, 38].

In orthopedic surgery, several biomaterials are currently used to fill bone defects. These include bone (allogenic or xenogeneic) but calcium-orthophosphate ceramics have the advantage of safer bacterial and viral security [39–42]. Calcium phosphate ceramics exist as granules of different sizes that lead to an interconnected porosity (essential for osteoconduction and thus osseointegration) when placed in the grafted area [43–46]. Solid blocks of porous orthophosphate-based ceramics have also been developed in the past but the osseointegration results were poor due to the lack of interconnected porosity [47]. Large ceramic scaffolds with an interconnected porosity

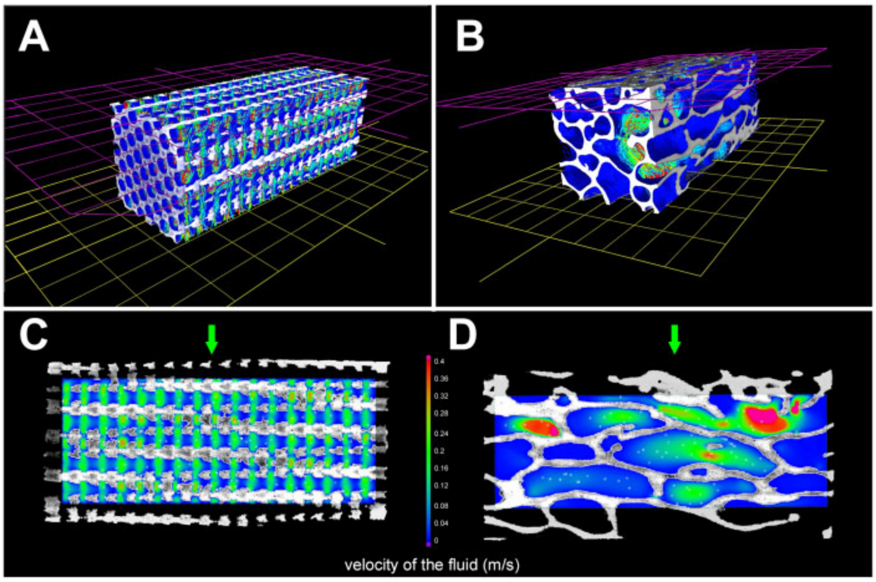

Figure 3. CFD between the two types of cylinders. (**A** and **D**) describe in 3D the principle of the simulated trajectory of a fluid from the pink to the yellow plane. The trajectories of the fluid are illustrated as colored lines. (**C** and **D**) are 2D sections from each type of cylinders showing the flow rate and the direction of the fluid. Velocity is color-coded according to the LUT from 0 to 0.4 m/s; streamlines appear in white. Trabecular cylinders are associated with a very heterogeneous distribution of the flow rate, but the mean flow rate was significantly lower than for geometric cylinders. The direction of the simulated fluid is indicated by a green arrow

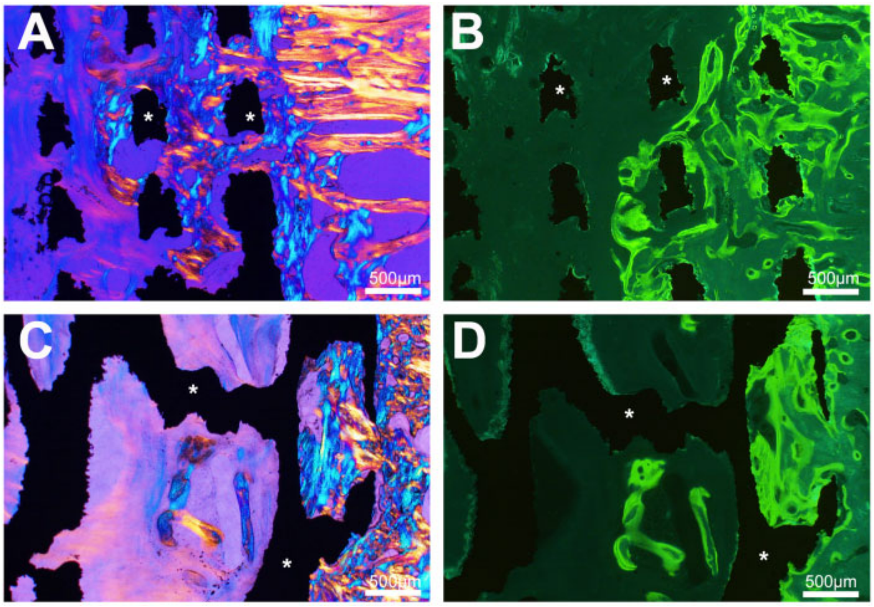

Figure 4. Histological analysis by light microscopy and fluorescence 90 days after cylinder implantation. Osseointegration is noted with both biomaterial whatever its geometry. (**A**) In cylinders with geometrical architecture, trabecular bone extends between the titanium septa (asterisks) from the peripheral zone of anchorage (polarized light). (**B**) fluorescence microscopy of the same cylinder, numerous double labels are evidenced between the biomaterial septa and in the surrounding bone. (**C**) Cylinders with a trabecular architecture, trabecular bone extends from the peripheral area into the cavities limited by the titanium trabeculae (asterisks). (**D**) Fluorescence microscopy of the same cylinder, numerous double labels within are observed in bone within the biomaterial cavities and the surrounding bone

have been developed by industry but they do not have a sufficient mechanical strength in load-bearing bone [7, 9, 48].

To overcome the mechanical strength issues, metal-based biomaterials with an interconnected porosity have been developed by the industry [11]. Tantalum is known to be a biocompatible metal [15, 17] and Trabecular metal® (Zimmer US), a tantalum-based metallic foam, is currently the only one available on the market for orthopedic surgery. It has an interconnected porosity and the microporous microarchitecture of the biomaterial (tetrakaidecahedron) would promote osseointegration.

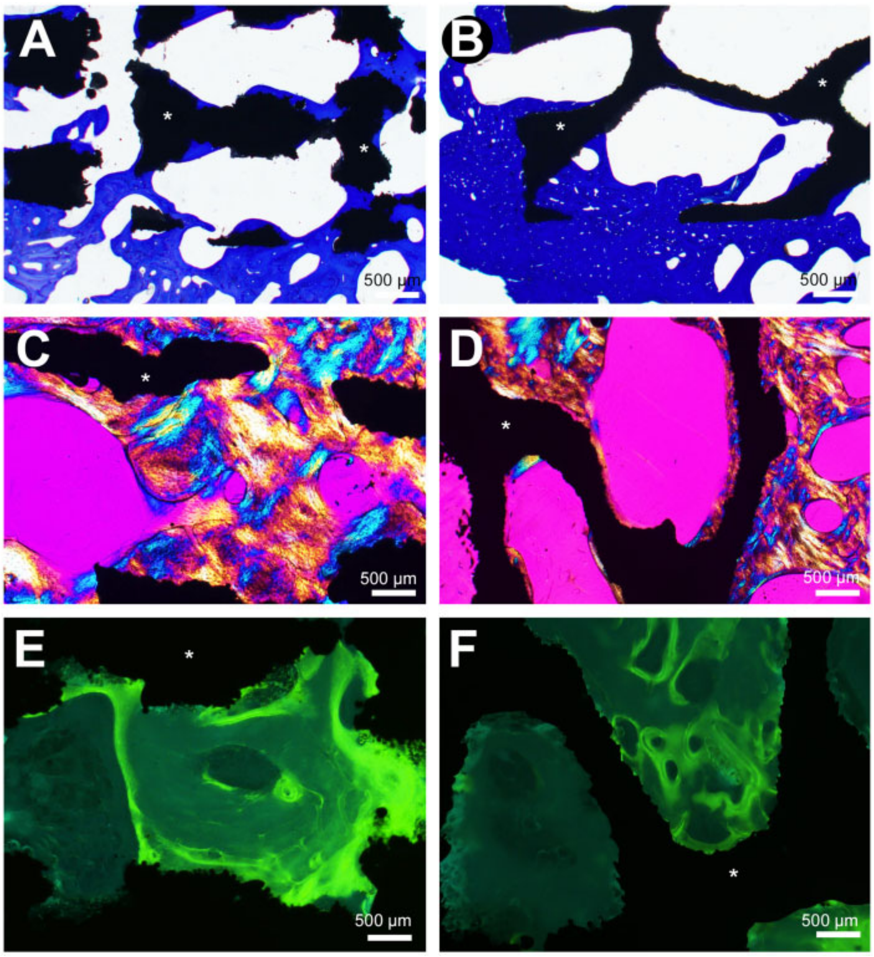

Figure 5. Histological analysis by light microscopy and fluorescence 270 days after cylinder implantation. (**A**) Trabecular bone is in direct contact with titanium septa (asterisks) (toluidine blue). (**B**) Trabecular bone is in direct contact with titanium trabeculae (toluidine blue). (**C**) Trabecular bone creeps between the titanium septa in the geometrical architecture cylinders (polarized light). (**D**) Trabecular bone creeps between the titanium trabeculae (polarized light). (**E**) Fluorescence microscopy, numerous labels are observed in bone within the biomaterial cavities limited by the titanium septa. (**F**) Fluorescence microscopy, numerous labels are observed in bone within the biomaterial cavities limited by the titanium trabeculae

Table 2. Histomorphometric parameters (results are expressed as mean ± SD)

		Group A (90 days)			Group B (270 days)		
	Unit	Subgroup g	Subgroup t	*P*	Subgroup g	Subgroup t	*P*
TitV/TV	%	40.1 ± 4.9	34.1 ± 3.3	0.009	41.6 ± 0.6	36.8 ± 6.2	0.009
BV/TV	%	6.0 ± 3.1	6.6 ± 4.2	NS	9.38 ± 1.8	7.9 ± 3.7	NS
BS/TitS	%	38.2 ± 7.9	23.6 ± 9.8	NS	55.4 ± 9.2	47.3 ± 6.5	NS
MAR_{cont}	µm/D	1.97 ± 0.10	2.02 ± 0.16	NS	1.63 ± 0.08	1.64 ± 0.07	NS
MAR_{dist}	µm/D	1.98 ± 0.09	1.97 ± 0.03	NS	1.63 ± 0.10	1.62 ± 0.17	NS

In this study, porous titanium was chosen because this metal is known to promote osteoblast affinity [8, 49, 50]. Several studies have reported the use of titanium biomaterials with good tolerance and osseointegration properties [8, 24, 51, 52]. Furthermore, titanium has long been known to be an excellent biocompatible metal with good tolerance and excellent osseointegration properties and has been used in orthopedic and dental surgery for decades (see reviews in [17, 53]). Surgical specialties such as orthopedics, neurosurgery, dental and maxillofacial surgery very commonly use implants to replace bone. Since the loss of substance cannot always be managed by an autologous graft, biomaterials are needed to manage this type of problem. 3D printing by addictive manufacturing makes it possible to obtain implants of any shape, suitable for many conditions. Therefore, the industry can produce these biomaterials that have, in addition, an absolute viral or bacterial safety compared with auto, allo or xenomaterials.

In this study, we found that the titanium cylinders were osseointegrated into the femoral bone of ewes as evidenced by the presence

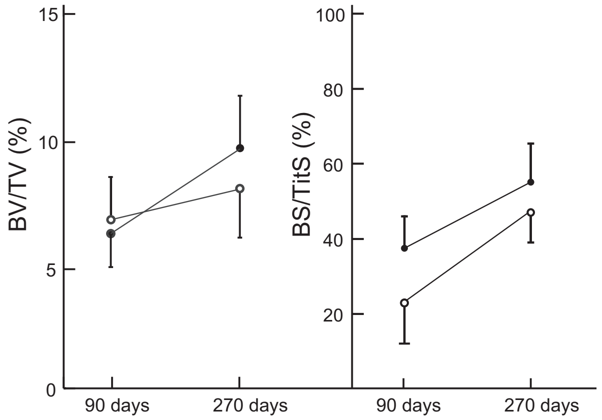

Figure 6. Evolution of histomorphometric parameters upon time. Opened circles represent cylinders with a trabecular microarchitecture; closed circles represent cylinders with a geometric microarchitecture

of trabeculae anchored on the external surfaces of the cylinders. Only the use of large animals (goats or sheep) allows accurate studies of biomaterials that can be used in orthopedics, such as prostheses or biomaterials intended to fill large bone cavities in weight bearing areas. Large animal allow the graft of large biomaterial samples in bone defects of critical size, close to the lesions observed in humans [35, 36]. Sheep have a trabecular microarchitecture close to that of humans, which allows histomorphometric and histodynamic analyses to evaluate the osseointegration of biomaterials at the tissue level [4, 38]. Finally, biomaterials are most often evaluated in young laboratory animals with a vigorous osteoblastic function whereas their main indications remain for aged patients [54]. The use of older animals is rare in the literature because of the high costs of rearing and stabling for experimentation purposes [4, 54].

Both implants exhibited interconnected porosity that promotes osseointegration and differed only in their microarchitecture. Microarchitecture has been reported to be a determining factor in the bone tissue response leading to osseointegration [14, 55]. Bone cells are known to have varying affinities with surfaces with different topographic geometries [56, 57]. In this study, the geometric microarchitecture corresponded to that used for fusion cages used in spine surgery, so this microarchitecture is routinely used with satisfactory results on intervertebral fusion rates with good osseointegration [58, 59]. Implants with trabecular microarchitecture were prepared using bovine trabecular bone as a template in additive manufacturing. Our hypothesis was that such a scaffold mimicking bone microarchitecture would promote osseointegration more than a purely geometric microarchitecture [55]. However, the cylinder microarchitecture did not influence osseointegration because the amount of bone (BV/TV) and the BS/TitS were never different at any time. In both cases, bone extended from the surface to the center of the cylinder but most of it was in the first few millimeters. The bone modeling and remodeling was different from what is seen in dental surgery. Continuous remodeling has been repeatedly shown to occur on the surface of dental implants, resulting in increased BV/TV, BS/TitS and bone quality over time, associated with a reduced osteoblastic activity in an 18-month study [60, 61]. Mineralization rates were not significantly different over time with a slight trend toward ‘return to normal’. Our results appear to be very similar to those obtained with Trabecular metal® tantalum foam in which osseointegration is limited to the most superficial areas of the implanted blocks [11, 62, 63]. Other authors have produced porous titanium materials with a lower porosity (23-32%) and a pore size of about 300 µm but they presented only *in vitro* results or indirect proofs of osseointegration in the rat without histological analysis [64, 65]. However, by additive printing, with a technology developed by Sirris, a reference center on this technique, it was not possible to obtain pores of size close to 300 µm without these being obstructed by the titanium powder or the porosity being interconnected. Here, large pores, already used for the fabrication of fusion cages in neurosurgery, were obtained using either a mathematical model or a replica of an aged bovine bone. The microarchitecture obtained is the same as that found in elderly human bones. In a recent paper, cylinders of porous titanium (6 mm in diameter) were also prepared by 3D printing with a mathematical model based on Voronoi 3D partition method [66]. In their study, the metal trabeculae were 200 µm in thickness without mentioning the pore size. Histological analysis revealed that the bone of the young sheep (2 years old) used in their study, had only partially colonized the titanium network by osteoconduction. In this series, a larger defect was created in aged ewes with the use of larger titanium cylinders.

Furthermore, it has been reported, in a series of 11 patients with these porous tantalum implants placed in the ankle that poor integration of the biomaterial results in non-union with bone. [10]. One explanation could be the absence of mechanical stress within the rigid implants whose pores create a protected volume disconnected from the stresses exerted on the graft. The absence of stress is deleterious to bone remodeling [67]. The phenomenon has been well described in orthopedic surgery and is known in hip arthroplasty as ‘stress-shielding’ [17, 68]. In the grafted cylinders in ewes, it can be assumed that integration occurs in the periphery where the mechanical stresses are sufficient to promote remodeling, whereas in the core of the cylinders, the stresses are too low and the bone cells do not perceive the signal. The absence of stress prevents remodeling.

In addition, another explanation for the lack of a statistically significant difference in the amount of bone grown in the titanium cylinders may be due to the positioning of the implant at the time of surgery. The cylinders were implanted parallel to the joint space. This difference could explain why the trabecular microarchitecture implants did not have the same mesh size as the neighboring bone of the ewes. On the contrary, the implants with geometric microarchitecture appeared much more regular. Finally, the question of the reproducibility of the surgical procedure for implanting the cylinders arises [4]. It can be assumed that depending on the orientation of the bone trabeculae in the operated bone, the cylinder is not placed parallel to the trabeculae and osseointegration is of poorer quality. In connection with the results of the fluid flow modeling, it is possible that implants mimicking the trabecular architecture require special placement to optimize osseointegration with the titanium trabeculae inserted parallel to the stress lines in the bone [23]. Cylinders with a geometrical architecture may not be subject to such a phenomenon because the fluid flow is the same whether the cylinder is vertical or horizontal. The CFD study shows that localized turbulent flow phenomena exist for implants with trabecular microarchitecture and that, conversely, implants with geometric microarchitecture exhibit laminar flow.

Conclusion

Titanium implants allow long-term osseointegration over time. Although the microarchitecture of implant used does not seem to influence the quality of osseointegration, it may not be necessary to reproduce a microarchitecture close to natural bone whereas a geometrical architecture is easier to design and produce.

Acknowledgements

Mrs I. Pavageau and I. Leborgne are thanked for their surgical help. The authors also thank R. Mallet for his help with the SEM. Authors also thank Sundeep K. Wing for having review the article.

Funding

This work was supported partially by the Walloon Region (CWALity project NEXTBONE: Convention n_1610093). This work was made possible by grants from the CHU of Angers (University hospital), project MOCONA and the French Ministry of Research.

Conflict of interest statement. None declared.

References

1. Sporer SM, Paprosky WG, O'Rourke M. Managing bone loss in acetabular revision. *J. Bone Joint Surg* 2005;**87**:1620–30.
2. Hollinger JO, Kleinschmidt JC. The critical size defect as an experimental model to test bone repair materials. *J Craniofacial Surg* 1990;**1**:60–8.
3. Hofmann A, Gorbulev S, Guehring T *et al.* Autologous iliac bone graft compared with biphasic hydroxyapatite and calcium sulfate cement for the treatment of bone defects in tibial plateau fractures: a prospective, randomized, open-label, multicenter study. *J. Bone Joint Surg* 2020;**102**: 179–93.
4. Rony L, Aguado E, Pascaretti-Grizon F *et al.* Hyaluronic acid stimulates osseointegration of β-TCP in young and old ewes. *Calcif Tissue Int* 2019; **105**:487–96.
5. Grambart ST, Anderson DS, Anderson TD. Bone grafting options. *Clinic Pod Med Surg* 2020;**37**:593–600.
6. Tricoteaux A, Rguiti E, Chicot D *et al.* Influence of porosity on the mechanical properties of microporous β-TCP bioceramics by usual and instrumented Vickers microindentation. *J Europ Ceram Soc* 2011;**31**: 1361–9.
7. Sous M, Bareille R, Rouais F *et al.* Cellular biocompatibility and resistance to compression of macroporous β-tricalcium phosphate ceramics. *Biomat* 1998;**19**:2147–53.
8. Albrektsson T, Brånemark P-I, Hansson H-A *et al.* Osseointegrated titanium implants: requirements for ensuring a long-lasting, direct bone-to-implant anchorage in man. *Act Orthopaed Scandinav* 1981;**52**:155–70.
9. Sakka S, Ayed FB, Bouaziz J. Mechanical properties of tricalcium phosphate–alumina composites. *IOP Conf Ser Mater Sci Eng* 2012;**28**: 012028.
10. Aubret S, Merlini L, Fessy M *et al.* Poor outcomes of fusion with Trabecular Metal implants after failed total ankle replacement: early results in 11 patients. *Orthop Traumatol Surg Res* 2018;**104**:231–7.
11. Cohen R. A porous tantalum trabecular metal: basic science. *Am. J. Orthop* 2002;**31**:216.
12. Roach RP, Clair AJ, Behery OA *et al.* Aseptic loosening of porous metaphyseal sleeves and tantalum cones in revision total knee arthroplasty: a systematic review. *J Knee Surg* 2020; DOI: 10.1055/s-0040-1701434.
13. Scarano A, Piattelli M, Vrespa G *et al.* Bone healing around titanium and titanium nitride-coated dental implants with three surfaces: an experimental study in rats. *Clin Implant Dent Rel Res* 2003;**5**:103–11.
14. Graziano A, d'Aquino R, Angelis MGCD *et al.* Scaffold's surface geometry significantly affects human stem cell bone tissue engineering. *J Cell Physiol* 2008;**214**:166–72.
15. Zardiackas LD, Parsell DE, Dillon LD *et al.* Structure, metallurgy, and mechanical properties of a porous tantalum foam. *J Biomed Mater Res* 2001;**58**:180–7.
16. de Viteri VS, Fuentes E. Titanium and titanium alloys as biomaterials. In: *Tribology-Fundumentals and Advancements*. Rijeka, Croati: IntechOpen, 2013,155–81.
17. Rony L, Lancigu R, Hubert L. Intraosseous metal implants in orthopedics: a review. *Morphologie* 2018;**102**:231–42.
18. Chappard D, Fressonnet C, Genty C *et al.* Fat in bone xenografts: importance of the purification procedures on cleanliness, wettability and biocompatibility. *Biomaterials* 1993;**14**:507–12.
19. Levai JP, Boisgard S. Acetabular reconstruction in total hip revision using a bone graft substitute. Early clinical and radiographic results. *Clin Orthop Relat Res* 1996;**330**:108–14.
20. Liebschner MA. Biomechanical considerations of animal models used in tissue engineering of bone. *Biomaterials* 2004;**25**:1697–714.
21. Wang X, Nyman JS, Dong X *et al.* Fundamental biomechanics in bone tissue engineering. *Synth Lect Tissue Eng* 2010;**2**:1–225.
22. Geurs NC, Jeffcoat RL, McGlumphy EA *et al.* Influence of implant geometry and surface characteristics on progressive osseointegration. *Int J Oral Maxillofac Implants* 2002;**17**:811–5.
23. Simmons CA, Meguid SA, Pilliar RM. Differences in osseointegration rate due to implant surface geometry can be explained by local tissue strains. *J Orthop Res* 2001;**19**:187–94.
24. Guyer RD, Abitbol J-J, Ohnmeiss DD *et al.* Evaluating osseointegration into a deeply porous titanium scaffold: a biomechanical comparison with PEEK and allograft. *Spine* 2016;**41**:E1146–50.
25. Mostaghimi P, Blunt MJ, Bijeljic B. Computations of absolute permeability on micro-CT images. *Math Geosci* 2013;**45**:103–25.
26. Fanchi JR. Rock-fluid interaction, Chapter 5. In: JR Fanchi (ed). *Principles of Applied Reservoir Simulation* (4th edn). Cambridge, MA: Gulf Professional Publishing/Elsevier, 2018,81–99.
27. Duda A, Koza Z, Matyka M. Hydraulic tortuosity in arbitrary porous media flow. *Phys Rev E* 2011;**84**:036319.
28. Espinoza-Andaluz M, Andersson M, Sundén B. Computational time and domain size analysis of porous media flows using the lattice Boltzmann method. *Comput Math Appl* 2017;**74**:26–34.
29. Baker RO, Yarranton HW, Jensen JL. 7 - conventional core analysis–rock properties. In: RO Baker, HW Yarranton, JL Jensen (eds). *Practical Reservoir Engineering and Characterization*. Cambridge, MA: Gulf Professional Publishing/Elsevier, 2015,197–237.
30. Chappard D. Technical aspects: how do we best prepare bone samples for proper histological analysis? In: *Bone Cancer* (2nd edn). London: Elsevier, Academic Press, 2015,111–20.
31. Dempster DW, Compston JE, Drezner MK *et al.* Standardized nomenclature, symbols, and units for bone histomorphometry: a 2012 update of the report of the ASBMR Histomorphometry Nomenclature Committee. *J. Bone Miner. Res* 2013;**28**:2–17.
32. Richmond J. Refinement, reduction, and replacement of animal use for regulatory testing: future improvements and implementation within the regulatory framework. *ILAR J* 2002;**43**:S63–S68.
33. Vesprey A, Suh ES, Ayturk DG *et al.* Bone marrow stromal cells in a mouse model of implant osseointegration. *bioRxiv* 2020. DOI: 10.1101/2020.08.17.254433.
34. Lakstein D, Kopelovitch W, Barkay Z *et al.* Enhanced osseointegration of grit-blasted, NaOH-treated and electrochemically hydroxyapatite-coated Ti–6Al–4V implants in rabbits. *Acta Biomater* 2009;**5**:2258–69.
35. Harris JS, Bemenderfer TB, Wessel AR *et al.* A review of mouse critical size defect models in weight bearing bones. *Bone* 2013;**55**:241–7.
36. Aguado E, Goyenvalle E. Modèles animaux et biomatériaux. In: B Guillaume, M Audran, D Chappard (eds). *Tissu Osseux et Biomatériaux en Chirurgie Dentaire*. Paris: Quintessence Int., 2014,307–22.
37. Nauth A, Schemitsch E, Norris B *et al.* Critical-size bone defects: is there a consensus for diagnosis and treatment? *J. Orthop. Trauma* 2018;**32**: S7–11.
38. Turner A. The sheep as a model for osteoporosis in humans. *Vet J* 2002; **163**:232–9.
39. Hernigou P, Dubory A, Pariat J *et al.* Beta-tricalcium phosphate for orthopedic reconstructions as an alternative to autogenous bone graft. *Morphologie* 2017;**101**:173–9.

40. Campana V, Milano G, Pagano E *et al.* Bone substitutes in orthopaedic surgery: from basic science to clinical practice. *J Mater Sci: Mater Med* 2014;**25**:2445–61.
41. Kankilic B, Dede EC, Korkusuz P *et al.* Apatites for orthopedic applications. In: *Clinical Applications of Biomaterials*. Switzerland: Springer, 2017,65–90.
42. Tanaka T, Komaki H, Chazono M *et al.* Basic research and clinical application of beta-tricalcium phosphate (β-TCP). *Morphologie* 2017;**101**: 164–72.
43. Lu J, Flautre B, Anselme K *et al.* Role of interconnections in porous bioceramics on bone recolonization in vitro and in vivo. *J. Mater Sci Mater Med* 1999;**10**:111–20.
44. Arbez B, Kün-Darbois JD, Convert T *et al.* Biomaterial granules used for filling bone defects constitute 3D scaffolds: porosity, microarchitecture and molecular composition analyzed by microCT and Raman microspectroscopy. *J Biomed Mater Res* 2019;**107**:415–23.
45. Dorozhkin SV. Calcium orthophosphates in nature, biology and medicine. *Materials* 2009;**2**:399–498.
46. Chappard D, Terranova L, Mallet R *et al.* 3D porous architecture of stacks of beta-TCP granules compared with that of trabecular bone: a microCT, vector analysis, and compression study. *Front. Endocrinol (Laussane)* 2015;**6**:161.
47. Li S, de Wijn JR, Li J *et al.* Macroporous biphasic calcium phosphate scaffold with high permeability/porosity ratio. *Tissue Eng* 2003;**9**:535–48.
48. Dorozhkin SV. Biocomposites and hybrid biomaterials based on calcium orthophosphates. *Biomaterials* 2011;**1**:3–56.
49. Stiehler M, Lind M, Mygind T *et al.* Morphology, proliferation, and osteogenic differentiation of mesenchymal stem cells cultured on titanium, tantalum, and chromium surfaces. *J Biomed Mater Res A* 2008;**86**:448–58.
50. Hirota M, Hayakawa T, Shima T *et al.* High porous titanium scaffolds showed higher compatibility than lower porous beta-tricalcium phosphate scaffolds for regulating human osteoblast and osteoclast differentiation. *Mater Sci Eng C* 2015;**49**:623–31.
51. Apostu D, Lucaciu O, Berce C *et al.* Current methods of preventing aseptic loosening and improving osseointegration of titanium implants in cementless total hip arthroplasty: a review. *J Int Med Res* 2018;**46**:2104–19.
52. Liu X, Chen S, Tsoi JK *et al.* Binary titanium alloys as dental implant materials—a review. *Regen Biomater* 2017;**4**:315–23.
53. Guillaume B. Dental implants: a review. *Morphologie* 2016;**100**:189–98.
54. Blouin S, Moreau MF, Weiss P *et al.* Evaluation of an injectable bone substitute (betaTCP/hydroxyapatite/hydroxy-propyl-methyl-cellulose) in severely osteopenic and aged rats. *J Biomed Mater Res A* 2006;**78**: 570–80.
55. Marques A, Miranda G, Silva F *et al.* Review on current limits and potentialities of technologies for biomedical ceramic scaffolds production. *J Biomed Mater Res B* 2020;
56. Anselme K, Bigerelle M. Topography effects of pure titanium substrates on human osteoblast long-term adhesion. *Acta Biomater* 2005;**1**:211–22.
57. Zhu X, Chen J, Scheideler L *et al.* Effects of topography and composition of titanium surface oxides on osteoblast responses. *Biomaterials* 2004;**25**: 4087–103.
58. Gittens RA, Olivares-Navarrete R, Schwartz Z *et al.* Implant osseointegration and the role of microroughness and nanostructures: lessons for spine implants. *Acta Biomater* 2014;**10**:3363–71.
59. Seaman S, Kerezoudis P, Bydon M *et al.* Titanium vs. polyetheretherketone (PEEK) interbody fusion: meta-analysis and review of the literature. *J Clin Neurosci* 2017;**44**:23–9.
60. Grizon F, Aguado E, Huré G *et al.* Enhanced bone integration of implants with increased surface roughness: a long term study in the sheep. *J Dent* 2002;**30**:195–203.
61. Chappard D, Aguado E, Huré G *et al.* The early remodeling phases around titanium implants: a histomorphometric assessment of bone quality in a 3- and 6-month study in sheep. *Int J Oral MaxillofacImplants* 1999;**14**: 189–96.
62. Breer S, Hahn M, Kendoff D *et al.* Histological ex vivo analysis of retrieved human tantalum augmentations. *Int Orthop* 2012;**36**:2269–74.
63. Christie MJ. Clinical applications of trabecular metal. *Am J Orthop* 2002; **31**:219–20.
64. Xue W, Krishna BV, Bandyopadhyay A *et al.* Processing and biocompatibility evaluation of laser processed porous titanium. *Acta Biomater* 2007; **3**:1007–18.
65. Bandyopadhyay A, Espana F, Balla VK *et al.* Influence of porosity on mechanical properties and in vivo response of Ti6Al4V implants. *Acta Biomater* 2010;**6**:1640–8.
66. Ragone V, Canciani E, Arosio M *et al.* In vivo osseointegration of a randomized trabecular titanium structure obtained by an additive manufacturing technique. *J Mater Sci Mater. Med* 2020;**31**:1–11.
67. Simon U, Augat P, Ignatius A *et al.* Influence of the stiffness of bone defect implants on the mechanical conditions at the interface—a finite element analysis with contact. *J Biomech* 2003;**36**:1079–86.
68. Bugbee WD, Culpepper WJ, Engh CA *et al.* Long-term clinical consequences of stress-shielding after total hip arthroplasty without cement. *J Bone Joint Surg* 1997;**79**:1007–12.

Partie 3 – Remodelage osseux et ostéonécrose aseptique de la tête fémorale

L'OstéoNécrose Aseptique (ONA) de la tête fémorale reste une pathologie relativement rare en Rhumatologie et en Chirurgie Orthopédique. C'est Arlet et Ficat qui en ont fait la description et qui ont laissé leurs noms à la classification radiographique qui reste à ce jour toujours en vigueur (117). En fonction du stade de la maladie, les patients souffrent de la hanche sans retentissement fonctionnel dans le premier stade de la maladie et présentent une arthrose avec perte de sphéricité de la tête fémorale dans le stade le plus avancé (118).

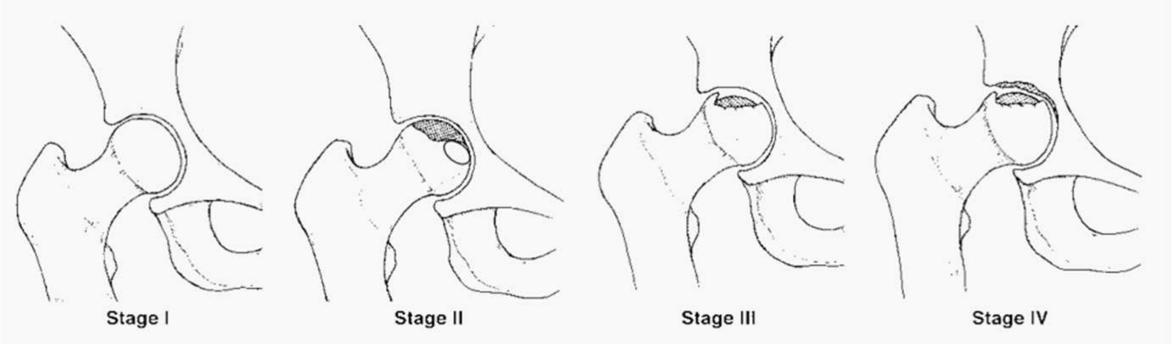

Figure 6 : Classification d'Arlet et Ficat.

D'un point de vue histologique, il est observé une nécrose du cartilage articulaire secondaire à une nécrose de l'os sous-chondral (119-121). Longtemps le cartilage garde sa fonction du fait de l'imbibition que lui procure le liquide articulaire mais l'évolution finale est une nécrose complète du cartilage (122-124). L'évolution finale de la pathologie est l'arthrose coxo-fémorale pour laquelle l'implantation d'une prothèse totale de hanche est la solution de choix. De fait, l'analyse des têtes fémorales des patients qui présentaient une ONA stade 4 et qui ont donc eu une PTH a permis d'une part une analyse en microCT (cf. Morphologie) et également une analyse microscopique conventionnelle couplée à la mise en évidence des ostéocytes vivants décrite dans un autre article (cf Microscopy, Research and Technique).

Une série de têtes fémorales humaines prélevée~~s~~ dans le cadre de la réalisation d'une arthroplastie totale de hanche ayant pour étiologie une ONA a pu être analysée par différentes techniques : microCT et microscopie optique (115, 125, 126). Ce projet a fait l'objet d'un soutien financier par le CHU d'Angers par le biais du projet MOCONA.

Les ostéocytes qui sont incorporés dans la matrice minéralisée de l'os communiquent entre eux grâce à des prolongements circulant dans les canalicules de la matrice osseuse. A l'extrémité des prolongements, des GAP jonctions (jonctions serrées) sont présentes permettant des interactions cellulaires (127, 128). Ces extensions dendritiques courent au sein de canalicules allant des surfaces endostéales à périostées (129-131). Depuis peu, il est admis que ces cellules jouent un rôle central dans le remodelage osseux et qu'elles peuvent contrôler la résorption et la formation osseuse (132). Les ostéocytes agissent comme mécanorécepteurs et sont impliqués dans l'homéostasie du calcium par leur fonction endocrine via la sécrétion du FGF23 (133).

La disparition des ostéocytes due à l'ischémie a été reconnue par d'anciens auteurs et est interprétée comme un signe de mort osseuse (121, 134). Il est difficile d'observer les ostéocytes et le système lacuno-canaliculaire. Pour ce faire, des techniques d'inclusion d'os non décalcifiés ont permis d'améliorer les observations avec notamment l'utilisation de colorations « en-bloc » par la Rhodamine (35, 42, 135). La première étude de cette partie avait pour but de mettre au point cette coloration des ostéocytes par la rhodamine permettant leur repérage en microscopie de fluorescence dans la matrice osseuse. En effet, l'utilisation de la fluorescence naturelle de la rhodamine permet de marquer les cellules qui deviennent alors visibles après excitation à la bonne longueur d'onde du fluorochrome. L'ajout de la technique de la microscopie confocale permet ensuite de localiser plus finement les cellules et leurs prolongements dans la matrice osseuse. Le principe de cet outil est de permettre une acquisition de plusieurs plans d'une même image pour en obtenir une vision 3D. L'addition de la fluorescence et du microscope confocal a permis de visualiser les ostéocytes dans la matrice osseuse. Par ce procédé, des ONA dues à différentes étiologies, ainsi que des arthroses ont été étudiées et ont permis de repérer les zones où les ostéocytes étaient présents ou absents.

ARTICLE 7

Osteocyte staining with rhodamine in osteonecrosis and osteoarthritis of the femoral head

Louis RONY, Rodolphe PERROT, Laurent HUBERT, Daniel CHAPPARD

Microscopy Research & Technique 82: 2072-8 (2019)

Impact Factor : 2,769 – SIGAPS : B

Received: 15 February 2019 | Revised: 27 August 2019 | Accepted: 9 September 2019

DOI: 10.1002/jemt.23379

RESEARCH ARTICLE

MICROSCOPY RESEARCH & TECHNIQUE WILEY

Osteocyte staining with rhodamine in osteonecrosis and osteoarthritis of the femoral head

Louis Rony[1,2,3] | Rodolphe Perrot[2] | Laurent Hubert[1,3] | Daniel Chappard[1,2]

[1]Groupe Etudes Remodelage Osseux et bioMatériaux, GEROM, EA-4658, SFR-4208, Univ-Angers, IRIS-IBS Institut de Biologie en Santé, CHU-Angers, Angers, France

[2]Service Commun d'Imagerie et Analyses Microscopiques, SCIAM, SFR-4208, Univ-Angers, IRIS-IBS Institut de Biologie en Santé, CHU d'Angers, Angers, France

[3]Département de Chirurgie Osseuse, CHU-Angers, Angers, France

Correspondence
Daniel Chappard, Groupe Etudes Remodelage Osseux et bioMatériaux, GEROM, EA-4658, SFR-4208, Univ-Angers, IRIS-IBS Institut de Biologie en Santé, Université d'Angers, CHU d'Angers, 49933 Angers, France.
Email: daniel.chappard@univ-angers.fr

Review Editor: Paolo Bianchini

Funding information
CHU d'Angers

Abstract

Death of osteocytes is synonymous of bone death. Aseptic osteonecrosis of the femoral head is a lesion characterized by the death of osteocytes occurring after major vascular changes. The evolution may lead to hip osteoarthritis, which requires total hip arthroplasty in most cases. Evolution of aseptic osteonecrosis in four radiological stages is well known. We analyzed 24 femoral heads from patients with osteonecrosis or osteoarthritis, retrieved at the time of surgery for a hip arthroplasty. The aim of the study was to clearly identify the necrotic bone from the living bone in the histological samples. The femoral heads were sawed, and a large sample was harvested in the superior zone; it was stained en-bloc with rhodamine dissolved in formalin to make the osteocytes fluorescent under UV light microscopy. Undecalcified sections, 7 μm thick, were obtained on a heavy-duty microtome. A micrographic analysis using two UV excitation wavelengths visualized the living osteocytes (in green) and the bone matrix (in blue). A simple method to prepare combined images is described. In addition, the blocks can be analyzed by confocal microscopy to visualize more details. It is possible to identify at low magnification the osteocytes within the bone matrix and the osteonecrotic areas where osteocytes have disappeared. Identification of osteocytes showed that newly formed bone packets are laid on dead trabeculae in patients with aseptic osteonecrosis or with osteoarthritis. In the osteosclerotic areas, the enlarged trabeculae have a dead central core surrounded by recently apposed bone structure units.

KEYWORDS
fluorescence microscopy, osteoarthritis, osteocytes, osteonecrosis, rhodamine

1 | INTRODUCTION

Osteocytes are dendritic cells, which are differentiated from osteoblasts and are embedded in the mineralized matrix of bone. Osteocyte dendrites run inside a considerably developed network of canaliculi extending from the periosteal to the endosteal surface in cortical bone and they are disseminated in all trabeculae of cancellous bone. Neighboring osteocytes contact each other within the canaliculi and are synchronized via intercellular communications made of gap junctions (Bonewald, 2011; Romanello & D'Andrea, 2001). Canaliculi and osteocyte lacunae form a set often referred as the lacuno–canalicular system. Direct cell-to-cell interactions have been shown several decades ago between osteocytes and other bone cells resting at the bony surfaces (osteoblasts and lining cells but also osteoclasts), marrow cells, and endothelial cells (Trueta, 1963). Although osteocytes represent ~95% of bone cells with a density of ~13,000¢/mm^3 of bone, the cell was poorly studied until recently. They are now considered to play a central role in bone remodeling and can control bone resorption and bone formation (Bellido, 2014). Osteocytes acting as mechanoreceptors are implied in calcium homeostasis; they are also considered as endocrine cells secreting factors such as FGF-23 acting on distant organs (Bonewald, 2017). Disappearance of osteocytes due to ischemia has been recognized by former authors and is interpreted as a sign of bone death (Catto, 1965; Trueta, 1963). Necrotic bone with dead osteocytes is observed associated with many disorders with osteonecrosis (also referred as avascular necrosis, aseptic necrosis, or ischemic bone necrosis). Several conditions cause osteocytes to die, leading to bone destruction, sequestration, or end-stage arthritis of the femoral head (Lespasio, Sodhi, & Mont, 2019; Shah, Racine, Jones, & Aaron, 2015). The hip joint is more frequently concerned by osteonecrosis. Death of osteocytes has also been observed in osteoarthritis of the hip and is due to vascular changes (Findlay, 2007; Goldring & Goldring, 2016).

Osteocytes are quite difficult to identify on decalcified sections due to considerable shrinkage of the cell body and cell processes during histological preparation. Undecalcified bone embedding in poly(methyl methacrylate) (pMMA) is now favored for the histopathological and histomorphometric diagnosis of bone diseases as it allows a clear identification of osteoid tissue, tetracycline labeling, and osteoclast identification (Chappard, 2014). Osteocytes and the lacuno–canalicular system remain still difficult to identify in routine histopathology on large tissue sections because of heterogeneity in staining achieved with classical stains such as Goldner trichrome or toluidine blue staining. In the course of studies on aseptic osteonecrosis of the hip and hip osteoarthritis, we wanted to analyze the accurate location of osteocytes within large tissue sections of pMMA-embedded specimens.

Fluorescence microscopy methods are known to have an increased sensitivity (when compared to conventional bright field imaging) to detect small details when a fluorochrome can be used to stain the cellular component of interest (Lichtman & Conchello, 2005). A most important advantage of fluorescence microscopy is that a low power objective lens (typically ×10 or ×20) can be used to identify osteocytes in a large surface area of the tissue section. For the recognition of osteonecrosis, it is important to clearly identify the areas devoid of osteocytes (Humphreys, Spencer, Tighe, & Cumming, 1989). By using sections stained with Goldner, hematoxylin phloxin, or toluidine blue, the images are not enough precise to allow a clear identification of empty lacunae or living osteocytes.

The aim of the present study was to describe a simple staining for osteocytes usable with a conventional fluorescence microscope and usable in research by confocal microscopy. The clinical relevance of this research was to identify osteocytes in two very common circumstances in orthopedic practice (osteonecrosis and osteoarthritis of the hip).

2 | MATERIAL AND METHODS

2.1 | Patients

We included 24 patients undergoing a first-line total hip arthroplasty for aseptic femoral head osteonecrosis or hip osteoarthritis. The bone samples were send to our histopathological bone unit fixed in formalin for routine analysis. All subjects gave their informed consent to participate in the study that was approved by the local Ethical committed.

2.2 | En-bloc bone staining

The fixed femoral head was sectioned with a scroll saw, and samples were harvested in the superior part of the femoral head in the area of the main compressive group of trabeculae. The samples included the bone surface (with articular cartilage when present), the subchondral bone, the osteonecrotic areas (when present), the condensed bone area, and the remaining trabeculae of the head. Samples were post-fixed in the fridge during 1 week in a mixture containing:

Rhodamine B	2 g
10% formalin	100 ml

Rhodamine B was obtained from Sigma (St Quentin-Fallavier, France) CAS Number: 81-88-9, CI 45170.

The blocks were then rapidly dehydrated and defatted in a mixture combining acetone and xylene in the same time (Beebe, 2000).

Bone samples were infiltrated by pMMA under a gentle constant agitation, which considerably shortened the infiltration time (Chappard, 2014). Embedding was done in the cold by using polyethylene molds (Peel-a-Way embedding system, Polyscience Inc., Warrington, PA) with a strip of polyester wadding placed at the bottom of the mold to avoid the interface-linked shrinkage during polymerization. Sections were obtained at 7 μm using a heavy duty microtome (e.g., Leica, Polycut-S) equipped with 50–60° tungsten carbide knives for histomorphometry. They were stained by Goldner trichrome for analysis of osteoid and mineralized bone matrix, toluidine blue at pH 4.3 for imaging bone cells under bright field microscopy, and mounted in NeoEntellan (Merck) without further treatment for analysis of osteocytes under fluorescence microscopy.

2.3 | Microscopic analysis

Sections were analyzed with an Olympus BX51 microscope equipped for bright field and for fluorescence microscopy with the following cubes: U-MWIB3 excitation filter 460–495 nm, emission filter 510 nm, dichromatic mirror 505 nm to detect rhodamine-stained cells in green, and U-MNU2; excitation filter 360–370 nm, emission filter 420 nm, and dichromatic mirror 400 nm to study the blue autofluorescence of the bone matrix.

For each field of interest, one image was captured with each cube. RGB (red–green–blue) images were acquired on a DP71 color digital CCD camera and stored in the .tif format. The images were transferred to Photoshop (release CS5, RGB Adobe).

The image of the bone matrix was decomposed into its three layers (R, G, and B) in the layer panel, and the red and green layer were black painted. Similarly, the image of the cells was decomposed into its three layers, and the green layer was copied. This layer was then copied to the green layer of the bone matrix image, and the RGB image was obtained with the bone matrix in blue and the cells in vivid green.

2.4 | Confocal microscopy

For confocal microscopy, the pMMA blocks were polished to a 0.5-μm finish with diamond particles and observed with a Leica TCS SP8 laser-scanning confocal microscope (Leica Microsystems, Heidelberg, Germany) with a HC PL APO CS2 ×20 objective (N.A. 0.75) and ×2.85 zoom. Excitation wavelengths were set at 405 and 488 nm, whereas fluorescence was collected between 409 and 513 and 565 and 730 nm, respectively. Multiple stacked images (1,120 pixels × 1,120 pixels) were taken at 400 Hz with *x*, *y*, and *z* spatial resolution of 200, 200, and 1,500 nm, respectively. The red fluorescence of the rhodamine was converted in green to improve visibility and the ability to discriminate fine structures such as the osteocyte canaliculi. The composite image was also made of green osteocytes and a variety of blue for the bone matrix.

3 | RESULTS

3.1 | Bright field microscopy

Figure 1 illustrates the process used to obtain an overimposition of the autofluorescence of the bone matrix in blue and the osteocytes and marrow cell in green. This figure clearly identifies the bone structure units devoid of osteocytes in the center of a trabecula. Figure 2 illustrates the application of the method in patients with aseptic osteonecrosis and osteoarthritis. Figure 3 depicts the radiological and magnetic resonance imaging of two patients with osteonecrosis of the hip, their correspondence in the harvested histological sections stained with Goldner trichrome, and the focus on the different areas of the lesion including the necrotic and condensed peripheral areas.

3.2 | Confocal microscopy

Figure 4 illustrates the process used to obtain an overimposition of the autofluorescence of the bone matrix in blue and the osteocytes and processes appear in green. The lacuno–canalicular system is much better defined with this method due to the thinnest resolution provided by the laser and the optical sectioning. However, the analyzed area is reduced.

4 | DISCUSSION

In the present study, we describe a simple method usable in routine bone histopathology to identify the osteocytes and the necrotic areas

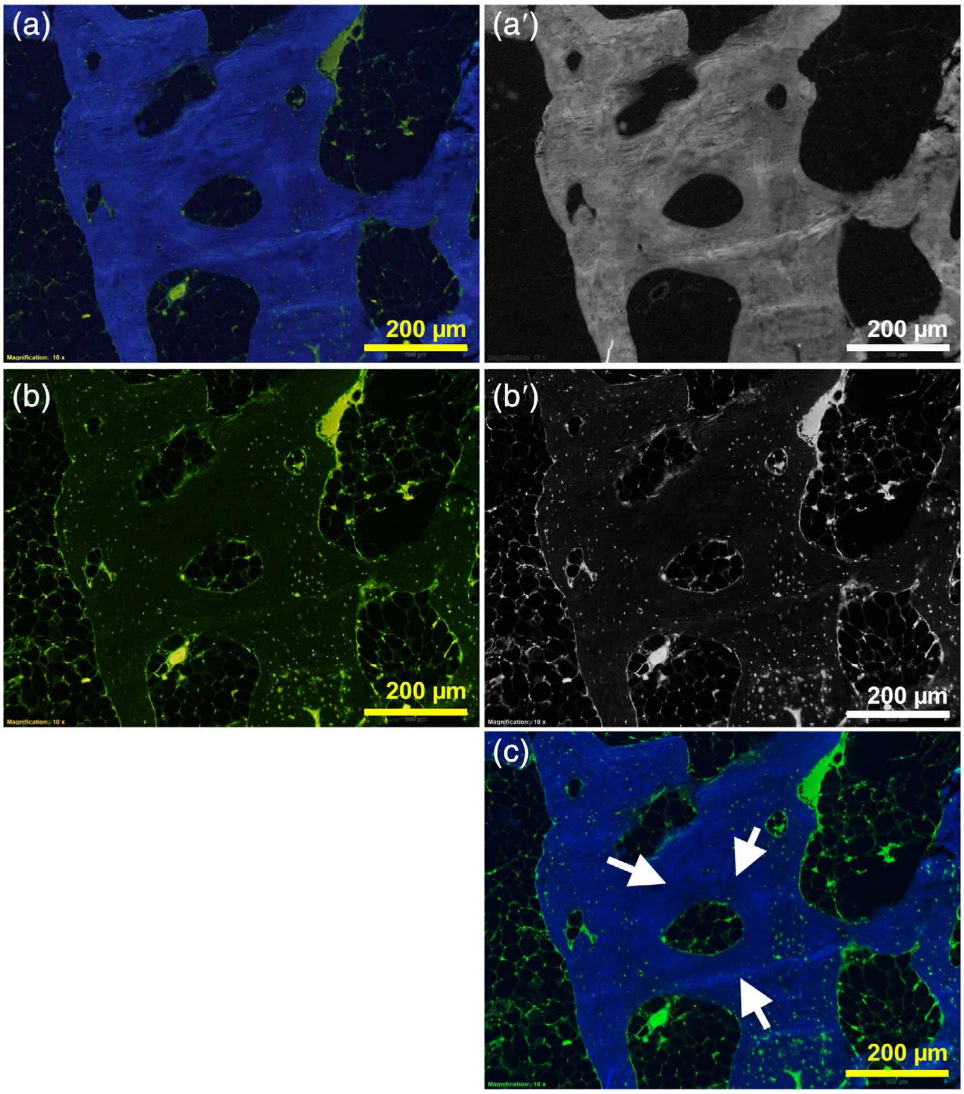

FIGURE 1 Method used to combine two fluorescent images of the same section to identify osteocytes in green and the bone autofluorescence in blue. (a) Image obtained with the cube U-MNU2 showing the fluorescence of the bone matrix in blue and a faint greenish staining in some osteocytes, marrow cells, and vessels. (a′) After separation of the three RGB layers in Photoshop, only the B(lue) layer is preserved. (b) Image obtained with the cube U-MWIB3, all osteocytes, marrow cells, and vessels, appear in green. (b′) After separation of the three RGB layers in Photoshop, only the G(reen) layer is preserved. (c) Combined image by pasting image a′ in the blue layer of b′ and black painting of the R(ed) layer. A bone structure unit devoid of osteocytes is clearly evidenced (arrows). RGB, red–green–blue

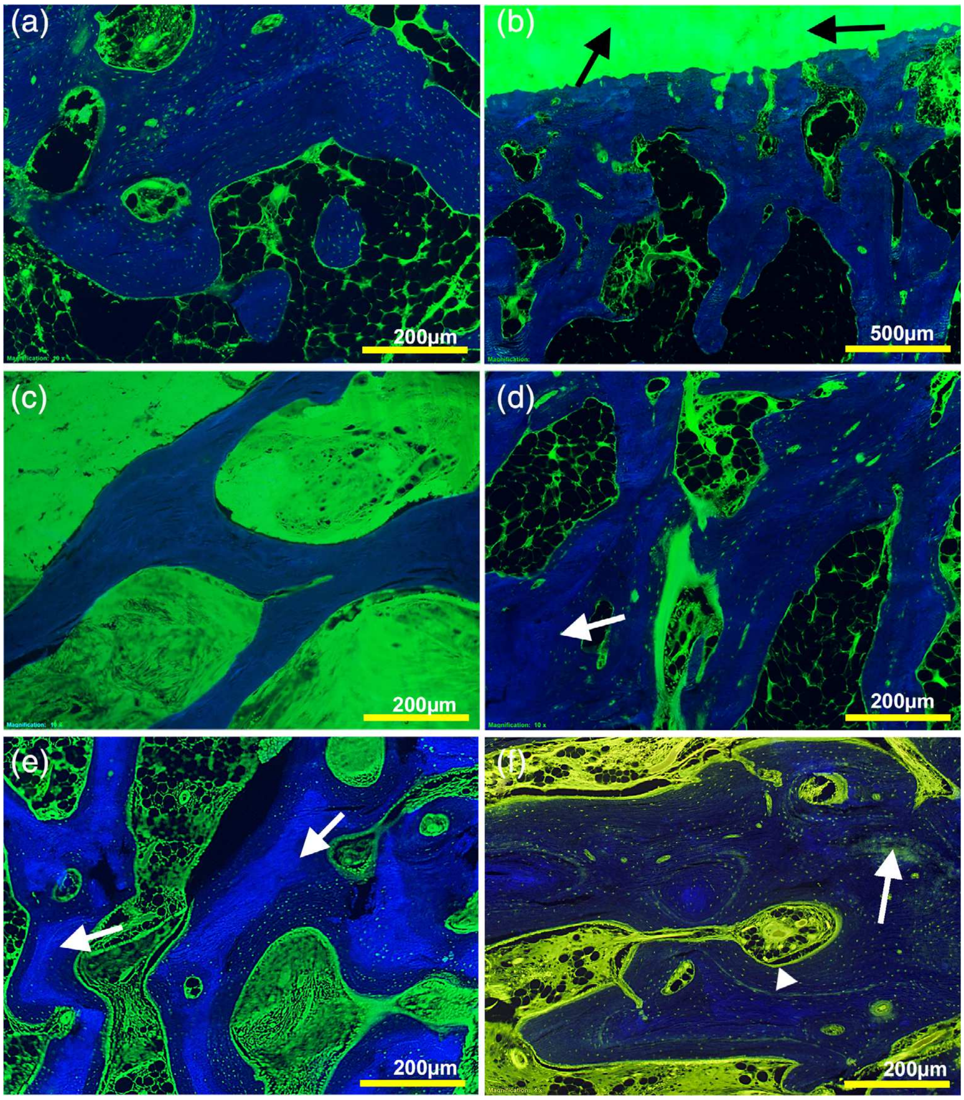

FIGURE 2 Application of the method in cases of aseptic osteonecrosis and osteoarthritis. (a) A large trabecula observed in the condensed region far from the necrotic area in a patient with Stage 2 osteonecrosis. The osteocytes are identified in all the structure units; the marrow cells are also evidenced. (b) The articular cartilage and subchondral bone in a Stage 3 osteonecrosis of the hip: note the complete absence of osteocytes in the subchondral plate, the matrix of the articular cartilage is heavily labeled by Rhodamine. (c) A patient with Stage 4 osteonecrosis: a necrotic trabeculae devoid of osteocytes, the fibrotic area in the marrow spaces is heavily labelled. (d) A patient with Stage 4 osteonecrosis; a thick trabeculae in the immediate vicinity of the necrotic area has a central core made of “old” and necrotic bone structure without osteocytes (arrow). (e) A patient with arthritis: the enlarged trabeculae present a central core with bone structure units lacking osteocytes, whereas the recently apposed ones contain numerous osteocytes. (f) Patient with a Paget's bone disease coxopathy in which the sclerotic bone has a very high remodeling rate and is made of a mosaic pattern of lamellar and woven bone structure units, resembling a jigsaw puzzle. The puzzle structure is clearly identified, and the very high number of osteocytes with a dense canalicular system is readily evidenced

in the bone trabeculae of osteonecrotic and osteoarthritic bone. The method can also be used in research as the bone blocks can be analyzed by confocal microscopy.

The number of osteocytes counted on routinely stained sections from patients with aseptic osteonecrosis has been documented but no histological finding nor inter/intra observer reproducibility was provided (Calder, Pearse, & Revell, 2001; Catto, 1965). Furthermore, measuring the density of osteocytes on two-dimensional sections is stereologically incorrect because of variation in the shape and size of this cell excepted if one uses the dissector method based on the Cavalieri principle must be applied (Bloch & Sørensen, 2010; Gundersen, Jensen, Kieu, & Nielsen, 1999). However, the method could not be used here on fluorescent sections. The only reliable method to count the exact density of the osteocyte lacuna is to determine them in three dimension by nanocomputed tomography, but this technique do not identify the living/dead cells, only their lacunae (Khoury et al., 2015; Vatsa et al., 2008).

Rhodamine has previously been used to identify either the lacuno–canalicular system or the osteocytes themselves. The stain has been

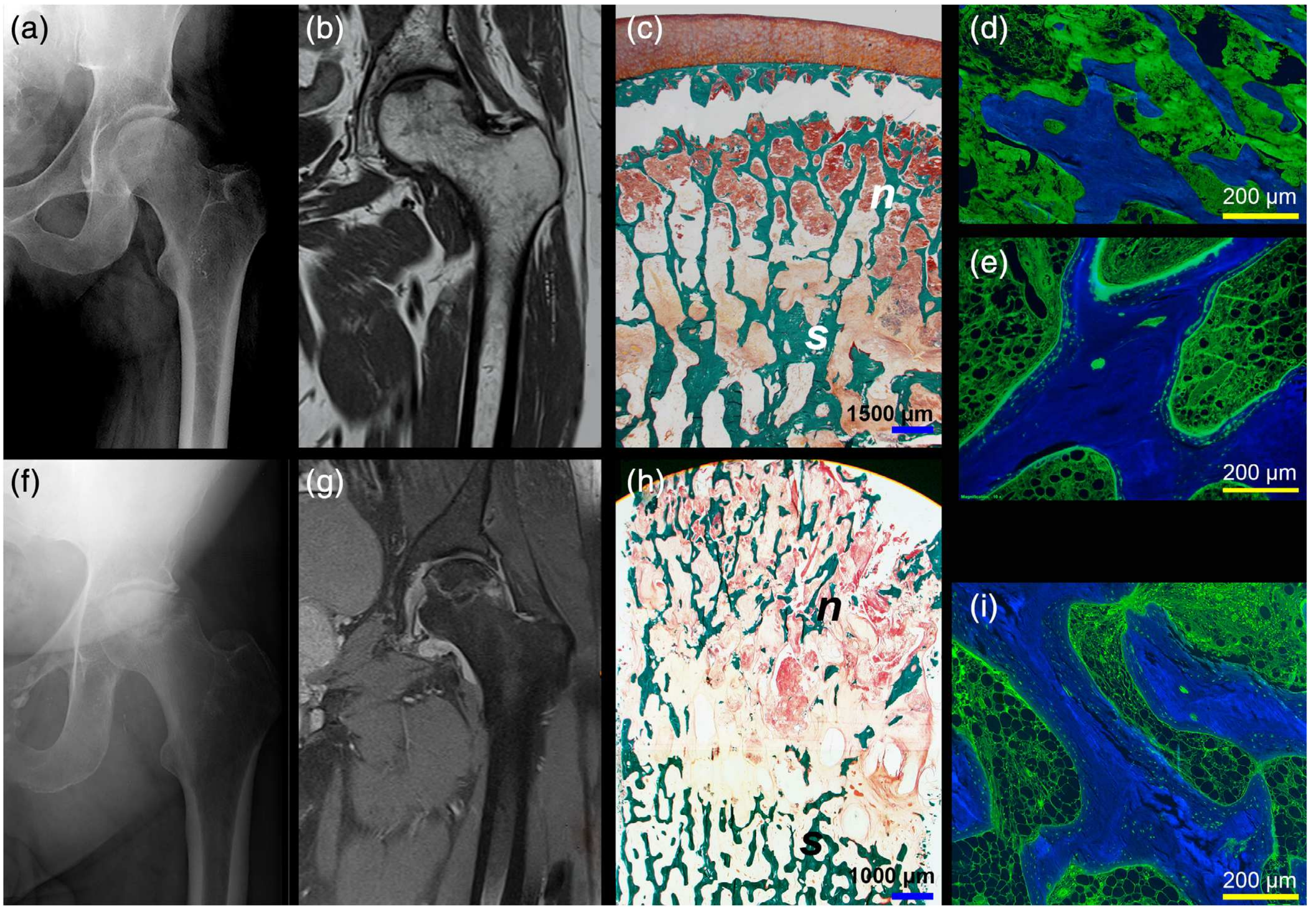

FIGURE 3 X-ray and MRI findings with the corresponding histological images in two cases of aseptic osteonecrosis of the hip. Upper row: (a–e) a Stage 3; lower row: (f–i) a Stage 4 according to Ficat and Arlet (Arlet, Ficat, & Durroux, 1971) and MRI classification of ARCO (Gardeniers, 1993; Sugano et al., 2002). (a) Note the crescent sign and a light loss of sphericity of femoral head. (b) The necrotic area is well evidenced under the articular cartilage in MRI. (c) Goldner-stained section of this area: the articular cartilage remained attached to the subchondral bone that is fractured from the trabecular network of the hip. An area of necrosis (*n*) is observed with presence of granular and acellular material in the medullary spaces; under the necrotic area, a zone of osteosclerosis is observed with enlarged trabeculae and fibrosis of the medullary spaces (*s*). (d) Fluorescence microscopy after rhodamine staining in the necrotic area, note the complete absence of osteocytes in the bone matrix.
(e) Fluorescence microscopy after rhodamine staining in the condensed area, note the absence of osteocytes in the central core of the trabeculae and the presence of newly apposed bone structure units rich in osteocytes at the surface of this dead area. Note the fibrotic marrow cavities. (f) The femoral articular surface is flattened with narrowing of the joint-space, collapse of the femoral head, and marginal osteophytes. (g) The large necrotic area is well defined on the MRI section. (h) Very low magnification of the necrotic zone (the articular cartilage has detached). The necrotic area (*n*) is well evidenced; it extends down to 8 mm under the articular surface, and then an area of osteosclerosis with enlarged trabeculae is observed (*s*). Two micrographs at low magnification (×0.5) have been stitched. (i) Fluorescence microscopy after rhodamine staining in the condensed area, note the absence of osteocytes in the central part of the trabeculae, the presence of newly apposed bone structure units, and the fibrotic marrow. MRI, magnetic resonance imaging

incorporated into the epoxy resin used to embed the bony samples, and fluorescence microscopy was used to detect the canaliculi filled with the doped resin (Baylink & Wergedal, 1971). The organization of the osteocyte network was carefully described by using rhodamine for en-bloc staining horse bones and analysis with fluorescence microscopy (Kerschnitzki et al., 2011; Kollmannsberger et al., 2017). Rhodamine B is a fluorescent stain which is recommended to stain mycobacteria in sputum (Churukian, 1991) and has also been used in other biomedical applications (Horobin, 2002). In another study on in the influence of microcracks on osteocyte apoptosis, another fluorochrome (basic fuchsin) was used to stain en-bloc the bone followed by a confocal analysis of tissue slabs (Colopy et al., 2004). To our knowledge, this study is the first attempt to use rhodamine to identify osteocytes in tissue sections from patients with bone diseases. We could easily identify the necrotic areas from the living ones by using a routine fluorescent microscope. In addition, the blocks can also be used with confocal microscopy if more focalized observations are necessary. The present method is much simpler than the technique proposed by Wong et al., which requires the use of fresh bone for the histochemical demonstration of lactico deshydrogenase activity in living osteocytes. The findings obtain in the present study are similar and identify dead osteocytes in the central part of enlarged trabeculae from osteoarthritic patients.

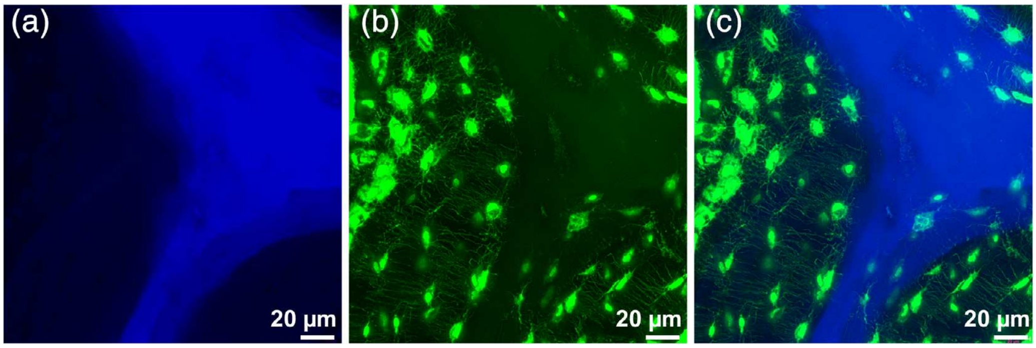

FIGURE 4 Confocal microscopy of a pMMA block from a patient with osteonecrosis. (a) Autofluorescence of the bone matrix. (b) Fluorescence of the rhodamine converted in green to improve visibility of the osteocyte canaliculi. (c) Composite image showing the lacuna–canalicular network, the presence of a small central area of bone matrix lacking osteocytes or with apoptotic osteocytes. pMMA, poly(methyl methacrylate)

ACKNOWLEDGMENTS

This work was made possible by grants from Angers CHU (University hospital). Mrs. N. Gaborit and S. Lemière are thanked for their technical help. They also wish to thank all the orthopedic surgeons from our hospital who were involved in the recruitment of the patients: Dr. Florian Ducellier, Vincent Steiger, Augustin Coupry, Nicolas Ruiz, and Dr. Romain Lancigu. This study was funded by the CHU d'Angers, project MOCONA.

CONFLICT OF INTEREST

The authors declare no potential conflict of interest.

ORCID

Daniel Chappard https://orcid.org/0000-0002-5886-9513

REFERENCES

Arlet, J., Ficat, P., & Durroux, R. (1971). Anatomo-clinical (radiological and etiological) forms of so-called primary chronic ischemia and osteonecrosis of the upper femoral epiphysis. *Revue du Rhumatisme et des Maladies Ostéo-Articulaires*, *38*(1), 41–49.

Baylink, D., & Wergedal, J. (1971). Bone formation by osteocytes. *American Journal of Physiology*, *221*(3), 669–678.

Beebe, K. (2000). Alcohol/xylene: The unlikely fixative/dehydrant/clearant. *Journal of Histotechnology*, *23*, 45–50.

Bellido, T. (2014). Osteocyte-driven bone remodeling. *Calcified Tissue International*, *94*(1), 25–34.

Bloch, S. L., & Sørensen, M. S. (2010). The viability and spatial distribution of osteocytes in the human labyrinthine capsule: A quantitative study using vector-based stereology. *Hearing Research*, *270*(1–2), 65–70.

Bonewald, L. F. (2011). The amazing osteocyte. *Journal of Bone and Mineral Research*, *26*(2), 229–238.

Bonewald, L. F. (2017). The role of the osteocyte in bone and nonbone disease. *Endocrinology & Metabolism Clinics of North America*, *46*(1), 1–18. https://doi.org/10.1016/j.ecl.2016.09.003

Calder, J., Pearse, M., & Revell, P. (2001). The extent of osteocyte death in the proximal femur of patients with osteonecrosis of the femoral head. *The Journal of Bone and Joint Surgery. British Volume*, *83*(3), 419–422.

Catto, M. (1965). A histological study of avascular necrosis of the femoral head after transcervical fracture. *The Journal of Bone and Joint Surgery. British Volume*, *47*(4), 749–776.

Chappard, D. (2014). Technical aspects: How do we best prepare bone samples for proper histological analysis? In D. Heymann (Ed.), *Bone cancer: Progression and therapeutic approaches* (2nd ed., pp. 111–120). London, UK: Academic Press.

Churukian, C. J. (1991). Demonstration of mycobacteria: A brief review with special emphasis on fluorochrome staining. *Journal of Histotechnology*, *14*(2), 117–121.

Colopy, S., Benz-Dean, J., Barrett, J., Sample, S., Lu, Y., Danova, N., … Muir, P. (2004). Response of the osteocyte syncytium adjacent to and distant from linear microcracks during adaptation to cyclic fatigue loading. *Bone*, *35*(4), 881–891.

Findlay, D. (2007). Vascular pathology and osteoarthritis. *Rheumatology*, *46*(12), 1763–1768.

Gardeniers, J. (1993). The ARCO perspective for reaching one uniform staging system of osteonecrosis. In S. A. J. Arlet, J. Gardeniers, & S. Hughes (Eds.), *Bone circulation and vascularization in normal and pathological conditions* (pp. 375–380). New York, NY: Plenum Press.

Goldring, S. R., & Goldring, M. B. (2016). Changes in the osteochondral unit during osteoarthritis: Structure, function and cartilage-bone crosstalk. *Nature Reviews Rheumatology*, *12*(11), 632–644. https://doi.org/10.1038/nrrheum.2016.148

Gundersen, H. J. G., Jensen, E. B. V., Kieu, K., & Nielsen, J. (1999). The efficiency of systematic sampling in stereology—Reconsidered. *Journal of Microscopy*, *193*(3), 199–211.

Horobin, R. W. (2002). Xanthenes. In R. W. Horobin & J. A. Kiernan (Eds.), *Conn's biological stains, a handbook of dyes, stains and Fluorochromes for use in biology and medicine* (10th ed., pp. 219–252). Oxford, UK: BIOS Scientific Pub. Ltd.

Humphreys, S., Spencer, J., Tighe, J., & Cumming, R. (1989). The femoral head in osteonecrosis. A quantitative study of osteocyte population. *The Journal of Bone and Joint Surgery. British Volume*, *71*(2), 205–208.

Kerschnitzki, M., Wagermaier, W., Roschger, P., Seto, J., Shahar, R., Duda, G. N., … Fratzl, P. (2011). The organization of the osteocyte network mirrors the extracellular matrix orientation in bone. *Journal of Structural Biology*, *173*(2), 303–311.

Khoury, B. M., Bigelow, E. M., Smith, L. M., Schlecht, S. H., Scheller, E. L., Andarawis-Puri, N., & Jepsen, K. J. (2015). The use of nano-computed tomography to enhance musculoskeletal research. *Connective Tissue Research*, *56*(2), 106–119.

Kollmannsberger, P., Kerschnitzki, M., Repp, F., Wagermaier, W., Weinkamer, R., & Fratzl, P. (2017). The small world of osteocytes:

Connectomics of the lacuno-canalicular network in bone. *New Journal of Physics*, *19*(7), 073019.

Lespasio, M. J., Sodhi, N., & Mont, M. A. (2019). Osteonecrosis of the hip: A primer. *The Permanente Journal*, *23*, 18–100. https://doi.org/10.7812/tpp/18-100

Lichtman, J. W., & Conchello, J.-A. (2005). Fluorescence microscopy. *Nature Methods*, *2*(12), 910–919.

Romanello, M., & D'Andrea, P. (2001). Dual mechanism of intercellular communication in HOBIT osteoblastic cells: A role for gap-junctional hemichannels. *Journal of Bone and Mineral Research*, *16*(8), 1465–1476.

Shah, K. N., Racine, J., Jones, L. C., & Aaron, R. K. (2015). Pathophysiology and risk factors for osteonecrosis. *Current Reviews in Musculoskeletal Medicine*, *8*(3), 201–209. https://doi.org/10.1007/s12178-015-9277-8

Sugano, N., Atsumi, T., Ohzono, K., Kubo, T., Hotokebuchi, T., & Takaoka, K. (2002). The 2001 revised criteria for diagnosis, classification, and staging of idiopathic osteonecrosis of the femoral head. *Journal of Orthopaedic Science*, *7*(5), 601–605.

Trueta, J. (1963). The role of the vessels in osteogenesis. *The Journal of Bone and Joint Surgery. British Volume*, *45*(2), 402–418.

Vatsa, A., Breuls, R. G., Semeins, C. M., Salmon, P. L., Smit, T. H., & Klein-Nulend, J. (2008). Osteocyte morphology in fibula and calvaria—Is there a role for mechanosensing? *Bone*, *43*(3), 452–458.

How to cite this article: Rony L, Perrot R, Hubert L, Chappard D. Osteocyte staining with rhodamine in osteonecrosis and osteoarthritis of the femoral head. *Microsc Res Tech*. 2019;82:2072–2078. https://doi.org/10.1002/jemt.23379

Le deuxième travail a analysé de manière plus précise la microarchitecture du tissu-osseux au cours de l'ONA en utilisant la microCT (microtomographie aux rayons X comportant une identification du cartilage articulaire après imprégnation par un métal) et l'analyse en microscopie photonique et en utilisant la coloration décrite précédemment.

La microarchitecture du tissu osseux de l'ONA est mal connue, ainsi que la relation entre l'os trabéculaire sous-jacent au cartilage et le cartilage. L'utilisation de la microCT a permis une analyse de la microarchitecture osseuse montrant à distance un os trabéculaire sain avec des travées normales avec une zone de travées denses en périphérie de la zone nécrotique. Son utilisation permet une analyse fine de l'os trabéculaire ; cependant, le cartilage hyalin articulaire étant principalement composé d'eau, il a été nécessaire d'utiliser une coloration à l'acide phosphotungstique qui rend le cartilage-radio-opaque (125, 136). L'analyse microCT de différents échantillons de tête fémorale a pu préciser les rapports entre le cartilage et l'os trabéculaire sous-jacent. Comme dit précédemment, le cartilage garde sa forme et une épaisseur assez importante et ce même à des degrés avancés de la pathologie et nous avons pu re-décrire les stades de lésions cartilagineuses. L'utilisation de la coloration de Goldner a permis de confirmer les analyses microCT avec un cartilage qui garde longtemps sa forme et ses propriétés et son épaisseur (115, 137). On peut observer des plages de résorption de l'os trabéculaire avec dans les stades les plus avancées une disparition complète des travées osseuses sous-jacentes. La coloration au bleu de toluidine a permis d'observer un phénomène de modelage - et non de remodelage - avec une apposition directe de nouvelles unités de structure osseuses à la surface de travées osseuses anciennes nécrotiques dont les ostéocytes avaient disparu (123, 138) Ceci est donc un phénomène de modelage comme visible dans le squelette fœtal, les cals fracturaires et les métaplasies osseuses d'origine tumorale (24, 139-141). Ce phénomène n'est donc pas un phénomène de remodelage osseux avec couplage ostéoclastes-ostéoblastes mais un phénomène de modelage pur (avec un découplage ostéoblastes-ostéoclastes) où une BSU commence sans qu'il n'y ait eu de résorption préalable (15, 142-144).

Classiquement, l'ONA de la tête fémorale est traitée soit par des méthodes conservatrices dans les stades et 1 et 2 de Arlet et Ficat soit par des arthroplasties totales de hanche (THA) dans les stades 3 et 4. A l'heure actuelle, de nouvelles techniques basées sur l'utilisation de cellules souches ont fait preuve de leur efficacité dans la prise en charge des stades précoces de l'ONA (145-147). Même si les arthroplasties totales de hanche ont une durée de vie qui augmente avec des taux de complications qui ont diminué au cours des dernières années, elles n'en demeurent pas moins une intervention majeure (148-151). L'ONA reste une pathologie qui touche le sujet jeune et pour laquelle des alternatives au traitement chirurgicale pourraient être intéressantes. Cette étude permet d’améliorer la compréhension de la physiopathologie de cette pathologie à l’échelle tissulaire.

ARTICLE 8

Necrosis of the femoral head, X-ray microtomography (microCT) and histology of retrieved human femoral heads

Ostéonécrose de la tête fémorale, microtomographie aux rayons X (microCT) et histologie de têtes fémorales humaines

Louis RONY, Daniel CHAPPARD

Morphologie 105 : 134-42 (2021)

Cite Score : 2,1 – SIGAPS : NC

Morphologie 105 (2021) 134—142

Disponible en ligne sur
ScienceDirect
www.sciencedirect.com

Elsevier Masson France
EM|consulte
www.em-consulte.com

MORPHOLOGIE
Bulletin de l'Association des Morphologistes

ORIGINAL ARTICLE

Necrosis of the femoral head, X-ray microtomography (microCT) and histology of retrieved human femoral heads

Ostéonécrose de la tête fémorale, microtomographie aux rayons X (microCT) et histologie de têtes fémorales humaines

L. Rony, D. Chappard*

GEROM — Groupe études remodelage osseux et biomatériaux, LHEA, Université d'Angers, CHU d'Angers, 49933 Angers cedex, France

KEYWORDS
Osteonecrosis ;
Femoral head ;
MicroCT ;
Modeling ;
Remodeling ;
Osteocytes

Summary Aseptic osteonecrosis of the hip (AON) is a rare, but well-known pathology in rheumatology and orthopedic surgery that is a necrosis of the articular cartilage secondary to a necrosis of the subchondral bone. The microscopic aspect is well known, but the microCT aspect has never been reported or correlated with histopathological findings. The objective of this study was to improve the knowledge of the pathophysiology of AON using histochemistry and microCT. One hundred and sixty femoral heads with stage 3 or 4 AON were analyzed: one half of the head was sent for microCT analysis after impregnation with phosphotungstic acid (PTA) and the other half was used for histological analysis without decalcification. The microCT analysis provides relevant information on the cracked articular cartilage and the relationship with the necrotic subchondral trabecular bone well illustrated on three videos. In histology, Goldner's trichrome showed that the articular cartilage remains well preserved for a long time. In addition, toluidine blue staining reveals a modeling process, i.e. the apposition of new bone without prior resorption by osteoclasts. Rhodamine B staining (fluorescence analysis) reveals that the osteonecrotic trabeculae and subchondral bone were devoid of osteocytes. Areas of peri-necrotic osteosclerosis are due to direct bone formation on the surface of pre-existing necrotic trabeculae.

Résumé L'ostéonécrose aseptique de la hanche (ONA) est une pathologie rare, mais bien connue en rhumatologie et en chirurgie orthopédique. C'est une nécrose du cartilage articulaire secondaire à une nécrose de l'os sous-chondral. L'aspect microscopique est bien connu, mais l'aspect microCT n'a jamais été rapporté ni corrélé avec les résultats histopathologiques.

---

[*] Corresponding author.
Adresse e-mail : daniel.chappard@univ-angers.fr (D. Chappard).

https://doi.org/10.1016/j.morpho.2021.02.008

L'objectif de cette étude était d'améliorer la connaissance de la physiopathologie des ONA en utilisant une méthode histochimique et la microCT. Cent soixante têtes fémorales avec des ONA de stade 3 ou 4 ont été analysées : une moitié de la tête était employée pour une analyse microCT après imprégnation à l'acide phosphotungstique (PTA) et l'autre moitié était utilisée pour analyse histologique sans décalcification. L'analyse microCT a donné des informations pertinentes sur le cartilage articulaire fissuré et sur la relation avec l'os trabéculaire nécrotique sous-chondral bien visualisé sur trois vidéos fournies en annexe. En histologie, le trichrome de Goldner a montré que le cartilage articulaire restait bien préservé pendant longtemps. De plus, la coloration au bleu de toluidine a révélé un processus de modelage, c'est-à-dire l'apposition d'os nouveau sans résorption préalable par les ostéoclastes. La coloration à la rhodamine B (analysée en fluorescence) a révélé que les travées ostéonécrotiques et l'os sous-chondral étaient dépourvus d'ostéocytes. Les zones d'ostéosclérose péri-nécrotique sont dues à un modelage osseux direct sur la surface de travées nécrotiques pré-existantes.

Introduction

Aseptic osteonecrosis of the hip (AON) is a rare, but well-known pathology in rheumatology and orthopedic surgery. AON of the femoral head is a lesion characterised by the death of osteocytes occurring after major vascular changes [1]. The evolution may lead to hip osteoarthritis, which requires total hip arthroplasty in most cases. Many risk factors have been identified [2]. Today, there are different treatments depending on the degree of the disease as it will be presented by others in this thematic issue of *Morphologie*. The evolution of AON in four radiological stages is well known. In the early stages (1 to 2 of the Arlet and Ficat radiographic classification [3] and 1 to 2 of the Steingerg MRI classification [4,5]), it is possible to perform conservative surgery to regenerate trabecular bone with a good quality and re-establish the support and anchor functions of hyaline articular cartilage. The articular cartilage is preserved for a long time because it is fed by the synovial liquid, but in the advance stages of the disease, the underlying osteonecrosis causes necrosis of the cartilage (Fig. 1). Currently, bisphosphonates have shown some efficacy as a medical treatment in AON at early stages of the disease (stages 1—2 of the Arlet and Ficat classification) [6]. Although total hip arthroplasty (THA) has taken a major place in the treatment of AON, there is still a place for conservative treatment, these treatments are mainly based on drilling and debridement of the necrotic area [7—10] or the injection of stem cells coming from the autologous bone marrow [11—14]. However, in advanced AON, often diagnosed at the stage of osteoarthritis, THA is the only solution [9]. Although the results of THA are excellent today, the fact remains that this procedure is non-conservative. Currently, use of Magnetic resonance imaging (MRI) is commonplace and almost systematic in clinical practice [15]. However, the micro-architectural modifications and tissue pathophysiology of AON are little studied and remain poorly known [16,17].

There are different causes for AON, such as a long-term corticosteroid therapy, a chronic alcohol intoxication, sickle cell disease and post-traumatic complications [18,19]. MRI analyses the extent of osteonecrosis; it also allows to analyze articular cartilage and its degree of alteration [20]. Nevertheless, it does not allow to correctly analyze the modification of trabecular bone of the femoral head, and in particular, loss of sphericity of the head. CT analysis remains rare in clinical practice. Microscopic aspect is also well known, but microCT aspect has never been reported nor correlation with histopathological findings.

The objectives of the present study were to improve knowledge of pathophysiology of AON and bone remodeling using a recently described histochemical method for identification of living osteocytes and to describe bone microCT microarchitecture lesions of the whole femoral head according to the four stages of the Arlet and Ficat classification.

Material and methods

Patients

Between January 2013 and December 2019, 133 patients: 45 women (34%) for 88 men (66%) were operated for a femoral head AON. Femoral heads were collected prospectively after the patients gave their informed consent to participate in the study; 160 femoral heads were analyzed, because 27 patients have a bilateral AON.

The mean age was 63.8 ± 12.3 years [22—95]. Etiologies encountered in this series are illustrated on Fig. 2. At time of diagnosis, 69 patients (51.8%) were non-smokers, 16 (12%) had been smokers for less than 3 years, and 48 (36%) had been active smokers. At time of surgery, 53 patients (40.8%) were Arlet and Ficat stage 3 and 80 patients (60.1%) had stage 4. MRI was more often requested in stage 3: 30 of the 53 patients (56.6%) had an MRI, whereas for stage 4, only 6 patients had had one (7.5%).

Femoral heads were sent to our laboratory fixed with formalin. They were sawed by the middle with a banding saw.

MicroCT analysis

A hemi-head was post-fixed for one week in phosphotungstic acid (PTA), a procedure that renders radiolucent cartilage opaque to X-rays [21,22]. In a preliminary series, a period of one week was necessary to completely impregnate

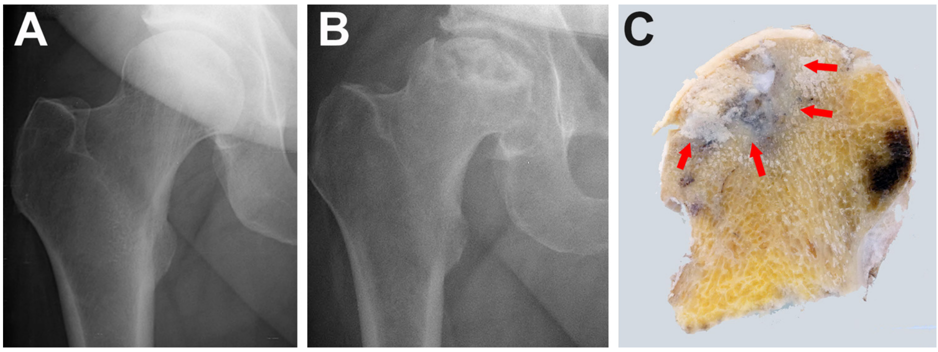

Figure 1 A. X-ray imaging of a control patient. B. X-ray of a patient with AON. Note the difference of head sphericity with A. C. Macroscopic aspect of a femoral head with AON, sectioned by the middle. The osteonecrotic zone is surrounded by red arrows.

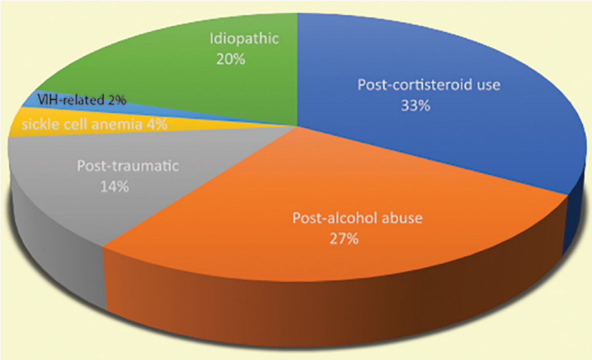

Figure 2 The main etiologies encountered in this series of 133 cases.

a large piece, such as a femoral half head. MicroCT was performed on a Skyscan-1272 system equipped with a microfocus X-ray tube (Bruker microCT, Kontich, Belgium) after having rinsed the samples in tap water to eluate the unbound PTA. The hemi-femoral heads were placed in a large plastic disk filled with tap water to avoid desiccation. Image acquisitions were done at 100 kV, 100 µA, pixel size corresponding to 26.47 µm, with 180° rotation and exposure with a 0.11 mm Cu filter. Multiple camera position facility was used and usually 4 to 6 fields were stitched to analyze a hemi-femoral head (size 28—50 mm in diameter). The total acquisition time for a femoral head varied between 6 and 9 hours. Cross-section 2D images of the samples were reconstructed from the projection images using a modified Feldkamp cone-beam algorithm, implemented in the NRecon software (Bruker release 1.7.3.0). For each hemi-femoral head, a stack of 2D-sections was obtained in indexed grey levels ranging from 0 to 255. Three-dimensional reconstructions were obtained using the CTVox software (Bruker, release 3.0) that provided images of the inner bone microarchitecture in 3D and visualized the radiopaque articular cartilage. Movies of the full hemi-head were obtained with CTVox.

Histological analysis

The other hemi-head was used to harvest a sample in the superior part of femoral head, in the area of the main compressive group of trabeculae. Samples included the bone surface (with articular cartilage when present), the subchondral bone, the osteonecrotic areas (when present), the condensed bone area and the remaining trabeculae of the head. Samples, usually 28 × 15 mm, were stained ''en bloc'' with rhodamine to make osteocytes fluorescent under UV light microscopy as previously described in this laboratory [23]. Staining occurred in the fridge during one week in a mixture containing:

- rhodamine B: 2 g;
- 10% formalin: 100 mL.

Rhodamine B was obtained from Sigma (France) CAS number: 81-88-9, CI 45170. This fluorochrome was chosen from a battery of dyes that can mark the cytoplasm of osteocytes and allow their precise detection under fluorescence microscopy.

Blocks were then rapidly dehydrated and defatted in a mixture combining acetone and xylene in the same time [24]. Bone samples were infiltrated by MMA (methyl methacrylate) under a gentle constant agitation, which considerably shortened the infiltration time [25]. Embedding was done in cold by using polyethylene molds (Peel-a-Way embedding system, Polyscience Inc., Warrington PA). Sections were obtained at 7 µm using a heavy-duty microtome (e.g., Leica, Polycut-S) equipped with 50—60° tungsten carbide knives for histology. They were stained by Goldner trichrome for analysis of osteoid tissue and mineralized bone matrix; toluidine blue at pH 4.3 for imaging bone cells under bright field microscopy and cement/arrest lines and mounted in NeoEntellan (Merck) or without further treatment for analysis of osteocytes under fluorescence microscopy. Sections were analyzed with an Olympus BX51 microscope equipped for bright field and for fluorescence microscopy with the following cubes: U-MWIB3 excitation filter 460—495 nm, emission filter 510 nm, dichromatic mirror 505 nm to detect rhodamine-stained cells in green and U-MNU2; excitation filter 360—370 nm, emission filter 420 nm, and dichromatic mirror 400 nm to study blue autofluorescence of bone matrix. Methodology to obtain combined images is fully described elsewhere [23].

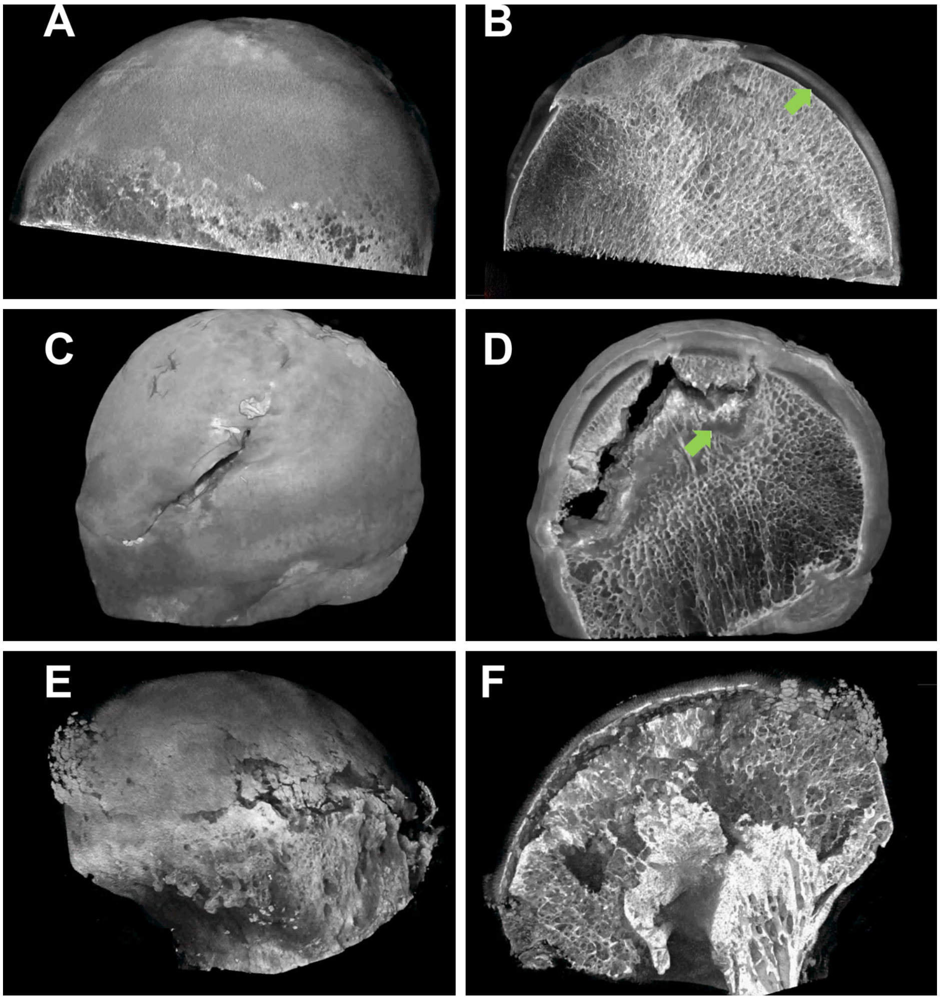

Figure 3 MicroCT analysis after PTA staining of the articular cartilage. A. Initial stage of AON, external view. B. Same sample, internal view with cartilage detachment (arrow). C. A more advanced stage with cartilage crack on the external view. D. Same sample with subchondral bone necrosis and fibrosis (arrow). E. Advanced stage of AON with loss of sphericity of the head and necrosis of the articular cartilage with (F) massive areas of bone necrosis and perinecrotic sclerosis.

Results and discussion

MicroCT analysis

A significant advance in bone field arose with the development of microCT around the 2000s. Unfortunately, microCT is only suitable for tissues with high inherent X-ray contrast, such as bone or grafting biomaterials [26—28]. Because soft tissues, such as articular cartilage, are non-mineralized, they are radiolucent, making them not visible with microCT. The use of a contrast agent is long recognised in X-ray analysis of non-bony tissues [29]. PTA rendered articular cartilage radio-opaque, and sometimes fibrotic areas were also faintly labeled due to deposition of tungsten in collagen fibers. Several other metal salts have been proposed to stain cartilage [30—33], but we failed to obtain suitable results excepted with uranyl acetate [21]. However, this metal accurately marks thin articular cartilages, such as those of the rat mandibular condyle, but it is expensive and cannot be used on large volume specimens. PTA used here was proposed by Metscher and allows a labeling of cartilage of femoral heads in one week, allowing a good analysis of bone-cartilage relationships [22]. In the present study, relationships between articular cartilage and bone were clearly analyzed by microCT in the different stages of AON on these very large bone samples (Fig. 3). Articular cartilage and subchondral bone were often detached from the more profound trabecular network in the first stages of the disease. These subchondral fractures progressively cause the articular surface to be destroyed, leading to the collapse of the femoral head [34]. In later stages, cartilage cracks were clearly evidenced at the surface of the femoral heads together with fractures and condensation of bone trabeculae around the necrotic areas. The video movies clearly evidenced the progression of the cartilage and bone defects deep inside the whole hemi-heads (see supplementary information). The videos give additional information compared to the images, as it is possible to analyze femoral heads in depth and highlight deep lesions that did not appear on a single section slice. Necrotic areas and the densified trabeculae

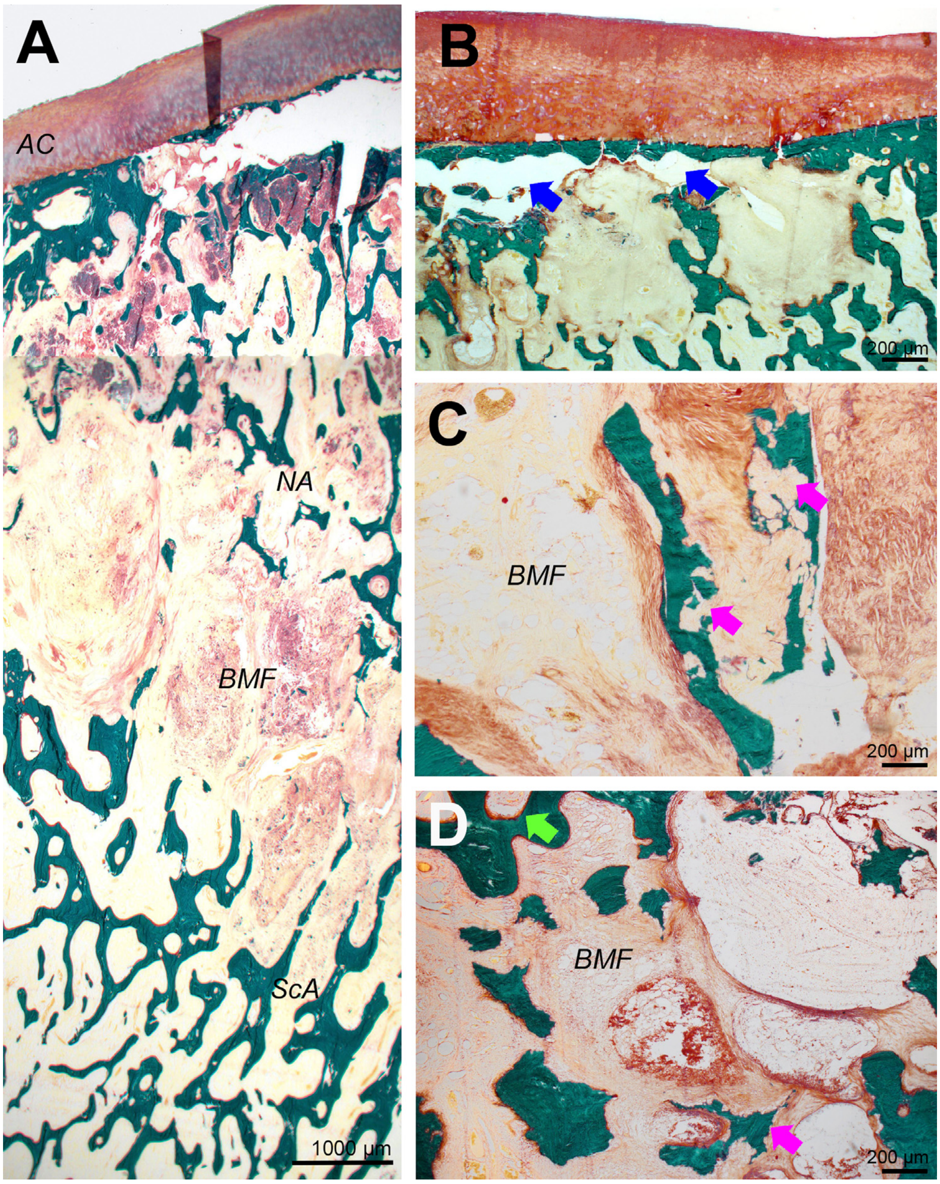

Figure 4 Histologic analysis with Goldner trichrome on undecalcified bone specimens. A. Photomontage of several micrographs starting from the articular cartilage (*AC*), the necrotic area (*NA*) with areas of bone marrow fibrosis (BMF) and the area of sclerotic trabeculae (*ScA*) in the depth of the sample. Note the articular cartilage detachment from the subchondral bone. B. Enlargement of a stage 1 patient with unaltered articular cartilage anchored on the subchondral bone and detachment (blue arrows) from the deep planes with areas of necrotic fibrosis. C. Necrotic zone showing the presence of numerous deep areas of scalloped osteoclastic resorption (pink arrows) surrounded by collagenous fibrosis. D. Demarcation zone between the necrotic region (on the bottom of the image — containing trabeculae with clear signs of osteoclastic resorption and fibrosis) and the area of osteosclerosis, whose trabeculae are thickened and covered with osteoid borders (green arrow). Note the presence of enlarged capillary sinusoids filled with blood.

were readily observed. Occasionally, some geodes can be encountered. However, as reported in conventional X-ray imaging, it is not possible to distinguish dead from living bone; only the enlarged trabeculae of the sclerosing area can be recognized. There are few articles in literature that have focused on the microarchitecture of trabecular bone in AON using microCT [16,35]. They have used areas harvested from specimens located in various locations (necrotic, sclerotic, compressive and tensile zone). These microCT studies never presented an analysis of bone-cartilage relationships or a global view of a femoral hemi-head.

Histological analysis

Goldner trichrome

On histological sections stained by Goldner's trichrome, the articular cartilage remains well preserved for a long time due to its nutrition by the synovial fluid. In the later stages of the disease, the articular cartilage presents extensive signs of fibrillation and finally disappeared [5,34,36]. Same images corresponding to those described on X-ray films and microCT images were observed with the occurrence of cartilage detachment and cracks, necrotic areas with marked fibrosis and peri-necrotic bone condensations (Fig. 4). Fig. 4A illustrates, on a large photomontage, the different zones from the growth cartilage to the living zones in the depth. Necrotic areas presented bone trabeculae disconnected from the trabecular network and the subchondral bone (Fig. 4B), often with large polycyclic resorption patterns [20]. Medullary spaces were filled with clumps of acellular granular material corresponding to adipocyte necrosis, and in places, there was an acellular edematous fibrotic area [37]. Remodeling of this necrotic zone is then done by complete resorption of trabeculae (leading to geodes) (Fig. 4C) and appearance of large dense collagen bundles with distended medullary sinusoids (Fig. 4B and C). Presence of clusters of inflammatory cells (polynuclear or lympho-plasmocytic cells) was never noted. The demarcation zone between the necrotic and sclerotic zones is progressive (Fig. 4D). The sclerotic trabeculae were thickened and have numerous osteoid seams on their surface. In these areas, the medullary spaces contained a looser fibrosis, which was highly vascularised by numerous dilated sinusoid capillaries. Finally, more deeply, bone network with a normal microarchitecture, made of thinner trabeculae directed along axis of the main femoral head bundles was encountered.

Toluidine blue staining

Toluidine blue staining was found much more accurate for analyzing cellular elements occurring in the osteosclerosis area. Near the demarcation zone between necrotic/osteosclerotic bones, the thickened trabeculae were often covered with numerous pseudo-epithelial alignments of osteoblasts that appose new bone structure units (BSU) onto surface of old trabeculae (Fig. 5A). Difference between old bone and newly affixed BSUs was sharply defined: it seems that osteocytes have disappeared in old bone, forming the centre of trabecula [38—40]. The most important finding always noted in this series of AON was that the interface between these two areas was represented by a smooth cement-line (Fig. 5B). This is characteristic of a modeling process, i.e. the apposition of new bone without prior resorption by osteoclasts [41]. Bone modeling phenomena are rare in adults. They can be observed in the development of the fetal skeleton, in areas of fast-growing bone (such as in contact with a biomaterial, in tumor bone metaplasia, in a fracture callus and in cases of mini-modeling) [42—44]. In this series of patients, modeling was consistently found. Apposition of new bone onto surface of old trabeculae has already been shown during AON and also osteoarthrosis on sections of decalcified bone [20,39,40,45—47]. However, it had not been noticed that this was a pure modeling process related to reactivation of lining cells and their transformation into active osteoblasts. Also, the possibility of double tetracycline labeling was not possible in this series of patients due to ethical reasons, presence of extended osteoblast alignments with numerous of thick osteoid seams clearly indicate a net apposition of new bone in sclerosis area.

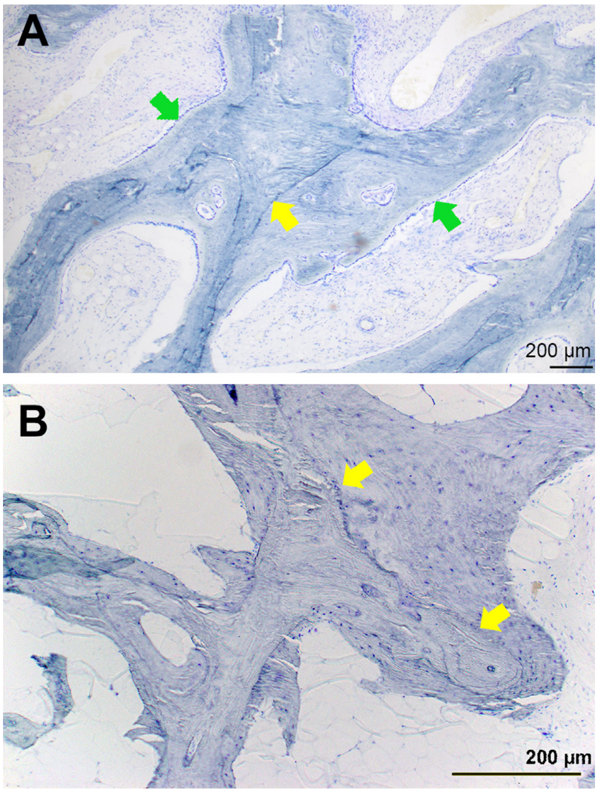

Figure 5 Histologic analysis of the sclerosing area stained with toluidine blue on undecalcified bone specimens. A. The trabeculae are enlarged and have numerous osteoblast borders with pseudo-epithelial arrangement (green arrows). These osteoblasts have applied new bone structure units onto a pre-existing bone core without prior osteoclastic resorption as shown by the smooth cement-line (yellow arrow). B. Larger magnification showing the smooth boundary (yellow arrows) between the old trabecula (without osteocytes) and the new BSU with numerous osteocytes.

Rhodamine B staining

Fig. 6 illustrates identification of osteocytes on ''en bloc'' non-decalcified bone. Articular cartilage matrix is heavily stained together with cell body of living osteocytes and marrow cells [23]. A histological section from a control healthy bone appears on Fig. 6A for comparison. Osteonecrotic trabeculae and sub-chondral bone are lacking osteocytes (Fig. 6B—C) and the demarcation zone between necrotic/living bones is clearly evidenced (Fig. 6D). In the osteosclerosis area, the enlarged trabeculae presented a central core with bone structure units lacking osteocytes while the recently apposed BSU contained numerous osteocytes (Fig. 6E—F). It should also be noted that the central parts of these trabeculae have a stronger blue autofluorescence than the recently apposed BSUs. This is due to the collagen properties of the bone matrix, which becomes more autofluorescent upon aging, with a simultaneous increase in degree of mineralisation [48]. This explains the results observed with Raman microspectroscopy that found and

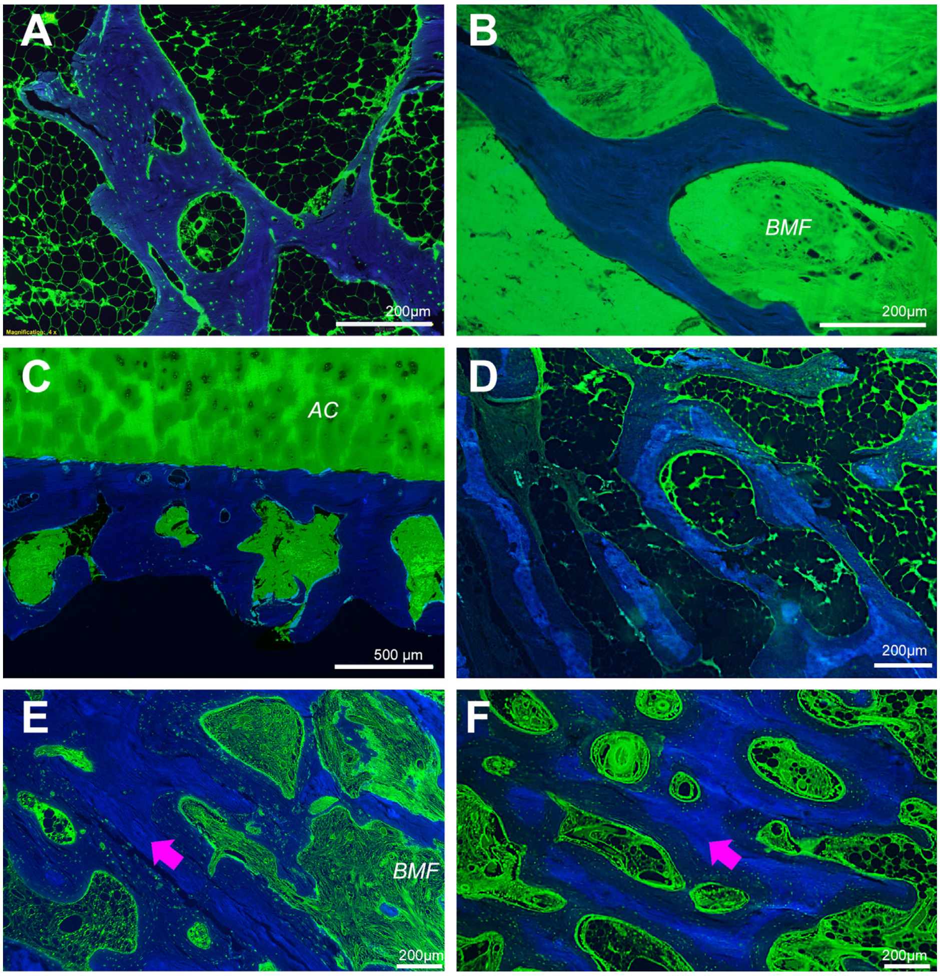

Figure 6 Histologic analysis after staining with rhodamine on undecalcified bone specimens analyzed under fluorescence microscopy. A. Control bone from a normal patient showing numerous osteocytes (green) buried in the autofluorescent blue matrix. Note that living cells from the bone marrow cells are also stained. B. Trabeculae from the osteonecrotic area without osteocytes in the bone matrix, the fibrosis has a green autofluorescence. C. Presence of living chondrocytes in the articular cartilage (whose matrix has a green autofluorescence), but subchondral bone does not contain living osteocytes. D. The boundary between the necrotic zone (left) where the trabeculae no longer possess osteocytes and the zone of osteosclerosis where the trabeculae begin to be covered by new osteocyte rich BSUs. E. Thickened trabeculae from the osteosclerosis zone surrounded by fibrosis (BMF) showing a trabecula whose central core (pink arrow) is devoid of osteocytes while the new BSUs contain many osteocytes. F. Another aspect showing thickened trabeculae with central cores (pink arrow) devoid of osteocytes while the new BSUs contain many osteocytes. The boundary between old and new bone is characterised by a smooth cement-line.

increase carbonate content and decrease phosphate to amide ratio in AON [49]. These observations are typically observed in newly formed bone with incomplete mineralization degree and increased carbonate substitution [48].

For recognition of osteonecrosis, it is important to clearly identify the areas devoid of osteocytes [39]. By using undecalcified sections stained with Goldner or toluidine blue, images are not enough precise to allow a clear identification of empty lacunae or living osteocytes. Furthermore, osteocytes are quite difficult to identify on decalcified sections due to considerable shrinkage of the cell body during histological preparation. Undecalcified bone embedding in pMMA is now favored for the histopathological and histomorphometric diagnosis of bone diseases. This ''en bloc'' rhodamine B method is simpler than the histochemical technique requiring use of fresh bone for the histochemical demonstration of lactico deshydrogenase activity (LDH) in living osteocytes [40]. Findings obtain in the present study are similar and identify dead osteocytes in central part of enlarged trabeculae from AON patients. The method is also more accurate than using the Hoechst 33342 intercalating fluorochrome than only stain the osteocyte nuclei [50].

Disappearance of osteocytes due to ischemia has been recognized by former authors and is interpreted as a sign of bone death [17,51]. Necrotic bone with dead osteocytes is observed associated with many disorders with osteonecrosis. Several conditions cause osteocytes to die, leading to bone destruction, sequestration, or end-stage arthritis of femoral head [19,52]. Apposition of new BSUs onto old trabeculae is also encountered is osteoarthritis [23,40].

Conclusion

In the present study, a simple method usable in routine bone histopathology to identify osteocytes and necrotic areas in bone trabeculae of AON was combined to microCT analysis and classical staining methods. MicroCT provided clear images of AON well identified on video movies. The corresponding histological changes showed the necrotic and fibrotic areas together with peri-necrotic osteosclerosis due to a direct bone modeling onto surface of pre-existing necrotic trabeculae. These findings could help optimise ONA's research and medical treatments.

Funding

This work was made possible by a grant from Angers CHU (University hospital) project MOCONA and the French Ministry of Research.

Disclosure of interest

The authors declare that they have no competing interest.

Acknowledgments

Mrs. N. Gaborit and S. Lemière are thanked for their technical help with microCT analysis. The authors also wish to thank all the orthopedic surgeons from our hospital who were involved in the recruitment of the patients: Dr. Florian Ducellier, Vincent Steiger, Augustin Coupry, Nicolas Ruiz and Laurent Hubert.

Appendix A. Supplementary data

Supplementary data associated with this article can be found, in the online version, at https://doi.org/10.1016/j.morpho.2021.02.008.

Références

[1] Lespasio MJ, Sodhi N, Mont MA. Osteonecrosis of the hip: a primer. Perm J 2019;23:1—100.
[2] Matsuo K, Hirohata T, Sugioka Y, Ikeda M, Fukuda A. Influence of alcohol intake, cigarette smoking, and occupational status on idiopathic osteonecrosis of the femoral head. Clin Orthop Relat Res 1988;234:115—23.
[3] Arlet J, Ficat P. Diagnosis of primary femur head osteonecrosis at stage 1 (preradiologic stage). Rev Chir Orthop Reparatrice Appar Mot 1968;54:637—48.
[4] Steinberg ME, Brighton CT, Corces A, Hayken GD, Steinberg DR, Strafford B, et al. Osteonecrosis of the femoral head. Results of core decompression and grafting with and without electrical stimulation. Clin Orthop Relat Res 1989;249:199—208.
[5] Steinberg ME, Steinberg DR. Classification systems for osteonecrosis: an overview. Orthop Clin North Am 2004;35:273—83 [vii—viii].
[6] Lai K-A, Shen W-J, Yang C-Y, Shao C-J, Hsu J-T, Lin R-M. The use of alendronate to prevent early collapse of the femoral head in patients with non-traumatic osteonecrosis: a randomised clinical study. JBJS 2005;87:2155—9.
[7] Castro Jr FP, Barrack RL. Core decompression and conservative treatment for avascular necrosis of the femoral head: a meta-analysis. Am J Orthop 2000;29:187—94.
[8] Marker DR, Seyler TM, McGrath MS, Delanois RE, Ulrich SD, Mont MA. Treatment of early stage osteonecrosis of the femoral head. JBJS 2008;90:175—87.
[9] Saito S, Saito M, Nishina T, Ohzono K, Ono K. Long-term results of total hip arthroplasty for osteonecrosis of the femoral head. A comparison with osteoarthritis. Clin Orthop Relat Res 1989;244:198—207.
[10] Mont MA, Carbone JJ, Fairbank AC. Core decompression versus non-operative management for osteonecrosis of the hip. Clin Orthop Rel Res 1996;324:169—78.
[11] Hernigou P, Guerin G, Homma Y, Dubory A, Chevallier N, Rouard H, et al. History of concentrated or expanded mesenchymal stem cells for hip osteonecrosis: is there a target number for osteonecrosis repair? Int Orthop 2018;42:1739—45.
[12] Hernigou P, Trousselier M, Roubineau F, Bouthors C, Chevallier N, Rouard H, et al. Stem cell therapy for the treatment of hip osteonecrosis: a 30-year review of progress. Clin Orthop Surg 2016;8:1—8.
[13] Zhao D, Cui D, Wang B, Tian F, Guo L, Yang L, et al. Treatment of early stage osteonecrosis of the femoral head with autologous implantation of bone marrow-derived and cultured mesenchymal stem cells. Bone 2012;50:325—30.
[14] Gangji V, De Maertelaer V, Hauzeur J-P. Autologous bone marrow cell implantation in the treatment of non-traumatic osteonecrosis of the femoral head: five-year follow-up of a prospective controlled study. Bone 2011;49:1005—9.
[15] Plenk Jr H, Gstettner M, Grossschmidt K, Breitenseher M, Urban M, Hofmann S. Magnetic resonance imaging and histology of repair in femoral head osteonecrosis. Clin Orthop Relat Res 2001;386:42—53.
[16] Tingart M, Beckmann J, Opolka A, Matsuura M, Schaumburger J, Grifka J, et al. Analysis of bone matrix composition and trabecular microarchitecture of the femoral metaphysis in patients with osteonecrosis of the femoral head. J Orthop Res 2009;27:1175—81.
[17] Catto M. A histological study of avascular necrosis of the femoral head after transcervical fracture. J Bone Jnt Surg Br 1965;47:749—76.
[18] Jones LC, Hungerford DS. The pathogenesis of osteonecrosis. Instr Course Lect 2007;56:179—96.
[19] Shah KN, Racine J, Jones LC, Aaron RK. Pathophysiology and risk factors for osteonecrosis. Curr Rev Musculoskelet Med 2015;8:201—9.
[20] Plenk Jr H, Gstettner M, Grossschmidt K, Breitenseher M, Urban M, Hofmann S. Magnetic resonance imaging and histology of repair in femoral head osteonecrosis. Clin Orthop Rel Res 2001;386:42—53.
[21] Kün-Darbois JD, Manero F, Rony L, Chappard D. Contrast enhancement with uranyl acetate allows quantitative analysis of the articular cartilage by microCT: application to mandibular condyles in the BTX rat model of disuse. Micron 2017;97:35—40.
[22] Metscher BD. MicroCT for comparative morphology: simple staining methods allow high-contrast 3D imaging of diverse non-mineralised animal tissues. BMC Physiol 2009;9:11.
[23] Rony L, Perrot R, Hubert L, Chappard D. Osteocyte staining with rhodamine in osteonecrosis and osteoarthritis of the femoral head. Microsc Res Tech 2019;82:2072—8.
[24] Beebe K. Alcohol/xylene: the unlikely fixative/dehydrant/clearant. J Histotechnol 2000;23:45—50.
[25] Chappard D. Technical aspects: how do we best prepare bone samples for proper histological analysis? In: Heymann D, editor. Bone cancer: progression and therapeutic approaches. 2nd Edition London: Acad. Press; Elsevier Inc; 2014. p. 111—20.

[26] Hildebrand T, Rüegsegger P. Quantification of bone microarchitecture with the structure model index. Comput Methods Biomech Biomed Engin 1997;1:15—23.

[27] Chappard D, Kün-Darbois J-D, Guillaume B. Computational fluid dynamics simulation from microCT stacks of commercial biomaterials usable for bone grafting. Micron 2020;133:102861.

[28] Salmon PL, Sasov AY. Application of nano-CT and high-resolution micro-CT to study bone quality and ultrastructure, scaffold biomaterials and vascular networks. Advanced bioimaging technologies in assessment of the quality of bone and scaffold materials. Berlin, Heidelberg: Springer; 2007. p. 323—31.

[29] Lusic H, Grinstaff MW. X-ray-computed tomography contrast agents. Chem Rev 2013;113:1641—66.

[30] Cockman MD, Blanton CA, Chmielewski PA, Dong L, Dufresne TE, Hookfin EB, et al. Quantitative imaging of proteoglycan in cartilage using a gadolinium probe and microCT. Osteoarthr Cartil 2006;14:210—4.

[31] Renders GA, Mulder L, Lin AS, Langenbach GE, Koolstra JH, Guldberg RE, et al. Contrast-enhanced microCT (EPIC-muCT) ex vivo applied to the mouse and human jaw joint. Dentomaxillofac Radiol 2014;43, 20130098.

[32] Xie L, Lin AS, Guldberg RE, Levenston ME. Non-destructive assessment of sGAG content and distribution in normal and degraded rat articular cartilage via EPIC-microCT. Osteoarthr Cartil 2010;18:65—72.

[33] Yoo HJ, Hong SH, Choi JY, Lee IJ, Kim SJ, Choi JA, et al. Contrast-enhanced CT of articular cartilage: experimental study for quantification of glycosaminoglycan content in articular cartilage. Radiology 2011;261:805—12.

[34] Fondi C, Franchi A. Definition of bone necrosis by the pathologist. Clin Cases Miner Bone Metab 2007;4:21.

[35] Ma J-X, He W-W, Zhao J, Kuang M-J, Bai H-H, Sun L, et al. Bone microarchitecture and biomechanics of the necrotic femoral head. Sci Rep 2017;7:13345.

[36] Im G-I, Kim D-Y, Shin J-H, Cho W-H, Lee C-J. Degeneration of the acetabular cartilage in osteonecrosis of the femoral head: histopathologic examination of 15 hips. Acta Orthop Scand 2000;71:28—30.

[37] Taljanovic MS, Graham AR, Benjamin JB, Gmitro AF, Krupinski EA, Schwartz SA, et al. Bone marrow edema pattern in advanced hip osteoarthritis: quantitative assessment with magnetic resonance imaging and correlation with clinical examination, radiographic findings, and histopathology. Skeletal Radiol 2008;37:423—31.

[38] Mutijima E, De Maertelaer V, Deprez M, Malaise M, Hauzeur J-P. The apoptosis of osteoblasts and osteocytes in femoral head osteonecrosis: its specificity and its distribution. Clin Rheumatol 2014;33:1791—5.

[39] Humphreys S, Spencer J, Tighe J, Cumming R. The femoral head in osteonecrosis. A quantitative study of osteocyte population. J Bone Jnt Surg Br 1989;71:205—8.

[40] Wong SY, Evans RA, Needs C, Dunstan CR, Hills E, Garvan J. The pathogenesis of osteoarthritis of the hip. Evidence for primary osteocyte death. Clin Orthop Rel Res 1987;214: 305—12.

[41] Chappard D. Modelage et remodelage au cours de l’ostéo-intégration. Rev Stomatol Chir Maxillofac Chir Orale 2013;114:159—65.

[42] Allen MR, Burr DB. Bone growth, modelling, and remodelling. Basic and applied bone biology. Elsevier; 2019. p. 85—100.

[43] Erben R. Vitamin D analogs and bone. J Musculoskelet Neuronal Interact 2001;2:59—70.

[44] Chappard D. Les cellules osseuses, le modelage et le remodelage osseux. In: Guillaume B, Audran M, Chappard D, editors. Tissu osseux et biomatériaux en chirurgie dentaire. Paris: Quintessence International; 2014. p. 21—41.

[45] Little C, Ruiz A, Harding I, McLardy-Smith P, Gundle R, Murray D, et al. Osteonecrosis in retrieved femoral heads after failed resurfacing arthroplasty of the hip. J Bone Jnt Surg Br 2005;87:320—3.

[46] Kamal KC, Alexandru DO, Rogoveanu OC, Pănuș C, Kamal D, Maria DT, et al. Immunohistochemical analysis of bone metabolism in osteonecrosis of the femoral head. Rom J Morphol Embryol 2018;59:819—24.

[47] Yamamoto T, DiCarlo E, Bullough P. The prevalence and clinicopathological appearance of extension of osteonecrosis in the femoral head. J Bone Joint Surg Br 1999;81:328—32.

[48] Chappard D, Baslé MF, Legrand E, Audran M. New laboratory tools in the assessment of bone quality. Osteoporos Int 2011;22:2225—40.

[49] Narayanan A, Khanchandani P, Borkar RM, Ambati CR, Roy A, Han X, et al. Avascular necrosis of femoral head: a metabolomic, biophysical, biochemical, electron microscopic and histopathological characterisation. Sci Rep 2017;7: 1—16.

[50] Russe P, Pascaretti-Grizon F, Aguado E, Goyenvale E, Filmon R, Baslé MF, et al. Does milling one-piece titanium dental implants induce osteocyte and osteoclast changes? Morphologie 2011;95:51—9.

[51] Trueta J. The role of the vessels in osteogenesis. J Bone Joint Surg Br 1963;45:402—18.

[52] Lespasio MJ, Sodhi N, Mont MA. Osteonecrosis of the hip: a primer. Perm J 2019;23:18—00.

Ces deux travaux réalisés à partir d'une collection de têtes fémorales humaines atteintes d'ONA permettent de mieux caractériser l'os trabéculaire dans cette pathologie. La disposition des ostéocytes dans le tissu osseux ainsi que les phénomènes de modelage (et non de remodelage) présents dans l'os trabéculaire sous-jacents laissent supposer un découplage ostéoblastes-ostéoclastes dans cette pathologie. D'autres travaux sur le sujet, notamment sur des modèles pré-cliniques, seraient intéressants pour préciser le dysfonctionnement supposé du couplage ostéoblaste-ostéclaste **(15, 142-144)**.

L'ONA de la hanche est une pathologie qui est maintenant bien connue, à l'heure actuelle, le traitement est souvent chirurgical soit conservateur avec de nouvelles techniques en cours d'exploration soit non conservateur par le biais des prothèses totales de hanche (152). Le succès de la chirurgie prothétique hanche supplante à ce jour les autres indications opératoires (146). Pour autant, les travaux réalisés permettent de comprendre que les pistes de réflexions autours de nouvelles thérapies sont possibles (147). Le phénomène de modelage observé est une des pistes de réflexion pour proposer des thérapeutiques dans le cadre du dysfonctionnement du couplage ostéoclastes-ostéoblastes.

Ce travail sur l'ONA a fait partie d'un numéro spécial de la revue Morphologie que j'ai coordonné. Tous les aspects de l'ONA, depuis le diagnostic par le rhumatologue, les aspects imagerie et les traitements ont été abordés pour les ONA de la hanche, de l'épaule mais aussi dans le cas particulier de la mandibule où les étiologies et la symptomatologie sont radicalement différentes.

EDITORIAL

Aseptic Osteonecrosis: From the rheumatologist to the surgeon

Ostéonécrose aseptique : du rhumatologueau chirurgien

Louis RONY, Daniel CHAPPARD

Morphologie 105 : 79 (2021)

Cite Score : 2,1 – SIGAPS : NC

N° 349 - Juin 2021
Volume 105 publication trimestrielle

90575
ISSN : 1286-0115

MORPHOLOGIE

Bulletin de l'Association des Morphologistes

SPECIAL ISSUE ON ASEPTIC OSTEONECROSIS
(NUMÉRO SPÉCIAL SUR L'OSTÉONÉCROSE ASEPTIQUE)
COORDINATED BY : LOUIS RONY AND DANIEL CHAPPARD

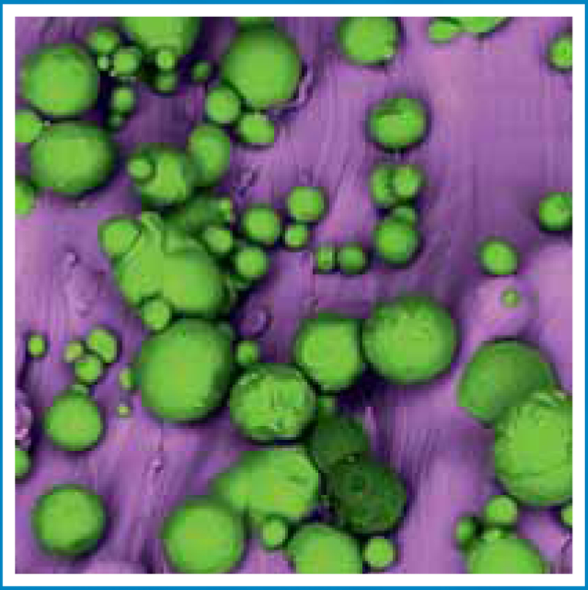

- Anatomie et organogenèse humaines et comparées
- Anthropologie
- Cytologie - Histologie - Embryologie - Cytogénétique
- Biologie de la reproduction et du développement

ELSEVIER

Morphologie (2021) **105**, v

Available online at
ScienceDirect
www.sciencedirect.com

Elsevier Masson France
EM|consulte
www.em-consulte.com

CONTENTS

Abstracted in: Current Contents/Clinical Medicine; CAB; Cardline; Embase (Excerpta Medica); Medline (Index Medicus); Pascal (INIST-CNRS); Science Citation Index; SCOPUS® and Science Direct

Special issue on Aseptic Osteonecrosis

Coordinated by Louis Rony and Daniel Chappard

Editorial

General reviews

Original articles

General review

Original articles

General review

Morphologie (2021) 105, vi

Disponible en ligne sur
ScienceDirect
www.sciencedirect.com

Elsevier Masson France
EM|consulte
www.em-consulte.com

SOMMAIRE

Cité dans : Current Contents/Clinical Medicine ; CAB ; Cardline ; Embase (Excerpta Medica) ; Medline (Index Medicus) ; Pascal (INIST-CNRS) ; Science Citation Index ; SCOPUS® et Science Direct

Numéro spécial sur l'Ostéonécrose Aseptique
Sous la direction de Louis Rony et Daniel Chappard

Editorial

Revue générales

Articles Originaux

Revue générale

Articles Originaux

General review

Morphologie 105 (2021) 79

Disponible en ligne sur
ScienceDirect
www.sciencedirect.com

Elsevier Masson France
EM|consulte
www.em-consulte.com

EDITORIAL

Aseptic osteonecrosis: From the rheumatologist to the surgeon

Ostéonécrose aseptique : du rhumatologue au chirurgien

Aseptic Osteonecrosis (AON) is a common condition that affects with a high frequency, the hip and shoulder. In this special issue, we wanted to cover all aspects of this pathology, from its rheumatological aspects, medical imaging, histopathology and surgical treatments. So, Guggenbuhl et al., (Rennes) provided the rheumatologist's vision and what to do in front of a patient consulting for AON, Tasu et al., (Poitiers) review the methods of evaluation by imaging of AON in the femoral head. Furthermore, sickle cell disease being a very particular etiology, Severyns et al. (Poitiers) go into more detail on its particularities. The various historical surgical treatments of AON of the hip are reported by Bourgoin et al., (Rennes), current surgical treatments by Ph. Massin (Paris), and perspectives by cell therapy are described by Hernigou et al., (Créteil). We present (Rony et al., Angers) the pathological aspects of hip AON in X-ray microtomography (after cartilage labeling) and histology (after histochemical detection of osteocytes). Finally, Aguado et al., (Nantes) show that Legg, Perthes Calvé disease of the dog is a good animal model.

AON at the shoulder (and its characteristics) are discussed by Lancigu et al., (Angers), the current surgical treatments are described by Le Coz et al., (Rennes) while the contribution of cell therapy is considered by Hernigou et al., (Créteil).

Finally, an exhaustive work by Kün-Darbois et al., (Angers) provides an update on osteonecrosis of the mandible, whether it is of post-radiotherapy origin or secondary to a treatment with bisphosphonates or other recently identified drugs.

All in all, this special issue is the only recent work on the subject in the literature that addresses all these topics. The various viewpoints will, we have no doubt, be of benefit to all physicians and surgeons confronted with this pathology.

D. Chappard (M.D., Ph.D)*
L. Rony
GEROM - Groupe Études Remodelage Osseux et bioMatériaux, Univ-Angers, 49933 Angers, France

* Corresponding author.
E-mail address: daniel.chappard@univ-angers.fr
(D. Chappard)

https://doi.org/10.1016/j.morpho.2021.03.002

Conclusion

A l'heure actuelle, il existe différents modèles de PTH avec des designs de tiges différents et des moyens de tenue dans l'os différents. Le couple de frottement est un élément déterminant de la prothèse totale de hanche, les couples métaux-PE ou céramique-PE sont très utilisés d'autant plus depuis que certaines techniques ont été mises au point pour limiter l'usure du PE (59, 61, 153). L'utilisation d'un couple de dur-dur est réservé au sujet jeune avec des exigences de pose plus grandes, l'utilisation de la céramique d'alumine est très utilisée dans ces indications en chirurgie prothétique de la hanche avec la réputation de ne pas libérer de particules d'usure. Nous avons pu voir que ces particules sont très fines mais qu'elles existent bien. Pour autant, elles n'entraînent pas la même réaction inflammatoire que les particules de PE. En effet, les particules d'alumine sont retrouvées dans des macrophages alors que les particules de PE sont retrouvées dans des cellules géantes bien connues dans les réactions inflammatoires chroniques. Ce constat pourrait expliquer pourquoi les descellements aseptiques dans les arthroplasties totales de hanche à couple de frottement Al-Al l'ostéolyse est bien moindre que dans les descellements aseptiques de PTH à couple de frottement utilisant du PE avec un épaississement des tissus péri-prothétiques (98).

Enfin, l'ostéointégration de biomatériaux massifs en titane est bien connue (46, 47). Les pertes de substances cavitaires et segmentaires restent un défi pour les chirurgiens orthopédistes (41, 154). Les biomatériaux à porosité interconnectés s'ostéointègrent et ceux qui sont en métal présentent l'avantage d'apporter une résistance mécanique. Pour autant, ces biomatériaux métalliques ne s'ostéointègrent que sur les premiers microns à l'interface os-métal (45). L'architecture de ces biomatériaux est généralement géométrique ne reproduisant pas ce que la nature produit (105). Néanmoins, les biomatériaux utilisés ici qui reproduisaient la micro-architecture de l'os trabéculaire ont présentés la même capacité d'ostéointégration sur la même profondeur os-métal. Il est probable que la transduction du signal mécanique soit plus importante pour l'ostéointégration que la microarchitecture du biomatériau (155, 156).

Quoi qu'il en soit, l'évolution des techniques d'investigation microscopique a permis de comprendre de nouvelles données concernant des problèmes anciens : la microCT a permis d'apporter de nouvelles données sur l'ONA, de nouvelles techniques de coloration histologique ont pu mettre en évidence des particules jusque-là non observées comme les particules d'alumine en rapport avec l'usure des couples de frottement de PTH utilisant ce type de couple de frottement. L'amélioration des techniques d'investigations montre bien que, quel que soit le type de biomatériau utilisé, celui-ci est soumis aux attaques biochimiques et aux contraintes mécaniques du corps humain et qu'il existe une usure, aussi minime soit-elle. Cette usure est responsable de relargage de particules qui doivent avoir le moins de conséquences sur l'environnement tissulaire dans lequel elles sont déposées. Cela montre bien que ce sont les biomatériaux prévus pour être inertes qui doivent s'adapter à la physiologie et à la biomécanique du corps humain.

Références

1. Toppets V, Pastoret V, De Behr V, Antoine N, Dessy C, Gabriel A. Morphologie, croissance et remaniement du tissu osseux. Ann Med Vet. 2004;148:1-13.
2. Reilly DT, Burstein AH. The mechanical properties of cortical bone. J Bone Joint Surg. 1974;56(5):1001-22.
3. Bousson V, Peyrin F, Bergot C, Hausard M, Sautet A, Laredo JD. Cortical bone in the human femoral neck: three-dimensional appearance and porosity using synchrotron radiation. J Bone Mineral Res. 2004;19(5):794-801.
4. Gibson L. The mechanical behaviour of cancellous bone. J Biomechanics. 1985;18(5):317-28.
5. Ammann P, Rizzoli R. Bone strength and its determinants. Osteopor Int. 2003;14(3):13-8.
6. Parfitt AM. Trabecular bone architecture in the pathogenesis and prevention of fracture. Am J Med. 1987;82(1):68-72.
7. Hvid I, Jensen N, Bünger C, Sølund K, Djurhuus J. Bone mineral assay: its relation to the mechanical strength of cancellous bone. Engineer Med. 1985;14(2):79-83.
8. Frost HM. Skeletal structural adaptations to mechanical usage (SATMU): 2. Redefining Wolff's law: the remodeling problem. Anatomic Record. 1990;226(4):414-22.
9. Teitelbaum SL. Bone resorption by osteoclasts. Science. 2000;289(5484):1504-8.
10. Blair HC, Teitelbaum SL, Ghiselli R, Gluck S. Osteoclastic bone resorption by a polarized vacuolar proton pump. Science. 1989;245(4920):855-7.
11. Arnold A, Dennison E, Kovacs CS, Mannstadt M, Rizzoli R, Brandi ML, et al. Hormonal regulation of biomineralization. Nature Revi Endocrinol. 2021;17(5):261-75.
12. Udagawa N. Mechanisms involved in bone resorption. Biogerontol. 2002;3(1):79-83.
13. Aubin JE, Triffitt JT. Mesenchymal stem cells and osteoblast differentiation. Principles of bone biology: Elsevier; 2002. p. 59-81.
14. Katagiri T, Takahashi N. Regulatory mechanisms of osteoblast and osteoclast differentiation. Oral Dis. 2002;8(3):147-59.
15. Cullinane D. The role of osteocytes in bone regulation: mineral homeostasis versus mechanoreception. J Musculoskelet Neuronal Interact. 2002;2(3):242-4.
16. Cowin S. Mechanosensation and fluid transport in living bone. J Musculoskelet Neuron Interact. 2002;2(3):256-60.
17. Robey PG. Bone matrix proteoglycans and glycoproteins. Principles of bone biology: Elsevier; 2002. p. 225-37.
18. Frost H. Some ABCs of skeletal pathophysiology III: Bone balance and the ΔB. BMU. Calcif Tissue Int. 1989;45(3):131-3.
19. Ott SM. Histomorphometric analysis of bone remodeling. Principles Bone Biolog. 2002:303-23.

20. Chappard D, Baslé M-F, Legrand E, Audran M. Trabecular bone microarchitecture: a review. Morphologie. 2008;92(299):162-70.

21. Hall AC, Horwitz ER, Wilkins RJ. The cellular physiology of articular cartilage. Experiment Physiol Translat Integrat. 1996;81(3):535-45.

22. Imhof H, Breitenseher M, Kainberger F, Rand T, Trattnig S. Importance of subchondral bone to articular cartilage in health and disease. Topic Magnet Resonnance Imag. 1999;10(3):180.

23. FitzGerald O, Bresnihan B. Synovial membrane cellularity and vascularity. Annal Rheumatic Dis. 1995;54(6):511.

24. Radnay CS, Scuderi GR. Management of bone loss: augments, cones, offset stems. Clinic Orthop Relat Res. 2006;446:83-92.

25. Ndiaye M, Terranova L, Mallet R, Mabilleau G, Chappard D. Three-dimensional arrangement of β-tricalcium phosphate granules evaluated by microcomputed tomography and fractal analysis. Acta biomaterial. 2015;11:404-11.

26. Blokhuis TJ, Termaat MF, den Boer FC, Patka P, Bakker FC, Henk JTM. Properties of calcium phosphate ceramics in relation to their in vivo behavior. J Trauma Acute Care Surg. 2000;48(1):179.

27. Christie MJ. Clinical applications of Trabecular Metal. American journal of orthopedics (Belle Mead, NJ). 2002;31(4):219-20.

28. Cohen R. A porous tantalum trabecular metal: basic science. American journal of orthopedics (Belle Mead, NJ). 2002;31(4):216-7.

29. Rony L, Lancigu R, Hubert L. Intraosseous metal implants in orthopedics: A review. Morphologie. 2018;102(339):231-42.

30. Albrektsson T, Brånemark P-I, Hansson H-A, Lindström J. Osseointegrated titanium implants: requirements for ensuring a long-lasting, direct bone-to-implant anchorage in man. Acta Orthopaedica Scandinavica. 1981;52(2):155-70.

31. Carlsson L, Röstlund T, Albrektsson B, Albrektsson T, Brånemark P-I. Osseointegration of titanium implants. Acta Orthopaedica Scandinavica. 1986;57(4):285-9.

32. Windler M, Klabunde R. Titanium for hip and knee prostheses. Titanium in medicine: Springer; 2001. p. 703-46.

33. Bouras T, Bitas V, Fennema P, Korovessis P. Good long-term results following cementless TKA with a titanium plasma coating. Knee Surg Sports Traumatol Arthroscop. 2017;25(9):2801-8.

34. Brockett CL, Harper P, Williams S, Isaac GH, Dwyer-Joyce RS, Jin Z, et al. The influence of clearance on friction, lubrication and squeaking in large diameter metal-on-metal hip replacements. J Material Science. 2008;19(4):1575-9.

35. Amstutz HC, Grigoris P. Metal on metal bearings in hip arthroplasty. Clinic Orthop Relat Res 1996;329:S11-S34.

36. Dowson D, Jin Z-M. Metal-on-metal hip joint tribology. J Engineer Med. 2006;220(2):107-18.

37. Watters TS, Cardona DM, Menon KS, Vinson EN, Bolognesi MP, Dodd LG. Aseptic lymphocyte-dominated vasculitis-associated lesion: a clinicopathologic review of an underrecognized cause of prosthetic failure. Am J Clinic Pathol. 2010;134(6):886-93.

38. Beauchamp J-E, Vendittoli P-A, Barry J, Pelet S, Belzile EL. Catastrophic failure of femoral stem modular junction when combined with metal-on-metal bearing in comparison to ceramic-on-ceramic: A retrospective cohort study. Orthop Traumatol Surg Res. 2021;107(1):102749.

39. Boutin P, Christel P, Dorlot JM, Meunier A, De Roquancourt A, Blanquaert D, et al. The use of dense alumina–alumina ceramic combination in total hip replacement. J Biomed Material Res. 1988;22(12):1203-32.

40. Sedel L, Chappard D, Belzile EL. Ceramic-on-ceramic bearing: Recent progress and solved controversies. Orthop Traumatol Surg Res. 2020:102799-.

41. Zichner LP, Willert H-G. Comparison of alumina-polyethylene and metal-polyethylene in clinical trials. Clinical orthopaedics and related research. 1992(282):86-94.

42. Essner A, Sutton K, Wang A. Hip simulator wear comparison of metal-on-metal, ceramic-on-ceramic and crosslinked UHMWPE bearings. Wear. 2005;259(7-12):992-5.

43. Bistolfi A, Turell MB, Lee YL, Bellare A. Tensile and tribological properties of high-crystallinity radiation crosslinked UHMWPE. J Biomedic Mater Res Part B: Applied Biomater. 2009;90(1):137-44.

44. Oral E, Muratoglu OK. Vitamin E diffused, highly crosslinked UHMWPE: a review. Int Orthop. 2011;35(2):215-23.

45. Bracco P, Oral E. Vitamin E-stabilized UHMWPE for total joint implants: a review. Clinic Orthop Rel Res. 2011;469(8):2286-93.

46. Eriksen E, Vesterby A, Kassem M, Melsen F, Mosekilde L. Bone remodeling and bone structure. Physiology and pharmacology of bone: Springer; 1993. p. 67-109.

47. Eriksen EF. Cellular mechanisms of bone remodeling. Reviews in Endocrin Metabolic Disord. 2010;11(4):219-27.

48. Weinans H, Huiskes R, Grootenboer H. The behavior of adaptive bone-remodeling simulation models. J Biomechanic. 1992;25(12):1425-41.

49. Chappard D. Modelage et remodelage au cours de l'ostéo-intégration. Rev Stomatol, Chir Maxillo-fac Chir Or. 2013;114(3):159-65.

50. Rodan GA. Bone homeostasis. Proceedings of the National Academy of Sciences. 1998;95(23):13361-2.

51. Wu M, Chen G, Li Y-P. TGF-β and BMP signaling in osteoblast, skeletal development, and bone formation, homeostasis and disease. Bone Res. 2016;4(1):1-21.

52. Sánchez-Duffhues G, Hiepen C, Knaus P, Ten Dijke P. Bone morphogenetic protein signaling in bone homeostasis. Bone. 2015;80:43-59.

53. Birkhold AI, Razi H, Duda GN, Weinkamer R, Checa S, Willie BM. The influence of age on adaptive bone formation and bone resorption. Biomaterials. 2014;35(34):9290-301.

54. Carter DR. Mechanical loading histories and cortical bone remodeling. Calcif Tissue Int. 1984;36(1):S19-S24.

55. Sumner DR, Galante JO. Determinants of stress shielding. Clinic Orthop Rel Res. 1992;274:203-12.

56. Glassman A, Bobyn J, Tanzer M. New femoral designs: do they influence stress shielding? Clinic OrthopaRel Res.. 2006;453:64-74.

57. Nagels J, Stokdijk M, Rozing PM. Stress shielding and bone resorption in shoulder arthroplasty. J Shoulder Elbow Surg. 2003;12(1):35-9.

58. Huiskes R, Weinans H, Van Rietbergen B. The relationship between stress shielding and bone resorption around total hip stems and the effects of flexible materials. Clinic Orthop Rel Res. 1992:124-34.

59. Chappard D. Technical aspects: how do we best prepare bone samples for proper histological analysis? Bone Cancer: Elsevier; 2015. p. 111-20.

60. Müller R, Van Campenhout H, Van Damme B, Van der Perre G, Dequeker J, Hildebrand T, et al. Morphometric analysis of human bone biopsies: a quantitative structural comparison of histological sections and micro-computed tomography. Bone. 1998;23(1):59-66.

61. Chappard D, Baslé M-F, Legrand E, Audran M. New laboratory tools in the assessment of bone quality. Osteopor Int. 2011;22(8):2225-40.

62. Weiss RJ, Stark A, Kärrholm J. A modular cementless stem vs. cemented long-stem prostheses in revision surgery of the hip: a population-based study from the Swedish Hip Arthroplasty Register. Act Orthop. 2011;82(2):136-42.

63. Barrack RL, Castro F, Guinn S. Cost of implanting a cemented versus cementless femoral stem. J Arthroplasty. 1996;11(4):373-6.

64. Khanuja HS, Vakil JJ, Goddard MS, Mont MA. Cementless femoral fixation in total hip arthroplasty. J Bone Joint Surg. 2011;93(5):500-9.

65. Garcia-Rey E, Bizot P, Garcia-Cimbrelo E. Ceramic-on-ceramic cementless total hip arthroplasty in patients aged 40 years or under: Do preoperative conditions affect long-term results? Orthop Traumatol Surg Res. 2021;107(1):102763.

66. Vendittoli P-A, Shahin M, Rivière C, Barry J, Lavoie P, Duval N. Ceramic-on-ceramic total hip arthroplasty is superior to metal-on-conventional polyethylene at 20-year follow-up: A randomised clinical trial. Orthop Traumatol Surg Res. 2021;107(1):102744.

67. Boutin P. Le frottement alumine-alumine en chirurgie de la hanche: 1205 arthroplasties totales: Avril 1970-Juin 1980. 1981.

68. Hamadouche M, Boutin P, Daussange J, Bolander ME, Sedel L. Alumina-on-alumina total hip arthroplasty: a minimum 18.5-year follow-up study. J Bone Joint Surg. 2002;84(1):69-77.

69. Livermore J, Ilstrup D, Morrey B. Effect of femoral head size on wear of the polyethylene acetabular component. J Bone Joint Surg Am. 1990;72(4):518-28.

70. Massin P, Viguier E, Flautre B, Hardouin P, Astoin E, Duponchel B. Migration of polyethylene debris along well-fixed cemented implants. J Biomedic Mater Res Part B: Applied Biomaterials: An Official Journal of The Society for Biomaterials, The Japanese Society for Biomaterials, and The Australian Society for Biomaterials and the Korean Society for Biomaterials. 2004;68(2):140-8.

71. Hernigou P, Zilber S, Filippini P, Poignard A. Ceramic-ceramic bearing decreases osteolysis: a 20-year study versus ceramic-polyethylene on the contralateral hip. Clinic Orthop Rel Res. 2009;467(9):2274-80.

72. Wirth MA, Agrawal CM, Mabrey JD, Dean DD, Blanchard CR, Miller MA, et al. Isolation and characterization of polyethylene wear debris associated

with osteolysis following total shoulder arthroplasty. J Bone Joint Surg Am. 1999;81(1):29-37.

73. Holding CA, Findlay DM, Stamenkov R, Neale SD, Lucas H, Dharmapatni A, et al. The correlation of RANK, RANKL and TNFα expression with bone loss volume and polyethylene wear debris around hip implants. Biomat. 2006;27(30):5212-9.

74. Hozack WJ, Mesa JJ, Carey C, Rothman RH. Relationship between polyethylene wear, pelvic osteolysis, and clinical symptomatology in patients with cementless acetabular components: a framework for decision making. J Arthroplasty. 1996;11(7):769-72.

75. Røkkum M, Brandt M, Bye K, Hetland K, Waage S, Reigstad A. Polyethylene wear, osteolysis and acetabular loosening with an HA-coated hip prosthesis: a follow-up of 94 consecutive arthroplasties. J Bone Joint Surg Br. 1999;81(4):582-9.

76. Zhu Y, Chiu K, Tang W. Polyethylene wear and osteolysis in total hip arthroplasty. J Orthop Surg. 2001;9(1):91-9.

77. Harris WH. Reconstruction at a high hip center in acetabular revision surgery using a cementless acetabular component. SLACK Incorporated Thorofare, NJ; 1998.

78. Ahmad AQ, Schwarzkopf R. Clinical evaluation and surgical options in acetabular reconstruction: A literature review. J Orthop. 2015;12:S238-S43.

79. Santaguida PL, Hawker GA, Hudak PL, Glazier R, Mahomed NN, Kreder HJ, et al. Patient characteristics affecting the prognosis of total hip and knee joint arthroplasty: a systematic review. Canad J Surg. 2008;51(6):428.

80. Johnson RL, Abdel MP, Frank RD, Chamberlain AM, Habermann EB, Mantilla CB. Impact of frailty on outcomes after primary and revision total hip arthroplasty. J Arthroplasty. 2019;34(1):56-64. e5.

81. Postler AE, Beyer F, Wegner T, Lützner J, Hartmann A, Ojodu I, et al. Patient-reported outcomes after revision surgery compared to primary total hip arthroplasty. Hip Int. 2017;27(2):180-6.

82. Refior H, Plitz W, Walter A. Ex vivo and in vitro analysis of the alumina/alumina bearing system for hip joint prostheses. Bioceramic. 1997;10:127-30.

83. D'Antonio J, Capello W, Manley M, Bierbaum B. New experience with alumina-on-alumina ceramic bearings for total hip arthroplasty. J Arthroplasty. 2002;17(4):390-7.

84. Bizot P, Nizard R, Hamadouche M, Hannouche D, Sedel L. Prevention of wear and osteolysis: alumina-on-alumina bearing. Clinic Orthop Rel Res. 2001;393:85-93.

85. Hatton A, Nevelos J, Nevelos A, Banks R, Fisher J, Ingham E. Alumina–alumina artificial hip joints. Part I: a histological analysis and characterisation of wear debris by laser capture microdissection of tissues retrieved at revision. Biomat. 2002;23(16):3429-40.

86. Tipper J, Hatton A, Nevelos J, Ingham E, Doyle C, Streicher R, et al. Alumina–alumina artificial hip joints. Part II: characterisation of the wear debris from in vitro hip joint simulations. Biomat. 2002;23(16):3441-8.

87. Lerouge S, Huk O, Yahia LH, Sedel L. Characterization of in vivo wear debris from ceramic—ceramic total hip arthroplasties. J Biomedic Mat Res: An

Official Journal of The Society for Biomaterials and The Japanese Society for Biomaterials. 1996;32(4):627-33.

88. Pizzoferrato A, Stea S, Sudanese A, Toni A, Nigrisoli M, Gualtieri G, et al. Morphometric and microanalytical analyses of alumina wear particles in hip prostheses. Biomat. 1993;14(8):583-7.

89. Affatato S, Goldoni M, Testoni M, Toni A. Mixed oxides prosthetic ceramic ball heads. Part 3: effect of the ZrO2 fraction on the wear of ceramic on ceramic hip joint prostheses. A long-term in vitro wear study. Biomat. 2001;22(7):717-23.

90. Joseph G. Scanning Electron Microscopy and X-RAY Microanalysis; A Text For Biologists, Materials Scientist, And Geologists. 1981.

91. Chappard D, Bizot P, Mabilleau G, Hubert L. Aluminum and bone: Review of new clinical circumstances associated with Al3+ deposition in the calcified matrix of bone. Morphologie. 2016;100(329):95-105.

92. Fernandez-Martin J, Menéndez P, Acuna G, Canteros A, Gómez C, Cannata J. Staining of bone aluminium: comparison between aluminon and solocbrome azurine and their correlation with bone aluminium content. Nephrol Dialysis Transplant. 1996;11(supp3):80-5.

93. Kaye M, Hodsman AB, Malynowsky L. Staining of bone for aluminum: Use of acid solochrome azurine. Kidney Int. 1990;37(4):1142-7.

94. Mold MJ, Kumar M, Chu W, Exley C. Unequivocal imaging of aluminium in human cells and tissues by an improved method using morin. Histochem Cell Biol. 2019;152(6):453-63.

95. Mirza A, King A, Troakes C, Exley C. The identification of aluminum in human brain tissue using lumogallion and fluorescence microscopy. J Alzheimer Dis. 2016;54(4):1333-8.

96. Odri G-A, Sanchez J, Sverzut J-M, Laredo J-D, Sedel L, Bizot P. Does load-bearing materials influence hip capsule thickness in total hip replacement? An MRI case-matched study. Orthop Traumatol Surg Res. 2019.

97. Bertrand J, Delfosse D, Mai V, Awiszus F, Harnisch K, Lohmann C. Ceramic prosthesis surfaces induce an inflammatory cell response and fibrotic tissue changes. Bone Joint J. 2018;100(7):882-90.

98. Bitar D, Parvizi J. Biological response to prosthetic debris. World J Orthop. 2015;6(2):172.

99. Sedel L, Chappard D, Belzile EL. Couple céramique-sur-céramique: progrès récents et controverses éclaircies. Elsevier; 2021.

100. Hirota M, Hayakawa T, Shima T, Ametani A, Tohnai I. High porous titanium scaffolds showed higher compatibility than lower porous beta-tricalcium phosphate scaffolds for regulating human osteoblast and osteoclast differentiation. Material Sci Engineer: C. 2015;49:623-31.

101. Guillaume B. Dental implants: a review. Morphologie. 2016;100(331):189-98.

102. Anselme K, Bigerelle M. Topography effects of pure titanium substrates on human osteoblast long-term adhesion. Act biomat. 2005;1(2):211-22.

103. Apostu D, Lucaciu O, Berce C, Lucaciu D, Cosma D. Current methods of preventing aseptic loosening and improving osseointegration of titanium implants in cementless total hip arthroplasty: a review. J Int Med Res. 2018;46(6):2104-19.

104. Mavrogenis A, Dimitriou R, Parvizi J, Babis GC. Biology of implant osseointegration. J Musculoskelet Neuronal Interact. 2009;9(2):61-71.

105. Stiehler M, Lind M, Mygind T, Baatrup A, Dolatshahi-Pirouz A, Li H, et al. Morphology, proliferation, and osteogenic differentiation of mesenchymal stem cells cultured on titanium, tantalum, and chromium surfaces. J Biomed Mater Res Part A: An Official Journal of The Society for Biomaterials, The Japanese Society for Biomaterials, and The Australian Society for Biomaterials and the Korean Society for Biomaterials. 2008;86(2):448-58.

106. Breer S, Hahn M, Kendoff D, Krause M, Koehne T, Haasper C, et al. Histological ex vivo analysis of retrieved human tantalum augmentations. Int Orthop. 2012;36(11):2269-74.

107. Zardiackas LD, Parsell DE, Dillon LD, Mitchell DW, Nunnery LA, Poggie R. Structure, metallurgy, and mechanical properties of a porous tantalum foam. J Biomedic Material Res: An Official Journal of The Society for Biomaterials, The Japanese Society for Biomaterials, and The Australian Society for Biomaterials and the Korean Society for Biomaterials. 2001;58(2):180-7.

108. Li S, De Wijn JR, Li J, Layrolle P, De Groot K. Macroporous biphasic calcium phosphate scaffold with high permeability/porosity ratio. Tis Engineer. 2003;9(3):535-48.

109. Lu J, Flautre B, Anselme K, Hardouin P, Gallur A, Descamps M, et al. Role of interconnections in porous bioceramics on bone recolonization in vitro and in vivo. J Material Sci: Mat Med. 1999;10(2):111-20.

110. Arbez B, Kün-Darbois JD, Convert T, Guillaume B, Mercier P, Hubert L, et al. Biomaterial granules used for filling bone defects constitute 3D scaffolds: porosity, microarchitecture and molecular composition analyzed by microCT and Raman microspectroscopy. J Biomedic Material Res Part B: Applied Biomaterials. 2019;107(2):415-23.

111. Chen Z, Yan X, Yin S, Liu L, Liu X, Zhao G, et al. Influence of the pore size and porosity of selective laser melted Ti6Al4V ELI porous scaffold on cell proliferation, osteogenesis and bone ingrowth. Material Sci Engineer: C. 2020;106:110289.

112. Spetzger U, Frasca M, König SA. Surgical planning, manufacturing and implantation of an individualized cervical fusion titanium cage using patient-specific data. Europ Spine J. 2016;25(7):2239-46.

113. Liljenqvist U, Lerner T, Bullmann V, Hackenberg L, Halm H, Winkelmann W. Titanium cages in the surgical treatment of severe vertebral osteomyelitis. Europ Spine J. 2003;12(6):606-12.

114. Chappard D, Terranova L, Mallet R, Mercier P. 3D porous architecture of stacks of β-TcP granules compared with that of trabecular bone: a microcT, vector analysis, and compression study. Frontiers Endocrinol. 2015;6:161.

115. Wang X, Nyman JS, Dong X, Leng H, Reyes M. Fundamental biomechanics in bone tissue engineering. Synth Lect Tissue Engineer. 2010;2(1):1-225.

116. Geurs NC, Jeffcoat RL, McGlumphy EA, Reddy MS, Jeffcoat MK. Influence of implant geometry and surface characteristics on progressive osseointegration. Int J Oral Maxillo-fac Implant. 2002;17(6).

117. Martini L, Fini M, Giavaresi G, Giardino R. Sheep model in orthopedic research: a literature review. Comparative Med. 2001;51(4):292-9.

118. Turner A. The sheep as a model for osteoporosis in humans. Veterinar J. 2002;163(3):232-9.

119. Rony L, Aguado E, Pascaretti-Grizon F, Hubert L, Chappard D. Hyaluronic acid stimulates osseointegration of β-TCP in young and old ewes. Calcif Tissue Int. 2019;105(5):487-96.

120. Palmquist A, Snis A, Emanuelsson L, Browne M, Thomsen P. Long-term biocompatibility and osseointegration of electron beam melted, free-form–fabricated solid and porous titanium alloy: Experimental studies in sheep. J Biomater Applic. 2013;27(8):1003-16.

121. Arlet J, Ficat P. Diagnosis of primary femur head osteonecrosis at stage 1 (preradiologic stage). Rev Chir Orthop Rep App Mot. 1968;54(7):637-48.

122. Lespasio MJ, Sodhi N, Mont MA. Osteonecrosis of the hip: a primer. Permanent J. 2019;23.

123. Petek D, Hannouche D, Suva D. Osteonecrosis of the femoral head: pathophysiology and current concepts of treatment. EFORT open reviews. 2019;4(3):85-97.

124. Guerado E, Caso E. The physiopathology of avascular necrosis of the femoral head: an update. Injury. 2016;47:S16-S26.

125. Catto M. A histological study of avascular necrosis of the femoral head after transcervical fracture. J Bone Joint Surg Br. 1965;47(4):749-76.

126. Huffman K, Bowers J, Dailiana Z, Huebner J, Urbaniak J, Kraus V. Synovial fluid metabolites in osteonecrosis. Rheumatol. 2007;46(3):523-8.

127. Im G-I, Kim D-Y, Shin J-H, Cho W-H, Lee C-J. Degeneration of the acetabular cartilage in osteonecrosis of the femoral head: histopathologic examination of 15 hips. Act Orthop Scand. 2000;71(1):28-30.

128. Fondi C, Franchi A. Definition of bone necrosis by the pathologist. Clinic Cases Mineral Bone Metabol. 2007;4(1):21.

129. Kün-Darbois J-D, Manero F, Rony L, Chappard D. Contrast enhancement with uranyl acetate allows quantitative analysis of the articular cartilage by microCT: Application to mandibular condyles in the BTX rat model of disuse. Micron. 2017;97:35-40.

130. Rony L, Perrot R, Hubert L, Chappard D. Osteocyte staining with rhodamine in osteonecrosis and osteoarthritis of the femoral head. Microsc Res Tec. 2019;82(12):2072-8.

131. Salmon PL, Sasov AY. Application of nano-CT and high-resolution micro-CT to study bone quality and ultrastructure, scaffold biomaterials and vascular networks. Advanced bioimaging technologies in assessment of the quality of bone and scaffold materials: Springer; 2007. p. 323-31.

132. Loiselle AE, Jiang JX, Donahue HJ. Gap junction and hemichannel functions in osteocytes. Bone. 2013;54(2):205-12.

133. Civitelli R. Cell–cell communication in the osteoblast/osteocyte lineage. Archiv Biochem Bioph. 2008;473(2):188-92.

134. Nakashima T, Hayashi M, Fukunaga T, Kurata K, Oh-Hora M, Feng JQ, et al. Evidence for osteocyte regulation of bone homeostasis through RANKL expression. Nature Med. 2011;17(10):1231-4.

135. Bonewald LF. The amazing osteocyte. J Bone Mineral Res. 2011;26(2):229-38.

136. Romanello M, D'Andrea P. Dual mechanism of intercellular communication in HOBIT osteoblastic cells: A role for gap-junctional hemichannels. J Bone Mineral Res. 2001;16(8):1465-76.

137. Bellido T. Osteocyte-driven bone remodeling. Calcifi Tissue Int. 2014;94(1):25-34.

138. Bonewald LF. The role of the osteocyte in bone and nonbone disease. Endocrinol Metabol Clinic. 2017;46(1):1-18.

139. Trueta J. The role of the vessels in osteogenesis. J Bone Joint Surg Br. 1963;45(2):402-18.

140. Metscher BD. MicroCT for comparative morphology: simple staining methods allow high-contrast 3D imaging of diverse non-mineralized animal tissues. BMC Physiol. 2009;9(1):1-14.

141. Wong S, Evans RA, Needs C, DUNsTAN CR, Hills E, Garvan J. The pathogenesis of osteoarthritis of the hip. Evidence for primary osteocyte death. Clinic Orthop Rel Res. 1987(214):305-12.

142. Biewener AA, Swartz SM, Bertram JE. Bone modeling during growth: dynamic strain equilibrium in the chick tibiotarsus. Calcifi Tissue Int. 1986;39(6):390-5.

143. Olsen BR, Reginato AM, Wang W. Bone development. An Rev Cell Devlop Biol. 2000;16(1):191-220.

144. Forwood MR. Physical activity and bone development during childhood: insights from animal models. J Appl Physiol. 2008;105(1):334-41.

145. Chen X, Wang Z, Duan N, Zhu G, Schwarz EM, Xie C. Osteoblast–osteoclast interactions. Connect Tissue Res. 2018;59(2):99-107.

146. Katagiri T, Takahashi N. Regulatory mechanisms of osteoblast and osteoclast differentiation. Oral dis. 2002;8(3):147-59.

147. Cao X. Targeting osteoclast-osteoblast communication. Nature Med. 2011;17(11):1344-6.

148. Hernigou P, Drescher WR. Stem Cell Therapy for the Treatment of Hip Osteonecrosis. Advances in Specialist Hip Surgery: Springer; 2021. p. 147-53.

149. Huten D, Bourgoin A, Lambotte J. Treatment of aseptic osteonecrosis of the femoral head: Historical aspects. Morphologie. 2021.

150. Hernigou J, Housset V, Dubory A, Lachaniette CF, Rouard H, Hernigou P. Cell therapy for post-traumatic hip osteonecrosis in young patients. Morphologie. 2020.

151. Karachalios T, Komnos G, Koutalos A. Total hip arthroplasty: survival and modes of failure. EFORT open reviews. 2018;3(5):232-9.

152. Caton J, Prudhon JL. Over 25 years survival after Charnley's total hip arthroplasty. Int Orthop. 2011;35(2):185-8.

153. Kurtz SM, Ong KL, Schmier J, Mowat F, Saleh K, Dybvik E, et al. Future clinical and economic impact of revision total hip and knee arthroplasty. J Bone Joint Surg. 2007;89(suppl_3):144-51.

154. Pedersen AB, Baron J, Overgaard S, Johnsen S. Short-and long-term mortality following primary total hip replacement for osteoarthritis: a Danish nationwide epidemiological study. J Bone Joint Surg Br. 2011;93(2):172-7.

155. Massin P. Treatments of avascular osteonecrosis of the hip: Current treatments. Morphologie. 2020.

156. Oral E, Wannomae KK, Rowell SL, Muratoglu OK. Diffusion of vitamin E in ultra-high molecular weight polyethylene. Biomater. 2007;28(35):5225-37.

157. Radnay CS, Scuderi GR. Management of bone loss: augments, cones, offset stems. Clinic Orthop Rel Res. 2006;446:83-92.

158. Bandyopadhyay A, Espana F, Balla VK, Bose S, Ohgami Y, Davies NM. Influence of porosity on mechanical properties and in vivo response of Ti6Al4V implants. Act Biomater. 2010;6(4):1640-8.

159. Simon U, Augat P, Ignatius A, Claes L. Influence of the stiffness of bone defect implants on the mechanical conditions at the interface—a finite element analysis with contact. J Biomechan. 2003;36(8):1079-86.

Table des matières

RÉSUMÉ

Ce travail est composé de trois parties permettant d'améliorer la compréhension du remodelage osseux dans des domaines concrets de la chirurgie osseuse.

La première partie porte sur les débris d'usure péri-prothétiques de prothèse totale de hanche utilisant un couple de frottement alumine-alumine réputé pour ne pas s'user. Pour autant, les travaux réalisés ont permis l'identification de particules d'usure d'alumine dans les tissus péri-prothétiques. Il s'agit des premiers travaux identifiant de telles particules.

La deuxième partie porte sur le remodelage d'implants en titane utilisés pour le comblement de défect osseux cavitaire dans des condyles fémoraux de brebis. L'analyse de la microarchitecture de ces implants réalisés par impression 3D a permis de comprendre que la rigidité des implants en titane ne permettait pas une meilleure intégration de ces implants malgré une microarchitecture reproduisant un os trabéculaire du fait de l'absence de transduction des contraintes mécaniques au sein de ces implants.

La troisième partie porte sur l'ostéonécrose aseptique de hanche où l'analyse en microtomographie et en microscopie optique a permis de mieux appréhender le découplage ostéoblaste-ostéoclaste existant dans cette pathologie. En effet, l'analyse réalisée a permis de démontrer qu'il existait un modelage et non un remodelage dans cette pathologie.

Ces trois parties permettent de mieux comprendre les phénomènes microscopiques du tissu osseux essentiels pour la réalisation de certaines interventions chirurgicales orthopédiques.

mots-clés : ostéonécrose aseptique de hanche, remodelage osseux, ostéointégration, impression 3D, implant titane

ABSTRACT

This work is composed of three parts to improve the understanding of bone remodeling in concrete areas of bone surgery.

The first part deals with the peri-prosthetic wear debris of a total hip prosthesis using an alumina-alumina friction couple known not to wear. However, the work carried out has allowed the identification of alumina wear particles in the periprosthetic tissues. This is the first work identifying such particles.

The second part deals with the remodeling of titanium implants used to fill cavitary bone defects in the femoral condyles of sheep. The analysis of the microarchitecture of these implants made by 3D printing allowed us to understand that the rigidity of the titanium implants did not allow a better integration of these implants despite a microarchitecture reproducing a trabecular bone because of the absence of transduction of mechanical constraints within these implants.

The third part deals with aseptic osteonecrosis of the hip, where microtomographic and optical microscopy analysis has allowed a better understanding of the osteoblast-osteoclast decoupling existing in this pathology. Indeed, the analysis carried out allowed to demonstrate that there was a modeling and not a remodeling in this pathology.

These three parts allow a better understanding of the microscopic phenomena of the bone tissue essential for the realization of certain orthopedic surgical interventions.

keywords : aseptic hip osteonecrosis, bone remodeling, osseointegration, 3D printing, titanium implant

Présidence de l'université
40 rue de rennes – BP 73532
49035 Angers cedex
Tél. 02 41 96 23 23 | Fax 02 41 96 23 00

université
angers

DOCTORAT BIOLOGIE
BRETAGNE SANTE
LOIRE

université
angers

Remodelage dans les explants orthopédiques et au contact des biomatériaux utilisés en chirurgie osseuse

Mots clés : Ostéonécrose aseptique de hanche, remodelage osseux, ostéointégration, impression 3D, implant titane

Résumé : Ce travail est composé de trois parties permettant d'améliorer la compréhension du remodelage osseux dans des domaines concrets de la chirurgie osseuse.

La première partie porte sur les débris d'usure péri-prothétiques de prothèse totale de hanche utilisant un couple de frottement alumine-alumine réputé pour ne pas s'user. Pour autant, les travaux réalisés ont permis l'identification de particule d'usure d'alumine dans les tissus péri-prothétiques. Il s'agit des premiers travaux identifiant de telles particules.

La deuxième partie porte sur le remodelage d'implants en titane utilisés pour le comblement de défect osseux cavitaire dans des condyles fémoraux de brebis. L'analyse de la microarchitecture de ces implants réalisés par impression 3D a permis de comprendre que la rigidité des implants en titane ne permettait pas une meilleure intégration de ces implants malgré une microarchitecture reproduisant un os trabéculaire du fait de l'absence de transduction des contraintes mécaniques au sein de ces implants.

La troisième partie porte sur l'ostéonécrose aseptique de hanche où l'analyse en microtomographie et en microscopie optique a permis de mieux appréhender le découplage ostéoblaste-ostéoclaste existant dans cette pathologie. En effet, l'analyse réalisée a permis démontrer qu'il existait un modelage et non un remodelage dans cette pathologie.

Ces trois parties permettent de mieux comprendre les phénomènes microscopiques du tissu osseux essentiels pour la réalisation de certaines interventions chirurgicales orthopédiques.

Remodeling in orthopedic explants and in contact with biomaterials used in bone surgery

Keywords : Aseptic hip osteonecrosis, bone remodeling, osseointegration, 3D printing, titanium implant

Abstract : This work is composed of three parts to improve the understanding of bone remodeling in concrete areas of bone surgery.

The first part deals with the peri-prosthetic wear debris of a total hip prosthesis using an alumina-alumina friction couple known not to wear. However, the work carried out has allowed the identification of alumina wear particles in the periprosthetic tissues. This is the first work identifying such particles.

The second part deals with the remodeling of titanium implants used to fill cavitary bone defects in the femoral condyles of sheep. The analysis of the microarchitecture of these implants made by 3D printing allowed us to understand that the rigidity of the titanium implants did not allow a better integration of these implants despite a microarchitecture reproducing a trabecular bone because of the absence of transduction of mechanical constraints within these implants.

The third part deals with aseptic osteonecrosis of the hip, where microtomographic and optical microscopy analysis has allowed a better understanding of the osteoblast-osteoclast decoupling existing in this pathology. Indeed, the analysis carried out allowed to demonstrate that there was a modeling and not a remodeling in this pathology.

These three parts allow a better understanding of the microscopic phenomena of the bone tissue essential for the realization of certain orthopedic surgical interventions.